AERODYNAMIC CONTROL OF FLOW DYNAMICS COUPLED TO A FREE-FLIGHT AXISYMMETRIC BODY

A Dissertation
Presented to
The Academic Faculty

by

Thomas John Lambert

In Partial Fulfillment
Of the Requirements for the Degree
Doctor of Philosophy in Mechanical Engineering

Georgia Institute of Technology
George W. Woodruff School of Mechanical Engineering

December 2016

AERODYNAMIC CONTROL OF FLOW DYNAMICS COUPLED TO A FREE-FLIGHT AXISYMMETRIC BODY

Approved by:

Professor Ari Glezer, Advisor
School of Mechanical Engineering
Georgia Institute of Technology

Professor Marilyn Smith
School of Aerospace Engineering
Georgia Institute of Technology

Professor Mark Costello
School of Aerospace Engineering
Georgia Institute of Technology

Dr. Bojan Vukasinovic
School of Mechanical Engineering
Georgia Institute of Technology

Professor Marc K. Smith
School of Mechanical Engineering
Georgia Institute of Technology

Approved: November 15, 2016

Dedicated to my mother and brother,
Joan Dickie and Robert Michael

and in loving memory of my father,
Robert Henry

ACKNOWLEDGEMENTS

I offer my sincerest gratitude to the many people who have helped me throughout my graduate school experience. Financially, this work was made possible with the support of the Army Research Office and Georgia Tech. This work would also not have been possible without my advisor, Professor Ari Glezer. In addition to supplying a tremendous amount of helpful advice, you have always been free for discussions about any current issues I have been running into from technical difficulties in experimental equipment, to theoretical formulations of aerodynamic equations, to personal difficulties, and many more. Thank you for personally helping me develop a strong work ethic and a direct approach to overcoming even the most perplexing of technical complications.

I am indebted to all my committee members for their time and patience with me throughout my proposal until my defense. To Dr. Bojan Vukasinovic, in many ways you have been a second advisor to me throughout my time here and I can always rely on your advice to be on point, accurate, and helpful. Believe it or not, you helped teach me LabVIEW when I got here, and without your help (in advice, programming, and even directly in experiments) I could not have overcome a lot of the challenges presented throughout this doctoral research. Thank you very much for your time, effort, and friendship. To Professors Marilyn Smith, Marc Smith, Mark Costello, thank you very much for taking the time to offer your helpful advice throughout this entire process from my proposal presentation to my dissertation defense. I would also like to thank a student in Professor Marilyn Smith's lab, Jagadeesh Movva, who provided a lot of insight into a computational approach for modelling the flow behind tethered bluff bodies with a reduced

order modelling technique. Your work provided personal insight into the unsteady contributions in some of the reduced frequency variation investigations in this Thesis.

I would like to thank my lab mates and coworkers in the Fluid Mechanics Research Laboratory. To the research engineers, John Culp, Dr. Slava Yorish, Dr. Pablo Hidalgo, and Dr. Tom Crittenden, thank you for providing time effective technical solutions and/or insight to numerous unforeseen experimental complications. To the older generation, Dan Brzozowski, and Michael DeSalvo, thank you for being immense sources of wisdom when I first began. Thank you to the senior students, George Woo, Abe Gissen, John Kearney, and Mark Simpson. You have all provided a lot of your time to teach me an uncountable amount of skills such as PIV, hotwire anemometry, optics, presentation design, electrical engineering, and how to pass my qualification exams, to name a few, and I am deeply indebted to all of you. Thank you to Tom Boziuk; our journey through grad school is quite a memorable one and you have set the standard very high for whoever I share an office with after Georgia Tech, and I am going to miss your sense of humor, intelligence, and devotion to detail. To Sourabh Jha, Yuehan Tan, Curtis Peterson, Travis Burrows, Alon Katz, I enjoyed most of our discussions in lab (technical or otherwise), and know your talents will lead all of you to succeed at Georgia Tech and afterwards. To Edward Lee, it was great to work with you over the last few months and I am glad this project is being continued by someone so capable, friendly, and smart. Thank you all for your friendship.

Thank you to my friends (both past in Las Vegas and Pittsburgh, and the present ones I met in Atlanta), and my main thank you goes to my family (especially my mom and brother). Without all of you, I would not have had the heart to continue my research and stay (relatively) optimistic throughout this process. I cannot thank all of you enough!

TABLE OF CONTENTS

LIST OF TABLES

LIST OF FIGURES

NOMENCLATURE

A	state transition operator between two times in a flow field, estimated by DMD
A_J	synthetic jet orifice area
a_n	growth rate of nth DMD mode
A_n	weighted time coefficient of nth POD mode
A_w	wake area resolved with hotwire anemometry, defined by $0.95U_o$
c	axisymmetric model chord
C_D, C_S, C_L	aerodynamic drag, side, and lift coefficients in x, y, and z, respectively
C_{Do}	aerodynamic drag coefficient of the centered bluff body model
C_R, C_M, C_Y	aerodynamic roll, pitch, and yaw coefficients in x, y, and z, respectively
C_μ	jet momentum coefficient: $C_\mu = (4U_J^2A_J)/(\pi U_o^2 D^2)$
D	axisymmetric model diameter
d_n	weighting coefficient of nth DMD mode
D_{SMA}	shape memory alloy wire diameter
D_{wire}	mounting wire diameter
E_n	nth POD mode energy contribution percentage
f	frequency, typically of the model motion
f_x, f_y, f_z	frequency of model motion in the x, y, and z directions
f_{act}, f_{act}^*	actuation frequency, scaled by $f_{act}^* = 2f_{act}h_J/U_o$
f_{shed}	dominant measured wake shedding frequency
f_{wire}	shedding frequency of a model mounting wire
$\overrightarrow{F_{A_{wires}}}$	aerodynamic force vectors on the mounting wires
$\overrightarrow{F_{A_{model}}}$	aerodynamic force vector on the model
$\overrightarrow{F_G}, \overrightarrow{F_I}$	gravitational and inertial force vectors on the model
f_n	frequency of nth DMD mode

F_{SMA}, C_{SMA}	resulting SMA wire force, scaled by $C_{SMA} = 2F_{SMA}/(\rho U_o^2 D_{SMA} L_{SMA})$
$\dot{F}_{SMA}$, $\dot{C}_{SMA}$	resulting SMA wire force rate, scaled by $\dot{C}_{SMA} = 2\dot{F}_{SMA}/(\rho U_o^3 D_{SMA})$
$\overrightarrow{F_T}$	tension forces of the mounting wires on the model
F_x, F_y, F_z	aerodynamic forces on the model in the *x*, *y*, and *z* directions
h_J	synthetic jet orifice height
h_S	backward-facing step height
I_x, C_x, K_x	Mounting inertia, damping, and spring constants for 'free' 3-DOF model roll
I_{yz}, C_{yz}	Mounting inertia and damping constants for 'free' 3-DOF model pitch and yaw
I_{1D}, C_{1D}, K_{1D}	Mounting inertia, damping, and spring constants for the 'free' 1-DOF model
k	reduced frequency of the model: $k = \pi fc/U_o$ (note: same as half-chord definition)
L_{SMA}	shape memory alloy wire length
M_R, M_P, M_Y	aerodynamic roll, pitch, and yaw moments in *x*, *y*, and *z*, respectively
Mod_L, Mod_R	modulation amplitude of left and right actuation resonance waveforms in 1-DOF
n	modal decomposition index for POD or DMD modes, ordered by energy
N	number of actuation pulses
NN	number of instantaneous vector fields in a POD or DMD analyses
N_{set}	number of calculated modes in a POD or DMD analyses
P_A, P_A^*	actuation power, scaled by $P_A^* = 24P_A/(\pi\rho U_o^3 D^2)$
P_{SMA}, P_{SMA}^*	applied SMA wire power, scaled by $P_{SMA}^* = 6P_{SMA}/(\rho U_o^3 D_{SMA} L_{SMA})$
psd	power spectral distribution of frequencies in a time trace
q	planar velocity resolved by hot-wire anemometry: $q = (U_x^2 + U_z^2)^{0.5}$
Q_{crit}	Q criterion to determine vector rejection from PIV measurements
R_C	Coanda surface radius
Re_D	flow Reynolds number: $Re_D = \rho U_o D/\mu$
Re_{wire}	wire Reynolds number: $Re_D = \rho U_o D_{wire}/\mu$
St_D	Strouhal number of wake shedding: $St_D = f_{shed} D/U_o$
t	elapsed time during an experimental acquisition

t_{ref}	reference time for plotting a 3-D stream surface from stereo PIV
T_o	nominal tunnel freestream temperature
$\widehat{U}_C$	cross-stream wake velocity for off-center PIV planes
U_J	maximum synthetic jet expulsion velocity
U_{max}	maximum tunnel freestream speed
U_o	nominal tunnel freestream speed
U_x, U_y, U_z	measured wake velocity in the streamwise, spanwise, and vertical directions
$\widehat{U}_{x,}$ $\widehat{U}_{y,}$ $\widehat{U}_z$	phase averaged wake velocities
x, y, z	reference coordinate axes with streamwise x, cross-stream y, and vertical z
x_{cp}	streamwise location of the model center of pressure
x_C	streamwise location of center of wire mounts
x_L	streamwise location of the laser vibrometer mounting location
x_m, y_m, z_m	coordinate axes at model bearing in the 'free' 3-DOF experiments
x_o	streamwise location for axis of free motions in 1-DOF or 3-DOF
x_s, y_s, z_s	coordinate axes at center of sting in the 'free' 3-DOF experiments
$\vec{X}$	state vector for POD analysis formed from 3-D velocity field
$\vec{X}$'	time shifted state vector of 3-D velocity field for DMD analysis
z_w	wake vertical centroid measured by hotwire anemometry, defined by $0.95U_o$
$\bar{\alpha}$	maximum stable offset angle when a 'free' model was controlled off-center
α_{RMS}	root mean square amplitude of angular displacement oscillations in 1-DOF
$\alpha_{x\text{-}RMS}$	root mean square amplitude of roll oscillations in 3-DOF
$\alpha_{y\text{-}RMS}$	root mean square amplitude of pitch oscillations in 3-DOF
$\alpha_{z\text{-}RMS}$	root mean square amplitude of yaw oscillations in 3-DOF
α_x, α_y, α_z	roll, pitch, and yaw angles around the x, y, and z, coordinates, respectively.
$\dot{\alpha}_x$, $\dot{\alpha}_y$, $\dot{\alpha}_z$	roll, pitch, and yaw rates
$\ddot{\alpha}_x$, $\ddot{\alpha}_y$, $\ddot{\alpha}_z$	roll, pitch, and yaw angular accelerations

δ	vector spacing in a PIV measurement
δt	time shift between states in DMD analysis
δU	velocity fluctuations in a phase averaged PIV measurement
$\delta\zeta$	vorticity fluctuations in a phase averaged PIV measurement
$\Delta C_{D,S,L}$	jet induced drag, side, and lift forces relative to an unactuated model
$\Delta C_{R,M,Y}$	jet induced roll, pitch, and yaw moments relative to an unactuated model
Δt	time between successive laser pulses in a PIV measurement
Δy	space between off-center cross-stream PIV measurement planes
$\vec{\varphi}_n$	nth pod mode with respective components: $\vec{\varphi}_{n,u}$, $\vec{\varphi}_{n,v}$, $\vec{\varphi}_{n,w}$
$\vec{\varphi}_{n,\zeta}$	derived vorticity of nth pod mode from the cross-stream components
κ_P, κ_I, κ_D	proportional, integral, and derivative coefficients of 1-DOF flow controller
$\kappa_{P,in}$, $\kappa_{I,in}$, $\kappa_{D,in}$	proportional, integral, and derivative coefficients of the traverse inner loop
$\kappa_{P,y}$, $\kappa_{D,y}$	proportional and derivative coefficients of 3-DOF pitch flow controller
$\kappa_{P,z}$, $\kappa_{D,z}$	proportional and derivative coefficients of 3-DOF yaw flow controller
$\kappa_{I,out}$	integral coefficients of the traverse outer loop controller
λ_n	eigenvalue of *n*th POD mode, with a real value
$\lambda_{n,DMD}$	eigenvalue of *n*th DMD mode, with an imaginary value
μ, ρ	dynamic viscosity and density of air
θ_y, θ_z	angular deflections of the wake based on $0.8U_o$ in SPIV measurements
τ_{act}	time duration of one actuation cycle
τ_{conv}	model convective time scale: $\tau_{conv} = U_o/c$
τ_{SMA}	convective time scale of an SMA wire: $\tau_{SMA} = U_o/L_{SMA}$
τ_y, τ_z, τ_{yz},	motion time constants in pitch, yaw, or combined pitch and yaw
ζ_x, ζ_y, ζ_z	measured wake vorticity in the streamwise, spanwise, and vertical directions
$\hat{\zeta}_x$, $\hat{\zeta}_y$, $\hat{\zeta}_z$	phase averaged wake vorticities

SUMMARY

This research focuses on the unsteady flow mechanisms of using aerodynamic flow control at the aft end flow boundary of a bluff body to modify the reciprocal coupling to its wake dynamics. Building on earlier findings at Georgia Tech which demonstrated that fluidic actuation can affect the global aerodynamic forces and moments on a stationary body, the present research hypothesizes that active alteration of the wake of a moving body can enable prescribed modification of the time-dependent aerodynamic loads (forces and moments), and, consequently, can lead to active control of its motion and stability. The present investigations utilize an axisymmetric model integrated with individually-controlled miniature synthetic jet actuators in multiple experimental setups, such as a wire-mounted programmable six degrees of freedom (6-DOF) traverse. The interactions between the actuation and the cross flow are investigated using particle image velocimetry (PIV), hot-wire anemometry, and a real-time motion analysis camera system. The present investigations elucidate aerodynamic control of the coupling mechanisms between the flow and the platform in prescribed motion (in which the effected changes in the flow and the induced aerodynamic loads do not affect the platform motion), and in free flight (in which the induced changes in the flow feedback to the motion). These investigations demonstrate that both open- or closed-loop actuation strategies for enhancement or suppression of the inherent flow coupling can have profound effects on the evolution and stability of the near wake and on the induced unsteady aerodynamic loads on the body.

CHAPTER I

PRIOR WORK AND PRESENT OBJECTIVES

This Thesis explores aerodynamic flow control of the unsteady mechanisms that couple between a stationary or moving 3-D bluff body and its wake, hypothesizing that active alteration of the embedding flow can lead to control of the body motion and stability. To introduce this research area, this chapter briefly reviews earlier studies of flow around 2- and 3-D bluff bodies (§**1.1**), stability characteristics of their near wakes (§**1.2**), aerodynamic control by mechanical devices (§**1.3**), examples of bluff body flow control (§**1.4**), techniques for installation in wind tunnel experiments (§**1.5**), and analysis of large sets of flow field data using decomposition techniques (§**1.6**). Lastly, the objectives of the present research are outlined in §**1.7**.

1.1 Flow Characteristics over 2- and 3-D Bluff Bodies

The present investigation is concerned with flow control over bluff bodies, specifically axisymmetric bluff bodies, which are typically defined as bodies in a flow that are dominated by pressure drag. The characteristics and complex structure and dynamics of spatially developing wakes of 2- and 3-D bluff bodies have been the subject of numerous theoretical, analytical, and experimental investigations that have been motivated by a broad range of technological applications, such as reduction of aerodynamic drag, mitigation of aeroelastic and structural vibrations, and noise abatement, to name a few. A large body of research has been devoted to the flow around stationary, nominally 2-D prismatic bluff bodies (or bluff bodies that are approximated as having infinite span) that are typically characterized by vortex formation and shedding in the near wake following the classic investigations of Roshko (1955), as discussed in a review by Berger and Wille (1972). More recent investigations have emphasized 2- and 3-D stability analyses of bluff body wakes (e.g., Monkewitz and Nguyen, 1987), as reviewed briefly in §**1.2**. Williamson

(1996) found that the wakes of nominally 2-D bluff bodies exhibit significant 3-D structure that depends on the spanwise boundary conditions and are manifested by cellular and oblique vortex shedding, and the formation of vortex loops which complicate analytical investigations of the 2-D flow. Given the apparent susceptibility of the base flow to weak disturbances (e.g., because of the edge conditions) numerous experimental and computational investigations have focused on the use of active and passive devices with the objective of suppressing the wake instabilities and thereby controlling the vortex shedding and potentially reducing drag (see also §**1.4)**.

A canonical 3-D bluff body flow that has been a subject of extensive research is the wake behind a sphere. Achenbach (1974) measured the variation of Strouhal number with Reynolds number between 200 and 300,000 and compared his findings with earlier data from the 1930s through the 1960s. More recently these measurements were extended in the experiments of Sakamoto and Haniu (1990), who used hot-wire anemometry to identify four unique shedding regimes that are classified by the Reynolds number and showed that the onset of the instability occurs at a critical Reynolds number of about 200. Linear stability analysis of the wake of a sphere by Kim and Pearlstein (1990) predicted a similar stability boundary. Several numerical investigations considered the effect of the flow speed on the evolution of the vortical structures in sphere wakes (e.g., Ploumhans et al., 2002, for $300 < Re < 1{,}000$).

Dynamic interactions between the bluff body and its wake have been a significant area of research that has been motivated by vortex-induced vibrations (VIV) in many geometric configurations. A subset of these phenomena has been investigated on 2-D circular cylinders whose axes are normal to an oncoming uniform flow. These cylinders are typically supported by springs at their spanwise edges, oscillate in a plane that is normal to the cross flow, and can be modeled as a forced second order system. In one of the first studies of the underlying dynamic of induced cylinder vibrations, Feng (1968) proposed a

'lock-in' mechanism by which the vortex shedding at a frequency that is close to the cylinder natural frequency excites oscillations thereby creating feedback that locks the vortex shedding to the cylinder natural frequency. Williamson and Roshko (1988) classified vortex regimes in the wake of a cylinder that is forced to oscillate transversely to the oncoming flow. They showed that combinations of trains of single vortices and vortex pairs (dubbed 'S' and 'P', respectively) yield distinct dominant vortical wake structures (dubbed '2S', '2P', and 'S+P'). Brika and Laneville (1993) confirmed experimentally that while '2S' and '2P' modes of the wake of a forced cylinder are also present in the vortex-induced oscillation of a free cylinder, while 'S+P' is not. A systematic consideration of the relevant reduced parameters in the numerical investigation of Leonard and Roshko (2001) suggested that the motion can be characterized by three primary parameters namely, the effective stiffness, damping, and Reynolds number that define branching of the realizable states.

In a review of flow-induced vibrations, Williamson and Govardhan (2004) showed that the vibration response has different regimes that depend on the physical parameters of the model and on the spatial modes of the shed vortices. In particular, the range of the flow conditions that induce a large amplitude cylinder oscillations depends on the ratio of the body mass to the fluid mass in the displaced volume, where a critical magnitude of this mass ratio delineates between an infinite response range for low mass ratios and a lock-in range for high mass ratios. Govardhan and Williamson (2002) showed that in the absence of the spring restoring force there are no cylinder oscillations for high mass ratios but the cylinder exhibits resonance for any mass ratio below the critical value. Moreover, without a restoring spring the resonant response of the cylinder is independent of the shedding

period (or inverse Strouhal number) as long as it is sufficiently large, and the response amplitude and frequency depend only on the mass ratio. While the vortex induced vibrations of a 2-D circular cylinder have arguably been the most frequently studied configuration of VIV other configurations that involve more complex motions have also been investigated. Flemming and Williamson (2005) noted that for a pivoted cylinder supported such that it can respond in two degrees of freedom of combined transverse-streamwise motion, the critical inertia (equivalent to the critical mass in 1-D transverse vibrations) is the bound below which resonant oscillations occur over a broad range of the flow speeds. Another variant configuration that has been investigated is that of tethered cylinders (e.g., Carberry and Sheridan, 2007) that exhibit three modes of oscillations namely, transverse, in-line, and a combination of the two, where the lock-in to the shedding frequency dominates the overall response. Furthermore, the wake of a tethered cylinder contains all three vortex shedding modes ('2S', '2P', and 'P+S').

Clearly, when the moving model is not 2-D, its interaction with the oncoming flow and its wake become more complex. Berger, Scholz, and Schumm (1990) investigated the wake structure of both a disk and a sphere by applying forced vibration through wires. These authors found that for $Re < 200{,}000$ the wake exhibited three primary instabilities: an axisymmetric pumping mode in the recirculation region, an antisymmetric helical shedding mode, and a high frequency instability in the separated shear layers. The forced vibrations could either excite a nutational instability of these bodies or a pumping instability in the streamwise direction, although only the nutational instability was observed in free falling spheres or non-spin stabilized bullets. In a numerical investigation

of the wake of a sphere, Mittal and Najjar (1999) demonstrated that, like a cylinder at low Reynolds numbers (around 500), the sphere is also susceptible to a 'lock-on' frequency.

When a 3-D geometry of the bluff body is not axisymmetric, the vortex phenomena in the wake become far more complex (e.g., the wake of a simplified car by Guilmineau, 2008), requiring significantly more involved experimental and numerical investigations. Numerical simulations can be simplified using reduced order modeling of the flow/body interactions. For example, Prosser and Smith (2015) developed a model for quasi-steady and unsteady effects for flow over bluff bodies and demonstrated good agreement with experimental measurements of the flow about a tethered bluff body. It is anticipated that these numerical approaches will ultimately be adapted to the flow about the axisymmetric model of the present investigations.

1.2 Stability Characteristics of the Near Wake of Bluff Bodies

The wake stability downstream of a bluff body is usually described in terms of its 'local' or 'global' stability characteristics (based on local velocity distribution or on the flow field within its vorticity bounds), as well as its "convective" or "absolute" instabilities (associated with propagation of disturbances within the flow either convectively or by broad spreading). Of relevance to the present investigations are the findings of Monkewitz and Nguyen (1987) that a global convective instability of 2-D bluff body wakes is preceded by and coupled to pockets of local absolute instability. In a related investigation, Chomaz, Huerre, and Redekopp (1988) showed that the existence of a local, absolutely unstable domain within the wake is necessary but not a sufficient condition for the development of a global instability. This argument was extended in a review of spatial local and global linear stability theory by Huerre and Monkewitz (1990) who suggested that the most effective means for suppressing the global instability of these wakes is to "eliminate" regions of local absolute instability. This notion was also shared by Oertel (1990) who

noted that the existence of local regions of an absolutely unstable flow could be utilized for wake control. The present investigations build on these approaches for controlling the dynamics of moving platforms by exploiting the reciprocal coupling between the moving body and its near wake.

An important aspect of the fundamental understanding of these wake instabilities is their receptivity to external perturbations. This is crucial to the development of control approaches which use small-scale fluidic manipulation for global control of the flow over a body. Earlier investigations have already demonstrated a significant degree of controllability of wake instabilities. Strykowski and Sreenivasan (1990) reported passive suppression of the global wake instability of a 2-D circular cylinder by placement of a secondary miniature "control" cylinder outside of the separated flow domain of the main cylinder and noted that the instability could be suppressed to higher Reynolds numbers with increasing the characteristic scale of the control cylinder. Schumm, Berger, and Monkewitz (1994) used an active approach, forcing low-amplitude transverse oscillations of an oblong cylinder, which reduced vortex shedding when the cylinder oscillated at about twice its natural shedding frequency. Leu and Ho (2000) investigated the flow behind a splitter plate in a water channel at Re = 2,000 and showed a breakdown of the global instability downstream of the plate by using base suction to reduce the length and alter the orientation (relative to the splitter plate) of the locally unstable region within the wake. Even in 2-D geometries, it was found that the flow stabilities could be significantly altered through spanwise variation of distributed 3-D forcing. An example of this approach was demonstrated by Kim and Choi (2005) who reported drag reduction on a 2-D cylinder through two slots on a cylinder that provided forcing through either suction or blowing that varied sinusoidally in the spanwise direction. These authors found an optimal drag reduction when the forcing in the two slots were applied in-phase at Re = 100, and out of phase at Re = 3,900. As noted by Choi, Jeon, and Kim (2008), these observations may be attributed to the high sensitivity of the absolutely unstable wake to spanwise disturbances.

In a recent experimental investigation of the 3-D wake instabilities behind a 2-D bluff body with a rounded leading edge and blunt trailing edge Naghib-Lahouti, Lavoie, and Hangan (2014) used flow visualization, hot wire anemometry, and proper orthogonal decomposition analysis to investigate secondary instabilities of the model trailing vortex sheet, and reported that these instabilities contributed to large- and small-scale streamwise and spanwise distortions, respectively.

In an investigation of the wake of an axisymmetric bluff body, Weickgenannt and Monkewitz (2000) considered the effects of a trailing disc normal to the axis of the body. They reported four drag regimes at different spacing between the disk and the body, each with a characteristic vortex-shedding pattern. In a study that is particularly relevant to the present configuration, Brücker (2001) compared the wakes of a streamwise cylinder with a rounded leading edge and a blunt trailing edge with the wake of a sphere, and reported that the rounded cylinder had the same wake bifurcations as the sphere, but at higher Reynolds numbers. In a recent linear global instability analysis of the laminar wake behind a streamwise axisymmetric bluff body Sanmiguel-Rojas et al. (2009) showed the existence of a critical base bleed level that can suppress the first wake bifurcation. Bohorquez et al. (2011) showed that the stability of the flow and its receptivity to the base bleed depends on the length to diameter ratio (L/D) of the cylinder, and reported the existence of an additional wake instability behind longer models, as the wake becomes receptive to instabilities originating in the boundary layer over the cylinder.

1.3 Aeromechanical Control of Flight Platforms

Axisymmetric airborne platforms have been historically stabilized in flight by using spin along the platform axis, or by using passive or active fins. Spin-stabilization has historically been favored for improving the accuracy of a large range of projectiles because the spin renders these platforms gyroscopically stable to axisymmetric moment instabilities. However, these spin-stabilized projectiles are susceptible to roll resonance (Price Jr., 1967), and to spin-yaw lock in (Murphy, 1989), which add non-linear effects to

the projectile dynamics that are typically hard to correct for. The basic motions of spinning projectiles (e.g., nutation and precession, linear and nonlinear instabilities, and damping) are discussed in detail by Nicolaides (1970), and instabilities of symmetric projectiles in the presence and absence of spin are discussed in detail by Murphy (1981).

Considerable attention has been devoted to the development of actively controlled fin- and spin-stabilized projectiles (typically referred to as 'smart projectiles'), which is implemented through a variety of mechanical devices. Barrett (1993) investigated the use of piezoelectric fins (that deflected around $\pm 3^{\circ}$) for effecting controllable steering moment. Although such fins do not occupy significant internal space in the platform, they increase the baseline drag. Harkins and Brown (1999) considered reduction in the dispersion of air to surface rockets using the thrust from pulse jets for damping off-axis motion following launch. Jitpraphai and Costello (2001) developed a control approach for reduced dispersion in the trajectory of these rockets, and parametrically investigated the effects of the number of jets and impulse strength. Another approach to projectile steering was investigated by Barrett and Lee (2004) who used a piezoelectrically-articulated nose section for changing the shape (or profile) of the projectile front end to effect aerodynamic forces. A different methodology was considered by Frost and Costello (2004) who developed the equations of motion for a projectile controlled by a spinning internal disk, and demonstrated that this mechanism would have sufficient control authority over the fast and slow epicyclic instability modes. Another recent concept was deployable mechanical protrusion actuators as an alternative to control the trajectory of a supersonic projectile in the absence of spin (Massey and Flick, 2007) which were measured in the steady, fully deployed configuration and yielded comparable effects to normal thrust jets. Rogers and Costello (2007) considered a computational model of a translational mass within a spinning projectile and reported significant control authority. Specifically, at roll rates greater than 1,000 rad/sec this mechanism could deflect the projectile on the order of 10°.

Significant effort has been devoted to the development of control systems for applying steering aerodynamic forces on airborne projectiles. Ollerenshaw and Costello (2008) derived closed-form solutions for the magnitude and phase response of the swerve angle on a projectile that is subject to a generic control force applied at an arbitrary point. These authors also found that when the control forces are applied on the aft end of a projectile with the center of pressure upstream of the center of gravity (such as in a typical spin-stabilized projectile), the swerve response is in phase with the applied force, and if the center of pressure was downstream of the center of gravity (such as in a typical fin-stabilized body), the response would be 180° out of phase. In a numerical investigation, Fresconi and Plostins (2010) varied the lift-to-drag ratio and the axial location of a control force on a projectile, and could maximize the control authority at the aft end and achieve higher lift to drag ratio. These authors also quantified the effect of the pulse width of the applied control force, and reported that the largest induced angle of attack was attained with continuous control effort. In addition, new aeromechanical devices for dispersion control are currently under development. For example, in a recent simulation, Abruzzo and Recchia (2016) reported that a computationally modeled drag-altering fuse that deploys fins in the center of a 155 mm projectile can reduce the range error by 50% if proportional-integral (PI) feedback is implemented using a single-axis accelerometer.

1.4 Flow Control of Bluff Body Aerodynamics

Numerous investigations have utilized active fluidic control to manipulate the local and global instabilities of the near wake and thereby effect significant changes in the flow-induced aerodynamic loads. Significant alterations of bluff body wakes have been achieved by passive control. An example that is particularly relevant to the present investigations is flow attachment along rounded aft solid surfaces, exploiting the Coanda effect that has been investigated extensively since the 1960s (e.g., Newman, 1961). Bypass of suppression of shed vortices using passive elements such as strakes, shrouds, fairings, and plates are discussed in the review articles by Zdravkovich (1981) and by Every, King,

and Weaver (1982). Other examples of the utilization of passive devices for affecting flows over bluff bodies include fins for altering the magnus characteristics of a projectile (e.g., Platou, 1965), a secondary off surface control cylinder for suppressing the locally unstable region in wakes (Strykowski and Sreenivasan, 1990), dimples for drag reduction and transition control (Bearman and Harvey, 1993), etc., as reviewed in a recent article on bluff body flow control by Choi, Jeon, and Kim (2008).

Considerable research effort involving active flow control has been devoted to controlling the wake of 2D bluff bodies to alter vortex shedding or the location of separation, or for drag reduction. An early example of 'hybrid', or combined passive and active control on a stationary 2D bluff body was demonstrated by Nagib, Reisenthel, and Koga (1985) who combined a small-scale (2-6 cm) backward facing step with an active flap to control local separation. Hsiao, Liu, and Shyu (1990) demonstrated a reduction in drag and increase in lift on a 2D circular cylinder using internal acoustic actuation through a slot placed near the separation point at an excitation frequency that was near the vortex shedding frequency. Active separation control strategies have implemented actuators that either coupled to the narrow-band receptivity of the near wake instability (e.g., unsteady bleed on a cylinder by Williams et al., 1991), or using a decoupled approach with an actuation frequency that is at least an order of magnitude higher (e.g., synthetic jets on a cylinder by Honohan, Amitay, and Glezer, 2000). Amitay et al. (1997) demonstrated that the latter approach effects the global flow instabilities by fluidic modification of the "apparent" aerodynamic shape of a 2-D circular cylinder using a synthetic jet. The utility of this approach was demonstrated in a related later investigation by Amitay et al. (2001) who reported 100% increase in lift, and 45% decrease in drag on an elliptic airfoil.

Flow control has also been demonstrated on 3-D bluff bodies. Freund and Mungal (1994) achieved up to 30% decrease in the aerodynamic drag of an axisymmetric body by induced attachment at the aft end using steady, circumferential blowing over a Coanda surface. Another example of hybrid flow control was demonstrated by Sigurdson (1995)

who used a sharp leading edge on a streamwise circular cylinder to induce local separation that was controlled by jet injection through an azimuthal downstream slot. Englar (2000) demonstrated control of separation by jet injection on the aft surface of bluff body models for road vehicles, achieving drag reduction of about 35% and thereby increasing their fuel economy. In an investigation that is particularly relevant to the present study, Rinehart, McMichael, and Glezer (2003) utilized synthetic jet actuation on the aft end of a body of revolution (having a similar geometry to the model used in the present work), and were able to effect a time-varying controlled normal force. A similar effect was reported by Corke et al. (2008) who used tangential plasma actuation placed upstream of a Coanda surface on a similar model to achieve a 50^{o} turning angle of the external flow and 30% reduction in drag. Abramson, Vukasinovic, and Glezer (2011) used a scale model of the present geometry instrumented with an array of four azimuthal synthetic jet actuators to induce a side force coefficient of 0.08 within seven jet actuation cycles. In a later investigation Abramson, Vukasinovic, and Glezer (2012) showed that amplitude modulation of the jets' actuation waveforms could lead to controlled, asymmetric aerodynamic loads.

In recent years, there have been several investigations of active manipulation on moving platforms where active control approaches are clearly attractive because spatial and temporal actuation can be adjusted to varying flow conditions. Vibration control of a 2-D flat plate was investigated by Munshi, Modi, and Yokomizo (1999) who used imbedded rotating cylinders to move the surface where the boundary layer was formed with variable speed to reduce its galloping instability. An active approach was also used to control the pitching moment on a 2-D moving airfoil (Brzozowski et al., 2008), where actuation by a spanwise array of synthetic jets was used to regulate vorticity flux in the boundary layer for disturbance rejection. In a recent investigation, Chen et al. (2013) demonstrated suppression of transverse oscillations of a spring-supported 2-D cylinder with high mass ratio (1,500) at Reynolds numbers up to about 150,000 using discretized suction. There

have also been numerous examples of active flow control on moving 3-D bluff bodies. In a study that is particularly relevant to the present work, McMichael et al. (2004) exploited a synthetic jet flow control approach to an axisymmetric 40 mm spin stabilized projectile to effect aerodynamic steering forces and moments that were sufficient to steer the projectile by about 30^o in a flight test when it was launched at about 80 m/s. This actuation approach was also used in the numerical investigations of Sahu (2006) who computed the aerodynamic loads and the unsteady asymmetric flow field around the model. Krakovich, Eshbal, and van Hout (2013) presented a feasibility study on application of external acoustic source for mitigation of vortex induced vibrations of the two tethered spheres with different mass ratios, at relatively low Reynolds numbers ($Re_D < 3{,}000$). These authors demonstrated that acoustic excitation at a varying excitation frequency can either amplify or suppress vortex induced vibrations, and speculated that these effects were induced by the synchronization (or lack thereof) of vortex shedding from the two bodies. Goyta, Mueller-Vahl, and Greenblatt (2013) demonstrated that plasma excitation of the flow off the leading edge of a tethered cube at Reynolds numbers up to about $Re_D \approx 50{,}000$ could manipulate the separation bubble for surface deflections away from or towards the free stream.

The present investigations include earlier work by Lambert, Vukasinovic, and Glezer (2012-2016c), with the goal of investigation of the mechanisms by which active flow control can be exploited for steering or stabilization of an airborne bluff body in the absence of spin.

1.5 Approaches for Wind Tunnel Mounting

An inherent difficulty with wind tunnel investigations of nominally ‘free’ aerodynamic bodies is their mounting in the tunnel test section. These difficulties have been recognized from early stages of wind tunnel testing (e.g., Bacon, 1923), and different methods for either calibration or correction for the support interference have been proposed since the early 1930’s. For most support structures it is desirable to differentiate between model

support interference and the 'true' flow dynamics for stationary and moving models which is typically exacerbated by interference between the model support and its wake and vortex shedding by the support (e.g., Tuttle and Gloss, 1981, Ericsson and Reding, 1983).

The most common support of 3-D models in wind tunnel investigation is an aft or side sting (e.g. Achenbach, 1972, who used a sting support for investigations of the drag and pressure distribution on a sphere at $Re_D \sim 6 \cdot 10^6$). This support method is typically chosen for ease of setup, but even applied corrections for a stationary sting support requires a fair amount of extra tests that are typically computational (e.g., corrections for sting interference on an aircraft model with varying Mach number in a transonic flow by Kozhai et al., 2010). However, as demonstrated by Beyers (1992), coupled interference of a sting support with both the tunnel walls and the wind tunnel model during a dynamic test precluded any analytical corrections. A less common method for support of wind tunnel models is a wire support system which can have reduced interference and vortex shedding (but is typically restricted to low-speed flows). An early example of a wire support system was demonstrated by Griffin, Crooks, and Mole (1991), who used wire mounting to a turntable (dubbed vane support system, VSS) for adjusting the model angle. Model support by struts was investigated by Taylor, Gursul, and Greenwell (2003) who demonstrated that the angle of attack and location of struts had a significant impact on the vortex breakdown of a delta wing, causing induced change in the drag as well, and noting that in some cases a streamlined support performed worse than a circular cylinder. An electromagnetic support demonstrated by Higuchi, Sawada, and Kato, (2008) for exploring the flow around a 3-D cylinder has virtually minimal or no aerodynamic interference but is burdened by significant complexity and cost. Another example of a dynamic model support was by Pattinson, Lowenberg, and Goman (2012), who used a 1/16 scale model of a BAE Hawk aircraft and moved it in multiple degrees of freedom through a combination of sting and strut supports. This support comprised of a 3-DOF gimbal that is rigidly attached to a sting, connected to another 2-DOF gimbal, and then attached to the model, which allowed for a

wide range of dynamics, but also had induced effects attributed to the physical model connection (although the authors create a mathematical model to compensate for friction).

The current investigations extend the earlier methodology developed by Abramson, Vukasinovic, and Glezer (2011) and demonstrates the utility of a thin wire support (where the characteristic length scale of the model is close to two orders of magnitude larger than the diameter of the support wires) that is capable of complex 3-DOF motion with minimal flow interference between the model and the traverse system. The eight-wire traverse is electromechanically driven by a dedicated feedback controller to remove the parasitic mass and inertia of the dynamic support system and of the model (cf., Chapter **II**).

1.6 Flow Field Decomposition Analysis

An important aspect to characterizing the structure and stability of the near-wake of the axisymmetric model in the present investigations is the decomposition of the velocity (or vorticity) field into a basis of spatial modes that are each characterized and ordered the fraction of the total energy of the flow. Two related methodologies are commonly used for this purpose namely, proper orthogonal decomposition (POD), and dynamic mode decomposition (DMD). This section reviews earlier investigations that have utilized these techniques in fluid mechanics research while the formulations of POD and DMD algorithms are described in Appendix **A**. An early adaptation of proper orthogonal decomposition for investigation of the structure of turbulent shear flows was suggested by Lumley (1967). However, other investigators independently suggested similar analyses between the 1940s and 1960s (e.g., Pugachev, 1953, and Obukhov, 1954), with a descriptive history in a review by Berkooz, Holmes, and Lumley (1993). Synonymous algorithms to POD have also been developed independently in other scientific fields, namely principle component analysis in statistics (e.g, Hotelling, 1933) or Karhunen-Loève transform in signal processing (e.g., Kosambi, 1943). In fluid mechanics, a subset of POD modes is often utilized to reconstruct the lower-ordered, time-dependent velocity field by using time-dependent coefficients. By comparison, dynamic mode decomposition

has been explored more recently. As described in one of the first investigations of this methodology by Schmid, Meyer, and Pust (2009), the DMD focus is to apply the decomposition to the evolution operator of a given flow field (generally referred to as the Koopman or composition operator), rather than directly to the flow field. As a result, unlike the POD modes, DMD modes do not need to be orthogonal, and a given mode is associated with a specific frequency (or spectral component) and a decay rate of fluctuating flow field. Although DMD modes in general are not composed of POD modes, it is common practice to project the DMD modes onto a POD basis, either to reduce the computation time of the DMD modes or to understand the temporal dynamics of the POD modes.

A common implementation of POD is accomplished using the method of 'snapshots' or 'strobes' described by Sirovich (1987), where a snapshot includes all of the vectors resolved in a spatial flow field at some fixed time (this method is especially useful for processing of PIV where the spatial flow field at some fixed time is acquired). Using high resolution direct numerical simulations, Ma and Karniadakis (2002) showed that the 3-D wake behind a cylinder could be accurately modeled with the first 23 POD modes of the flow. In principle, POD can not only be applied to the velocity field, but also directly to the vorticity field, as shown by Kostas, Soria, and Chong (2005) who demonstrated that the reconstruction of the wake flow behind a backward facing step using vorticity modes has slightly lower error than with velocity modes, although at an added computation cost. Alternatively, Ausseur, Pinier, and Glauser (2006) suggested instead to decompose the convective acceleration of a flow field, instead of its velocity, due to their occurrence in the Navier-Stokes equations, and found modes that resembled the shedding pattern when applied to a NACA-4412 airfoil. A POD approach by Feng, Wang, and Pan (2010) was used to characterize the effect of the suction to blowing duty cycle in a synthetic jet near the separation point of a cylinder to characterize how the ejected vortex pairs couple to the shedding modes. A similar analysis is done in the present work (varying amplitude modulation frequency instead of duty cycle), which is shown in Chapter **VI**.

DMD was used by Schmid (2010) to create a modal decomposition that was orthogonal in time (or frequency) for three separate flow fields: cavity flow, flow over a flexible membrane, and flow between an array of 2-D cylinders. He was able to identify 'intuitive' modes where each was characterized by a given fluctuation time and growth rate that can be easily related to the flow physics and was compared to conventional POD modes. A numerical simulation of relevance to the current study was performed by Gilka et al. (2010) who used two zero-net-mass-flux actuators to reduce the drag of a 2-D rounded nose bluff body and applied DMD to quantify the dominant vortex shedding frequencies (and their corresponding spatial modes in the velocity flow field) before and after actuation. More recently, Tu and Rowley (2012) extended the DMD formulation to an eleven-step memory-efficient singular value decomposition approach, and demonstrated its application for identifying the global instability modes around a 2-D cylinder. This approach is also used in the present investigations.

1.7 Focus of the Thesis

In the current investigations, the coupling between a stationary and moving axisymmetric fluff body and its near-wake, and the effects of this coupling on the aerodynamic loads in the absence and presence of flow actuation are investigated in several wind tunnel experiments. These investigations are conducted using 2- and 3-D particle image velocimetry (PIV), hot-wire anemometry, and load cell measurements. The body/wake coupling mechanisms are investigated when the body is stationary, moving in 6-DOF in prescribed trajectories, and freely in either 1-DOF or 3-DOF.

The primary goals of the present investigation are:

i. Characterize the structure of the near-wake of a stationary model and the induced effects of azimuthal, aft-body synthetic jet actuation on the evolution of the wake and on the aerodynamic loads on the model over a broad range of attitude angles.

ii. Investigate the coupling between the flow over a moving body and its near wake in controlled motion in which the effected changes in the flow and the induced aerodynamic loads do not affect the motion of the platform.

iii. Investigate the receptivity of the coupled body/wake motion to flow manipulation in examples of free flight in which the inherent feedback of the induced changes in the flow and consequently in the aerodynamic loads affects the motion of the platform and thereby can potentially control its motion and stability.

iv. Develop a dynamically-controlled wind tunnel traverse mechanism in 6-DOF to enable investigations of the coupling between an axisymmetric model and the embedding flow during controlled maneuver.

The Thesis is structured as follows: Chapter **II** describes the experimental setups and the data acquisition methodology that were developed for the present research. Chapter **III** presents an investigation of the coupling between aerodynamic loads and wake structure during time-stationary or slow (quasi-steady aerodynamics) changes in model attitude, and depicts the changes in this coupling by fluidic actuation. Chapter **IV** considers the wake dynamics of a 'free' 1-DOF yawing body, driven by the flow, and demonstrates the control authority of the fluidic actuators for motion response. Chapter **V** extends the investigation of Chapter **III** to a prescribed fast (highly unsteady aerodynamics) harmonic motion trajectories (in pitch, plunge, and streamwise displacement) using an eight-wire 6-DOF traverse. Chapter **VI** describes the flow over the model in a prescribed coupled pitch-yaw rotation that mimics a free-flight instability and the use of actuation to control the motion-driven wake instabilities. Chapter **VII** details a case study of the control authority of fluidic actuation developed in Chapter **VI** on an axisymmetric model that is free to respond to induced aerodynamic loads in 3-DOF (pitch, yaw, and roll). The analysis of the wake structure and instabilities in Chapters **VI** and **VII** employs flow field decomposition (POD and DMD) that are discussed in Appendix **A**. In addition, the various flow control

strategies (e.g., open-loop, PID, or coupled PID) utilized in Chapters **IV** through **VII** are depicted in Appendix **B**. Finally, Chapter **VIII** presents discussion of the results and of the main findings of this research, as well as suggestions for potential future investigations.

CHAPTER II

EXPERIMENTAL METHODOLOGY

2.1 Wind Tunnel Facility

The present investigations are conducted in an open-return wind tunnel at Georgia Tech, having a 3 m long test section with a cross section measuring 91 x 91 cm. The tunnel test section is driven from upstream by an axial blower coupled with a 1.1 kW VFD-driven motor through a square cross section partitioned diffuser (area ratio 1:3.8), a settling section with turbulence manipulators, and a contraction (area ratio 8.9:1). The downstream end of the settling section is equipped with a thin symmetric vertical airfoil for delivery of seed fog particles through a slot at its trailing edge for particle image velocimetry (cf., §**2.7**). The tunnel maximum free stream speed is $U_o = 40 \pm 1$ m/s with free stream turbulence level of less than 0.25% (Amitay and Glezer, 2002) at nominally $T_o = 20 \pm 2\ ^{\circ}C$. A more detailed description of this tunnel can found in Brzozowski (2011) and Woo (2014).

The present investigations utilized four different experimental setups for investigations of the flow around stationary and moving axisymmetric bluff body models:

1) Axisymmetric hoop frame which can dynamically vary the attitude of a wind tunnel model in pitch and/or yaw using shape memory alloy (SMA) wire actuators at operating frequencies below 5 Hz (§**2.3)**
2) One degree of freedom (1-DOF) free-yawing wire mounted model (§**2.4)**
3) 6-DOF wire traverse (eight wires actuated with servo motors) with feedback-controlled dynamics in pitch, plunge, roll and three-axis (*x*-*y*-*z*) translation and a tested bandwidth of up to 20 Hz (§**2.5)**
4) Sting-mounted 3-DOF (pitch, yaw, and roll) "free flight" model where the sting is mounted on the 6-DOF wire traverse (§**2.6)**

The axisymmetric model and the flow control actuators are described in §**2.2.** The wake velocity measurement systems (particle image velocimetry) are described in §**2.7**, with the low-speed PIV system in §***2.7.1***, the high-speed PIV system in §***2.7.2***, and their respective processing settings in §***2.7.3***.

2.2 The Axisymmetric Model and Synthetic Jet Actuators

As mentioned in Chapter **1.1**, the goal of the present experiments is to investigate active aerodynamic flow control of the trajectory and stability of an axisymmetric bluff body in the absence of axial spin. The model utilized in the present investigations is a scale model of the DARPA SCORPION projectile configuration that was used to demonstrate the effectiveness of flow control for steering during spin-stabilized flight (McMichael et al., 2004). The present scaled-up wind tunnel model (D = 90 mm, c = 165 mm, Figure 2.1a) is constructed using stereo-lithographed and aluminum components. The mid-section and nose are hollow and connected to the tail section by a central shaft (following assembly, the model surface is painted black and then machined flush on a lathe). Four

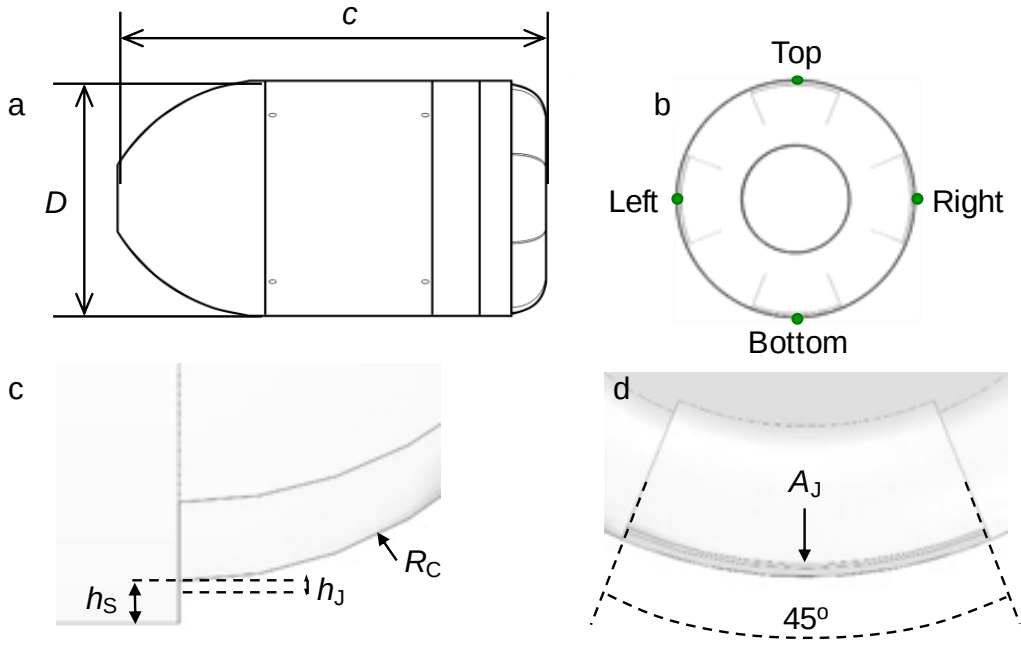

Figure 2.1. Side (a) and upstream (b) views of the wind tunnel model with four synthetic jet actuators. The actuator is shown in a side view with the backward-facing step upstream of the aft section (c) and an upstream view with a recessed surface (d). Each of the jets are labeled in **green** for reference.

independently-driven synthetic jet actuators (labeled the top, left, bottom, and right actuators, as shown in Figure 2.1b) are equally distributed along the perimeter of the tail section and are used to effect aerodynamic control forces and associated moments. Each jet is issued in the streamwise direction with the orifice (height h_J = 0.38 mm, and area A_J = 13.03 mm^2) placed at the bottom of a backward-facing step of height h_S = 1.5 mm to the circumference, extending into a Coanda surface (radius R_C = 12.7 mm) that are based on the design of Rinehart (2011) and depicted in side and upstream views in Figures 2.1c and d. The aft segment contains a streamwise recess downstream of the orifice edge which bounds the jet over a segmented arc. Jet actuation leads to the partial attachment of an azimuthal segment of the separating shear layer at the aft end of the model along the Coanda surface and turns the outer flow into the wake resulting in an aerodynamic reaction force that is normal to a jet centerline with an accompanying moment.

While all the models in the present investigations are geometrically similar, the test model is modified for the investigations involving free-moving responses (cf., §**2.4** and §**2.6**), where the metal shaft, mid-section, and nose pieces are replaced with light-weight shells constructed using stereolithography. The models that are used with the wire-traverse (cf., §**2.3** and §**2.5**) are fabricated using metal components to ensure structural rigidity.

The synthetic jet actuators are calibrated over a wide range of actuation frequencies, f_{act}, and applied powers P_A. The actuation frequency is scaled by the model hydraulic diameter (~$2h_J$) and the free stream velocity $f_{act}^* = 2f_{act}h_J/U_o$, where the actuation convective time scale is $2h_J/U_o$ = 19 μs, and the actuation power is scaled as $P_{act}^* = 24P_{act}/(\pi\rho U_o^3 D^2)$. The jet actuators are calibrated using hot-wire anemometry in a test stand where the time-resolved velocity of the jet is measured at the center of each of the actuator orifices yielding a rectified time-periodic waveform representing alternate suction and expulsion during the jet formation. The peak of the expulsion velocity, U_J, is recorded over a frequency range of $0.035 < f_{act}^* < 0.050$ at excitation powers of $P_{act}^* \cdot 10^3 = 2.0$, 3.3, and 4.6. The variation of the jet momentum coefficient $C_\mu = (4U_J^2 A_J)/(\pi U_o^2 D^2)$ with f_{act}^* is shown in Figure 2.2

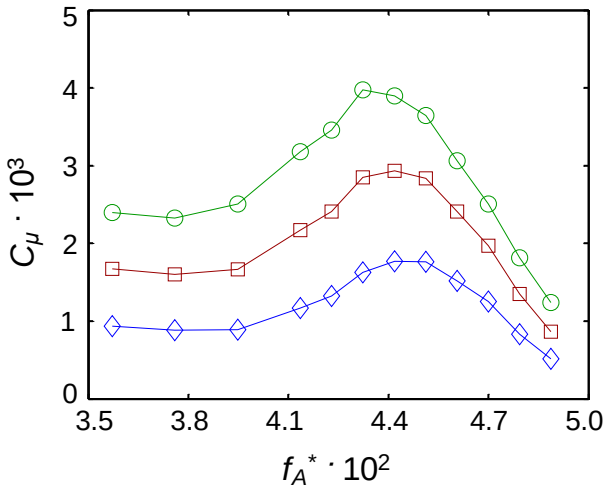

Figure 2.2. Variation of the jet momentum coefficient, C_μ, with the actuation frequency, f_A^*, for three levels of actuation power: $P_A^* \cdot 10^3 = 2.0$ (◊), 3.3 (□), and 4.6 (○).

and it is used to select the operational range in the present investigations. These data exhibit mild resonance peaks where the resonance frequency decreases with increasing actuation ostensibly owing to heating or weak nonlinear effects.

2.3 Axisymmetric Hoop Frame

A hoop frame which was originally designed for characterization of aerodynamic loads and the wake of the axisymmetric model at a static attitude (Abramson, Vukasinovic, and Glezer, 2011) is modified to perform controlled low frequency changes in attitude (in pitch) that are discussed in detail in Chapter **III**. The components of the hoop frame that are used for mounting the model in the wind tunnel are depicted in Figure 2.3. The basic structure is a cylindrical frame that is secured to the tunnel wall, as shown in side view in Figure 2.3a and back view in Figure 2.3b. This frame consists of two steel circular rings that are connected by four streamwise cylindrical rods. The connection to the wind tunnel wall utilizes dampers, to isolate the model from tunnel vibrations. The wind tunnel model is mounted within the frame using eight stainless steel wires, which are each coupled directly to a L_{SMA} = 10 cm long, and D_{SMA} = 0.5 mm diameter shape memory nickel-titanium alloy (SMA) wire (Figure 2.3b). The model mounting cables are oriented such that they are not

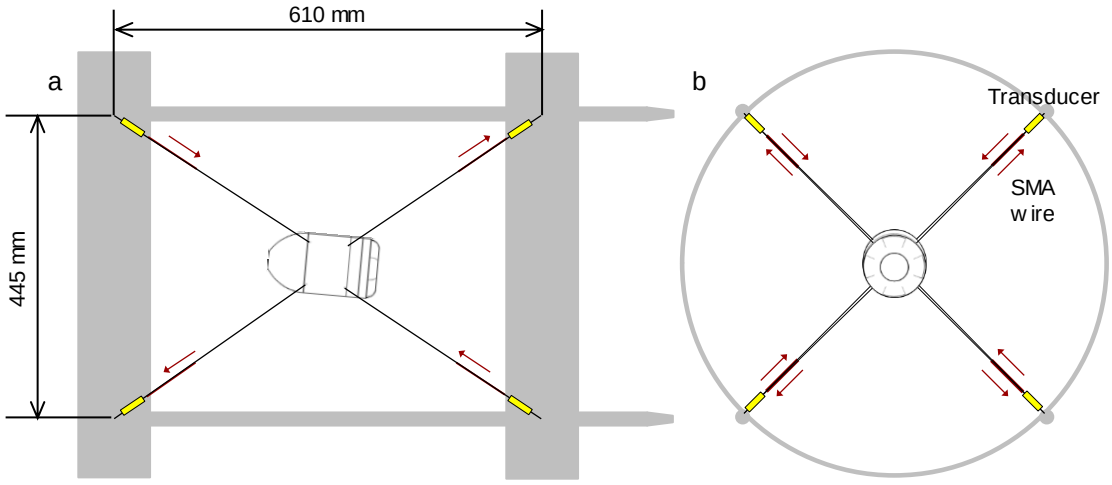

Figure 2.3. Side (a) and upstream (b) schematic views of the axisymmetric model setup in the hoop frame oriented in a pitch up position by the SMA wires.

in line with the model centerline, forcing the body to rotate under offset tension (marked notionally in Figure 2.3). Each of the eight SMA wires can be individually actuated from the laboratory computer using an eight-channel amplifier that supplies electrical power to each SMA segment through thin electrical wires that are fastened directly to the frame. Each SMA wire is directly connected to an inline force measurement transducer (characterized by Abramson, Vukasinovic, and Glezer, 2011) for measuring the time-dependent tension in the mounting wires to determine the aerodynamic loads on the model. The inline transducer is connected to a modified violin string tuner embedded in the frame which controls the initial model pretension (the auxiliary circuitry is mounted directly onto the frame). The model position is initially set manually through the violin tuners, while the dynamic motion from the initial state is achieved through activation of the SMA wires. The electrical wires for each of the synthetic jet actuators are supported by the four downstream mounting wires and are arranged to avoid interference with the force transducers. In the present investigations, the model is either held stationary or pitching at a frequency of $f = 1$ Hz (a reduced frequency $k = \pi fL/U_o = 0.013$), and it has a vortex shedding frequency of $f_{shed} = 105$ Hz ($St_D = f_{shed}D/U_o = 0.24$), while the frame system has a

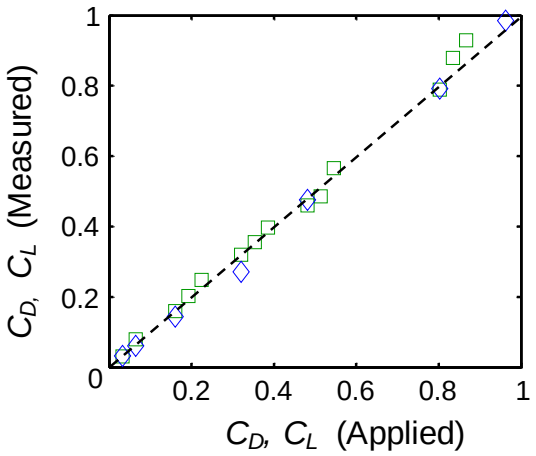

Figure 2.4. Variation of the measured with the applied drag (◊) and lift (□) forces.

resonance frequency of 23 Hz. The present system provides pitching range of ±3° at 0.5 Hz to ±1° at 5 Hz.

Each of the force transducers is independently calibrated ahead of the tunnel measurements using precision weights to produce a set of linear calibration curves (output voltage vs. applied load). The transducers are also calibrated to check and correct for their weak temperature dependence (output voltage vs. ambient temperature). The customary respective force (F) coefficient for each of the lift (C_L), side force (C_S) and drag (C_D) forces is $C = 8F/(\pi\rho U_o^2 D^2)$, and the moment ($M$) coefficient for each of the pitch (C_M) and yaw (C_Y) moment (the roll moment is not resolved) is $C = 8M/(\pi\rho U_o^2 D^2 c)$. The resolution of the force and moment coefficients are $\delta C = 1 \cdot 10^{-2}$, and $1 \cdot 10^{-3}$, respectively. The resulting calibration is checked periodically by applying known static loads on the model in the lift and drag directions and measuring the resulting force. Figure 2.4 shows the variation of the measured and applied lift and drag forces during the calibration procedure which are in good agreement especially within the primary range of interest (C_D and $C_L < 0.5$).

In the present experiments, the model is translated and rotated using individually-controlled currents through each of the SMA wires from a computer-controlled power supply for time-dependent increase or decrease in tension relative to a selected operating point (the wire temperature is controlled by Joule heating, e.g., Nemat-Nasser and Guo,

2006). The transient activation of an SMA wire with applied electrical power, P_{SMA}, is analyzed to determine the activation timing necessary for a desired model response. A fixed level of electrical power is provided to a wire embedded in the setup for a predetermined top-hat duration (the response time of the amplifier provided P_{SMA} is two orders of magnitude faster than the response time of the wire, and is neglected). The wire response is parametrically modeled by a linear tension rate of change, $\dot{F}_{SMA}$, after which the maximum tension, F_{SMA}, is established. After wire deactivation, it then retracts back to its initial state, although the $\dot{F}_{SMA}$ for retraction is typically different than for contraction since the cooling of the wire by convection occurs on a different time scale than the Joule heating. The scaling of the SMA parameters in Figure 2.5 is given for the convective time

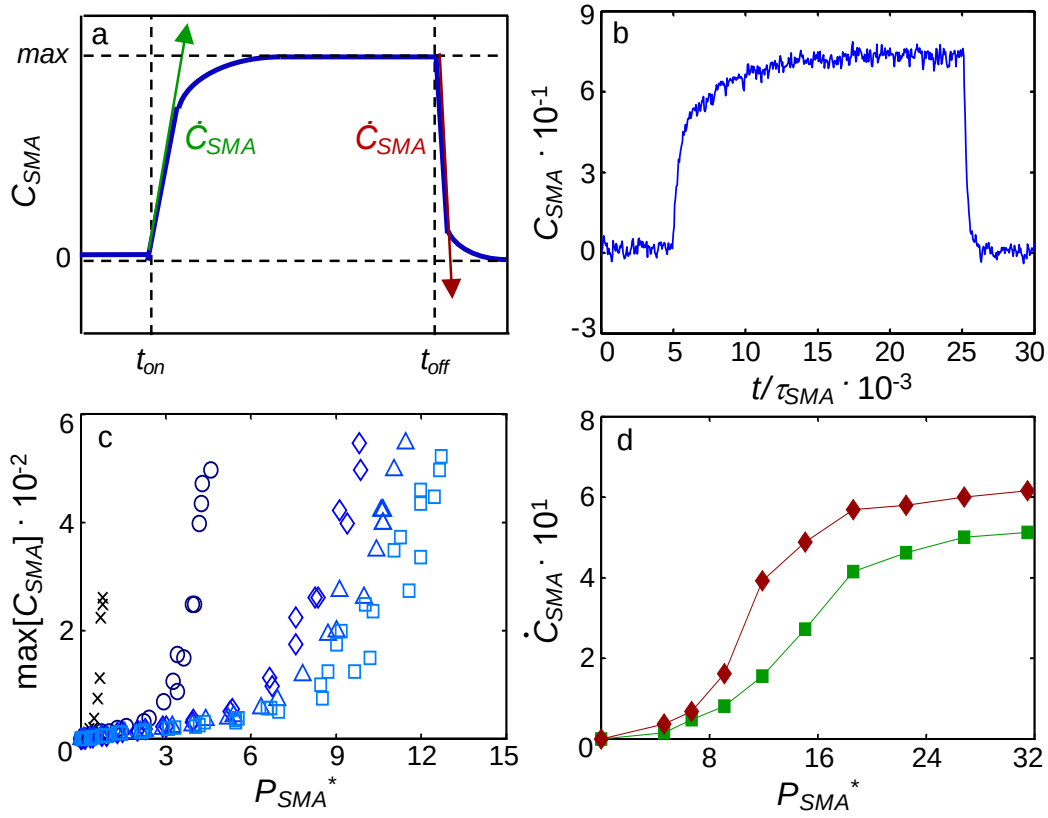

Figure 2.5. Variation with time of an ideal (a) and an example measured (b) SMA force coefficient, C_{SMA}, along with the variation of the maximum C_{SMA} with applied electrical power, P_{SMA}^* for varying tunnel speeds, U_o/U_{max}= 0 (x), 0.2 (o), 0.5 (◊), 0.75 (Δ), and 1 (□) (c), and variation of $\dot{C}_{SMA}^*$ onset (■) and termination (♦) rates with P_{SMA}^* for U_o/U_{max}= 1 (d).

scale ($\tau_{SMA} = U_o/L_{SMA}$), force coefficient [$C_{SMA} = 2F_{SMA}/(\rho U_o^2 D_{SMA} L_{SMA})$], force rate coefficient [$\dot{C}_{SMA} = 2\dot{F}_{SMA}/(\rho U_o^3 D_{SMA})$], and applied power [$P_{SMA}^* = 6P_{SMA}/(\rho U_o^3 D_{SMA} L_{SMA})$]. A depiction of this parametric representation of the SMA wire operation is shown in Figure 2.5a and an example experimental measurement of the SMA contraction at the tunnel nominal speed U_{max} = 40 m/s with $P_{SMA}^* \sim 12$ is shown in Figure 2.5b. The SMA contraction effect is tested at multiple speeds (U_o/U_{max} = 0, 0.2, 0.5, 0.75, and 1) and the resulting maximum force coefficients, C_{SMA}, are shown as a function of applied power, P_{SMA}^*, in Figure 2.5c. The force rate coefficient, $\dot{C}_{SMA}$, for both contraction and expansion varies with P_{SMA}^* and these rates are examined in Figure 2.5d for $U_o = U_{max}$. Since the relaxation $\dot{C}_{SMA}$ is higher than the contraction $\dot{C}_{SMA}$ a square wave power history would induce a non-symmetric cyclic oscillation, and therefore the timing of the applied power is compensated during contraction and relaxation to enable a symmetric model motion. For transitory motion, short rise and fall times (large $\dot{C}_{SMA}$) are achieved with increased applied contraction power and a large, fast, transition of P_{SMA}^*.

In the present investigation, the SMA wires are used to manipulate the model pitching motion (although other prescribed motions can be easily commanded). In order to manipulate a positive model pitching angle (nose up), the tension is increased in the upstream two wires at the bottom of the model and the downstream two wires at the top of the model, as well as decreasing the power in the other four wires, and the opposite SMA power pattern is applied for a negative pitch orientation. The pitch motion of the model is measured by a laser vibrometer, which is mounted directly above the test section and is focused on the model upper surface along its centerline at a given position downstream from the model center x_L. The pitch angle α_y is extracted from x_L, D, and the time-resolved model displacement measured by the laser vibrometer.

Model alignment with the flow is achieved using both the violin tuners on the frame (an initial manual pretension) and an additional controlled pretension the SMA wires. First, each support wire on the frame is manually pre-tensioned ($C_{SMA} \sim 400$) in still air.

Afterwards, the test section speed is varied, and the measured forces are monitored. The wire tensions are slightly adjusted until there is negligible change in the lift or side forces with varying tunnel speed (typically less than 5% of the increase in drag force). After the initial alignment procedure, the power to the SMA wires are activated such that they are at an intermediate temperature near the beginning of their material transition (~25°C), which adds an additional tension on each wire ($C_{SMA} \sim 150$).

As an illustration of the induced pitch motion, two test cases are shown in Figure 2.6, which correspond to transitory motion and a simple harmonic pitching motion of frequency $f = 1$ Hz, both of which have an amplitude of $\alpha_y = 1.5°$. The time in this study is scaled by the convective time scale of the model, $\tau_{conv} = U_o/c$, and the reduced frequency is $k = \pi fc/U_o$. In the first test case, shown in Figure 2.6a, the model is kept stationary at its centered orientation from $t/\tau_{conv} = 0$-480 and then the power to the SMA wires is altered such that it would pitch up to $\alpha_y = 1.5°$ for $t/\tau_{conv} = 480$-960. It takes the model approximately $t/\tau_{conv} = 25$ to reach its steady orientation from the prescribed command. The SMA wire power commands are shown in Figure 2.6c, where the commands to the four wires that move the model to pitch up and down are shown in green and red, respectively. Since the applied power determines the rate of change in the SMA wires, and the pitching orientation, the command power amplitude is proportional to the desired pitching rate. As the model pitches up, the power to the wires that induce a pitch down motion is reduced to increase the turning rate. The power spectrum of the resulting transitory motion measurement is shown in Figure 2.6e, and this power spectrum shows a dominant peak at multiples of $f \sim 14.3$ Hz, which is associated with the angular rate of the transitory change measured (0.24 rad/s in Figure 2.6a). In the second test case, in Figure 2.6b, the SMA wires are driven to induce a time harmonic waveform at a reduced frequency $k = 0.013$ with an amplitude of $\alpha_y = 1.5$. The respective SMA power commands (Figure 2.6d) are skewed (to the right) to compensate for the hysteresis between the relaxation and

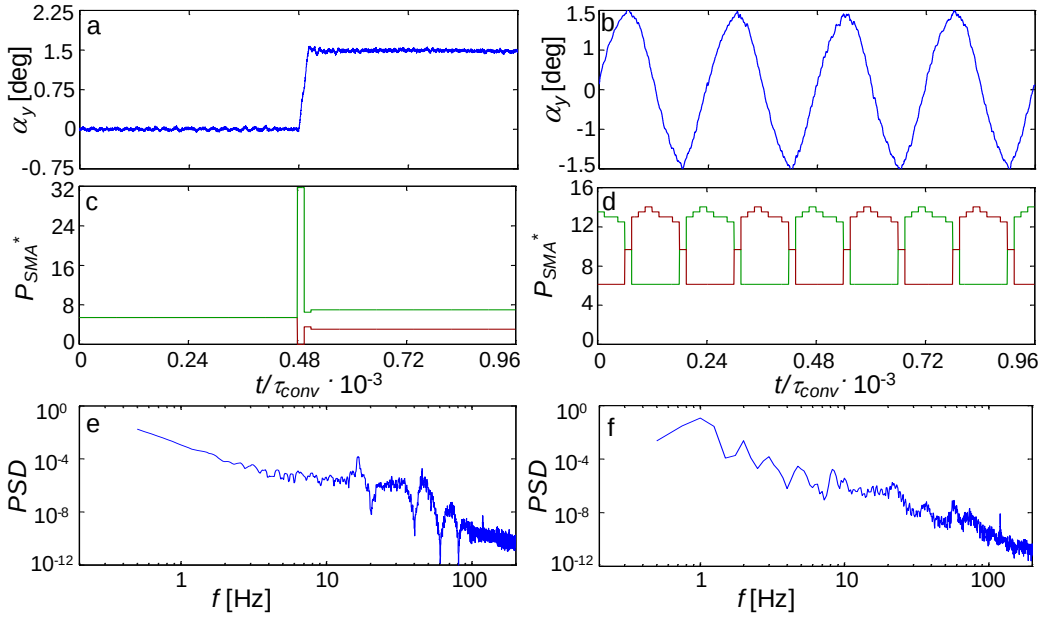

Figure 2.6. Respective time traces of the $\alpha_y = 1.5^\circ$ amplitude pitch angle (a, b), the corresponding SMA power command, P_{SMA}^* (**pitch-up** and **pitch-down**) (c, d), and the power spectra (e, f) for transitory motion (a, c, and e) and for quasi-sinusoidal pitching at $k = 0.013$ (f = 1 Hz) (b, d, and f).

(the longer) contraction time (cf., Figure 2.5d), and the normalized power spectrum of α_y in Figure 2.6f exhibits a peak at $f = 1$ Hz (with its respective harmonics). The present model trajectories are commanded under open-loop control, which does not take into account deviations of real-time aerodynamic loads that can, in principle, be addressed using a closed-loop controller.

2.4 1-DOF Free Yawing Model

The second experimental setup developed during the present investigations is designed to characterize free response of the axisymmetric model in 1-DOF (described in Chapter **IV**). As noted in §**2.2**, the weight of the model in these experiments is minimized using a thin shell fabricated using stereolithography having a total mass of 0.11 kg. As shown in Figures 2.7a and b, the model is supported by a $D_{wire} = 1$ mm diameter steel wire whose characteristic shedding frequency at the present free stream speeds (2.1 kHz < f_{wire} < 8.4 kHz at $6.3 \cdot 10^2 < Re_{wire} < 2.5 \cdot 10^3$) is decoupled from the nominal shedding frequency of the model (27 Hz < f_{shed} < 110 Hz at $5.7 \cdot 10^4 < Re_D < 2.3 \cdot 10^5$). Each

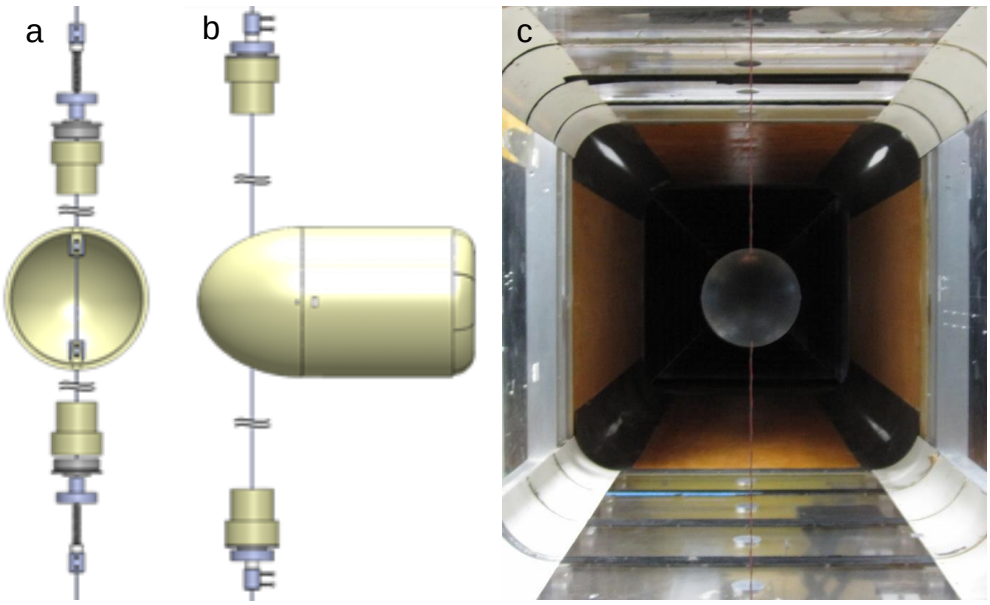

Figure 2.7. CAD open front (a) and assembled side (b) views of the axisymmetric model and mounting mechanism, and an upstream view of the model mounted in the wind tunnel (c).

end of the wire-mounting mechanism is secured to the tunnel wall and is coupled through a ball bearing to a wire segment that passes through the front end of the model and attaches internally to integrated connectors. The yaw axis is placed at $x_o = 0.18c$, upstream of the model static center of pressure $x_{cp} \sim 0.33c$ to yield a semi-stable response (cf., Chapter **IV**). The tension in the mounting wire is adjusted using a vented screw that is secured to a shaft connector. The electrical connection for the synthetic jet actuators is provided by four ultrathin wires (36 AWG, and the support wire provides electrical ground) that are weaved along the primary support wire (the overall diameter is 1.5 mm) and through the tunnel walls. The supported model within the test section is shown in Figure 2.7c.

The model instantaneous attitude is measured using a laser vibrometer sensor that is mounted normal at the level of the model centerline on the side wall of the test section $x_L = 0.36c$ downstream of the mounting wire. The laser vibrometer measures the position and velocity of the model surface along the laser beam and is sampled at 5 kHz (although the vibrometer utilizes an internal 200 Hz low pass filter). The measured respective amplitudes of the support wire displacement and speed which vary with wind tunnel speed

and are below $\sigma_{wire} = \pm 0.16$ mm and ±2 mm/s (measured directly). The angular attitude angle of the model centerline α_z (measured relative to the streamwise x direction) is extracted from the laser vibrometer measurements, and the uncertainties of the model yawing angle and rate (α_z and $\dot{\alpha}_z$) owing to the wire vibrations are estimated as $\Delta\alpha_z = 2 \cdot \sigma_{wire}/x_L \cdot 180/\pi = 0.31^\circ$ and 3.9°/s, respectively.

The model dynamic response to aerodynamic forces can be described by a second order system:

$$I_{1D}\ddot{\alpha}_z + C_{1D}\dot{\alpha}_z + K_{1D}\alpha_z = M_z(t) \tag{2.1}$$

where I_{1D}, C_{1D}, and K_{1D} are time-independent inertia, damping, and spring coefficients of the mounting system (in the present system $K_{1D} = 0$). The inertia $I_{1D} = 7.9 \cdot 10^{-4}$ Nms^2/rad is extracted from CAD software, neglecting only the weight of electrical wires that power the flow control actuators. The motion damping constant (not including the aerodynamic damping) is caused by the wire and bearing mount, and it is estimated through a forced 'ping' perturbation of the model in the absence of external flow. This perturbation moment was provided manually such that the model would move from a centered position to a deflection comparable to the aerodynamic induced vibration amplitude (~8°). The resulting

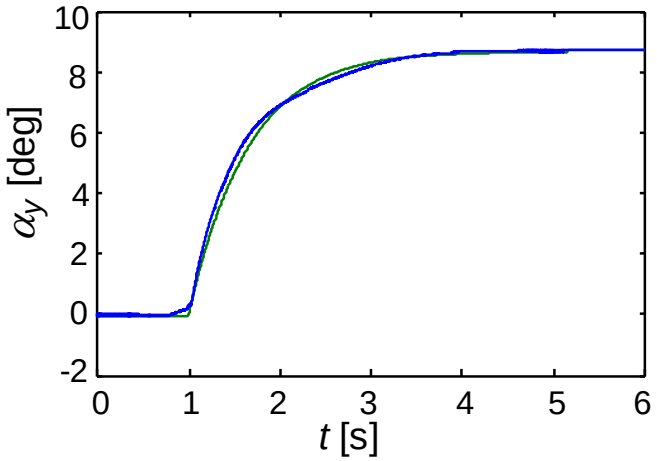

Figure 2.8. Time traces of the motion of the 1-DOF model following a yaw perturbation (**blue**) designed to measure the characteristic damping constant of the system (the inertia is extracted from CAD software, and the spring constant is neglected). The corresponding least squares fit to a mass-damper model is shown in **green**.

measured 'ping' motion is shown in Figure 2.8 in blue. The numerical derivatives of this 'ping' measurement are then computed numerically ($\dot{\alpha}_z$, $\ddot{\alpha}_z$) from a centered 2nd order finite difference stencil, and substituted into Equation (2.1), assuming $M_z = 0$ (the 'ping' data used is after the model is perturbed, at $t > 1$). This yields many data points in the trajectory measurement to estimate the damping constant of the 1-DOF model, which is implemented through a least squares fit and yields a resultant damping of $C_{1D} = 1.2 \cdot 10^{-3}$ Nms/rad. This fit is shown in Figure 2.8 in green and is in good agreement to the measured response for $t > 1$ (for $t < 1$, the fit is replaced with $\alpha_z = 0$).

2.5 6-DOF Wire Traverse

The flow about the axisymmetric model moving in commanded, time-dependent six degrees of freedom at characteristic frequencies of up to 20 Hz (unsteady aerodynamic range, $k < 0.259$) is investigated using a novel, 6-DOF wire traverse with a design range of controlled motion of up to 5 mm model deflection at 50 Hz. In the present investigations, the traverse is used in several motion configurations: ***i.*** Canonical 1-DOF pitch, plunge, and streamwise displacement (Chapter **V**); ***ii.*** 2-DOF rotations in pitch and yaw (Chapter **VI**); and ***iii***. Free 3-DOF motion in pitch, yaw, and roll (§**2.6** and Chapter **VII)**. This section is comprised of the following subsections that describe: the traverse structure (§***2.5.1***), the motion analysis system (§***2.5.2***), the electrical system (§***2.5.3***), the motion control system (§***2.5.4***), and validation of the resulting force and motion responses (§***2.5.5***).

2.5.1 Traverse Components

The support mechanism utilizes 8 stranded (0.6 mm diameter) support wires to suspend various platforms within the wind tunnel test section as shown in Figure 2.9a with minimal aerodynamic interference. The position and orientation of the suspended aerodynamic platform are varied using independently-controlled servo motor actuators (having peak torque of 9.55 N-m and a 6,000 rpm peak) that are connected with a pulley to the end of each support wire (through small openings with sufficient clearance) and are mounted outside the tunnel test section. The actuators are mounted in a box configuration 120 cm

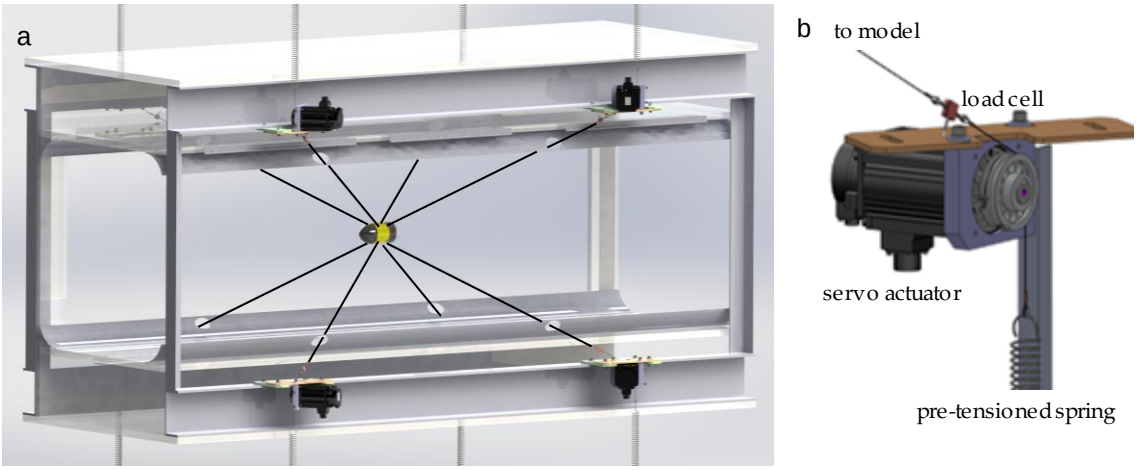

Figure 2.9. Side view of the 6-DOF traverse (a), and the servo motor assembly (b).

high, 128 cm long, and 176 cm wide. Each driving pulley is attached to an extension spring (208.4 N/m) that provides preload tension to its respective wire when the model is in equilibrium (in the present investigations the preload is approximately 60 N). The tension in each mounting wire is measured using an inline miniature load cell (having a range of 0-110 N, repeatable to within 0.055N). The servo actuator assembly is shown in Figure 2.9b. The servo actuators are designed to provide up to 5 mm displacement at a maximum frequency of 50 Hz and a maximum tension of 110 N. Power is provided to flow control actuators on the model by weaving small-gage insulated electric wires providing voltage signals around the electrically grounded support wires.

The range of translational and rotational motions of the traverse depend on the location of the attachment points of mounting wires to the model (the range of translational motions also depend on the locations of the eight servo actuators). For example, roll motion is impossible if the wires are attached such that they are equally distributed azimuthally, 90° apart as shown in Figure 2.10a. However, a non-uniform azimuthal distribution of the support attachment enables the two symmetric groups of wires to be tightened or loosened to provide roll, as shown in Figure 2.10b. The theoretical maximum roll (with full controllability) occurs when one of these symmetric wire groups is in line with the center

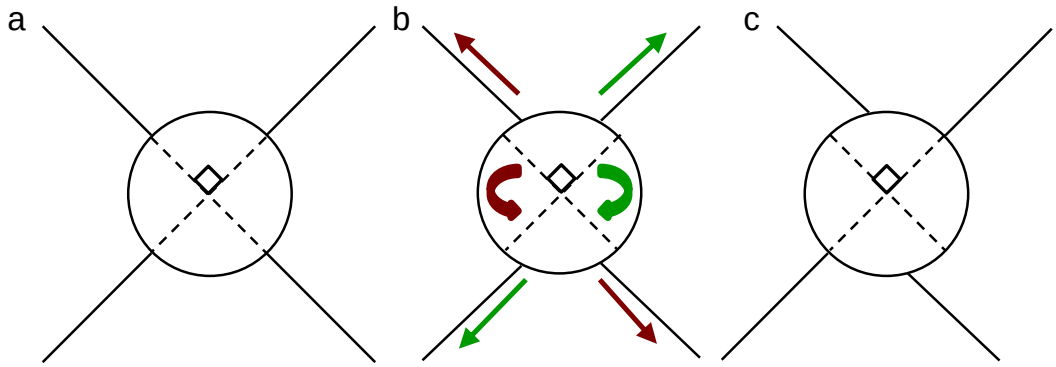

Figure 2.10. Orientation of the wire support support for which roll is disabled (a) and enabled (b), along with a respective maximum roll deflection (c).

of the wire mounts as shown in Figure 2.10c. Similar restrictions apply to the pitch and yaw motions of the model. The current mounting locations are centered on the model and displaced by ±35.7, ±27.4, and ±26.3 mm in the vertical, spanwise, and streamwise directions, respectively, and are selected to enable the angular ranges of ±15°, ±9°, and ±8° in pitch, yaw, and roll, respectively.

2.5.2 Motion Analysis System

A *VICON* MX Motion Capture System is used to measure the spatially- and temporally-resolved motion of the wire-mounted model in the wind tunnel. This system consists of: ***i.*** 6 MX-T40S cameras, each with a 12.5 mm lens (capable of up to 515 fps at full frame, and 2000 fps with a limited view), an electronic freeze frame shutter, and a resolution of 4 megapixels, ***ii.*** MX-Giganet interface of the cameras to a camera host computer (that provides power, synchronization, and data transfer), and ***iii.*** *VICON* Tracker 2.0 Software for low latency data streaming to the traverse controller computer.

The cameras are mounted around the wind tunnel test section and are focused on the wire-mounted model as depicted in Figure 2.11. The current system utilizes overlapping fields of view to determine the time-resolved (6-DOF) position of the moving model in the wind tunnel at a frequency of 600 Hz. The model position is tracked using an optical correlation based on small reflective round markers that are affixed to the model to reflect

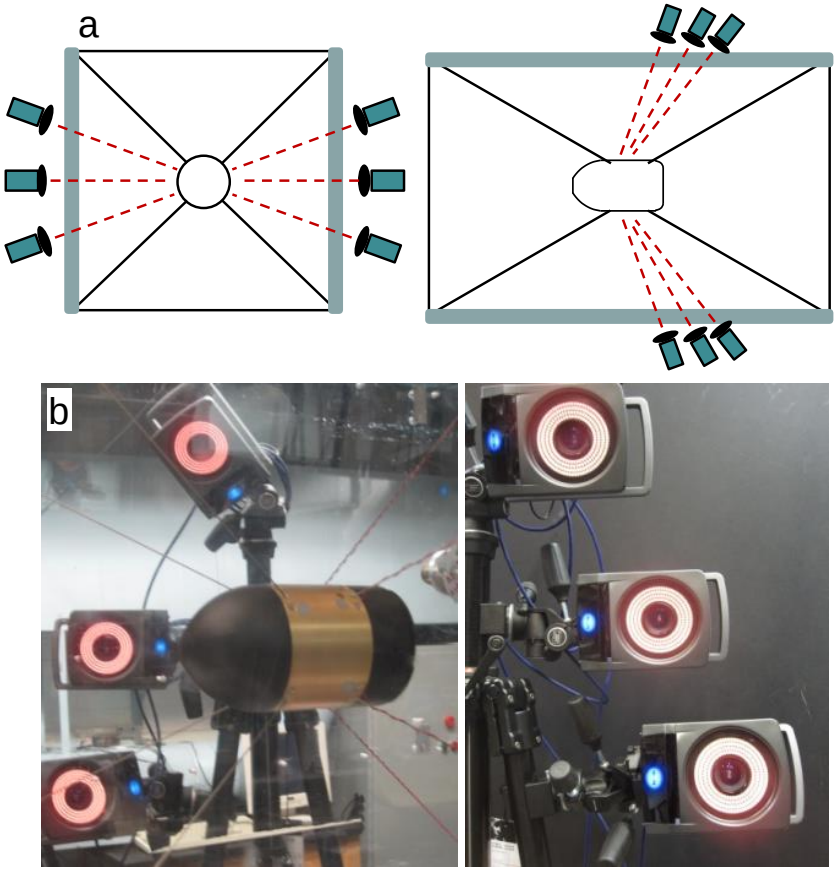

Figure 2.11. Schematics (a) and images (b) of the six-camera positioning of the motion analysis system.

near infrared (NIR) light that is emitted by diode array built into each camera. Six reflective circles of 7 mm diameter 0.4 mm thick are attached to the surface of the model for capturing its motion. These markers are arbitrarily placed so that each camera can see three of them (three markers are visible on the model in Figure 2.11b). The placement of the cameras can be arbitrary as long as the six projected images of these markers measured by the cameras have sufficient information to fully define the 6-DOF motion of the model (an example of the camera locations is shown in Figure 2.11b). The camera system is calibrated by moving a calibration target with three reflective markers through the measurement volume. Once the system is calibrated, a static image of a calibration plate of reflective markers is measured to construct a template that is saved on the host computer to transform the marker measurements into the dynamic aerodynamic model coordinates

with respect to the wind tunnel frame of reference. After the system is calibrated, the *VICON* Tracker software calculates the error in each marker (having typical values between 0.05 and 0.5 mm, dependent on the calibration and camera locations), which are used to calculate the error in the measured model coordinates through propagation of errors from the known geometries. In other words, substitution of the marker locations with their maximum error values will yield a non-zero model location, and this calculation is an estimate of the 6-DOF error.

2.5.3 Electric System Components

The electrical subsystem of this traverse comprises three separate elements. The first element is the 'host' computer which is used for implementing the real time traverse controller and has two *Quanser* Q8 real time data acquisition boards which are used for signal communication of the servo motor command and encoder signals, as well as providing the flow control actuator commands. The second element is a power distribution system that routes up to 1 kW power to servo amplifiers for each of the servo motors. Specific attention was given to proper wire routing and grounding in order to minimize electromagnetic interference (EMI) with the measured signals. Each servo actuator motor has an integrated 20-bit differential quadrature absolute encoder, where the output is converted to a single ended signal by electronic hardware that was built in house, and is sampled by the host computer through one of the Q8 boards. The third element is a multichannel Ethernet data acquisition (DAQ) system that samples the load cells. The load cell signals are on the order of mV and are susceptible to noise, so each load cell is routed with a short cable to signal conditioning electronics that have an instrumentation amplifier and passive RC filtering. These signals are then transmitted through universal data protocol (UDP) packets at a nominal frequency of 1 kHz to the host computer.

The user interfaces with a master computer that uses *Simulink* as an interface to build the controller. Upon completion of the desired controller, *Simulink* generates a compiled *QNX* binary. This binary is copied across an Ethernet network to the host computer (which

utilizes a *QNX* operating system). When the master computer sends the execution command, the controller binary on the host machine is executed in a hard real time environment, which sends time-stamped signals back over Ethernet to the master computer for accurate data recording. The host machine is also connected via Ethernet to the broadcasted signal from the *VICON* machine to use the position measured from the camera system for feedback to the control system code. The triggering signals for flow control and PIV are also generated by the controller and output from the host computer for synchronization of external equipment.

2.5.4 System Control

The designed traverse is controlled through the trajectory tracking controller depicted in Figure 2.12. First, the user can provide two command inputs; a time trace for the desired model trajectory in 6-DOF, and a time trace for flow control actuation commands (e.g., amplitude modulation of the synthetic jet actuator resonance carrier waveforms). Second, the 6-DOF commanded motion is converted into eight servo motor commands (6-DOF to 8-DOF), which are calculated through the geometry of the model and chosen mounting points, assuming the wires are incompressible. The command signal to each servo actuator is then generated using eight proportional-integral-derivative (PID) controllers with the same coefficients [$\kappa_{P,in} = 4.24$ Nm/rad, $\kappa_{I,in} = 21.20$ Nm/(rad·s), $\kappa_{D,in} = 0.02$ Nm·s/rad] which are found from manual iteration and used to command the torque in the motors. With pure feedback control, there is a phase lag between the desired command and the resulting command, so the motions are currently restricted to time-periodic motions where optimal PID coefficients yield an output that is self-similar to the desired command with a change in phase and amplitude. The motion is then estimated by measuring the conditioned encoder signals and inverting these servo motor positions to the model position using a least squares algorithm (8-DOF to 6-DOF). This control loop is considered the 'inner loop controller' in Figure 2.12. This inner loop controller is sensitive to errors in the geometric parameters of the traverse (e.g. mounting locations, or damping and friction of the motors).

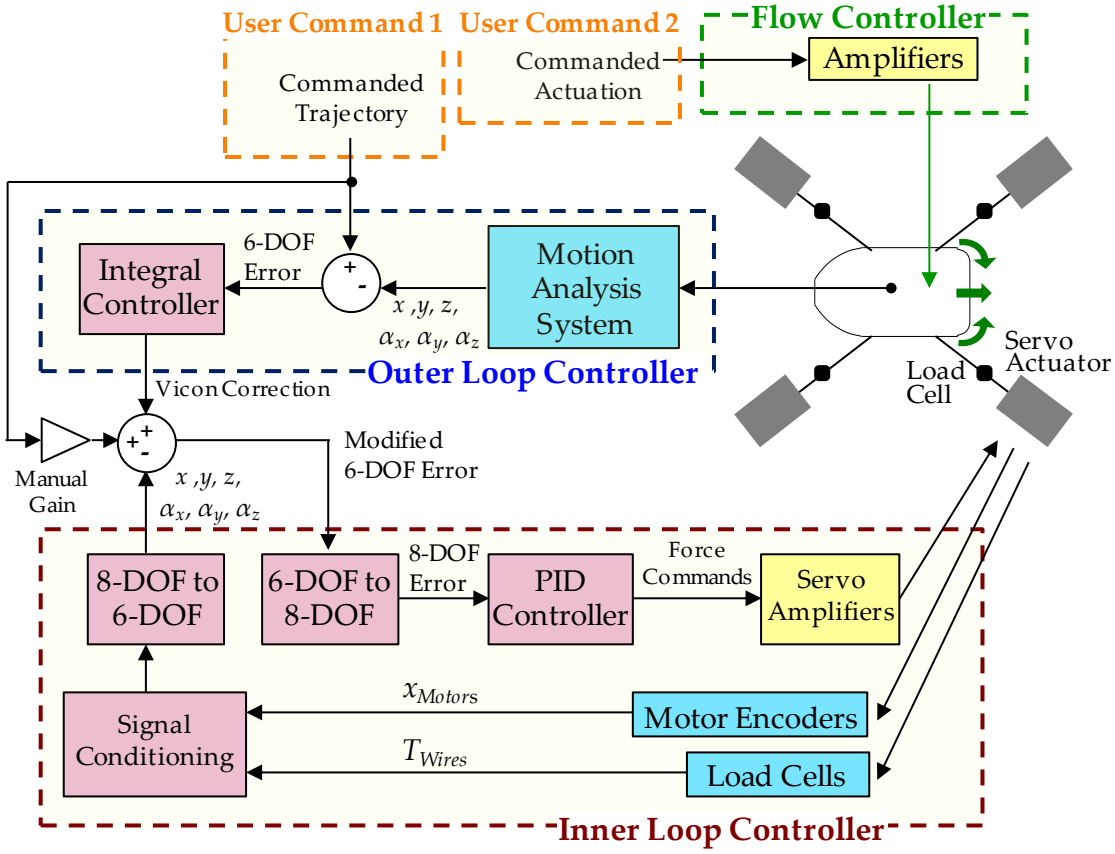

Figure 2.12. Schematics of the traverse trajectory tracking controller.

In order to compensate for this geometric model, as well as the change in the amplitude of the desired command, an 'outer loop controller' shown in Figure 2.12 is implemented to adjust the command of the inner loop based on the motion analysis system to allow for accurate trajectory tracking. The outer loop uses an integral error feedback controller that is set such that the measured trajectories reach the desired ones within 10 seconds ($\kappa_{1,out}$ = 0.3/s for the 3-DOF translational commands and 0.1/s for the 3-DOF rotational commands). In addition, a manual gain of the inner loop command is implemented, determined by matching the magnitudes of the measured amplitude to the desired amplitude, which depends on the frequency and desired motion.

The real time wire tensions are measured using the load cells and are used to extract the aerodynamic forces and moments on the model. This is calculated by using a free body

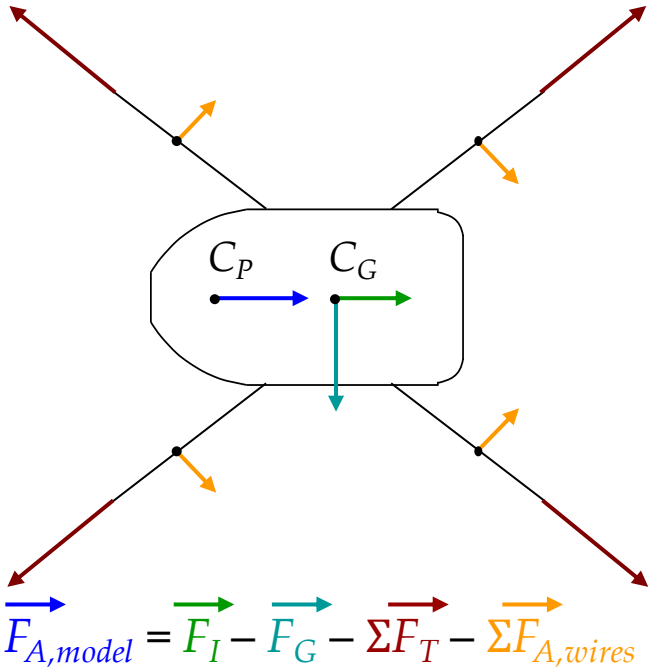

Figure 2.13. Free-body diagram of the aerodynamic platform and support wires.

diagram in a control volume (CV) shown in Figure 2.13, where the aerodynamic forces are calculated by the inertial force, $\vec{F}_{\mathrm{I}}$, of the model (acting at the center of gravity, CG, and calculated from its estimated acceleration) with all other forces subtracted. These other forces include the weight of the model ($\vec{F}_{\mathrm{G}}$, acting at CG), the tension in the wires, $\vec{F}_{\mathrm{T}}$, and the estimated aerodynamic drag of the wires alone, $\vec{F}_{\mathrm{A_{wires}}}$. The aerodynamic force on a wire is estimated as pressure form drag normal to each wire ($C_{\mathrm{D}} = 1.25$), acting at the midpoint between the tunnel flange and the corresponding real time location of the wire mount on the model, using the component of the free stream velocity that is not parallel to each wire (i.e., ignoring friction drag). The force balance yields the resultant aerodynamic force on the model $\vec{F}_{\mathrm{A_{model}}}$. A similar approach is used to determine the moments by weighting each force by the location at which it acts. Measurements of the aerodynamic forces for the axisymmetric body using this force balance are presented in Chapters **V** and **VI**.

2.5.5 The Dynamic Response of the Traverse

The dynamic performance of the 6-DOF traverse is characterized in terms of displacement range and frequency of sinusoidal commands as depicted in Figure 2.14. The range of model motion at increasing operating frequency is restricted by the tension limit of the mounting wires and the mechanical connection to the model, and diminishes with increasing frequency. Therefore, the current controller is tested with a maximum wire tension of 110 N, and the results for translations and rotations are shown in Figures 2.14a and b, respectively. The resulting translation and rotation along and about the *x*, *y*, and *z* axes at f = 0.5 Hz are *x*, *y*, *z* = 50 mm with rotations of $\alpha_x = 8^\circ$, $\alpha_y = 15^\circ$, and $\alpha_z = 9^\circ$, and at f = 20 Hz decrease to *x*, *y*, *z* = 5 mm and to $\alpha_x = 1^\circ$, $\alpha_y = 3^\circ$, and $\alpha_z = 2^\circ$. Streamwise (*x*)

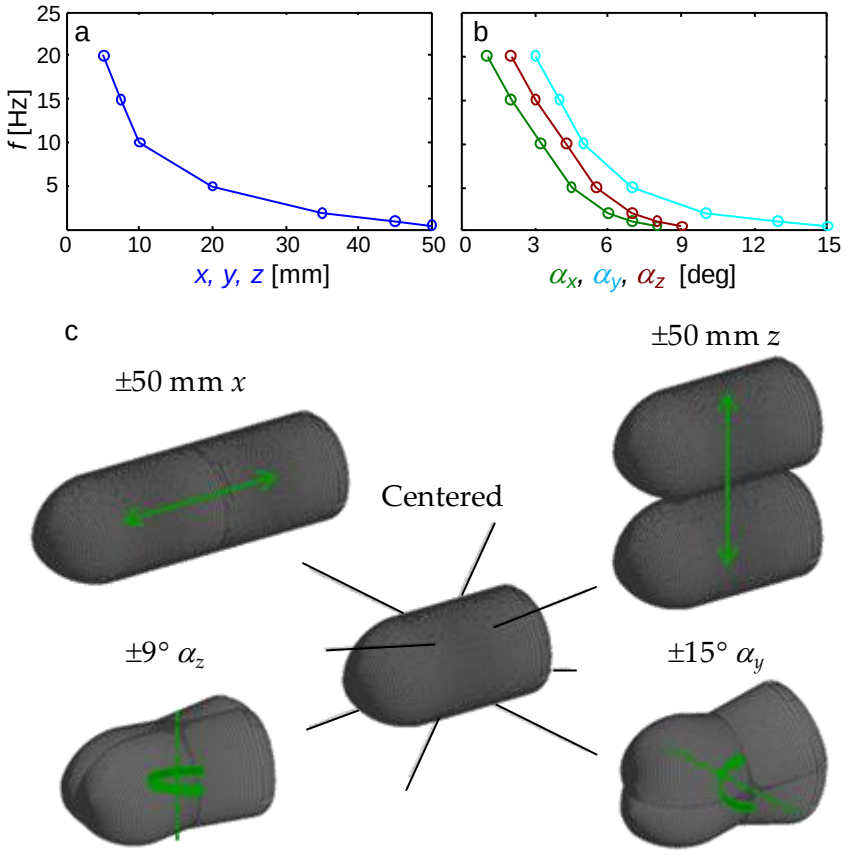

Figure 2.14. Frequency response of translational (a), and rotational (b) motions, with an illustration of the maximum displacements in the streamwise and vertical directions and in yaw and pitch angles (c).

and vertical (z) translations, and pitch (α_y) and yaw (α_z) rotations are shown in Figure 2.14c.

The tracking control authority of the traverse in 6-DOF motion is tested in the presence of flow in the wind tunnel ($Re_D = 2.3 \cdot 10^5$) by using a commanded pitch and yaw time-harmonic motion with amplitudes of 3° and 90° out of phase. The instantaneous trajectories (commanded, and measured by the motion analysis system, cf., §***2.5.2***) are recorded 10 seconds after the traverse is activated to avoid transient response and shown in Figure 2.15. These motions are commanded at representative 'low' and 'high' frequencies of 1 Hz (Figures 2.15a,c,e,g,i, and k) and 10 Hz (Figure 2.15b,d,f,h, and j) with: streamwise translation (x, Figure 2.15a-b), spanwise translation (y, Figure 2.15c-d), vertical translation (z, Figure 2.15e-f), roll (α_x, Figure 2.15g-h), pitch (α_y, Figure 2.15i-j), and yaw (α_z, Figure 2.15k-l). These data show good agreement between the commanded and measured trajectories in terms of peak-peak magnitude (within 5% at 1 Hz in Figure 2.15i and k and 7% at 10 Hz in Figure 2.15j and l), with a phase lags of 40° at 1Hz and 30° at 10Hz. The simultaneous deviations in the four other degrees of freedom that are not commanded are small: within 0.5° in roll (Figure 2.15g and h), and within 0.3 mm in all translations (Figure 2.15a-f). As noted in Section 2.2, the errors in measured motions based on the calibration error of the motion analysis system (0.45 mm per marker on average) are 0.18 mm in translation and 0.02° in rotation through propagation of errors from the known marker locations and model geometry. The measurements in Figure 2.15 can also be used for triggering flow diagnostics (e.g., PIV) and/or feedback for flow control. In fact, as long as the flow control is triggered relative to the measured model location, the phase lag between the commanded and measured trajectory is inconsequential as long as the measured response is the same shape and amplitude as the commanded (this also requires the motion to be harmonic, such that the resulting response is just a time shift of the commanded response).

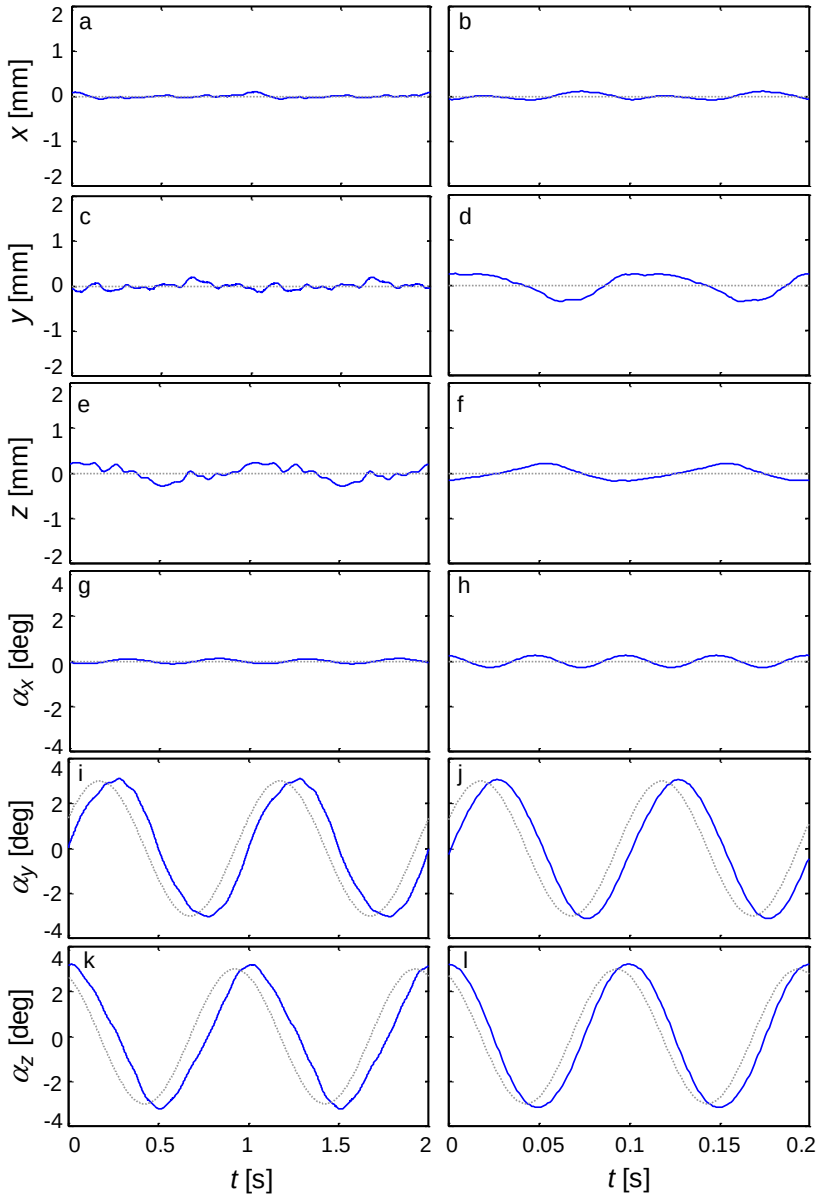

Figure 2.15. Commanded time-harmonic pitch and yaw motions (amplitude 3°, 90° out of phase, dotted gray) at $Re_D = 2.3 \cdot 10^5$, and measured instantaneous trajectories (**blue**). The motions are commanded at 1 Hz (a, c, e, g, i, and k) and 10 Hz (b, d, f, h, and j) with translation in x (a, b), y (c, d), and z (e, f), and rotation in roll α_x (g,h), pitch α_y (i,j), and yaw α_z (k,l)

The measurements of the loads are validated by comparing the measured (traverse) drag with published data. The drag force on the stationary centered model (F_D) is measured over a range of wind tunnel speeds, U_o, of up to 40 m/s ($Re_D < 2.3 \cdot 10^5$), and these data are shown in Figure 2.16 (plotted as dynamic pressure, $\frac{1}{2}\rho A_D U_o^2$, for a linear plot). The

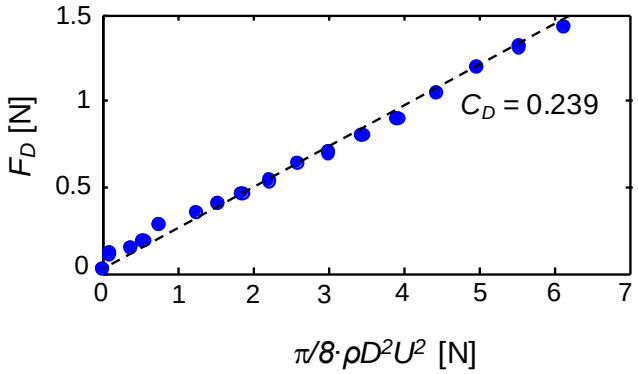

Figure 2.16. Variation of measured model drag with wind tunnel dynamic pressure.

traverse measured drag coefficient (the respective slope) is C_D = 0.239 and is in good agreement with the published drag coefficient for a similar ogive model with a sharp aft end, C_D = 0.25 (Hoerner, 1965). For this stationary centered model, all other forces are nominally zero, and are omitted for brevity.

2.6 3-DOF Free-Flight Model

The axisymmetric model is investigated in 'free flight' in 3-DOF (pitch, yaw, and roll, see Chapter **VII)** using a short sting attachment to the 6-DOF wire traverse (§**2.5**). The model is modified to allow coupling of its nose section to a stationary gimbal that enables the 3-DOF rotations in response to aerodynamic pitch, yaw, and roll moments. To this end, the nose section comprises a stereo-lithographed thin outer shell that houses a central bearing and a (bronze) counterweight that is connected to the moving model, as shown in Figure 2.17a. The design and construction of the moving nose elements placed specific attention on minimizing mounting friction and shell interference. The bearing is placed at $x_o = 0.25c$ downstream of the nose, and upstream of the static center of pressure on this model ($x_{cp} \approx 0.33c$). The aft end of the model is shown in Figure 2.17b. The four actuation jets on this model are referred to as jets 1 through 4 to avoid confusion owing to roll (compare Figures 2.1b to 2.17b). The stationary segment of the model is attached to an external sting as shown in Figure 2.17c, and the resulting limits of the motion in pitch, yaw, and roll are ±16°, ±18°, and ±180°, respectively. The center of gravity of each of the

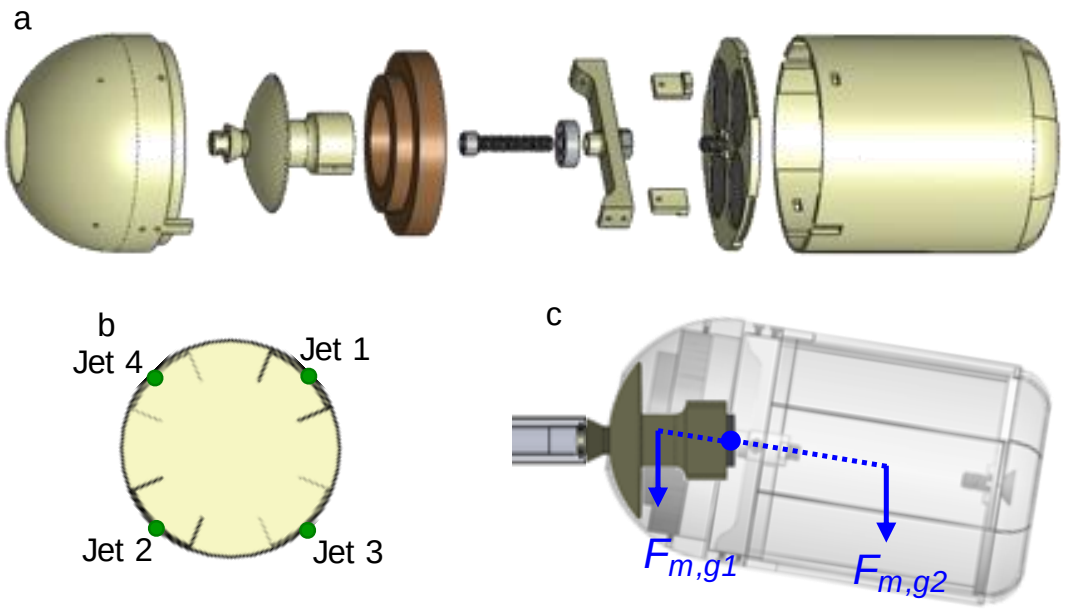

Figure 2.17. Expanded view of the 3-DOF model components (a), upstream view of the model with the four synthetic jet actuators (b), and depiction of the counterbalanced model when it is mounted through the inner nose piece (c).

model components upstream and downstream of the bearing is placed along the axis of symmetry so that it can reach moment equilibrium at any angle of pitch or yaw (marked in blue). Due to imperfections in the model fabrication and weight of the electrical wires that drive the actuators there is a preferential roll equilibrium at which the model comes to rest.

The sting motion is controlled using the dynamic 6-DOF wire-mounted traverse (§**2.5**). Figure 2.18 shows the (right-handed) frames of reference that are used to describe the motion of the sting (x_s, y_s, z_s), and of the model (x_m, y_m, z_m), the rotation angles about each axis are α_x (roll), α_y (pitch), and α_z (yaw). The 16 mm diameter sting is 30.5 mm long, and the center of the wire mounts are placed 25.8 and 58.8 mm upstream of the model nose, and the wire mounting locations on the sting form angles of 105° and 75° with respect to the *y* and *z* axes. The mass of the model is 625g, and in the absence of air flow it exerts a moment of 0.187 N·m on the traverse. The attitude of the sting is controlled by the traverse and in the base position its attitude is designed to coincide with the direction of the free

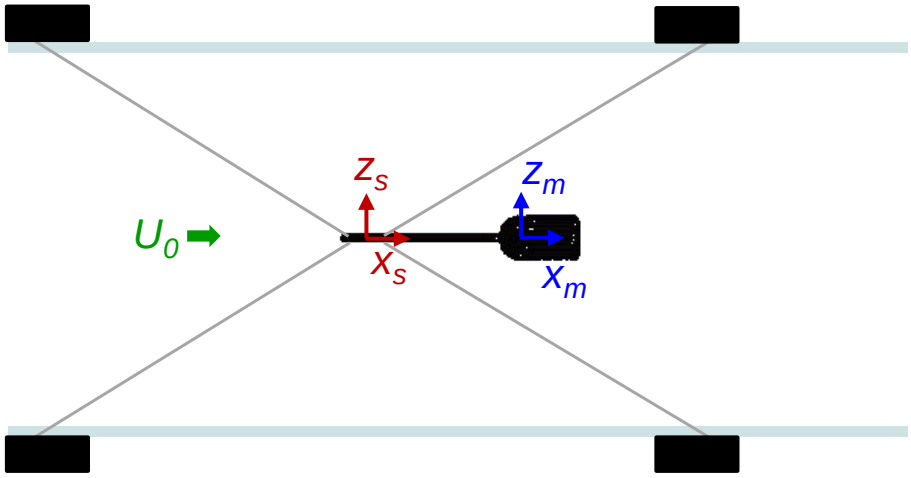

Figure 2.18. Side view of the 3-DOF sting-mounted model, sting coordinate system (**red**), and model coordinate system (**blue**).

stream. The electrical wires for the flow control synthetic jets are weaved along the back four support wires of the sting and along the sting, and the support wires and sting provide electrical ground.

The model dynamics are estimated as a combination of second order mass-spring-damper systems with spring constant K_x, damping constants C_x and C_{yz}, inertias I_x and I_{yz}, and external roll, pitch, and yaw moments (M_R, M_P, and M_Y):

$$I_x\ddot{\alpha}_x + C_x\dot{\alpha}_x + K_x\alpha_x = M_R(t), \quad I_{yz}\ddot{\alpha}_y + C_{yz}\dot{\alpha}_y = M_P(t), \quad I_{yz}\ddot{\alpha}_z + C_{yz}\dot{\alpha}_z = M_y(t) \qquad (2.2)$$

This model excludes any friction effects caused by the bearing and assumes that the system responds symmetrically in pitch and yaw (with the same damping and inertia), and that these parameters are independent of the roll dynamics (which have separate damping, inertia, and spring constants). Within the entire range of realizable pitch and yaw angles the model can be in equilibrium, and therefore the spring constant in pitch and yaw is considered negligible (otherwise the model would restore to center). As noted in the discussion of 2.17c, there is only one equilibrium point at roll at some fixed roll angle which is defined as the zero roll angle. The response dynamics of the model to external moments in either pitch and yaw are each measured from different perturbations of the model (the dynamic perturbations are measured using the motion analysis system). These

perturbations are performed manually by hand, and designed such that the model would start at an amplitude comparable to the expected aerodynamic vibrations (~ -10°), are introduced to a manual external force at t = 1 s, and end at the opposite amplitude (~10°), with negligible motion in the other degrees of freedom. The corresponding measured time traces are shown in blue in Figure 3b and c. The damping and spring constant in roll are estimated from a different model perturbation shown in Figure 3a in blue with the initial model attitude set to α_x = -50°. The model is released at t = 0, where the spring constant causes the model to oscillate and the damping constant reduces its kinetic energy.

In order to estimate the dynamic parameters, the inertia components $I_x = 6.45 \cdot 10^{-4}$ Nms^2/rad and $I_{yz} = 1.25 \cdot 10^{-3}$ Nms^2/rad are extracted from CAD software ignoring the weight of electrical wires. The measured perturbation traces in Figure 2.19 and their numerical derivatives are then computed and the substituted into their respective degree of freedom in Equation (2.2), setting the external moments equal to zero (similar to Figure 2.8, the measured perturbation data for pitch and yaw are only used for t > 1, after the moment is applied). The result yields three sets of data points: one in roll which is used to estimate the least squares fit to K_x and C_x, one in pitch which is used to estimate the least squares fit to C_{yz}, and one in yaw which is used to produce another least squares fit to C_{yz}. The results are $K_x = 3.2 \cdot 10^{-3}$ Nm/rad, $C_x = 1.8 \cdot 10^{-4}$ Nms/rad, and $C_{yz} = 8.5 \cdot 10^{-3}$ Nms/rad (Cyz is taken as the average of the two estimates, each with a difference of $\sim 0.2 \cdot 10^{-3}$ from the average). The fit to the roll dynamics are shown in Figure 2.19a in green and are in good agreement to the measured response, with a similar frequency and decay rate. The fits to the pitch and yaw dynamics with the same damping coefficient is shown in Figure 2.19b and c, showing a reasonable agreement for t > 1 (for t < 1, the fit is replaced with α = 0). The least squares fit to pitch and yaw does not capture the initial overshoot of the model which is attributed to frictional effects in the bearing, but accurately captures the steady state response in both pitch and yaw, even with the same damping coefficient.

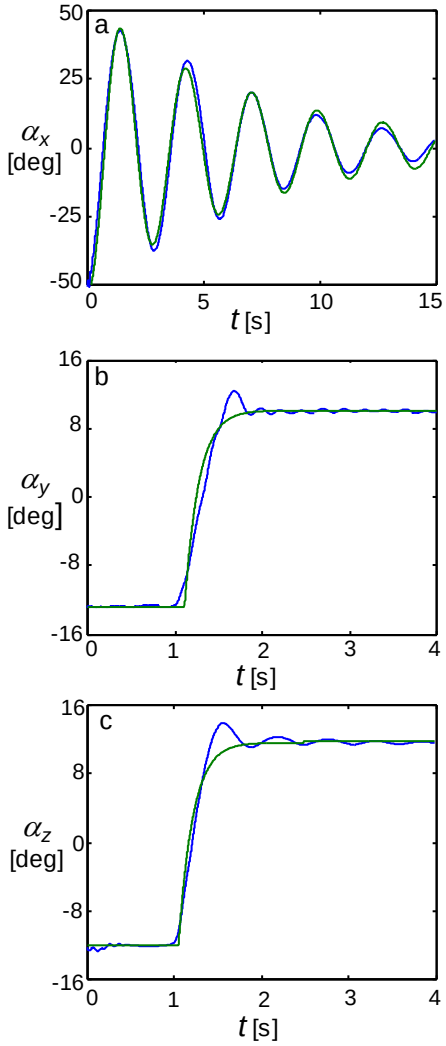

Figure 2.19. Time traces of the motion of the 3-DOF model following three different perturbations (**blue**) in**:** roll (a), pitch (b), and yaw (c), each designed to measure their characteristic damping and spring constants (the inertia is extracted from CAD software). The corresponding least squares fit to three mass-spring-damper models are shown in **green**.

2.7 Velocity Measurements in the Model Wake

One of the primary objectives of the present research is to measure the coupled flow in the wake to the stationary and moving model in the absence and presence of actuation. These flow field measurements are acquired using low- and high-speed particle image velocimetry (PIV) described in §***2.7.1*** and §***2.7.2***, respectively. In addition, some hot wire anemometry was also used to characterize the flow in the far wake and is described briefly in Chapter **V**. Low-speed PIV (frame rates lower than 15 fps) is used when the model is

stationary and the actuation is time-periodic, or when motion of the model is nominally time-periodic with a clear phase reference and the measurements can be acquired phase-locked to its motion (or to its attitude) such as in the: hoop frame (Chapter **III),** 'free'1-DOF (Chapter **IV**), and controlled 6-DOF (Chapters **V** and **VI**). High-speed PIV (at 500 fps) is used in the absence of a clear phase reference as during the motion of the free 3-DOF model (Chapter **VII**). The data processing for all PIV measurements is described in §***2.7.3***. Seed particles are provided by a thin vertical airfoil which has a slot along its trailing edge and is mounted in the center of the tunnel plenum upstream of the test section. The fog is produced by a theatrical fog machine and create 0.25-0.60 μm particles in a sheet that is nominally 20mm thick and 100 mm high. The vertical spreading of the fog sheet allows multiple regions of the flow to be characterized by varying the location of the PIV laser sheet.

2.7.1 Low-Speed PIV

The low-speed PIV measurements are acquired using conventional 2-D and stereo PIV (LaVision) hardware and software. The standard stereo optical system includes two CCD imagers (14 bit, 1,200 x 1,600 pixels), a programmable trigger timing unit, and a 50 x 50 mm calibration plate, a dual head 120 mJ Nd:YAG Laser (532 nm, maximum pulse frequency 15 Hz, pulse width 3-5 ns). This system was previously used by Kearney (2015, 2-D PIV) and Simpson (2015, stereo PIV). The time interval Δt between successive laser pulses varies with the field of view and flow speed and in the present experiments is within the range $15\mu s < \Delta t < 40\mu s$ (see Table 2.1).

The low-speed 2-D PIV system is utilized in two configurations as shown in Figures 2.20a and b (used for the hoop frame in Chapter **III** and the 6-DOF traverse in Chapter **V**), and in Figures 2.20c and d (used for the 1-DOF in Chapter **IV**). Side- and top-views of these configurations are shown in Figures 2.20a and c, and Figures 2.20b and d. In Figure 2.20a, the field of view measures 1.75D and 1.4D in the streamwise and cross-stream directions, and the laser sheet thickness at the center of the domain is about 3mm. All of

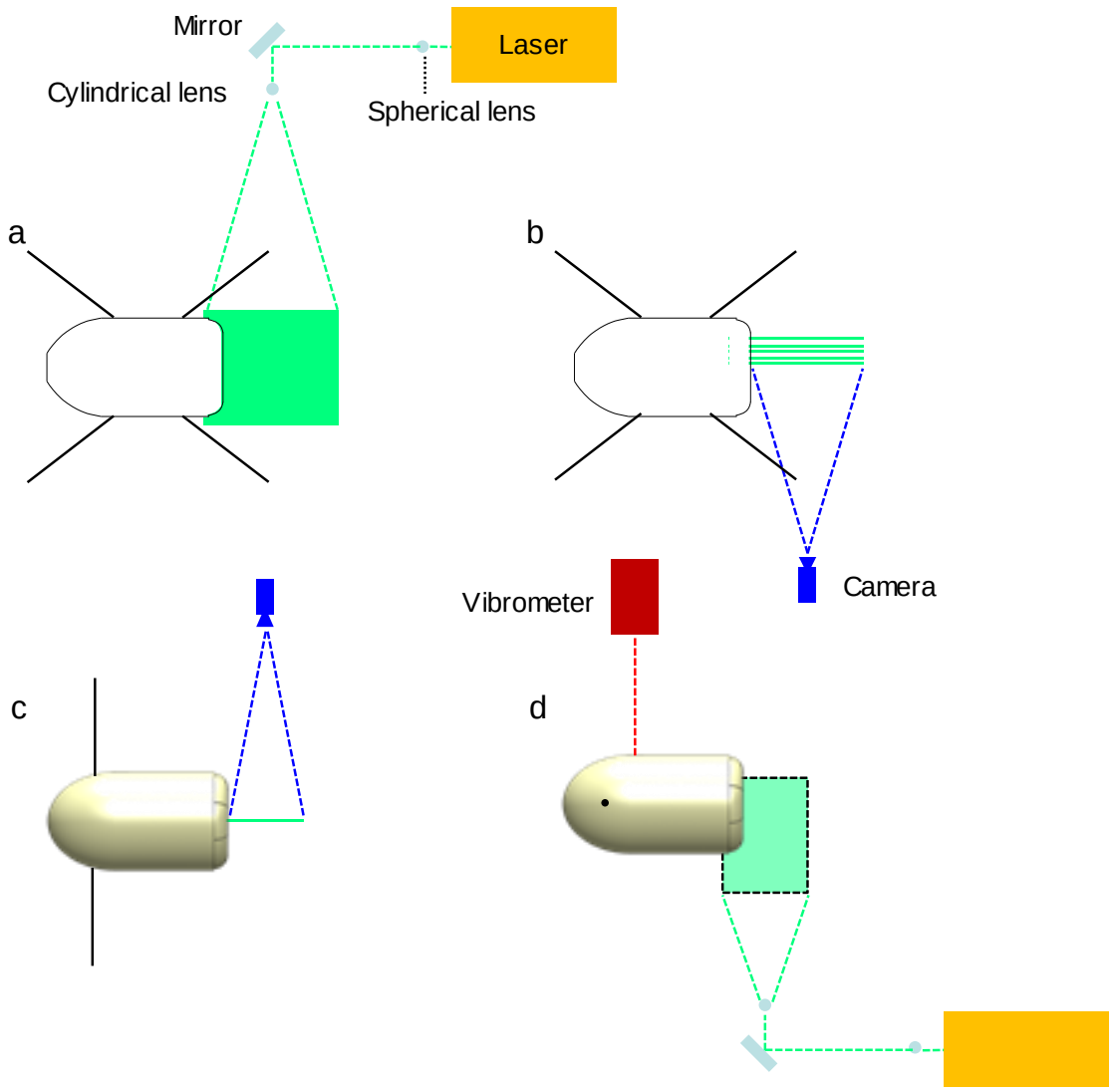

Figure 2.20. Side (a,c) and top (b,d) views of the low-speed 2-D (single-CCD) PIV system, showing the eight-wire (a,b), and single-wire (1-DOF) (c,d) setups. The laser sheet (**green**) is shown to scale with the model. The laser and camera optical paths (dotted **green** and **blue**) are not to scale.

the laser sheets in the present work are created with the same optics at different locations. Four off-center laser planes are also utilized in Chapter **III** to characterize spanwise effects, and are spaced $\Delta y/D = 0.07$ apart (Figure 2.20b). The 1-DOF (Chapter **IV**) PIV field of view is within the model (horizontal) meridional plane (Figure 2.20c). The PIV camera is mounted above the tunnel test section, and the field of view measures $0.9D$ x $1.2D$ in the streamwise and cross-stream directions and is utilized in multiple locations to form a

mosaic of 0.9*D* x 1.8*D*. The model blocks the light emitted by the horizontal laser from entering the vibrometer (Figure 2.20d).

The low-speed stereo PIV system that is shown schematically in a top view in Figure 2.21a includes two identical CCD cameras that are placed at angles of 20° on each side of to the normal of the image plane. Each camera is used with a Scheimpflug adapter for perspective correction so that the fog particles are in focus in the entire image plane of each camera. This setup resolves all three components of the velocity field in a measurement

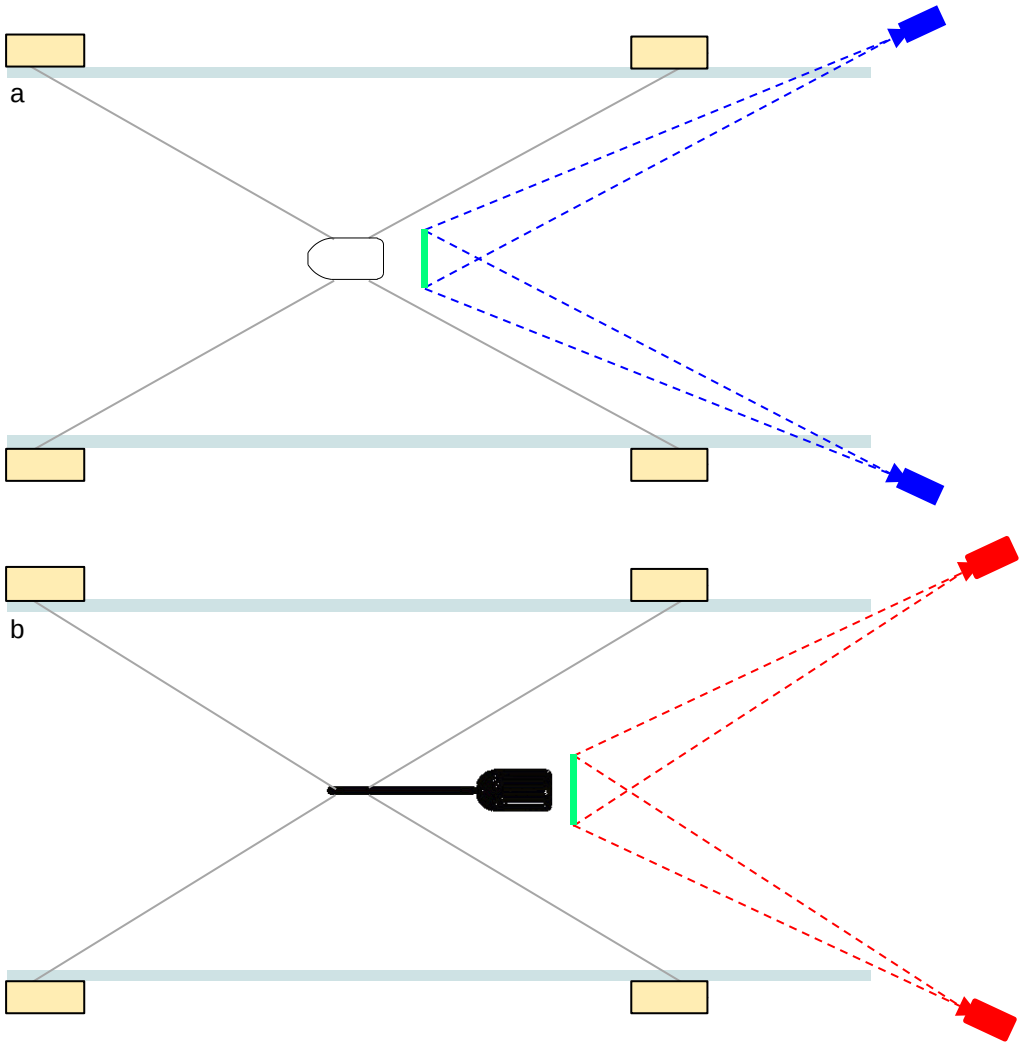

Figure 2.21. Top views of the stereo PIV system, including both the 6-DOF low-speed (a, **blue**), and the 3-DOF high-speed (b, **red**) PIV setups. The wires, motor, and laser sheet are to scale with the model and test section.

domain measuring 1.3*D* x 1.3*D*, 1*D* downstream of the aft end of the model (1.9*D* downstream of the center of the wires).

2.7.2 High-Speed PIV

The velocity in the wake is also measured using a high speed (f = 500 Hz) stereo particle image velocimetry (SPIV) system (Figure 2.21b) to characterize the wake dynamics behind the free 3-DOF model (Chapter **VII**) using the same optical components as in the low-speed stereo PIV setup (and similar to the setup of Woo, 2014). This setup uses a programmable timing unit high speed controller, and two CCD cameras capable of 6200 fps at 1,280 x 800 pixels, and 12-bit depth. The high-speed ND:YLF laser has 25 mJ/pulse at 527nm and pulse width of 120 ns. The thickness of the laser sheet at the center of the measurement domain is about 5mm. The cameras are each placed at an angle of 25° to the normal to the laser sheet and the field of view measures 1.8*D* x 1.8*D*, and is located 0.25*D* downstream of the aft end of the model (1.63*D* downstream of the axis of pitch/yaw rotation).

2.7.3 Processing of the PIV Data

The PIV data are processed using commercial software (LaVision) based on a standard double frame FFT cross-correlation method (e.g., Raffel, Willert, and Kompenhans, 1998). The calculations start with an initial image preprocessing (i.e., subtracting off a background image without fog), and applying a mask to delete the part of the image with the body of the model (in views where the body is present). The cross-correlation algorithm is applied in multiple passes over smaller interrogation windows, each with 50% overlap, where vectors are then rejected based on their correlation peak ratios ("Q ratios" less than a certain criterion, Q_{crit}). In addition, if the vectors exist in groups of less than 5 vectors or are different than 1.5 standard deviations of the average, they are also removed. The number of passes, size of the interrogation windows, and maximum Q ratios are varied depending on the dataset and are included in Table 2.1. These calculations yield the velocity vectors on a grid whose dimensions depend on the size of the final interrogation window (e.g., if

the image includes 1,600 x 1,200 pixels and the final interrogation window includes 32 x 32 pixels with 50% overlap, the vector grid include 1/16 points of the pixel array, or 100 x 75). Once these velocity vectors are calculated, the vorticity normal to the interrogation region, ζ, is postprocessed using an initial 3 x 3 Gaussian smoothing filter with a standard deviation of half the vector spacing, and then a 3 x 3 centered finite difference stencil. In addition, it is important to estimate the non-repeatability of the vector fields that are presented. The error analysis of the PIV measurements was discussed in detail by Woo (2014), and as a guideline the present measurements will present the resulting RMS of instantaneous measurements about their average (omitting any vectors that fluctuate across a zero value). This is an upper bound on the velocity and vorticity fluctuations because it does not decouple any turbulent RMS, or any of the wake dynamics that are not in phase with the model motion. To this end the fluctuations of the velocity and vorticity (δU and $\delta\zeta$) are shown in each of the PIV setups resolved, and these fluctuations are shown along with the relevant processing parameters (Δt, Q_{crit}, interrogation windows, and number of averages), as well as the location of the window with respect to the shear layer and the extent of the motion of the model. For the high-speed stereo PIV system, the images were filtered using a proper orthogonal decomposition (POD) approach, instead of a phase average. This method is discussed in Appendix **A**, and the velocity and vorticity fluctuations in this data set are instead approximated by the average RMS of the instantaneous velocity vectors about their POD reconstruction rather than a phase average (again, omitting any vectors that fluctuate across zero). The resulting fluctuations in the wake velocity and vorticity for all of the varying PIV data sets are shown in Table 2.1.

Table 2.1: Measured velocity and vorticity fluctuations for each experiment.

Setup	Model Motion	Location	Δt	Q_{crit}	Interrogation Windows	# of Averages	$\delta U/U$	$\delta\zeta/\zeta$
Wire-Mounted 2-D PIV	1 Hz, 1.5° pitch	**III**	15μs	1.8	Two:64px x 64px Two:32px x 32px	270	2.0%	9.8%
1-DOF 2-D PIV	Various amplitude yaw ~2 Hz	**IV**	40μs	2.1	Two:64px x 64px Two:32px x 32px	170	3.2%	8.2%
Wire-Mounted 2-D PIV	20 Hz, 3° pitch, and 20 Hz, 5 mm plunge	**V**	15μs	1.8	Two:64px x 64px Two:32px x 32px	270	2.4%	10.2%
6-DOF SPIV	12 Hz, 3° pitch and yaw out of phase	**VI**	27μs	2.5	Two:64px x 64px Two:32px x 32px	600	4.9%	14.5%
3-DOF High Speed SPIV	Various amplitude pitch and yaw ~2 Hz	**VII**	32μs	2.8	One:48px x 48px Two:24px x 24px	N/A, POD used instead	4.1%	12.7%

CHAPTER III

QUASI-STEADY MODEL-WAKE COUPLING

This chapter focuses on characterization of the near-wake dynamics and induced aerodynamic loads on a nearly-stationary axisymmetric model (cf., Chapter **2.2**) undergoing low-frequency pitch oscillations at a reduced frequency $k = \pi cf/U_o < 0.013$ (or 1 Hz) in the absence and presence of actuation (this motion is directly equivalent to yaw oscillations since the gravitational effects are negligible). The experiments are performed using the axisymmetric hoop frame (Chapter **2.3**). The effects of synthetic jet actuation on the near wake and the aerodynamic loads are characterized for a stationary centered model (§**3.1**), when the model is set to (or transitioning to) a fixed offset pitching angle (§**3.2**), and when the body is undergoing simple time-harmonic pitching motion and the actuation is amplitude-modulated (§**3.3**).

3.1 Centered Static Model

The earlier work of Abramson, Vukasinovic, and Glezer (2011) established the effect of continuous actuation of synthetic jets on a stationary 80 mm diameter axisymmetric model oriented along the streamwise direction ($\alpha_x = \alpha_y = \alpha_z = 0$). Specifically, they showed that a significant increase in lift force and pitching moment magnitudes could be attained using jet actuation with a slight penalty in drag. In the present investigations, the actuation frequency is set near the actuator resonance (cf., Figure 2.2, $f_A^* = 0.045$), and C_μ is varied by amplitude modulation of the actuation waveform. In this chapter, time is scaled by the model convective time scale, $\tau_{conv} = c/U_o = 4.1$ ms. Initially, the 'top' jet (cf., Figure 2.1) is tested with $C_\mu \cdot 10^3 = 0.2$, 0.8, 2.0 and 3.0, and the variation with time of the three aerodynamic forces (C_D, C_S, C_L), and the pitch and yaw moments (C_M, and C_Y) on the

model are recorded (at 2000 Hz) prior to ($0 < t/\tau_{conv} < 500$), during ($500 < t/\tau_{conv} < 1{,}500$) and following the termination of ($1{,}500 < t/\tau_{conv} < 2{,}000$) the actuation. These time ranges are chosen such that both transient and quasi-steady effects associated with actuation onset and termination can be captured. The corresponding time traces of the actuation-induced changes in the induced loads ΔC_D, ΔC_S, ΔC_L, ΔC_M, and ΔC_Y are shown in Figures 3.1b-f,

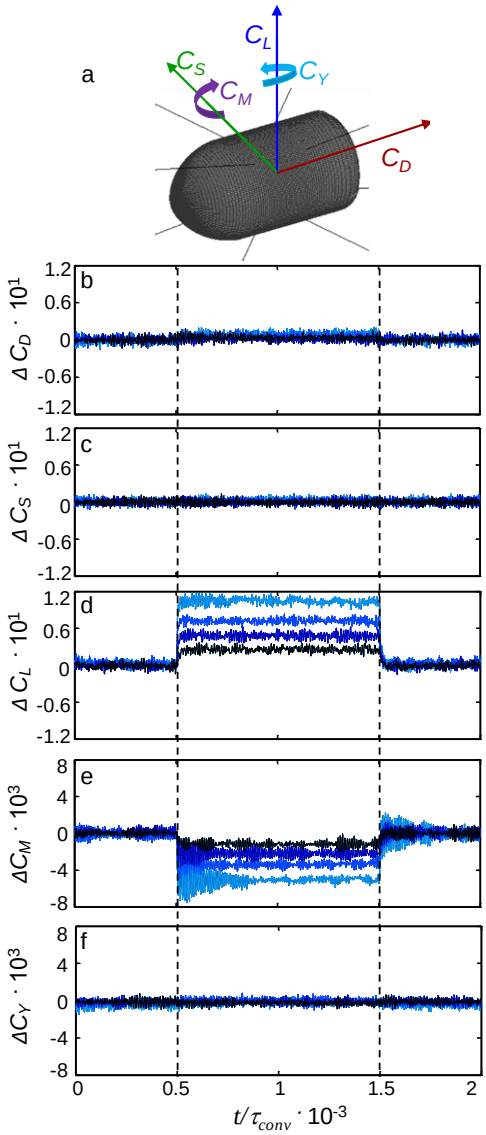

Figure 3.1. Schematic diagram of the model and the coordinate system (a), and time traces of the jet induced loads (relative to the base flow): drag (b), side (b), and lift (c) forces, and pitch (d) and yaw (e) moments. The flow is continuously actuated during $0.5 < t/\tau_{conv} \cdot 10^3 < 1.5$, with square amplitude modulation at $C_\mu \cdot 10^3 = 0.2$, 0.8, 2.0 and 3.0, from darkest to lightest color, respectively.

respectively. Here, the moment coefficients are defined relative to the center of the wire mounts on the model ($x_C = 0.54c$ from the nose), and the sign convention of the forces is based on a right handed coordinate system (Figure 3.1a). The moments are taken to be CCW-positive around the force (positive) directions such that a positive ΔC_M is associated with pitch up. Hence the alteration of the aerodynamic flow on the aft end of the model by the top jet induces positive C_L and negative ΔC_M. These results are in accord with the earlier study of Abramson, Vukasinovic, and Glezer (2012), yielding a maximum $\Delta C_L = 0.1$, weak $\Delta C_D \sim 0.01$, $\Delta C_M = 0.006$, and negligible ΔC_S and ΔC_Y. The pitch measurement has a transient oscillating rise and decay at a period of $t/\tau_{conv} = 10.5$ (~23 Hz), which is associated with the natural frequency of the system. The excited pitch resonance decays back to baseline level in $t/\tau_{conv} \sim 300$ because of the natural damping of the system. It should be emphasized that this oscillation (seen clearly in pitch from $t/\tau_{conv} = 0.5$ to 0.75 and 1.5 to 1.75 in Figure 3.1d) is not a component of the aerodynamic force itself but is instead caused by the natural vibration of the supported model, and is clearly dependent on the model inertia and the mounting structure. The quasi-steady level of the induced pitching moment is established once the transient rise of the pitching moment decays, and it remains nearly-unchanged until the actuation termination.

The individual effects of the remaining (three) jets are characterized in a similar manner, and the variations with C_μ of the steady time-averaged induced lift and pitching moment are shown in Figures 3.2a and b, respectively. These data show that ΔC_L and ΔC_M initially increase linearly with C_μ, but that this increase begins to saturate approximately when the jet peak velocity exceeds the free stream speed ($C_\mu = 3 \cdot 10^{-3}$) for which $\Delta C_L = 0.1$ and $\Delta C_M = 0.006$ indicating an upper bound on the deflection of the separating shear layer into the near wake of the model. The corresponding variation of the C_D, C_S, and C_Y with C_μ (not shown) exhibit no noticeable trends. Based on these characterizations, the operating C_μ is set to 0.003.

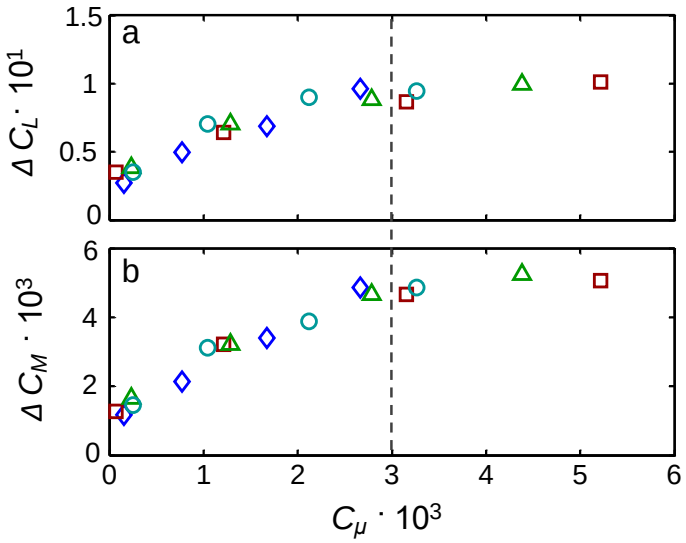

Figure 3.2. Variation of the induced changes in effective lift (a), and pitching moment (b), with the jet momentum coefficient, C_μ, for top (◊), right (□), left (Δ) and bottom (o) jets (the selected operating C_μ for Chapter **III** is shown with a dashed line).

Similar to Figure 3.1, step activation and deactivation of the control jets introduces transient vibrations at the model natural resonance, which is particularly evident in the measured ΔC_M, and are clearly dependent on the support system and are also coupled to the flow field about the model. These transients can be mitigated by slowing the step changes in the onset and termination of actuation. To illustrate this, the jet activation is applied using both a sinusoidal and a square-wave amplitude modulation of the bottom jet actuation signal. Figure 3.3 compares the two modulation approaches in terms of ΔC_L and ΔC_M at $C_\mu = 0.003$, and two notable differences in the sinusoidal modulation relative to the step modulation are observed: a) the natural resonance of the model is bypassed (Figure 3.3b), and b) the saturation effect in the induced ΔC_L and ΔC_M (cf., Figure 3.2) by the sinusoidal modulation (Figure 3.3a and b). Figure 3.3 indicates that amplitude modulation of the actuation signal can be utilized to control an arbitrary time varying responses in the induced aerodynamic loads within the ranges $-0.1 < \Delta C_L < 0.1$, and $-0.006 < \Delta C_M < 0.006$.

The effects of the actuation are also assessed using PIV measurements (cf., Chapter ***2.7.1***) in the central vertical plane of the near wake. Color raster plots of ensemble-

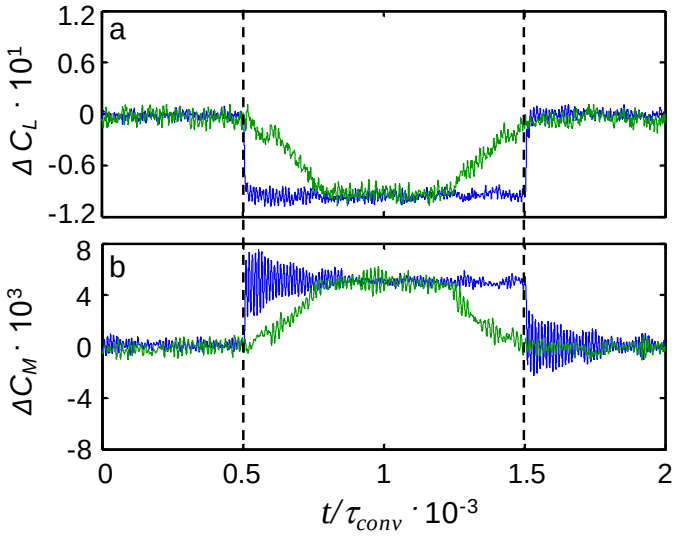

Figure 3.3. Time traces of the relative lift (a), and pitching moment (b) when the flow is continuously actuated during $0.5 < t/\tau_{conv} \cdot 10^3 < 1.5$ with sinusoidal (**green**) and square (**blue**) modulation of the bottom jet at maximum $C_\mu = 3 \cdot 10^{-3}$.

averaged distributions of the normalized azimuthal vorticity $\hat{\zeta}_y(x, z)$ superposed with velocity vectors in the base flow in the presence of actuation by the top and bottom actuator jets are shown in Figure 3.4 for $\alpha_y = 0$. The base flow (Figure 3.4a) is fairly symmetric, where the reversed flow domain of the wake extends to slightly less than $x/D = 1$. The axisymmetric shear layer that forms at the point of flow separation off the body is marked by high concentrations of vorticity ($|\hat{\zeta}_y D/U_o| > 20$). There is an opposite sense of vorticity in the top and bottom shear layers, which is an artifact of the x-z coordinate system utilized,

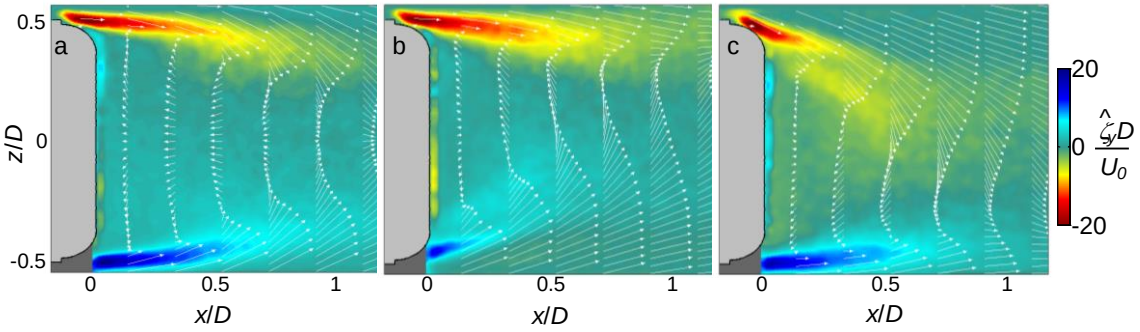

Figure 3.4. Color raster plots of the time-averaged azimuthal vorticity, $\hat{\zeta}_y$, overlaid with velocity vectors ($\alpha_y = 0$) for the base flow (a), and in the presence of bottom (b) and top (c) jet actuation at $C_\mu = 3 \cdot 10^{-3}$.

in place of a cylindrical one. When either jet is activated (C_μ = 0.003, Figure 3.4b and c), the shear layer on the actuated side of the wake is rotated approximately 10° towards the wake centerline, and the induced asymmetry largely suppresses the reversed flow region at that side. These data show that the effects of the individual top and bottom jets on the flow field are approximately symmetric with respect to the streamwise direction, as expected.

To understand the global wake development outside of the plane of symmetry, the alteration of the wake behind the model is investigated using PIV in the equally-spaced parallel planes offset by $\Delta y = 0.07D$ relative to the center x-z plane $y = 0$. The axisymmetric geometry is utilized to produce five effective rotated fields of view, and the ensemble averaged cross-stream velocity, $\widehat{U}_c$, is extracted as a representative parameter. This $\widehat{U}_c$ is not the same as $\widehat{U}_y$ or $\widehat{U}_z$, and instead is defined as the velocity away from the centerline (in the vertical planes above and below the centerline, $\widehat{U}_c = +\widehat{U}_z$ and $-\widehat{U}_z$, respectively, and in the horizontal planes in the +y and -y directions $\widehat{U}_c = +\widehat{U}_y$ and $-\widehat{U}_y$, respectively). Figure 3.5 shows color raster plots of distributions of the measured $\widehat{U}_c$ in the PIV planes (reflected about the center plane) superposed with an image of the model ($-0.25 < \widehat{U}_c/U_o < 0.25$, and $\widehat{U}_c > 0$ is the region of the flow away from the model centerline). Figure 3.5a shows the base velocity field, where the outer flow is vectored towards the center of the wake and the flow near the aft surface of the model is recirculated away from the centerline. Upon activation of all four jets in Figure 3.5b, the magnitude of the wake flow that is directed away from the centerline is diminished in the center plane, and is intensified in the off-center planes. The slight enlargement of the reversed flow domain is in agreement with the small increase on model drag in the presence of actuation (cf., Figure 3.1a). The activation of a single jet (Figure 3.5c) induces significant flow asymmetry which results in an increase in C_S and C_Y (the cross-stream equivalent of Figures 3.1c and d). Figure 3.5d shows the effects of activation of two adjacent jets, which appear to be

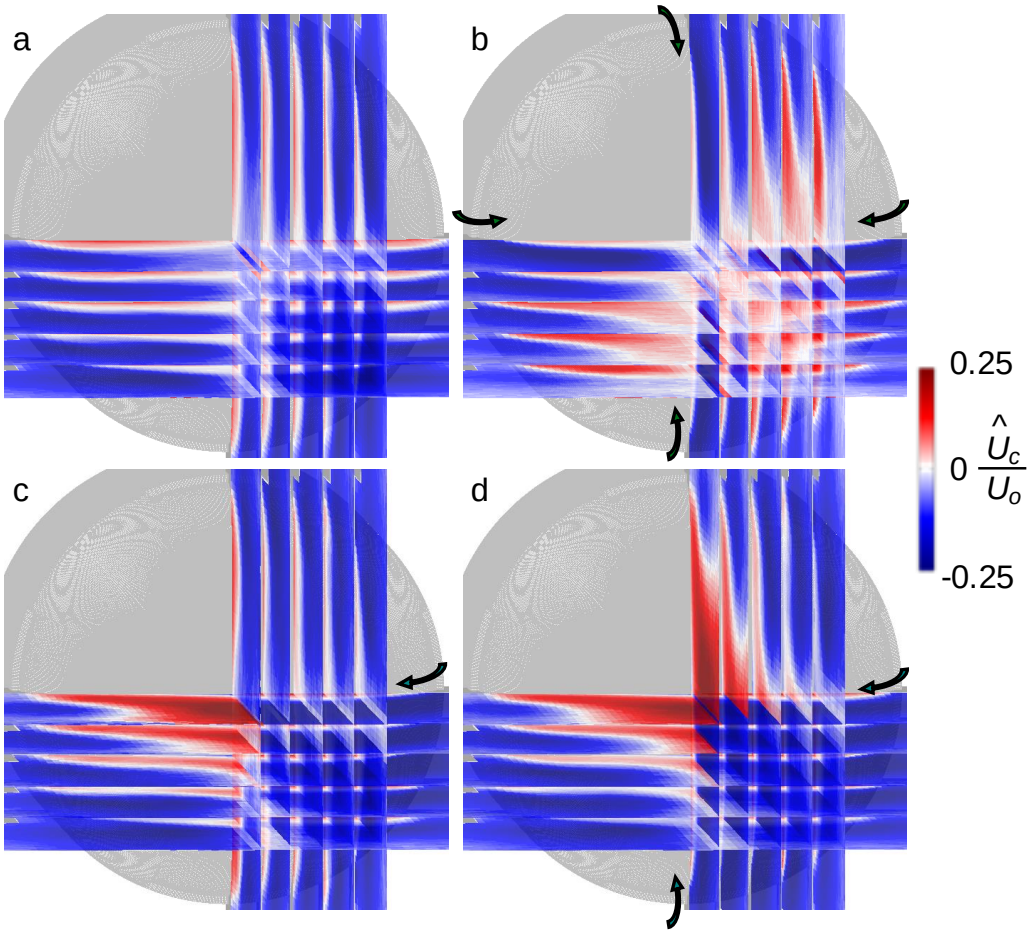

Figure 3.5. Color raster plots of $\hat{U}_c$ in the center x-z plane and at four parallel planes offset incrementally by $\Delta y/D = 0.07$ in the base flow (a), and in the presence of actuation with four (b), one (c), and two (d) jets at $C_\mu = 3 \cdot 10^{-3}$.

simply additive (compare Figures 3.5c and d). This implies that there is little interference between adjacent jets and therefore when the model attitude is in the streamwise direction, the induced effects of the top and bottom jets primarily affect ΔC_D, ΔC_L, and ΔC_M, and have little or no effect on ΔC_S and ΔC_Y.

3.2 Transitory Pitching Motion

The effects of the actuation on the flow over the model and on the aerodynamic loads is investigated over a range of pitch angles when the model is stationary or when the model is moving at a low pitch rate. The actuation can be used to either cancel or enhance asymmetric aerodynamic loads that are engendered at off-center model attitudes (using the SMA wires, as described in Chapter **2.3**). Figure 3.6 shows the variation of the loads with

α_y ($-4.5^\circ < \alpha_y < 4.5^\circ$, $C_\mu = 3 \cdot 10^{-3}$) in the absence of actuation (C_D, C_S, C_L, C_M, and C_Y in Figures 3.6a-e, respectively), along with incremental loads induced by the top jet (ΔC_D, ΔC_S, ΔC_L, ΔC_M, and ΔC_Y, Figures 3.6f-j, respectively). Figure 3.6a shows the variation in C_D which is measured relative to the base drag on the streamwise-aligned model C_{Do}, and is symmetric about $\alpha_y = 0$. For this Reynolds number and body shape, C_{Do} is expected to be about 0.25 (this agrees with Hoerner, 1965, and is also verified on the wire-mounted traverse in ***2.5.5***). The measured C_S and C_Y shown in Figures 3.6b and e, respectively, are nominally zero, and the measured small but nonzero changes are attributed to deviations

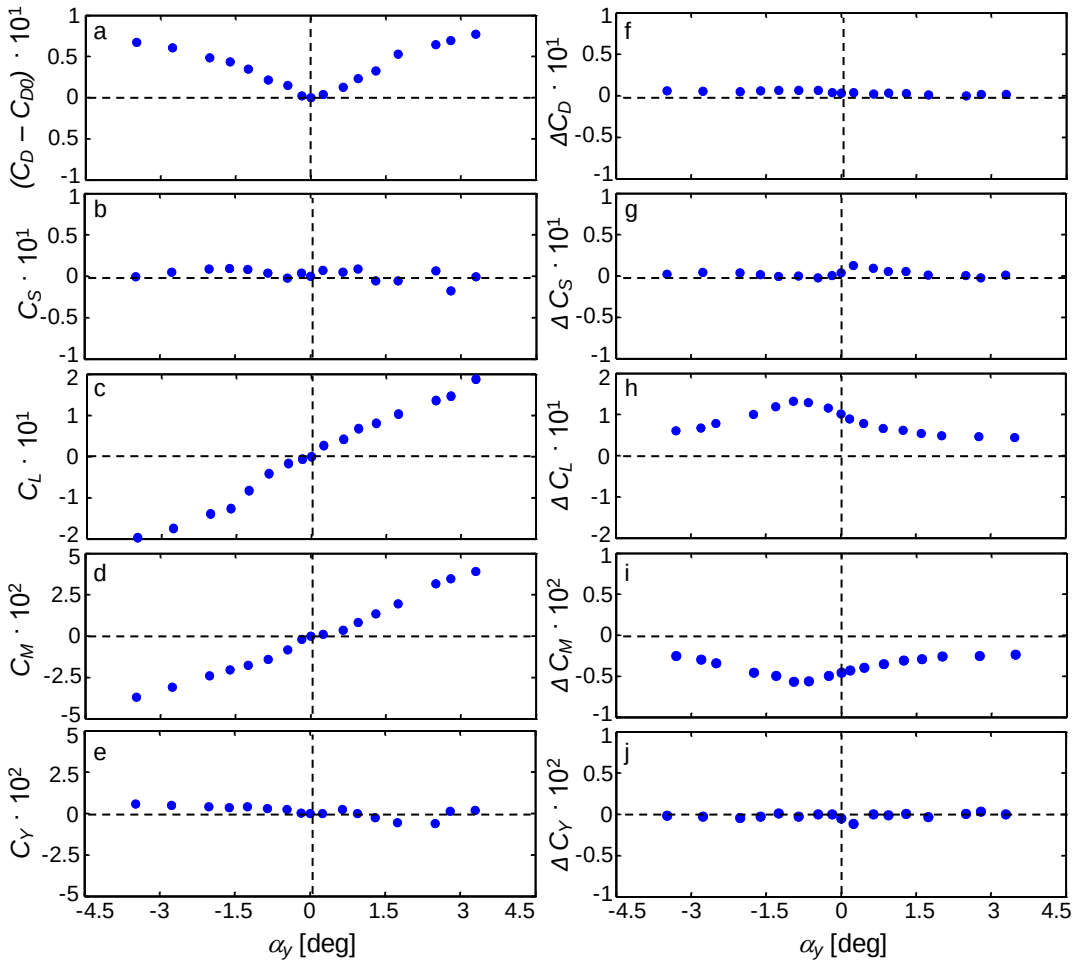

Figure 3.6. Variation with the pitch angle α_y of the resultant static drag (a,f), side (b,g), lift (c,h) forces and pitching (d,i), and yawing (e,j) moments: induced changes due to the model attitude only (a-e), and changes relative to the base flow due to actuation (f-j).

in attitude during model positioning and/or small model imperfections. Other characteristics of these measurements are similar to low-angle pitching of airfoils, such as a linear variation of the C_L and C_M with small α_y (Figures 3.6c and d, respectively). The data in Figure 3.6d show that the present model is unstable, in that when the model is pitched (up or down), the change in C_M has the same sense as the change in α_y, so that C_M acts to further deflect the model off center. This instability of the model in the present arrangement is due to setting the pitching axis (the center of the wire mount) downstream of the aerodynamic center of pressure. Figure 3.6f shows the ΔC_D which is slightly positive at all α_y. Similar to Figures 3.6b and e, Figures 3.6g and j show nominally zero ΔC_S and ΔC_Y, with some deviation. The most dominant induced changes on the model are observed in ΔC_L (Figure 3.6h) and ΔC_M (Figure 3.6i). For this range of α_y, the ΔC_L is approximately the same order of magnitude as the C_L. However, the actuation induced moment increments, ΔC_M, are similar in magnitude to the pitching moment of the base flow in for $|\alpha_y| < 0.5^\circ$, while ΔC_M is smaller than C_M at larger α_y ($\Delta C_M \sim 0.1 C_M$ at $\alpha_y = 4.5^\circ$). A notable feature of the actuation is that the ΔC_L and ΔC_M have a maximum magnitude when the actuation jet is tilted towards (into) the free stream (i.e., when the top jet is actuated, the peak magnitudes of the ΔC_L and ΔC_M occur at $\alpha_y \sim -1^\circ$). Although the effects of actuation remain significant over the entire range of α_y, these data imply that the actuators optimal performance (peak magnitudes of ΔC_L and ΔC_M) is associated with the orientation into the free stream that is ostensibly affected by the thickness of the boundary layer along the cylindrical model.

To illustrate the flow control effect on the near wake behind the body at nonzero pitch angle, PIV measurements are taken at $\alpha_y = 3^\circ$ (Figure 3.7). Contrary to the effects of the actuation at $\alpha_y = 0$ (cf., Figure 3.4, where the wake of the base flow is nominally axisymmetric), the baseline wake at $\alpha_y = 3^\circ$ is asymmetric in a manner that alters the interaction of the actuation with the Coanda surface at the tail section (Figure 3.7a). These

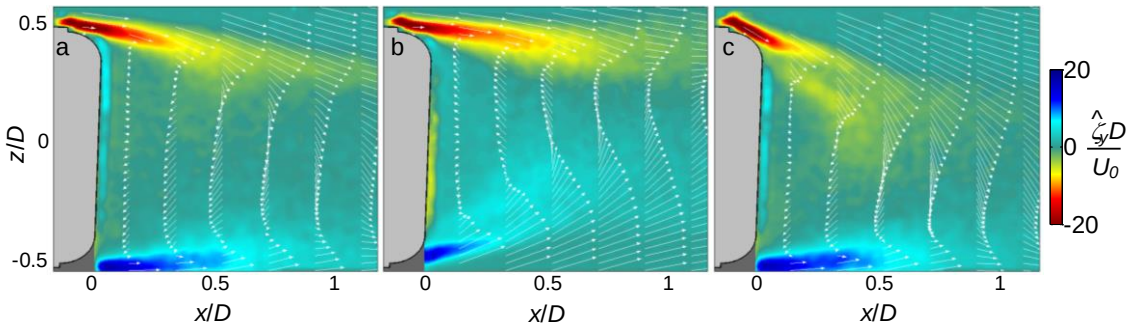

Figure 3.7. Color raster plots of time-averaged azimuthal vorticity concentrations, $\hat{\zeta}_y$, overlaid with velocity vectors at $\alpha_y = 3^o$ in the base flow (a), and in the presence of actuation with the bottom (b) and top (c) jets at $C_\mu = 3 \cdot 10^{-3}$.

data show that the jet-induced wake flow fields are similar to the respective flow fields at $\alpha_y = 0$ (compare Figures 3.7b and c to 3.4b and c). The major difference is that the activation of either jet in the present configuration is coupled with the alteration of the outer flow and the pre-existing asymmetry in the flow field as shown in Figure 3.7a. The orientation-induced vectoring of the outer flow becomes enhanced upon activation of the top jet, and is manifested by enhanced wake asymmetry (Figure 3.7c). Likewise, when the bottom jet is activated, significant vectoring of the outer flow at the bottom edge is achieved, which partially suppresses the pre-existing vectoring on the upper side (Figure 3.7b). Because the jet-induced flow fields are similar to the flow of the streamwise-oriented model (compare Figure 3.7b and c with Figure 3.4b and c), and the base flow is initially vectored downwards, the effect of the top jet which vectors the wake downwards is less pronounced while the effect of the bottom jet which vectors the wake upwards is more pronounced. This observation is in agreement with the findings of Figure 3.6 in which the actuators have a stronger effect when they are inclined into the free stream.

To characterize transient effects during pitching and their coupling to the actuation, the time-resolved force and moment on the model in the absence and presence of actuation are recorded during transitory pitch motion. Initially ($0 < t/\tau_{conv} < 500$), the model is streamwise-oriented, and at $t/\tau_{conv} = 500$ it undergoes a transitory change in angle of attack to $\alpha_y = 1.5^o$ (cf., Chapter **2.3**), and at $t/\tau_{conv} = 1{,}000$ it is returned back to $\alpha_y = 0$, and is held

at that position for 1,000 < t/τ_{conv} < 1,500. The measured C_D, C_L, C_M, and α_y are shown in Figure 3.8 (C_S and C_Y are omitted). As expected, the terminal values of C_D, C_L, and C_M are in agreement with the levels of the static model at $\alpha_y = 1.5^\circ$ (compare Figures 3.8 and 3.6). Actuation of either of the top and bottom jets is synchronized with the model initial motion ($t/\tau_{conv} = 500$) and then terminated when the model starts returning to the streamwise attitude ($t/\tau_{conv} = 1{,}000$) as shown in Figure 3.8. Here, the top jet actuation amplifies C_L and suppresses C_M, while the bottom jet actuation has the opposite effect

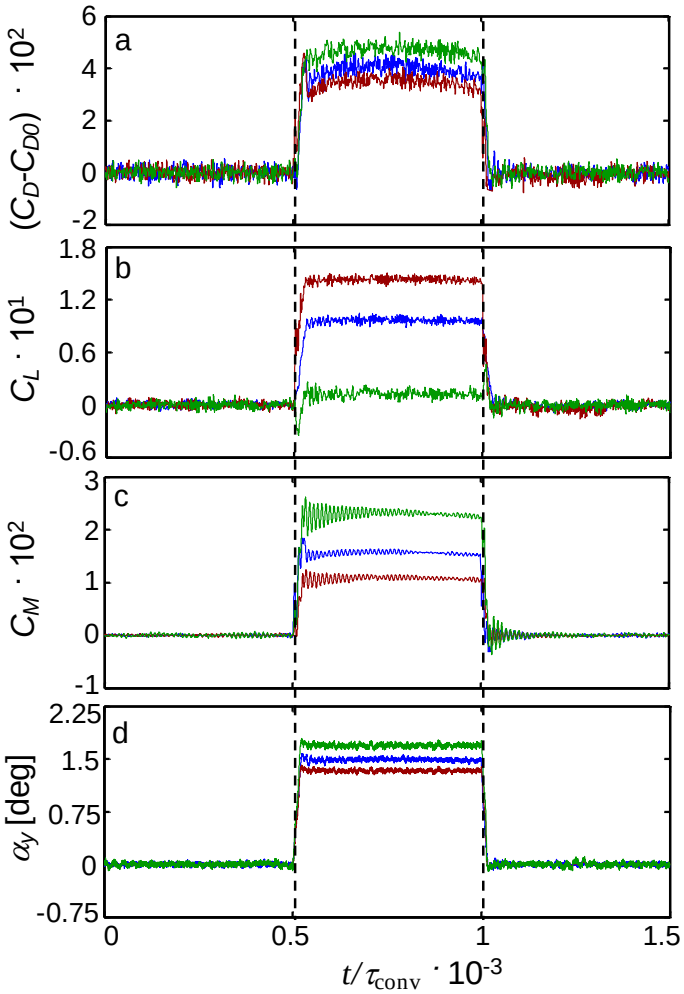

Figure 3.8. Time traces of relative drag (a), lift (b) forces and the pitching moment (c), and of α_y (d) for the base flow (**blue**), and in the presence of square amplitude modulated actuation for commanded transient motion $0 < \alpha_y < 1.5^o$ during $0.5 < t/\tau_{conv} \cdot 10^3 < 1.5$ using top (**red**) and bottom (**green**) jets.

(Figure 3.8b and c). The variation of the magnitudes of C_D, C_L, C_M, and α_y with actuation are analyzed further in Figure 3.9.

There are several distinctions between the effects of actuation on the transitory motion (Figure 3.8) and on the equivalent static angle of attack α_y (Figure 3.6). First, upon the onset and termination of actuation of the bottom jet C_L exhibits transient spikes, which in the case of the control onset ($t/\tau_{conv} = 500$) induces an initial negative C_L (Figure 3.8b). Knowing that actuation of the bottom jet induces a ΔC_L that is opposite the sense of the C_L induced by the pitch-up motion (and vice versa), this transient spike can be explained by considering the relevant time scales. The actuation induces a flow response on the order of the model convective time scale (as shown in Figure 3.1c) and hence the corresponding change in ΔC_L is much faster than the change in C_L due to the transitory motion of the model that is an order of magnitude slower ($\sim 10\,\tau_{conv}$, as shown in Figure 2.6a). As the model approaches its equilibrium position, ΔC_L balances the base C_L and results in virtually no net lift. Similarly, at the termination of the actuation ($t/\tau_{conv} = 1{,}000$), the actuation effect relaxes much faster than the repositioning of the model back to streamwise attitude, and the net C_L has a transient positive spike before settling back to zero. To suppress these transients, the onset and termination of the actuation needs to be amplitude modulated to delay the actuation by the time scale of the model dynamics. The onset of the actuation signal excites a resonance in the system as is evident in trace of C_M (Figure 3.8c) which is similar to the resonance observed for the streamwise-oriented model (Figure 3.3b). As already discussed in §**3.1**, this resonance is attributed to the mounting structure that supports the model and is not aerodynamic. Although the resonance lasts on the order of $t/\tau_{conv} \sim 300$, the amplitude of the resonance is more severe in the presence of actuation that increases C_M, and less severe for actuation that suppresses C_M. The observation that the resonance is not noticeable in the absence of actuation suggests that it is excited by the onset of the actuation with a time scale that is commensurate with the effect of the

actuation. Because the model is pitched in open loop, the fluidic control imposed by the actuation can cause a slight deviation in its attitude (Figure 3.8d). As noted in Chapter **2.3**, the deviation between the command and achieved attitudes with this open loop control can increase in faster-dynamic motions and can be minimized using a closed loop controller. Finally, the fractional change in C_D in the presence of actuation is smaller than the corresponding changes in both C_L and C_M (Figure 3.8b), indicating that the commensurate effects of the actuation on the base pressure of the model lead to smaller changes in the drag.

The full effect of the actuation on the aerodynamic loads in this transitory motion is not entirely evident from Figure 3.8, due to a secondary change in the aerodynamic loads that result from the fact the model does not quite reach the same α_y during the transitory motion because the open loop command to the SMA wires is the same and therefore is insufficient in the presence of actuation. To quantify the actuation-induced changes in the steady state magnitudes of C_D, C_L, and C_M in Figure 3.8 ($750 < t/\tau_{conv} < 1{,}000$), these parameters are plotted in Figure 3.9 with their respective α_y. In addition, the static-induced changes in C_D, C_L, and C_M with α_y are also overlaid on Figure 3.9, based on the data in Figures 3.6a, c, and d. Although C_D varies significantly in Figure 3.8a, it becomes apparent in Figure 3.9a that this variation is coupled with the attained α_y of the model, and that C_D measured in the presence of either the top or bottom jet actuation is close to the static C_D. Figure 3.9b shows that when bottom actuation is applied during the transitory motion, C_L is almost entirely dampened and the resulting α_y is higher causing a decrease in C_L/α_y by 92%. When the top actuation is applied, C_L is augmented and the resulting α_y is lower causing an increase of C_L/α_y of 65%. Similarly, Figure 3.9c shows respective 23% decrease and 30% increase in C_M/α_y when either the top or bottom actuators is active.

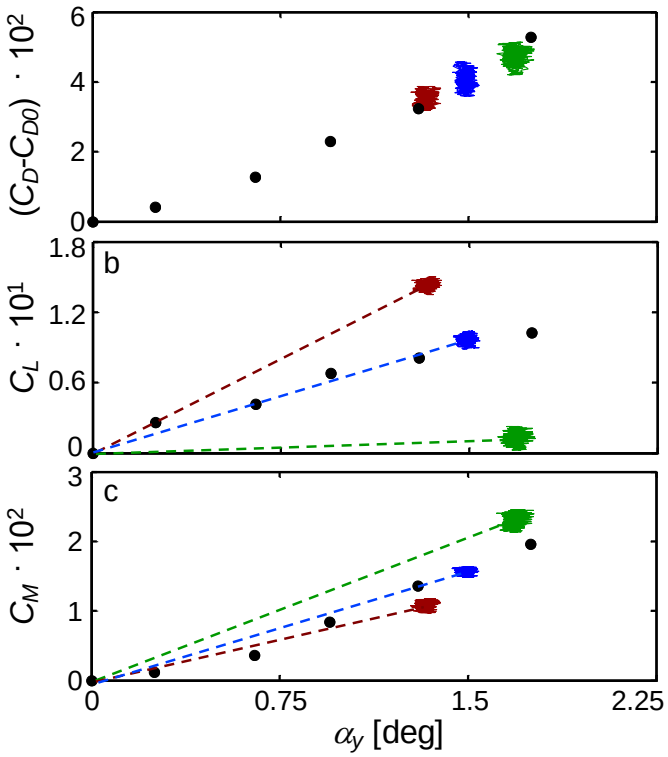

Figure 3.9. Quasi-static magnitudes of relative drag (a) and lift (b) forces, and pitching moment (c) from Figure 3.8, with the corresponding pitch angle, measured for the base flow (**blue**), and in the presence of actuation by top (**red**) and bottom (**green**) jets. The corresponding static measurements (●) are also shown for reference.

3.3 Active Decoupling of the Near Wake in Quasi-Steady Pitch

The effect of synthetic-jets actuation is investigated in the presence of a continuous variation in the model attitude (using the SMA wires, cf., Figure 2.6b). The aerodynamic loads (C_D, C_L, and C_M) are measured when the model is pitching time-periodically (sinusoidal waveform with amplitude $\alpha_y = 1.5^\circ$, at $k = 0.013$ or period of ~420 τ_{conv}), and is compared with the corresponding loads at static attitude (α_y). The aerodynamic loads are recorded for the base model and in the presence of actuation (top jet) during the entire cycle. Figures 3.10d-f show the differences between the loads in the presence and absence (in Figures 3.10a-c) of actuation. The corresponding motion-induced and actuation-induced loads at static α_y from Figure 3.6 are overlaid on Figure 3.10, for comparison.

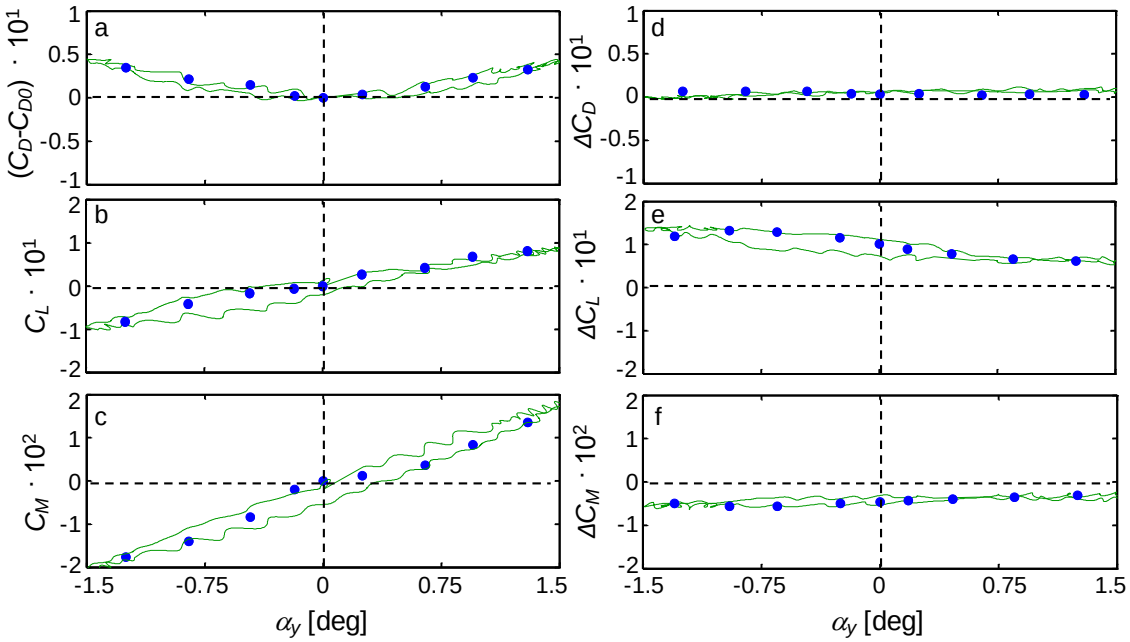

Figure 3.10. Resultant motion-induced (a,b,c) and actuation-induced (d,e,f) drag (a,d), and lift (b,e) forces, and pitching moment (c,f) with pitching amplitude $\alpha_y = 1.5^o$ at $k = 0.013$. The corresponding static measurements (●) are shown for reference.

Figures 3.10a-c show that C_D, C_L, and C_M during static and the time-varying pitch are similar, indicating that unsteady aerodynamic effects at this low pitch rate are small. In fact, the pitch oscillation frequency is much lower than the model natural shedding frequency ($k = 0.013$ compared to about ~ 1), and therefore there is no direct manipulation of the model wake shedding. Similarly, Figures 3.10d-f also show that the actuation-induced changes in aerodynamic loads (ΔC_D, ΔC_L, and ΔC_M) during the time-varying pitch are similar for the static changes. The slight hysteresis that is observed in Figure 3.10 is attributed to the small deviation of the actual model motion from the commanded sinusoidal trajectory (cf., Figure 2.6b), which may cause slight changes in acceleration and artifacts in the aerodynamic effects. For this amplitude and frequency, the magnitudes of the C_L (Figure 3.10b) and ΔC_L (Figure 3.10e) are approximately equal, and therefore the actuation-induced loads are deemed sufficient to strongly affect the base load on the model and therefore affect its stability and trajectory. Furthermore, in agreement with the static

measurements, Figure 3.10e shows that ΔC_L during the oscillatory motion is larger when the actuator is inclined into the free stream.

The previous results indicate that the fluidic actuation has the control authority to fully modify the wake when the model varies its attitude. Such a wake 'decoupling' from the body motion is further explored with the goals of either restoring the wake symmetry relative to the model, or augmenting its motion-induced asymmetry. These effects would, in turn, either suppress or enhance the respective asymmetric aerodynamic loads. The model trajectory α_y during a single period of the oscillation is shown in Figure 3.11a. Three actuation programs for open-loop control of the body wake (and thereby the aerodynamic loads) are shown in Figure 3.11. As shown in Figure 3.7a, when the model pitches up ($0 < t/\tau_{conv} < 105$), the wake becomes increasingly asymmetric by vectoring of the top shear layer into the wake. Therefore, if symmetry of the wake is to be restored (about the

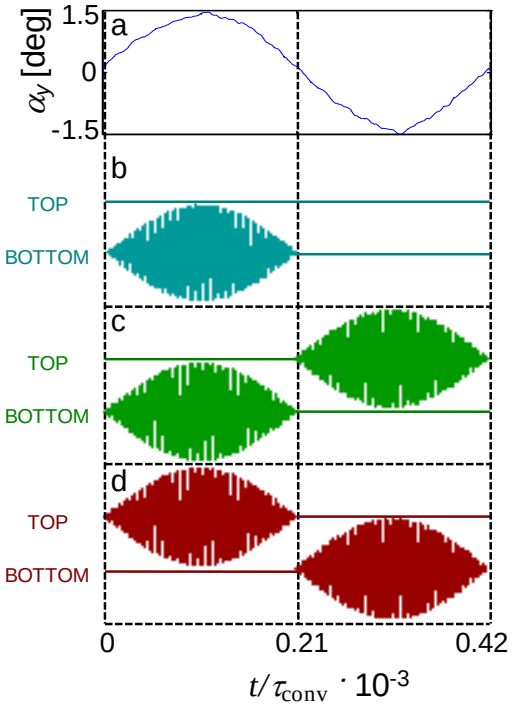

Figure 3.11. Time traces of the pitching angle of SMA-controlled model oscillation (a), and the actuation waveforms of the top and bottom jet for half-cancellation (b), full-cancellation (c), and full-amplification (d) of the lift force coefficient.

model axis), the bottom jet needs to induce opposing vectoring of the bottom shear layer using actuation with increasing C_μ over time. Similarly, past the pitch apex, during the model retreating motion ($105 < t/\tau_{conv} < 210$), C_μ should continuously diminish as the vectored shear layer is aligned in the streamwise direction. The first two actuation functions in Figure 3.11 are designed to restore the symmetry of the wake over the first half of (Figure 3.11b) or over the entire (Figure 3.11c) oscillation cycle by activation of opposite jets to counter the asymmetry induced by the vectoring of the separating shear layer during pitch-up and -down ($C_\mu = 2 \cdot 10^{-3}$ is sufficient to restore a symmetric wake). If the objective is to augment the motion-induced wake asymmetry, the actuation program (Figure 3.11d) is designed to assist the motion-induced shear layer vectoring so that when the shear layer is vectored towards the wake core, the actuator jet is activated to vector it even further into the wake core at $C_\mu = 3 \cdot 10^{-3}$. This actuation program is essentially 180° out of phase relative to the program shown in Figure 3.11c. While open-loop control is deemed robust enough to demonstrate control authority in the present Chapter, a closed-loop feedback control has to be implemented when the model is free to respond, such as in the free flight experiments in Chapters **IV** and **VII**.

Examples of the instantaneous wake flow fields under each of the three control programs of Figure 3.11 are shown in Figure 3.12. Phase-locked PIV measurements are acquired at 12 equally-spaced time increments of $35\,\tau_{conv}$ during the oscillation cycle (starting at $t = 0$). The phase-averaged velocity profiles are overlaid on raster plots of the phase-averaged azimuthal vorticity concentrations, and are shown at the apexes of pitch-up ($t/\tau_{conv} = 105$, Figures 3.12a–d) and pitch-down ($t/\tau_{conv} = 315$, Figures 3.12e–h) motions for wake asymmetry amplification (Figures 3.12a and e), the base flow (Figures 3.12b and f), and half- and full-period symmetry restoration (Figures 3.12c and g, and 3.12d and h, respectively). The base flow demonstrates the motion-induced wake asymmetry. Actuation for asymmetry augmentation leads to a significant increase in the wake asymmetry with more pronounced flow turning over one side of the model (Figure 3.12a

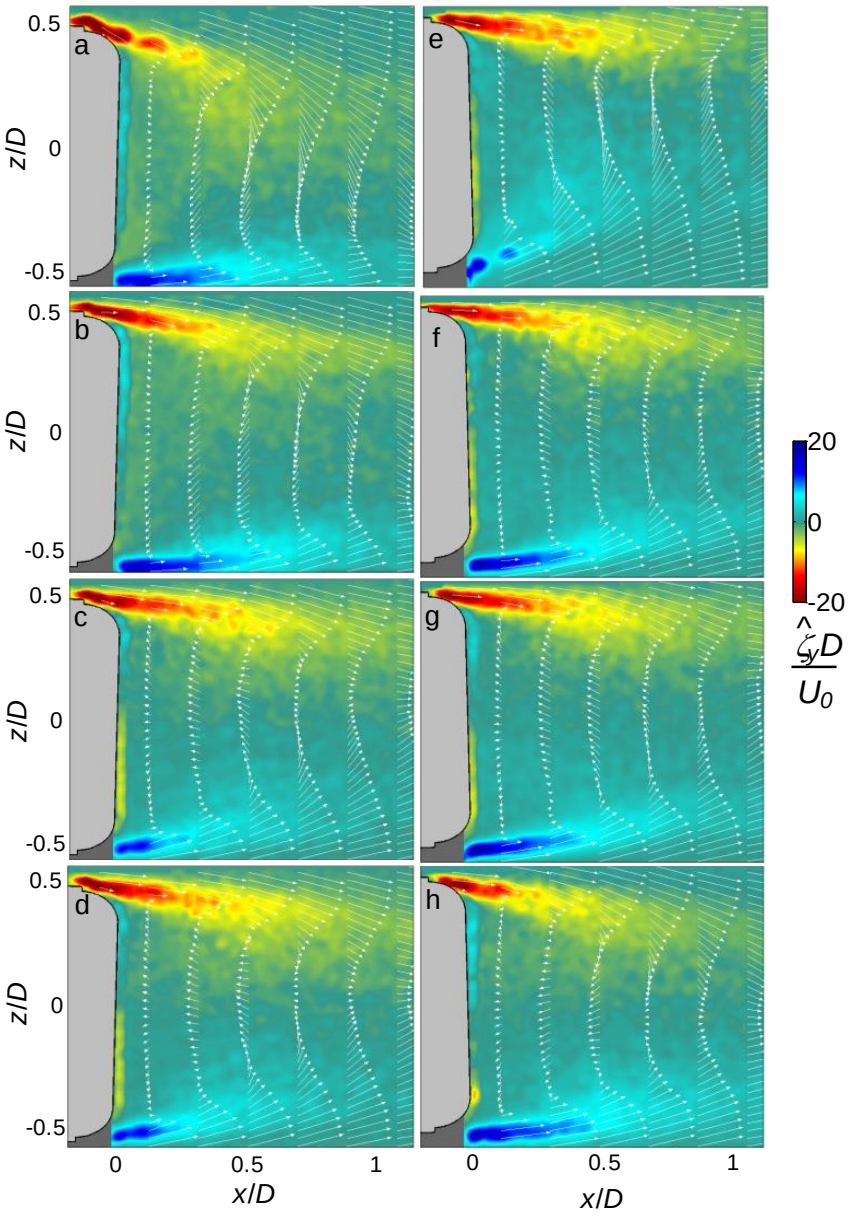

Figure 3.12. Color raster plots of phase-averaged azimuthal vorticity concentrations with overlaid velocity vectors for pitch oscillation at extremum phases t/τ_{conv}= 105 (a–d) and 315 (e–h), for full-amplification (a, e), base flow (b, f), half-cancellation (c, g), and full-cancellation (d, h), as depicted in Fig. 3.11.

and e). Both symmetry-restoring actuation programs lead to some restoration of the wake symmetry during pitch-up in Figures 3.12c and d. Since during pitch-down the half-cycle restoring program (cf., Figure 3.11b) is inactive, the flow in Figure 3.12g is identical to the

base flow (Figure 3.12f) but the full-period restoration program (Figure 3.11c) also restores some symmetry during pitch-down as shown in Figure 3.12h.

To illustrate the effects of the wake decoupling on the resulting aerodynamic loads, time-resolved measurements of the lift are shown in Figure 3.13 for the three control programs of Figure 3.11. The periodic variation in C_L due to the base oscillations of the model is included for reference in each of the plots. Due to the low oscillation frequency ($k = 0.013$), C_L closely follows the model trajectory implying a quasi-steady wake coupling. When the actuation is designed to restore symmetry in the wake during pitch-up deflection ($0 < t/\tau_{conv} < 120$), $C_L \approx 0$ during either half- or the full- period (Figures 3.13a and b, corresponding to Figures 3.11b and c, respectively). These data show that when the actuation is applied as the model undergoes pitching oscillations, the aerodynamic loads respond as if the flow is aligned with the model axis. In Figure 3.11b, C_L returns to the

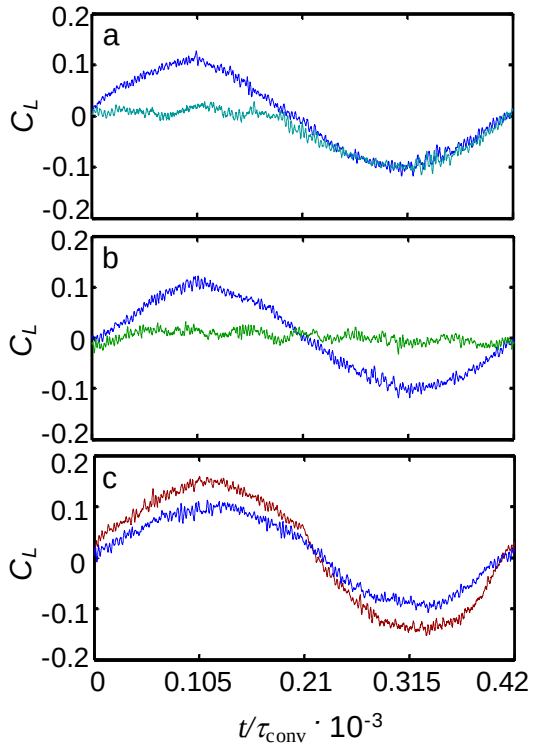

Figure 3.13. Time traces of lift coefficient for the half-cancellation (a), full-cancellation (b), and full-amplification (c) actuation program as depicted in Figure 3.11, with the base flow lift coefficient shown in **blue** (pitch amplitude of $\alpha_y = 1.5^o$, $k = 0.013$: maximum $C_\mu = 2 \cdot 10^{-3}$ for cancellation and $3 \cdot 10^{-3}$ for amplification).

base load lift during the second (inactive) half of the oscillation cycle (Figure 3.13a), and the full-period actuation completely suppresses C_L (Figure 3.13b). These changes in C_L are accompanied by nominal alignment of the wake with the model axis regardless of its attitude (cf., Figure 3.12). Finally, when the phase of the actuation is reversed in order to enhance the flow-induced effect (cf., Figure 3.11d), there is about 45% increase in the motion-induced amplitude of C_L (Figure 3.13c), in phase with the base C_L (this result also agrees well with the increase in the slope of C_L in Figure 3.9, which yielded an enhancement of 43%). These findings underscore the observation that the top and bottom jets are the most effective when operated opposite to the pitch direction, and therefore for the same C_μ suppression of C_L has a stronger effect than its amplification. Therefore, C_μ should be actively adjusted to achieve similar amplification and suppression effects.

CHAPTER IV

MOTION CONTROL OF A YAWING MODEL

This chapter focuses on aerodynamic control of a wire-mounted axisymmetric model (cf., Chapter **2.4**) that is free to rotate about its yaw axis. The dynamics of the free model are described in §**4.1**, transitory effects of pulsed synthetic jet actuation on the near wake and yaw attitude are discussed in §**4.2**, and the aerodynamic effects induced by open- and closed-loop pulsed actuation are described in §**4.3**, and §**4.4**, respectively.

4.1 Dynamic Response of the Free Yawing Model

The interaction of the wire-mounted, free yawing model (cf., Chapter **2.4**) with the cross flow is characterized using laser vibrometer and PIV measurements over a range of wind tunnel speeds corresponding to $0.57 < Re_D \cdot 10^{-5} < 2.30$ (limited by the lowest stable tunnel speed and by the optical range of the vibrometer at large lateral yaw oscillations). As noted in Chapter **2.4**, the instantaneous time dependent attitude (or angular position) of the model $\alpha_z(t)$ is inferred from measurements of the lateral displacement of the model surface near the mounting wire at $x_L = 0.36c$. An example of the natural lateral oscillations of $\alpha_z(t)$ of is shown in Figure 4.1a when the flow speed is set to $U_o = 20$ m/s ($Re_D = 1.15 \cdot 10^5$), and the model response appears to be nearly time-harmonic with a characteristic period $\tau_z = 0.585$ sec or $71\tau_{conv}$ ($\tau_{conv} = c/U_o$). These two different orders of magnitude exemplify the disparity between the rotational (yaw) and streamwise time scales (the ratio τ_{conv}/τ_z is, in fact, directly proportional to the Strouhal number $St_z = f_z D/U_o$ of the attitude oscillations). The corresponding power spectrum of the oscillations (Figure 4.1b, frequency resolution of ~0.085 Hz) exhibits a peak at the fundamental oscillation frequency $f_z = 1.7$ Hz ($St_z = 7.6 \cdot 10^{-3}$), and its higher harmonics. At this Re_D, the average oscillation amplitude of

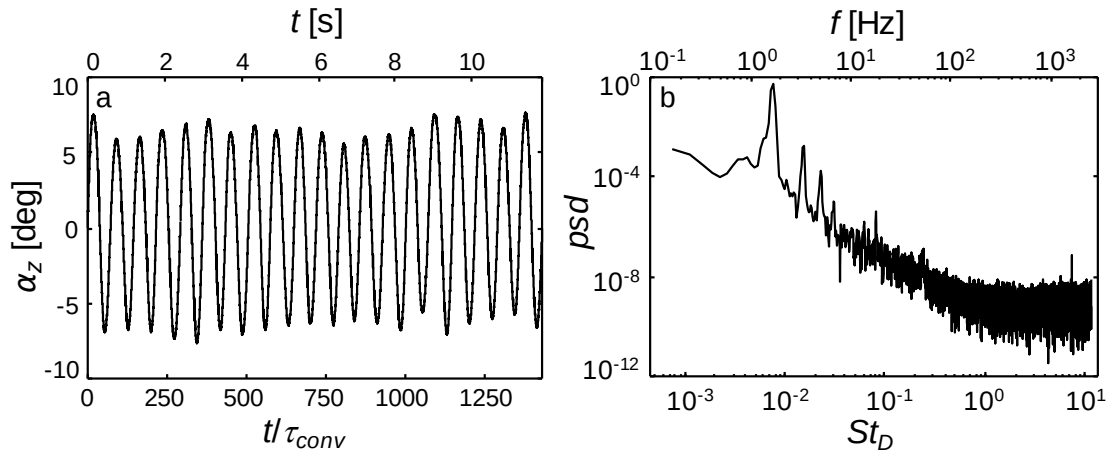

Figure 4.1. Time trace of an instantaneous model attitude $\alpha_z(t)$ ($Re_D = 1.15 \cdot 10^5$) (a), and its power spectrum (b), over twenty oscillation cycles.

$\alpha_z(t)$, computed over an extended time record (200 sec, rounded to the nearest full cycle) is 6.9° (with RMS of ~4.8°).

This measurement is repeated for several Re_D, and $\alpha_{z,RMS}$ is extracted from the time traces while f_z are extracted from the spectral analysis. These data show that within the present range of flow speeds, the $\alpha_{z,RMS}$ and f_z, of the lateral oscillations increase nearly linearly with Re_D (Figures 4.2a and b, respectively). While f_z increases with Re_D, the ratio of the convective and lateral time scales, τ_{conv}/τ_z (Figure 4.2c) diminishes to a steady value of 0.013 at higher Re_D, indicating that the convective and motion frequencies become 'locked in' to multiples of each other at the highest measured flow speeds. In fact, the nominally-steady Strouhal number is $St_z \sim 0.007$, which is more than an order of magnitude lower than the natural shedding frequency of a similar model of a cylinder with its flat end facing the oncoming flow (e.g., $St_D \sim 0.2$ for cylinders at multiple angles of attack with $L/D \sim 2$ at $Re_D = 3.4 \cdot 10^4$, Sarioglu, Akansu, and Yavuz, 2005).

Based on the observed quasi-periodic (limit cycle) motion of the model, its attitude (yaw) angle is taken to be of the form $\alpha_z(t) = A(t) \cos[\omega_z(t) \cdot t]$. It is argued that the aerodynamic moment that drives this angular motion should also be of the same form i.e.,

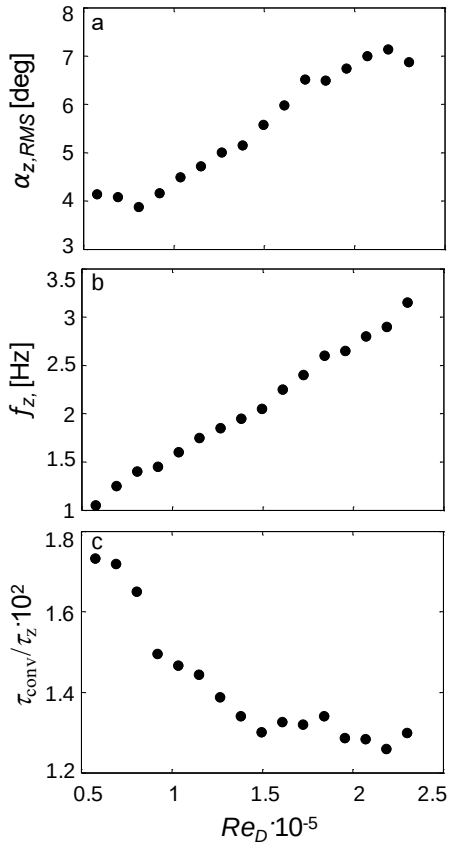

Figure 4.2. The variation with Re_D of the RMS amplitude of the attitude α_{RMS} (a), the model dominant lateral oscillation frequency f_z (b), and the ratio of the convective (streamwise) and lateral time scales τ_{conv}/τ_z (c).

$M_z(t) = B(t)\cdot\cos[\omega_z(t)\cdot t + \varphi_z(t)]$. When the moment and yaw angle are of this form, the aerodynamic moment can be written in the form $M_z(t) = M_{z1}(t)\alpha_z + M_{z2}(t)\dot{\alpha_z}$, that is similar to Theodorsen's formulation for the aerodynamic moment of an unsteady thin airfoil undergoing simple harmonic motion ($M(k) = M_1(k)\alpha_z + M_2(k)\dot{\alpha_z}$, by Bisplinghoff, Ashley, and Halfman, 1996, and Leishman, 2006). The motion of the model in Equation (2.1) in Chapter **2.4** can then be written in terms of a time dependent natural frequency, $\omega_n(t)$, and damping ratio, $\xi(t)$:

$$\ddot{\alpha_z} + 2\omega_n(t)\xi(t)\dot{\alpha_z} + {\omega_n}^2(t)\alpha_z = 0 \qquad (4.1)$$

where the parameters $\omega_n(t)$ and $\xi(t)$ depend on physical (I_{1D}, C_{1D}) and aerodynamic properties [$M_{z1}(t)$ and $M_{z2}(t)$]:

$$\omega_n(t) = \sqrt{\text{-}M_{z1}(t)/I}, \text{ and } \xi(t) = \left(C_{\text{damp}}\text{-}M_{z2}(t)\right)/\sqrt{\text{-}I\cdot M_{z1}(t)},$$

where the aerodynamic force has to be restoring for oscillation [$M_{z1}(t) < 0$].

The fidelity of this formulation is evaluated by considering the temporal variation of ω_n and ξ when the motion of the wind tunnel model commences from a stationary streamwise attitude. This test is performed by holding the model nearly stationary at a given tunnel speed using the actuation jets (as described in detail in §**4.4**), and then abruptly terminating the actuation. The time-dependent trajectory $\alpha_z(t)$ of the model is measured phase-locked to the termination of the actuation as the model begins to oscillate laterally with increasing amplitude, and the nearly-quasi-steady amplitude is reached within ~$3\tau_z$ (Figure 4.3a). Also shown in Figure 4.3a is a series of discrete model attitudes α_z^i at equally-spaced time increments. The angular velocity and acceleration $\dot{\alpha}_z^i$, and $\ddot{\alpha}_z^i$ are evaluated at each time step, and ω_n^i, and ξ^i are computed using a least square fit to $\alpha_z(t)$ within a time window $t\text{-}\Delta t < t < t\text{+}\Delta t$, where Δt is taken to be 0.4s and each time step is spaced by 0.2s ($0.68\tau_z$ wide windows, spaced by $0.34\tau_z$, and yielding 75% overlap). The resulting distributions of ω_n^i, and ξ^i estimated at each time increment are shown in Figures 4.3b and c, respectively. When the model is initially at equilibrium, its lateral motion starts due to stochastic vortex shedding, and Equation (4.1) is inadequate to describe the initial motion in the presence of secondary frequencies as is evident for $t/\tau_z < 0.5$ in Figure 4.3b, (for this reason, the first time window is omitted). Each of Figures 4.3b and c also include an exponential fit of $\omega_n(t) = 10.74 + 4.67e^{-t/0.56s}$ rad/sec, and $\xi(t) = -0.479e^{-t/0.56s}$, where an exponential model with the same time constants was selected for simplicity. These data show that the respective transitory magnitudes of the natural frequency and of the damping decrease and increase with time, and attain a nearly asymptotic level within ~$3\tau_z$ when the limit cycle of the natural oscillatory motion is reached (for which $\omega_{n0} = 10.74$ rad/sec and ξ is approximately zero). The natural frequency of the limit cycle is used to estimate the static moment slope of the wind tunnel model about the mounting wire:

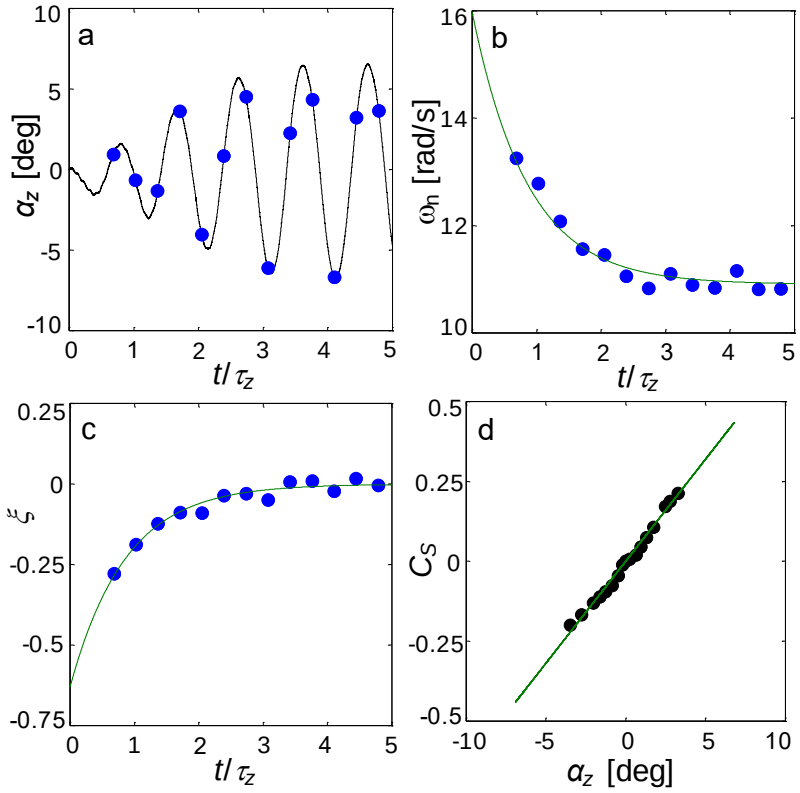

Figure 4.3. Transitory variation of the model lateral oscillations through its limit cycle including the magnitude at equally-spaced time increments (•) (a), the respective natural frequency ω_h, and damping ratio, ξ, computed at each of the time increments in (a) each along with an exponential fit (**green**, b and c), and a comparison of the resultant aerodynamic side force computed from the exponential fits (**green**, d) with a previous data set on a static model (•).

$$M_z|_{\dot{\alpha}_z=0,\ t\to\infty} = M_{z1}|_{t\to\infty}\cdot\alpha_z = -I\omega_{n0}^2\alpha_z \tag{4.2}$$

which is used to approximate the side force, F_y, by taking the moment balance about the model center of pressure (where the aerodynamic moment vanishes):

$$F_y\big|_{\dot{\alpha}_z=0,\ t\to\infty} = \frac{M_z|_{\dot{\alpha}_z=0,\ t\to\infty}}{x_0 - x_{cp}} = \frac{I\omega_{n0}^2\alpha_z}{0.15c} \tag{4.3}$$

where $C_S = \frac{F_y}{\frac{\pi}{8}\rho U^2 D^2}$ is the side force coefficient, x_o and x_{cp} are the respective streamwise positions of the model center of lateral oscillation, and its center of pressure. The predicted side force is shown in in Figure 4.3d and is in good agreement with the measurements of the side force on the stationary model (cf., Chapter **3.2**) that are included for reference.

The good agreement of the static side force predicted by the dynamic model with the actual side force measured on a static model supports the validity of the dependence of the aerodynamic moment on the angular position and angular velocity within the present range of Reynolds numbers. This agreement also suggests that the oscillation frequency of the model primary limit cycle about another center of rotation upstream of the center of pressure can, in principle, be estimated from the static aerodynamic force measurements, in the same fashion.

The fidelity of the predicted $\omega(t)$ and $\xi(t)$ is validated by comparing the predictions of α_z and $\dot{\alpha}_z$, with the measurements. To this end, Equation (4.1) is first rewritten as:

$$\left[\begin{matrix}\dot{\alpha}_z\\ \ddot{\alpha}_z\end{matrix}\right]\Big|_t = \left[\begin{matrix}0 & 1\\ -\omega_n^2 & -2\omega_n\xi\end{matrix}\right]\left[\begin{matrix}\alpha_z\\ \dot{\alpha}_z\end{matrix}\right]\Big|_t \tag{4.4}$$

using a time step that is small enough for a forward Euler update rule:

$$\left[\begin{matrix}\alpha_z\\ \dot{\alpha}_z\end{matrix}\right]\Big|_{t+1} = \left[\begin{matrix}\alpha_z\\ \dot{\alpha}_z\end{matrix}\right]\Big|_t + \left[\begin{matrix}\dot{\alpha}_z\\ \ddot{\alpha}_z\end{matrix}\right]\Big|_t \cdot \Delta t \tag{4.5}$$

The comparisons of the predicted trajectories α_z and $\dot{\alpha}_z$ with the measurements (using the laser vibrometer) are shown in Figures 4.4a and b, respectively. The initial condition is taken to be at rest ($\dot{\alpha}_z = 0$) at an initial attitude $\alpha_{z,0}$ that is selected to minimize the error between the predicted and measured trajectories (it is found that $\alpha_{z,0} = 0.15^\circ$). Figure 4.4b shows the presence of a secondary frequency, $St_z = 0.081$ in the time derivative of the measured model response which is not captured by the prediction (it is also noticeable in the model attitude in Figures 4.3a and 4.4a). This secondary frequency is attributed to oscillations of the support wire that are presumably triggered by aerodynamic perturbation applied by the model from its rest attitude. As the model approaches its limit cycle ($2\tau_z$ or $t > 250\tau_{conv}$) the higher frequency component diminishes significantly. The model motion is also shown in phase plots of $\dot{\alpha}_z$ and of C_Y with respect to α_z (Figure 4.4c and d, respectively), where $C_Y = \frac{(M_z)}{\frac{\pi}{8}\rho U^2 D^2 c}$ is the moment coefficient of M_z that is predicted using Equation (2.1). The phase plot of C_Y (Figure 4.4d) shows the development of moment

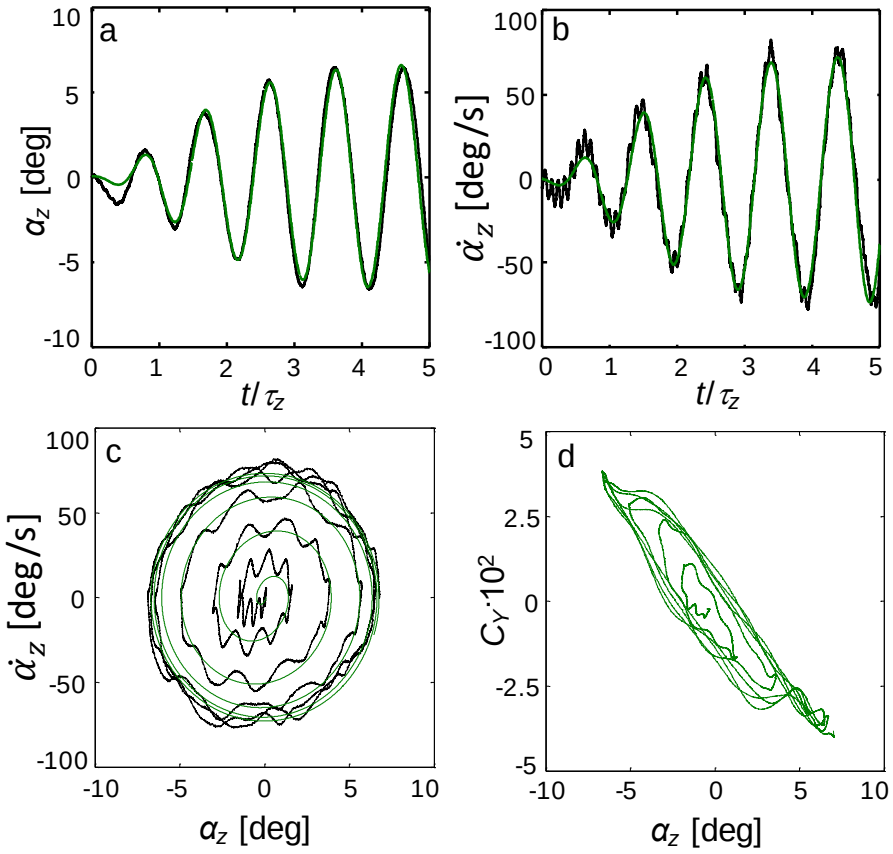

Figure 4.4. Time traces of **measured** and **predicted** model yaw attitude trajectories $\alpha_Z(t)$ (a) and $\dot{\alpha}_z$ (t) (b). Corresponding phase plots $\dot{\alpha}_z(t)$ - $\alpha_z(t)$ and of $C_Y(t)$ - $\alpha_z(t)$ are shown in (c) and (d), respectively.

peaks at the maximum excursion ends of the lateral motion that are attributed to vortex shedding as the model changes its direction similar to a pitching airfoil (e.g., $k = 0.05$ pitch over different angle ranges shown by Rival and Tropea, 2010). Similar phase plots are used in §**4.3** and §**4.4** to characterize the respective state transition of the model dynamics with open- and closed-loop actuation.

The structure of the model near-wake during its free yaw oscillations (in the absence of actuation) are captured using phase-locked PIV measurements in the horizontal *x*-*y* center (meridional) plane during a complete (phase-averaged) oscillation cycle (the average oscillation period at $Re_D = 1.15 \cdot 10^5$ is $\tau_z = 0.575$ sec). The PIV measurement domain is $1.3 < x/D < 2.2$ and $-0.9 < y/D < 0.9$ ($x = y = 0$ is the position of the mounting wire). These

PIV data are acquired at a fixed rate and are sorted into 28 “bins” of equally spaced yaw angles during the nominally time-periodic lateral oscillations and at each yaw angle the phase-averaged velocity field is computed using 170 realizations. Eight measurements at (approximately) equal increments during a single oscillation cycle are shown in Figure 4.5.

The flow measurements in the meridional plane demonstrate that the near wake flow is dominated by partial, time periodic attachment to the Coanda surface of the aft segment of the model. The cross flow over the model also becomes partially attached to the Coanda surface along azimuthal segments that are normal to the *x*-*y* meridional plane and as the model moves, the near wake which is nominally axisymmetric when the model attitude is aligned in the streamwise direction becomes laterally-distorted. Similar effects are measured in the near wake of a static model (cf., Chapter **III**), where the wake is either aligned with the model (Figure 2.4), or distorted (Figure 2.7). In fact, the near wake distortion alternates with the model yaw oscillations, is nominally symmetric about the meridional plane, and is associated with alternating aerodynamic side forces on the model. Figures 4.5*a*.1-8, *b*.1-8, and *c*.1-8 show a sequence of color raster plots of concentrations of phase-averaged streamwise, $\widehat{U}_{\mathrm{x}}(t)$, and cross-stream, $\widehat{U}_{\mathrm{y}}(t)$, velocity components and of the azimuthal vorticity, $\hat{\zeta}_{\mathrm{z}}(t)$, during the oscillation cycle ($0 < t/\tau_{\mathrm{z}} < 0.875$, at increments of $0.125\,\tau_{\mathrm{z}}$). The aft end of the body and its attitude are also shown for reference in each part Figure 4.5.

The streamwise velocity distribution (Figures 4.5*a*.1-8) within the meridional plane exhibits a clear reversed flow domain within a local “bubble” that is bounded by a counter-current separating shear layer on each cross-stream end. The reversed streamwise velocity region has a local maximum that decays towards the upstream and downstream edges of the bubble and oscillates transversely. The offset of this maximum relative to the model centerline when it is aligned with the direction of the tunnel flow at $t/\tau_{\mathrm{z}} = 0$ and 0.5 ($y/D = \pm 0.075$, $x/D = 1.9$) is indicative of the inherent flow latency relative to the motion of the model, and may contribute to the aerodynamic damping in the model represented in

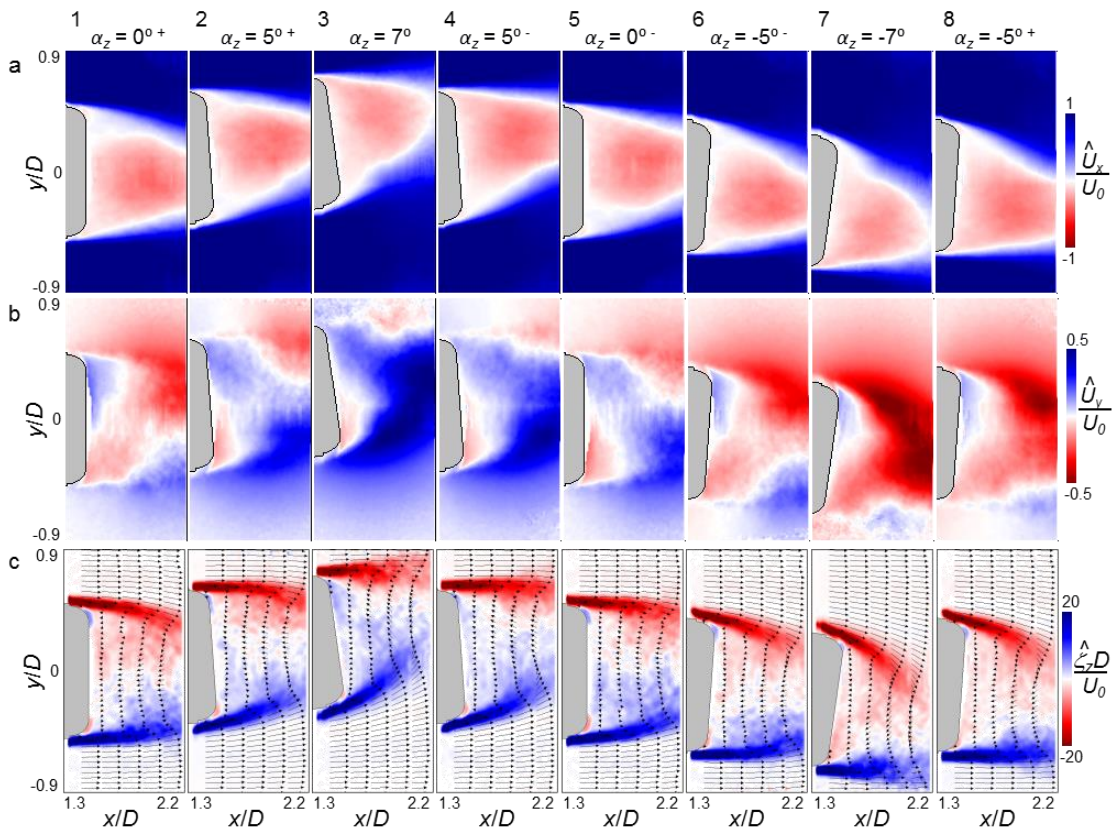

Figure 4.5. Color raster plots of concentrations of phase-averaged streamwise [$\widehat{U}_x$ (t), a.1-8] and cross-stream [$\widehat{U}_z$ (t), b.1-8] velocity components and of the azimuthal vorticity [$\widehat{\zeta}_z$ (t), c.1-8], respectively, in the near wake of the free-oscillating model ($Re_D = 1.15 \cdot 10^5$) during the oscillation cycle ($0 < t/\tau_z < 0.875$, at equal increments $0.125\,\tau_z$).

Equation (4.1). The transverse asymmetry of the flow during the oscillation cycle is also evident by alternating attachment to the aft Coanda (nominally on opposite sides of the model centerline to the position of its front stagnation point). This attachment is accompanied by significant cross-stream flow as demonstrated in Figures 4.5*b*.3 and 7 which accentuate the asymmetry of the near wake near the transverse extremes of the model motion. The residual transverse asymmetry at the midpoints of the oscillation cycle (Figures 4.5*b*.1 and 5) is another indication of the latency in the wake flow as it follows the motion of the model. While the asymmetry of the opposite, separating shear layer segments at the midpoints of the oscillation cycle (Figures 4.5*c*.1 and 5) is somewhat less pronounced, the partial attachment of these shear layer segments to the aft Coanda surface (Figures 4.5*c*.3 and 7) results in strong deflection into the near wake that is coupled to the

attitude of the model. During the peak of these opposite deflections, the internal vorticity concentrations within the near wake bubble are of the same sense as the corresponding deflecting shear layer segment. This deflection is accompanied by strong cross-stream velocity distribution, $\widehat{U}_{\mathrm{Y}}(t)$(Figures 4.5*b*.3 and 7), indicating entrainment of the cross flow into the near wake although this entrainment does not significantly diminish the reversed flow within the wake (Figures 4.5*a*.3 and 7) nor does it lead to pronounced changes in the spreading of the separating shear layer at the cross-stream edges of the near wake bubble. In fact, as shown by Sarioglu, Akansu, and Yavuz (2005), the characteristic frequency of the separating shear layer shedding of a cylindrical model with an aspect ratio of $L/D = 2$ and flat front and rear end surfaces are nearly invariant with attitude at $Re_{\mathrm{D}} = 3.4{\cdot}10^4$ (although the shedding frequency can vary with different aspect ratios, typically decreasing with higher L/D).

Following the procedure of Ploumhans et al. (2002), the velocity measurements in the near-wake can be used to estimate the induced aerodynamic moment on the model. Such an estimate is useful for identifying the coupling between the wake and the model motion, and is also used in §**4.4** to evaluate the flow control efficacy. These authors used a control volume formulation that encompass the flow surrounding a body in a uniform stream to calculate the force that is exerted on the body, $\vec{F}$, based on the vortex impulses, $\vec{I}$, in the wake:

$$\vec{F}(t) = -\rho \frac{d}{dt}\vec{I}(t) = -\rho \frac{d}{dt}\left(\frac{1}{2}\iiint \left(\vec{r} \times \vec{\zeta}\right) d\forall\right) = \iiint \frac{\rho}{2}\frac{d}{dt}\left(\vec{\zeta} \times \vec{r}\right) d\forall = \iiint d\vec{F} \qquad (4.6)$$

where $\vec{r}$ is the distance of a fluid particle in the wake from a fixed origin which, in the present experiments, is taken to be the axis of the mounting wire, and the flow is assumed to be incompressible. This formulation can be extended to account for the aerodynamic moment of the present model about its mounting wire:

$$M_{\mathrm{z}} = \hat{z}\cdot \iiint \vec{r} \times d\vec{F} = \hat{z}\cdot \iiint \vec{r} \times \left(\frac{\rho}{2}\frac{d}{dt}\left(\vec{\zeta} \times \vec{r}\right) d\forall\right)$$

$$= \iiint \frac{\rho}{2}\left(-\zeta_x(r_x U_z) - \zeta_y(r_y U_z) + \zeta_z(r_x U_x + r_y U_y) - \dot{\zeta}_x(r_x r_z) - \dot{\zeta}_y(r_y r_z) + \dot{\zeta}_z(r_x^2 + r_y^2)\right) d\forall \quad (4.7)$$

and is shown for the phase averaged data [$\widehat{U}_x(t)$, $\widehat{U}_y(t)$, and $\hat{\zeta}_z(t)$] in Figure 4.5. Since the phase-averaged flow is taken to be symmetric about the meridional measurement (*x*-*y*) plane it is argued that $\widehat{U}_z(t)$, $\hat{\zeta}_y(t)$, and $\hat{\zeta}_x(t)$ vanish in this plane leaving the contribution to the moment from the meridional plane as:

$$d\widehat{M}_z\big|_{z=0} = \iint \frac{\rho}{2}\left(\dot{\hat{\zeta}}_z(r_x^2 + r_y^2) + \hat{\zeta}_z(r_x\widehat{U}_x + r_y\widehat{U}_y)\right) dydx = \iint d\widehat{M}_{xyz}\, dydx = \int d\widehat{M}_{xz} dx \quad (4.8)$$

Although the present measurements do not encompass the entire streamwise extent of the wake, the measurements in the meridional plane within the domain in Figure 4.5 yield some useful indication of the wake contribution to the aerodynamic yawing moment through the integrands of Equation (4.8), $d\widehat{M}_{xyz}(x, y, t)$, and $d\widehat{M}_{xz}(x,t)$. The time derivative of the measured vorticity, $\dot{\hat{\zeta}}_z$, was estimated using the 28 measured phases throughout the wake oscillation, and the contribution from the unsteady term, $\dot{\hat{\zeta}}_z(r_x^2 + r_y^2)$ is approximately an order of magnitude smaller than the steady term, indicating the absence of large unsteady aerodynamic effects.

Figures 4.6a-c are color raster plots of $d\widehat{M}_{xyz}(x, y, t)$ during a lateral oscillation cycle. Due to the phase averaged velocities that are used in this calculation, these moments contributions are caused entirely by the quasi-steady time varying near wake structure and not the shedding frequency. Figures 4.6a and b show $d\widehat{M}_{xyz}(y, t;\ x = \text{constant})$ for two representative streamwise positions, $x/D = 1.8$ and 2.05, while in Figure 4.6c, $d\widehat{M}_{xyz}$ is integrated in *y* (across the wake) to yield a map of $d\widehat{M}_{xz}(x,t)$ within the entire interrogation domain of $1.3 < x/D < 2.2$. The data in Figures 4.6a show that the contributions to the induced moment at $x/D = 1.8$ downstream of the model come from the vorticity concentrations within the separating shear layers that undulate along the *y* axis during the lateral oscillations of the model, where each shear layer has a similar contribution. This is

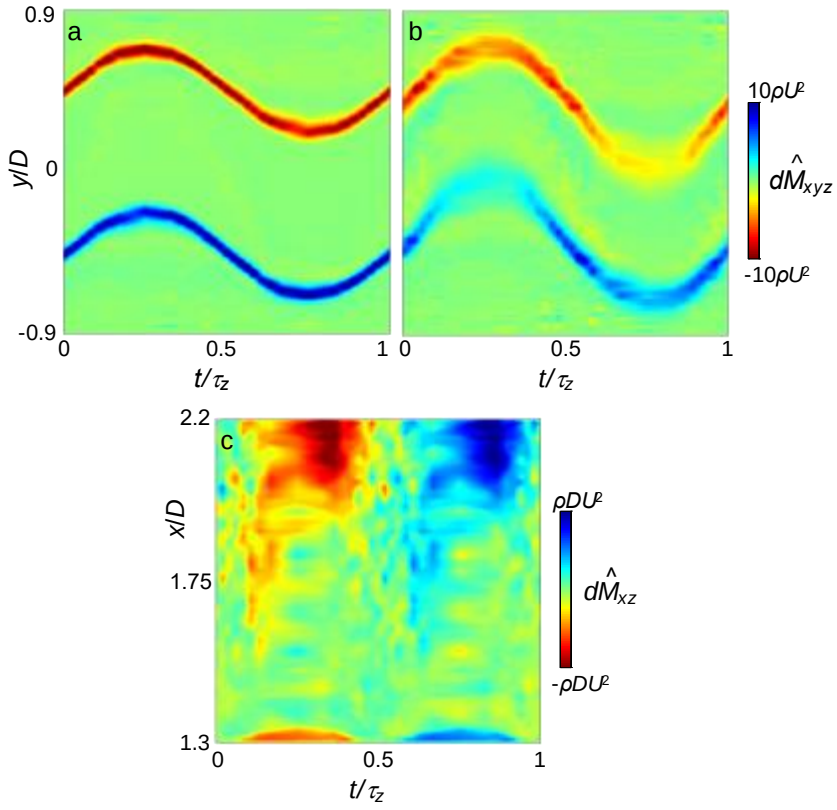

Figure 4.6. Color raster plots of $d\widehat{M}_{xyz}$ (y, t, x = constant) in the meridional x-y measurement domain (cf., Figure 4.5) at x/D = 1.8 (a), and 2.05 (b); and the variation of $d\widehat{M}_{xz}$ (x, t) during the base lateral oscillation cycle.

also shown in Figure 4.6c, where the vorticity concentrations integrated in the cross-stream (y) direction lead to small net contributions to the model moment at x/D = 1.8. However, at x/D = 2.05 in Figure 4.6b, these contributions alternately intensify at the model reaches each lateral extreme (as the weaker layer rolls up to a large scale vortex in Figures 4.5c.3 and c.7). This is in concert with Figure 4.6c for $x/D > 1.85$ where for $0 < t/\tau_z < 0.5$ and $0.5 < t/\tau_z < 1$ the vorticity concentrations in the shear layers lead to respective CW, or negative, followed by CCW, or positive, contributions to the yawing moment. The data in Figure 4.6c show that the contribution to the yawing moment from the vorticity layers within the streamwise domain $1.35 < x/D < 1.85$ nearly cancel out indicating that the cross-stream (phase-averaged) distributions become nearly identical as a result of the nearly identical convective speeds. The mismatch between the layer intensifies for $x/D > 1.85$

when they become alternately rolled up into opposite-sense vortices that scale with the width of the near wake (cf., Figure 4.5c). There is also a difference in the vorticity concentrations for $x/D < 1.35$ due to the alternating sense of boundary layer vorticity on the aft surface (in Figures 4.5c.3 and 4.5c.7). The data in Figure 4.6c indicate that the moment induced by the near wake is mostly out of phase with the model motion (with a minimum at $t/\tau_z = 0.33$ and a maximum at $t/\tau_z = 0.83$) and contributes to a net stabilizing moment that opposes the deflection of the model relative to the streamwise direction. This is in agreement with the measured aerodynamic moment in Figure 4.4d, with a minimum and maximum C_Y near the largest positive and negative α_z, respectively, with a slight hysteresis (or phase lag).

4.2 Transitory Actuation

The response of the free-moving model to fluidic control is first investigated using transitory pulsed (burst) actuation that is effected at a given phase of the during uncontrolled oscillations. The effects of the actuation on the evolution of the separated flow over the aft Coanda surface and in the near wake are assessed using a sequence of a varying number of successive discrete jet actuation pulses that are formed by pulsed amplitude modulation of the actuators resonance waveform (similar to a study of synthetic jet pulses on an airfoil by Amitay and Glezer, 2006). A yawing angle that is nearly half of the mean unforced yawing amplitude ($\alpha_z = -3^\circ$, $\dot{\alpha}_z < 0$) is selected as an arbitrary starting point so that the actuation jet whose centerline lies in the plane of the lateral motion in the $-y$ direction induces an aerodynamic moment that accelerates, or amplifies, its motion (the sense of this moment is determined from Chapter **3.1**). The actuation frequency at resonance in this model is $f_{act}^* = 0.4$ ($\tau_{act} = 0.91$ ms), $C_\mu = 3.2 \cdot 10^{-3}$ ($U_{jet} = 25$ m/s). The response of the flow downstream of the aft end of the model is measured phase-locked to the crossing of the yaw angle $\alpha_z = -3^\circ$, as the model translates towards its peak excursion ($\alpha_z = -6.9^\circ$). The results are shown in a sequence of color raster plots of the phase averaged

azimuthal vorticity $\hat{\zeta}_z$ downstream of the active jet for the base flow (Figures 4.7a.1-4), and in the presence of amplitude modulated actuation using a single actuation pulse (N = 1, Figures 4.7b.1-4) and 15 successive actuation pulses (N = 15, Figures 4.7c.1-4), at t/τ_{act} = 0 (Figures 4.7a-c.1), 5 (Figures 4.7a-c.2), 10 (Figures 4.7a-c.2) and 15 (Figures 4.7a-c.4) following the yaw angle crossing. The base flow (Figures 4.7a.1-4) hardly changes during the elapsed time ($15\,\tau_{act} = 0.023\,\tau_z$). The deflection of the separating shear layer that is

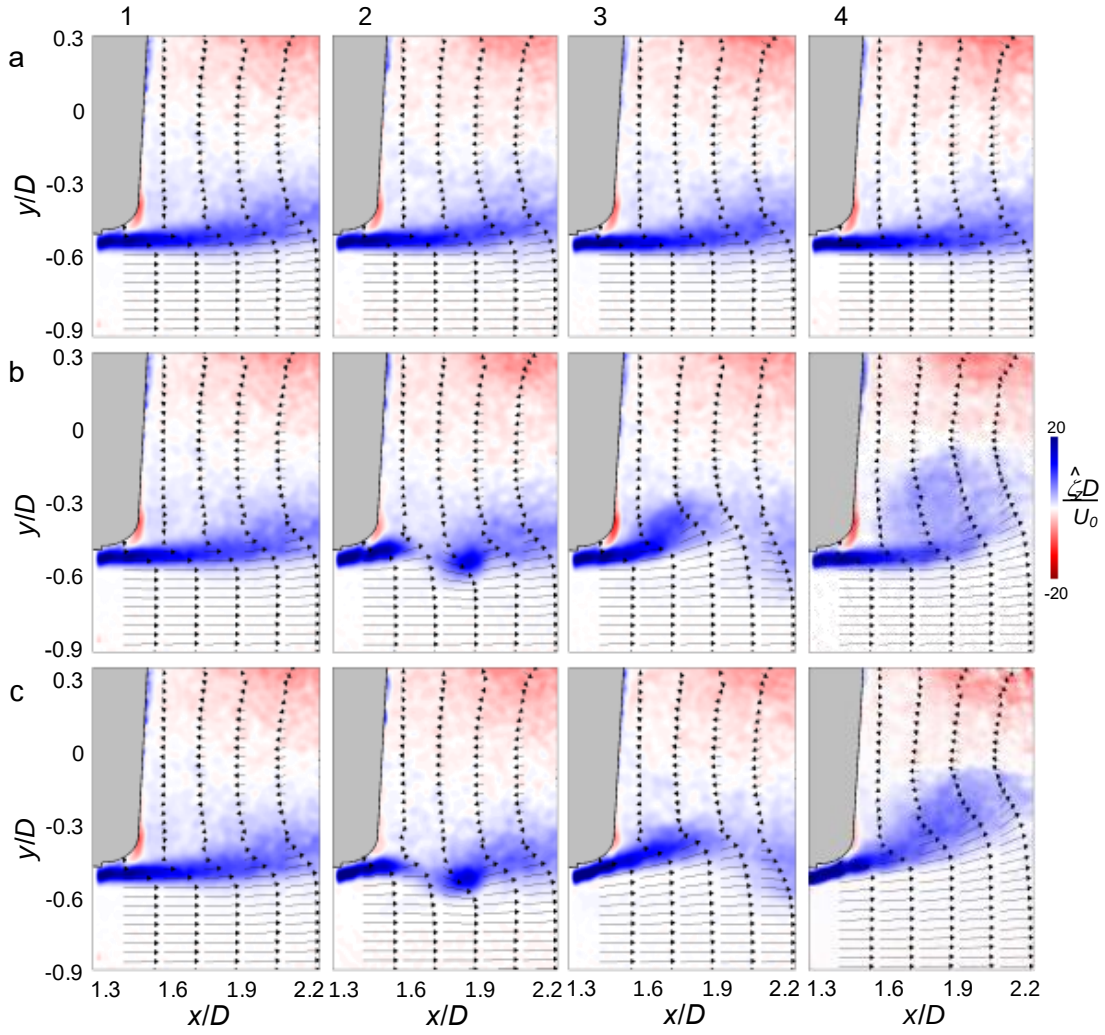

Figure 4.7. Color raster plots of phase-locked azimuthal vorticity concentration $\hat{\zeta}_z$ overlaid with velocity vectors showing the transitory response of the base flow to pulse-modulated actuation ($Re_D = 1.15 \cdot 10^5$) at an initial model deflection of α_z = -3° for N = 0 (a.1-4), 1 (b.1-4), and 15 (c.1-4) successive jet pulses from the start of acquisition. Measurements are taken at t/ τ_{act} = 0 (a-c.1), 5 (a-c.2), 10 (a–c.3), and 15 (a-c.4).

characterized by predominantly CCW vorticity towards the Coanda surface owing to the model attitude is insufficient to induce partial attachment, although the entrainment near the aft end of the model is marked by the formation of CW vorticity concentration in the boundary layer of the entrained flow along the aft surface. Immediately following the onset of the single pulse actuation (Figure 4.7b.1), the response of the flow is barely noticeable. However, by $t/\tau_{act} = 5$ (Figure 4.7b.2), a large-scale vortex is formed by the transitory severing of the separating shear layer as the upstream vorticity layer begins to deflect towards the surface while the severed segment rolls up to form a CCW vortex that is advected with the cross flow (similar to a study of transitory actuation on an airfoil by Woo, Crittenden, and Glezer, 2008). By $t/\tau_{act} = 10$ (Figure 4.7b.3), the severed vortex is out of the field of view while the deflection of the vorticity layer continues and the induced entrainment along the aft surface of the model is evident by the strength of the CW vorticity layer above the deflected shear layer. As the effect of the single pulse actuation begins to diminish by $t/\tau_{act} = 15$ (Figure 4.7b.4), the separated shear layer rolls into a CCW vortex that scales with about half the cross-stream width of the near wake and entrains fluid from the outer flow into the wake. Because the actuation affects only an azimuthal segment of the separating shear layer, the rollup of the upstream and downstream edges of the severed vorticity are clearly azimuthally-limited and merge with vortex lines of the unforced flow at both azimuthal edges. However, these azimuthal changes in the vorticity flux into the near wake and the deflection of the outer flow into the wake (Figures 4.7b.3 and 4) are associated with changes in the induced aerodynamic loads, and result in a momentary side force (and change in the yawing moment) that acts to increase the azimuthal yawing angle (this is discussed in detail in Figure 4.8). When the actuation is applied using a train of 15 successive jet actuation pulses (Figures 4.7c.1-4), the severing of the shear layer and the onset of the severed CCW vortex are nearly identical to the effect of the single pulse, but the vectoring of the upstream vorticity later towards the inner part of the wake continues at $t/\tau_{act} = 15$ (compare Figures 4.7b.4 and 10c.4). This indicates that the duration of the

induced side force that is associated with the local vectoring of the external flow is extended. The formation of the CCW vortex as the actuation is terminated in Figure 4.7b.4 is clearly associated with the radial "recoil" of the vorticity layer which has not yet occurred in Figure 4.7c.4, because the actuation was just terminated.

The cumulative effect of pulse-modulated actuation is demonstrated by tracking the changes in the model yaw angle $\alpha_z(t)$ following the application of the (single jet) actuation at $\alpha_z = -3^\circ$ or $+3^\circ$ (the actuation is applied as the model moves away from center), similar to in Figure 4.7. Here, the single jet actuator is selected on the $-y$ side of the model (or the 'left' jet in Figure 2.1a) and induces a moment that amplifies (at $\alpha_z = -3^\circ$) or reduces (at $\alpha_z = +3^\circ$) the amplitude of the lateral (base) oscillations in the absence of actuation. Pulse modulation is effected with $N = 1$, 5, 10, 50, and 100 successive actuation cycles of the synthetic jet. Following the application of each (fixed) actuation burst, the model is allowed to return to the unforced (natural) spanwise oscillations (actuation is terminated until four cycles after the last actuation) before the actuation is re-applied on the next crossing through $\alpha_z = -3^\circ$ or $+3^\circ$ (the sequence is repeated fifty times for each burst, and phase averaged). Figure 4.8 shows time traces of the phase-averaged transitory attitude of the model following the onset of the pulse-modulated actuation for $\alpha_z = -3^\circ$ (Figure 4.8a) and $+3^\circ$ (Figure 4.8b), where the bars at the top of each figure mark the duration of the actuation cycles. When the pulses that tend to amplify the lateral oscillation amplitude are applied, it is observed that even a single actuation pulse ($\tau_{act} = 0.0016\,\tau_z$) leads to an appreciable increase in the angular velocity of the model. Despite the pulsed onset of the actuation its effect on the model attitude is not apparent (owing to its own inertia) until $t/\tau_{act} > 20$ (well after the actuation is terminated), and persists through $t/\tau_{act} \approx 100$ (at this point, the nominal attitude of the model is increased relative to the base flow with all pulse durations). As noted in Figure 4.7b.2-3, a single-pulse actuation leads to severing of a segment of the separating shear layer at the aft end of the model and to a momentary

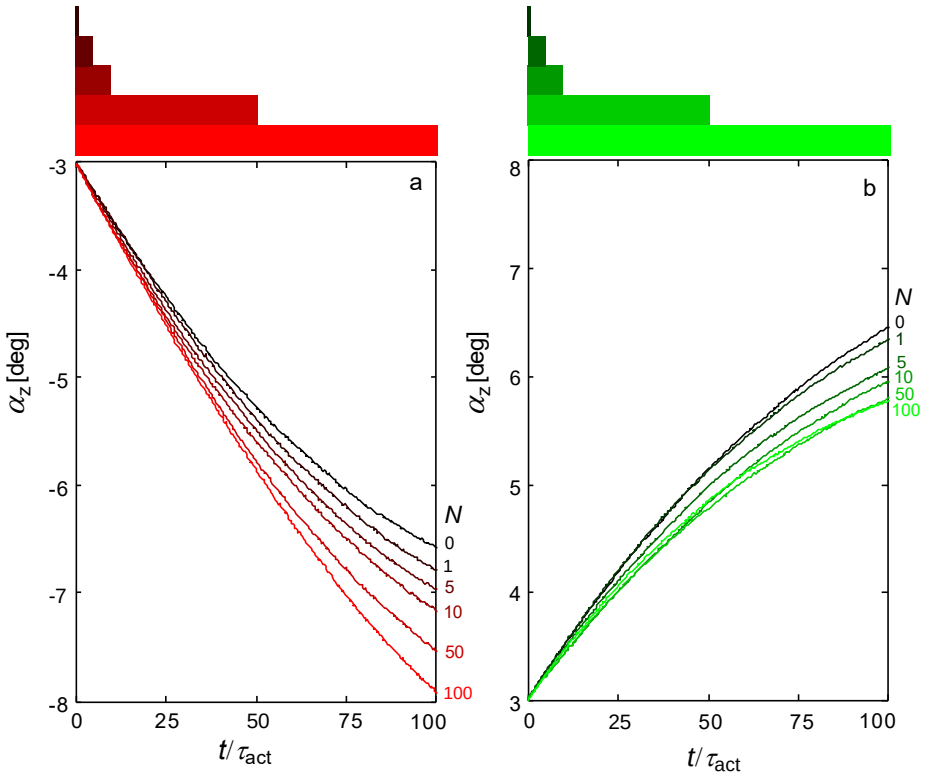

Figure 4.8. Time traces of the phase-averaged transient attitude of the model following the onset of open-loop pulse-modulated actuation of a single jet (located on the –*y* side of the model) with bursts of N = 0 (baseline), 1, 5, 10, 50 and 100 actuation cycles for cycle amplitude amplification at α_z = -3° (a) and attenuation at α_z = +3° (b). The traces are shown in shades of **red** (amplification) and **green** (suppression) that vary from dark to light with increasing N cycles (N = 0 is marked in black), and the bars at the top of each figure shows the corresponding time duration of the actuation bursts.

attachment that can result in a yawing moment increment significant enough to effect the direction of yawing motion. Furthermore, the data in Figure 4.7 also indicate that the relaxation of the near wake flow following the termination of the pulsed actuation is significantly longer than the onset time indicating that the temporal increase in the yawing moment persists well past the termination of the actuation. This is apparent from the monotonic increase in the time rate of change of $\alpha_z(t)$ following the termination of the actuation for N = 100 compared to the base motion (the initial delay in the effect of the actuation also diminishes with increasing duration of the actuation burst). The corresponding reductions in $\alpha_z(t)$ by effecting a similar (same sense) yawing moment that

resists the motion when the same jet (on the $-y$ side of the model) is activated at $\alpha_z = +3^\circ$ are shown in Figure 4.8b. Again, a single jet pulse leads to a measurable reduction in the attitude and the angular yawing velocity, but, in fact, the delay in the noticeable change of the model attitude is longer ($t/\tau_{act} > 55$) and the deceleration of the angular velocity persists past the end of the data record. Similar to actuation for amplification, the delay in the reduction in model attitude diminishes with increasing actuation burst. However, while the reduction in the attitude angle intensifies monotonically with burst length up to $N = 10$, the reduction for $N = 50$ is nearly identical to $N = 100$ for $t/\tau_{act} < 45$, is greater than $N = 100$ for $45 < t/\tau_{act} < 60$ and is less than $N = 100$ at $t/\tau_{act} > 90$. It is conjectured that, in comparison to actuation at $\alpha_z = -3^\circ$, the less pronounced attenuation effect of is associated with the changes in controlling the separating shear layer in the presence of an adverse pressure gradient in the upstream boundary layer. These data seem to suggest that the separating layer is more susceptible to the transients that are associated with the onset and termination of the actuation rather than to sustained, long actuation bursts.

The variation of the phase averaged attitude angle with pulsed actuation is compared with the base flow, $\alpha_{z\text{-act}}(t)$ with $\alpha_{z\text{-base}}(t)$, respectively in Figure 4.9. Similar to Figure 4.8, the synthetic jet located at $-y$ on the centerline is activated at either $\alpha_z = -3^\circ$ (Figure 4.9a and c, amplification) or $\alpha_z = 3^\circ$ (Figure 4.9b and d, attenuation), shown for the full lateral oscillation cycle (Figure 4.9a-b, where the angle at which the actuation is applied is marked), and with a magnified view immediately following actuation (Figure 4.9c-d). The trajectories in Figures 4.9a and c show that amplifying actuation leads to an increase in the lateral amplitude of the oscillation beginning with a single actuation pulse (about 0.3°) and an increasing change with N up to nearly 1.9° degrees for $N = 100$. Following the discussion of Figure 4.8, it is observed that even though the actuation is terminated well before the model reaches its maximum lateral excursion, these extended excursions persist throughout the entire cycle (Figure 4.9a) and are also evident by the change of slope of

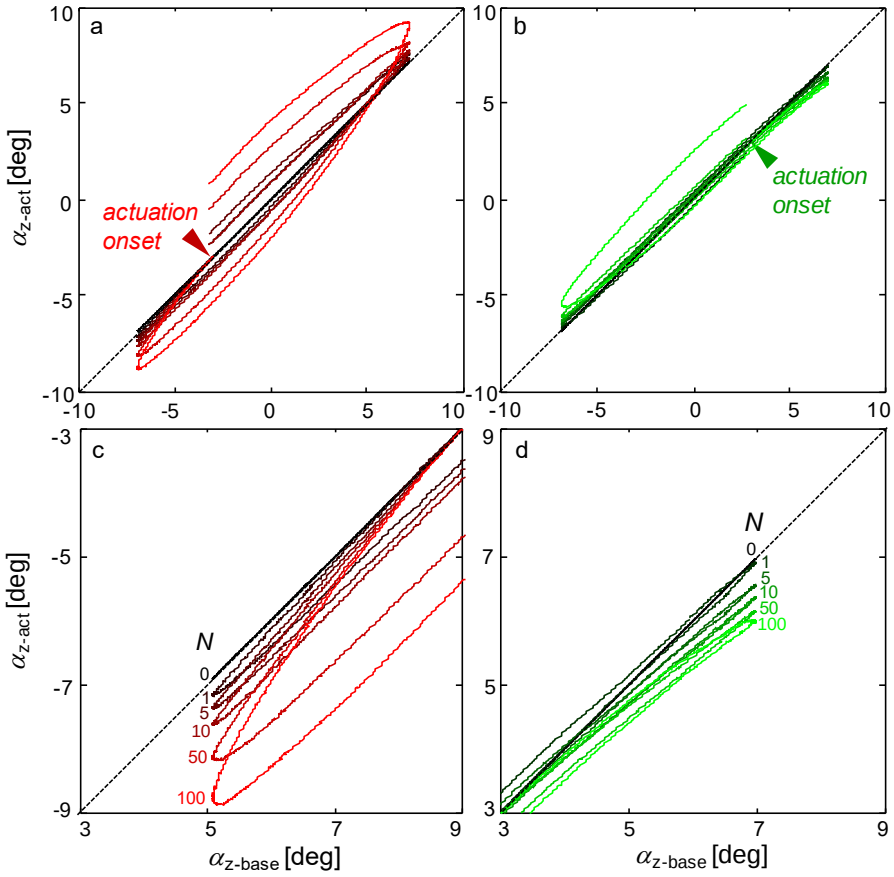

Figure 4.9. Phase-plots of the transient attitude of the model following the onset of open-loop pulse-modulated actuation $\alpha_{z\text{-act}}$ relative to the base flow attitude $\alpha_{z\text{-base}}$, with the same color map as in Figure 4.8. The full cycle (a,b) and magnified views (c,d) following the onset of actuation are shown for amplitude amplification at α_z = -3° (a,c) and attenuation at α_z = +3° (b,d).

$\alpha_{z\text{-act}}$ relative to $\alpha_{z\text{-base}}$. The response of the model to the actuation indicates the receptivity of the flow and the coupling between the model and its near wake. Similarly, when the actuation is applied with the intent of diminishing the lateral oscillations of the model (Figures 4.9b and d), the excursion amplitude is reduced although the decrements are smaller than for amplification (for N = 100, the reduction is about 1° in Figure 4.9d). As noted in Figure 4.8b, the effect of the actuation with N = 100 seems to intensify following the termination of the actuation, and the data in Figures 4.9b indicates a strong reduction

in $\alpha_{z\text{-act}}$ at the opposite end of the cycle (when $\alpha_{z\text{ -base}}$ was about -6.9°, $\alpha_{z\text{-act}}$ was reduced to about -5.6°).

The temporal evolution of the trajectory changes effected by enhancing and suppressing actuation following burst actuation of $N = 100$ pulses at $\alpha_z = 3^o$ are illustrated in Figure 4.10 during four periods of the model oscillations in the absence of actuation ($4\tau_z$). In these measurements, the starting attitude of the actuation is set to $\alpha_z = +3^o$, and suppression or enhancement are implemented by using one of the two opposite actuation jets, respectively. Even though the actuation is applied for $100\tau_{act}$ (or $0.163\tau_z$), its transitory effects on the ensuing trajectory are felt for 2-3 oscillation cycles as is evident by the monotonic decay of the initial reduction (80%) or enhancement (130%) of the first peak relative to the base flow. It is observed that even though the three waveforms of $\alpha_z(t)$ become nearly identical to the attitude waveform of the unforced flow after 3 oscillation cycles, but end with what appears to be fixed phase lead (by 40°) and lag (by 75°) relative to the base cycle because of the respective temporary reduction and increase in the lateral oscillation periods. The increased phase lag from amplification actuation demonstrates that the open-loop receptivity to amplification is higher, as was also evident from Figures 4.8 and 4.9.

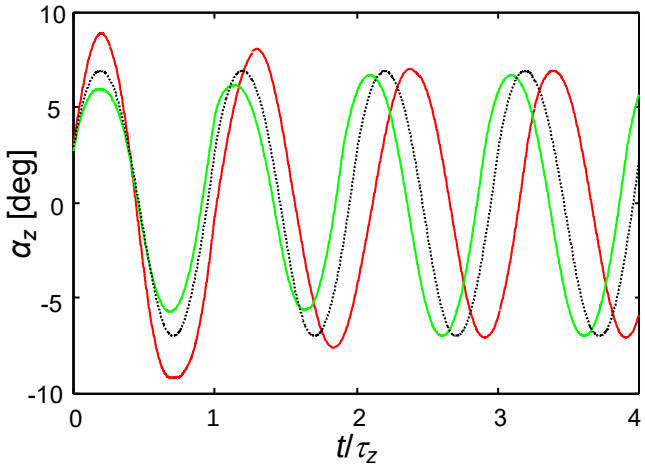

Figure 4.10. The time evolution of α_z(t) over four baseline cycles in the absence (dotted black) and presence of burst actuation (N = 100) for amplification (**red**), or attenuation (**green**).

4.3 Open-Loop Actuation

The transitory effects associated with pulsed actuation where the actuation burst is longer than the transitory interactions of the onset and termination of the actuation with the model near wake are investigated using single and opposite actuation jets. Figure 4.11 shows instantaneous measurements of the model attitude over $2{,}400\tau_{conv,}$ or $34\tau_z$ (of the base flow), where actuation is activated at $t/\tau_{conv} = 600$ and terminated at $t/\tau_{conv} = 1{,}800$ (relative to the beginning of the data record). Time traces of the base model oscillations (in the absence of actuation) are shown Figure 4.11a (cf., Figure 4.1a), demonstrating the characteristic cycle-to-cycle variations in amplitude and period (the time averaged attitude is aligned with the free stream, i.e., $\bar{\alpha}_z = 0$). Step-modulated actuation of a single jet (in this case, the at $+y$ jet, or the 'right' jet in Figure 2.1a) is triggered at $\alpha_z = 3^\circ$, $\dot{\alpha}_z > 0$, and shown in Figure 4.11b. As discussed in connection with Figure 4.7, the actuation of the jet at $-y$ leads to a predominantly CW, or negative, yawing moment and, by symmetry, the $+y$ jet should lead to a predominantly CCW, or positive, moment. This moment would support or resist the motion of the model depending on what orientation the jet is activated (cf., Figure 4.9). Upon single jet activation, the model time-averaged attitude changes to $\bar{\alpha}_z = +3.2^\circ$, its average peak lateral excursion increases to 8.5° from 6.9°**,** and its oscillation amplitude decreases by approximately 20%. While the peak lateral excursion of the model ($\alpha_z > 0$, which is in the direction of the actuation-induced yawing moment) is reasonably stable during the actuation, the opposite excursion ($\alpha_z < 0$) exhibits low-frequency variations that are similar to the variations in the absence of actuation, if not larger. In addition, these low frequency fluctuations seem more significant in the cycles directly after actuation, and therefore suggests these changes in the excursion amplitude may be associated with transitory response to the actuation although the transition in the model average attitude appears to occur within a single oscillation cycle. In fact, following the termination of the actuation the model overshoots to the opposite direction ($\alpha_z \approx 9.5^\circ$) and

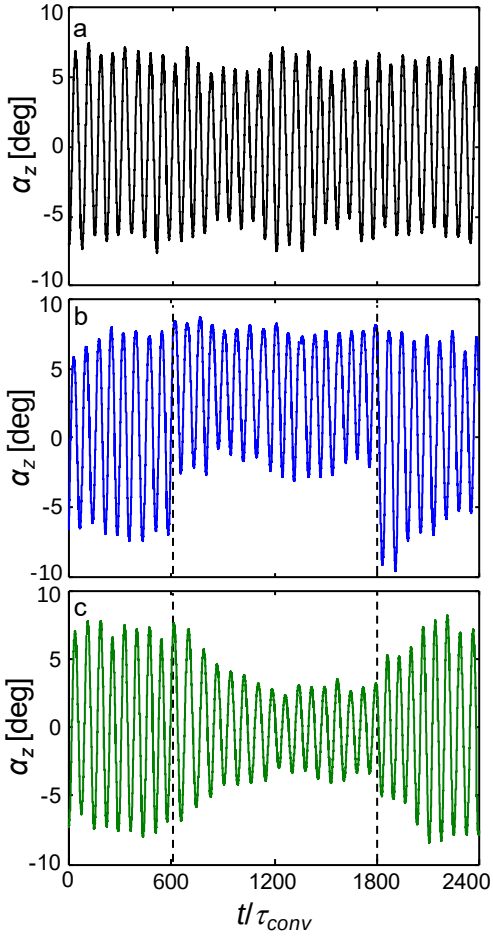

Figure 4.11. Instantaneous variation of the model attitude in the absence of actuation (a), and with continuous actuation using a single jet (b), and two opposing jets (c).

thereafter the amplitude decays to the nominal level of the unforced model within 4-5 oscillations. When the model is forced symmetrically by both side actuators (Figure 4.11c), again triggered to crossing +3°, it remains centered about $\alpha_z = 0$ (similar to the base flow) but with a significant decrease in the peak-to-peak lateral excursion of about 60%. The yawing moments induced by each actuation jet continuously oppose each other, but similar to the quasi-steady model are not equal throughout the cycle (cf., Figure 3.6i in Chapter **3.2**). This measurement showed that the maximum jet effect occurs when the model is inclined by about 1° into the freestream, and decays from that maximum. The cumulative effect of the offset of these jet induced aerodynamic moments leads to a net reduction in the model oscillations, but has a larger time scale than the single jet application

(compare Figures 4.11b and c) because the deviations of the jet moments are smaller than an individual jets net moment.

The evolution of the actuation in Figures 4.11b and c is demonstrated during the onset and termination ($-100\,\tau_{conv} < t < +600\,\tau_{conv}$, or $-1.4\,\tau_z < t < +8.4\,\tau_z$) of the actuation for single jet actuation (Figure 4.11b) in Figures 4.12a.1-4 and for two-jet actuation (Figure 4.11c) in Figures 4.12b.1-4 using phase plots of $\dot{\alpha}_z$ vs. α_z (Figures 4.12a.1-2 and 4.12b1-2) and C_Y vs. α_z (Figures 4.12a.3-4 and 4.12b3-4). The phase plots are produced by phase averaging 25 instantaneous measurements for which M_z (and therefore C_Y) is computed using the measured damping constant (cf., Figure 2.8) and numerical derivatives of α_z (cf., Equation 2.1). For the activation onset plots (Figure 4.12a1,3 and b.1,3), the actuation start occurs at $\alpha_z = 3^\circ$ with $\dot{\alpha}_z > 0$, in the same fashion as Figure 4.11 (the segments of the phase traces without actuation are marked in black and with actuation in blue). The actuation termination plots (Figure 4.12a.2,4 and b.2,4) occur at t/τ_{conv} = 1,200 after the actuation

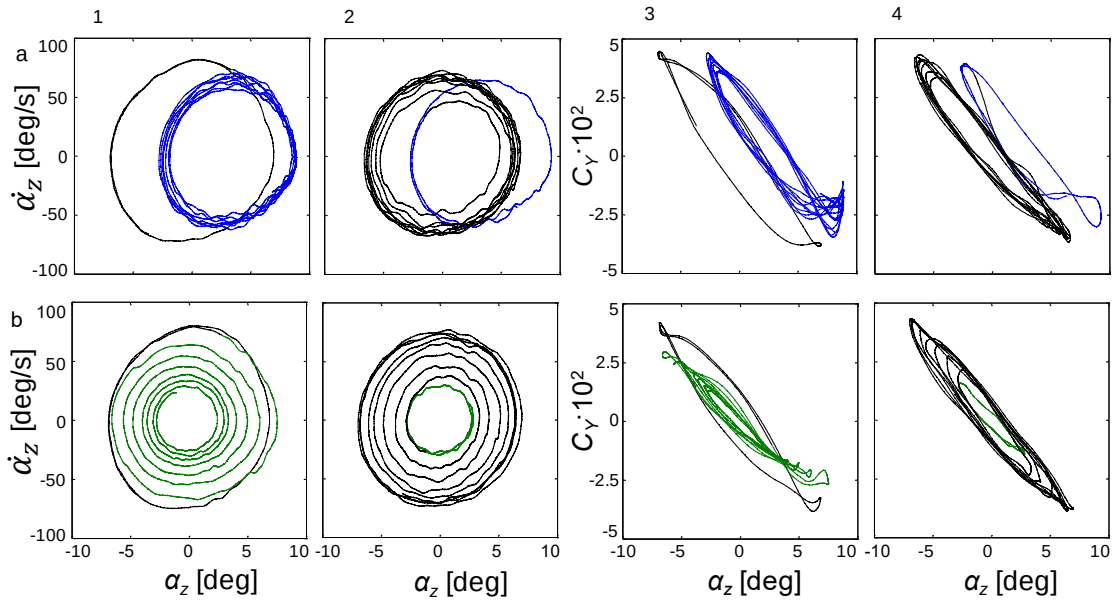

Figure 4.12. Phase-averaged (25 realizations) traces of $\dot{\alpha}_z$ and C_Y vs. α_z during ($-1.4\,\tau_z < t < +8.4\,\tau_z$) after the onset (at $\alpha_z = 3^\circ$, $\dot{\alpha}_z > 0$) and termination ($1200\,\tau_{conv}$ after onset) of single jet actuation [10a.1-2 ($\dot{\alpha}_z$) and 10a.1-3 (C_Y)], and of two-jet actuation [10b.1-2 ($\dot{\alpha}_z$) and 10b.3-4 (C_Y)]. The phase traces without actuation are marked in black and during actuation in **blue** (single jet) and **green** (two jets).

onset, which occurs at α_z = -2° with $\dot{\alpha}_z > 0$ for a single jet, and at α_z = 1° with $\dot{\alpha}_z < 0$ for two-jets. The phase plots of $\dot{\alpha}_z$ vs. α_z in the base flow prior to the onset of the actuation (Figures 4.12a.1 and 4.12b.1) exhibit a slightly tilted (elliptical) path which is a result of the lag (~π/2) between the angular velocity and the attitude in approximate sinusoidal motion. Following the onset of actuation with a single jet, the mean attitude of the model is offset (to $\bar{\alpha}_z \sim 3.2°$, Figure 4.12a.1) within one oscillation cycle but the peak to peak variations in the attitude and angular velocity diminish from ±6.9° to ±5.5° and ±80°/s to ±60°/s. As noted in Figure 4.11b, the motion of the model following the actuation exhibits significant variations in its peak excursion when $\alpha_z < 0$ which are also apparent in the dispersion of the phase trajectory (although the phase averaging may mask some transients that are associated with the transition following the actuation). Upon termination of actuation (Figure 4.12a.2), the model exhibits a sharp change in α_z (to the left) within a single oscillation cycle. While this change does not initially overshoot (as did the corresponding change in Figure 4.11b), possibly as a result of the phase averaging, the trajectory does not exhibit a full return to the base flow (compare Figure 4.12a.2 with 4.12a.1) and indicates that full relaxation of the actuation effects may last for ~8 lateral oscillation cycles. Since the motion of the model is strongly coupled to the dynamics of the near wake, this indicates that the relaxation of the transitory actuation effects in the presence of a free moving body are coupled to the characteristic time of the lateral oscillations rather than to the convective time scale of the flow. The corresponding phase traces of C_Y (Figures 4.12a.3-4) exhibit a negative slope (to the left) as expected from the dominant yaw moment on a body in a nominally-harmonic yaw motion. The yaw moment also exhibits hysteresis (caused by aerodynamic damping), and sharp changes at the peak excursions owing to vortex shedding as the direction of the lateral motion changes (cf., §**4.1**). When single-jet actuation is applied (Figure 4.12a.1), the range of C_Y is diminished somewhat (from ±0.043 to ±0.034). Perhaps more prominent are the differences in the

characteristics of C_Y at the peak excursions. At the peak deflection near $\alpha_z = +8.5^\circ$ C_Y appears to overshoot (within a ΔC_Y of about 0.01) and then relaxes and remains nearly invariant at a $C_Y = -0.024$ in the range from $+5^\circ < \alpha_z < +9^\circ$ before it continues in a loop that resembles the baseline motion. The sense of the variation of C_Y with α_z about the $+\alpha_z$ peak excursion (CCW) is opposite to its sense within the main range of oscillation (CW), similar to the two small peaks in the baseline motion at each side, and it is conjectured the growth of the region with changed sense at the peak is commensurate with its increase in its stability (or decrease in its fluctuations). These changes in C_Y indicate significant changes in the shedding of vorticity concentrations as the model rotation changes its direction at the edge of the lateral oscillation about $\alpha_z = +8.5^\circ$ compared to the edge at about $\alpha_z = -2.5^\circ$. This is also clearly associated with the periodic change in the sense of the restoring aerodynamic yawing moment while the sense of the actuation induced yawing moment remains in the same direction (CCW, or positive). This edge effect then vanishes following the termination of the actuation (Figure 4.12a.4). While the range of C_Y increases, it does not reach its full pre-actuation extent within eight cycles following the termination, again, indicating the lingering effects of the coupling between the actuation and the near wake.

The corresponding phase plots that are associated with the simultaneous actuation of two opposite jets (Figure 4.11c) are shown in Figures 4.12b.1-4 (the phase traces in the presence of actuation are marked in green). In contrast to the rapid change in the model attitude by single jet actuation, actuation by two jets leads to a slower transition to the new state. As noted in discussion with Figure 4.11c, the actuation jets effects nearly-identical time-averaged yawing moments that are symmetrically opposite (i.e., CW and CCW) but vary somewhat with the model yawing angle during the oscillation cycle. This results in slow convergence (within about 6 oscillation cycles) to the new limit-cycle of the model ($\bar{\alpha}_z = 0$) which has significantly smaller peak-to-peak attitude excursions ($\pm 3^\circ$) and range of angular velocity ($\pm 30^\circ$/s) than the base flow, and indicates that the slow convergence to

the new limit cycle is the result of the small cyclical differences between the opposing yawing moments that are induced by the opposite actuators. The limit cycle is reached when the spanwise yawing motion is diminished to the point where the cyclical variations in the actuation-induced yawing moments are virtually balanced (Figure 4.12b.1). Upon termination of the actuation (Figure 4.12b.2) the model returns to the base motion in a similar manner to the termination of the actuation in Figure 4.12a.2 but, evidently, the lateral position and angular velocity of the model when the actuation is terminated lead to a different relaxation to the base limit cycle. The phase traces of C_Y indicate that the nominally-symmetric actuation by the opposite jets (Figure 4.12b.3) results in phase traces that have diminished ranges of α_z and C_Y (of about 60% each) but are nominally similar to the traces of the base flow (including the details associated with shedding of vorticity concentrations at the edges of the lateral excursion). As with single-jet actuation the return of the model to the base motion is incomplete at the end of the present data record in eight lateral time scales.

Similar studies to those shown in Figures 4.11 (and Figure 4.12) are also conducted over the range $0.57 < Re_D \cdot 10^{-5} < 2.00$. The effects of continuous actuation are analyzed using the time-averaged model deflection $\bar{\alpha}_z$ (by one jet), and the average model oscillation amplitude $\alpha_{RMS\text{-}act}$ (by two jets) in Figures 4.13a and b, respectively. These parameters are plotted as a percentage of the RMS attitude of the base flow, $\alpha_{RMS\text{-}base}$, which increases approximately linearly with Re_D (cf., Figure 4.2a). In Figure 4.13a, the model deflection $\bar{\alpha}_z$ seems to saturate at 70% of the baseline oscillation RMS (or approximately half of the baseline amplitude) at $Re_D \geq 1.15 \cdot 10^5$, with smaller percentage deflection at $Re_D < 1.15 \cdot 10^5$. This indicates that the absolute jet deflection is growing linearly with flow speed for $1.15 < Re_D \cdot 10^{-5} < 2$. In Figure 4.13b, a similar phenomenon is observed for the RMS amplitude with two jets actuated, where the vibration percentage reduces for $Re_D < 1.15 \cdot 10^5$ and then saturates from $1.15 < Re_D \cdot 10^{-5} < 1.72$ with a value of 35% of the unactuated oscillation (a 65% reduction). However, at the highest $Re_D = 2.0 \cdot 10^5$, the two

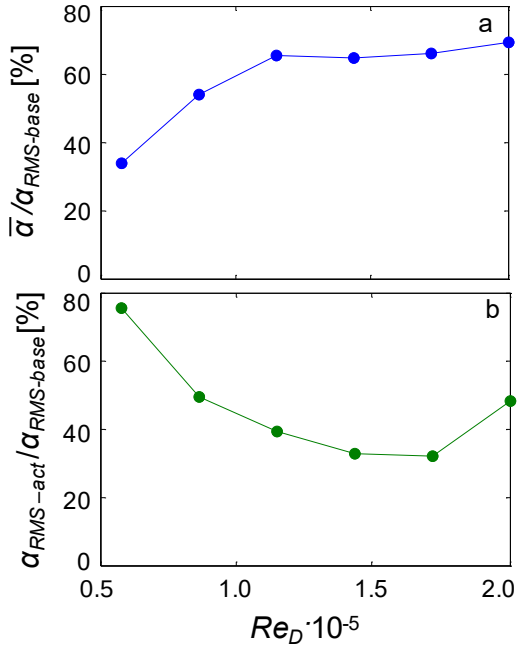

Figure 4.13. Open-loop variation with Re_D of the model average attitude effected by single jet actuation (a, **blue**), and of the RMS attitude effected by two jet actuation (b, **green**). Each is normalized by the RMS attitude of the baseline flow.

jet activation suppression shrinks somewhat, presumably because the jet expulsion velocity U_{jet} at this Re_D needs to be increased in both jets for complete flow attachment (and a similar C_μ). These results show a significant change in the flow with untimed burst actuation (or open-loop flow control), and as suggested in the analysis of Figure 4.8 and 4.9, these results can be improved even more with timed actuation (or closed-loop flow control). For comparison, the commensurate results of the application of closed-loop flow control with varying Re_D are shown in §**4.4.**

4.4 Closed-Loop Actuation

The effects of closed loop feedback control on the attitude of the 'free' yawing model are investigated using a modified PID controller (Appendix **B.1**). Three programs for attitude control are investigated, namely, stabilizing the model about $\alpha_z = 0^\circ$, steering the model to a prescribed attitude offset $\alpha_z > 0^\circ$, and transient steering by amplification of base flow vibrations. Figures 4.14a-c show instantaneous time traces $\alpha_z(t)$ corresponding to

these three control goals, respectively, immediately before and following the onset of control actuation $-100\,\tau_{conv} < t < +300\,\tau_{conv}$ (longer-term effects of these control goals are discussed in connection with Figure 4.15): suppressed vibration about $\alpha_z = 0^\circ$ (Figure 4.14a.1), offset angle about $\alpha_z = 2^\circ$ (Figure 4.14b.1), and amplified vibrations (Figure 4.14c.1). The corresponding controller modulation of the actuators resonance waveforms for yaw rotation to the right $Mod_R(t)$ (Figure 4.14a.2. - c.2) and left, $Mod_L(t)$ (Figure 14a.3 – c.3). In Figures 4.14a.2 and a.3, both actuation jets are activated (mostly out of phase) for controlled attitude about $\alpha_z = 0^\circ$. The degree of modulation initially is nearly 100% and the actuation primarily opposes the model natural angular motion (Figure 4.14a.1, $t < 100\,\tau_{conv}$). As the model oscillations diminish ($t > 100\,\tau_{conv}$), the controller reduces the

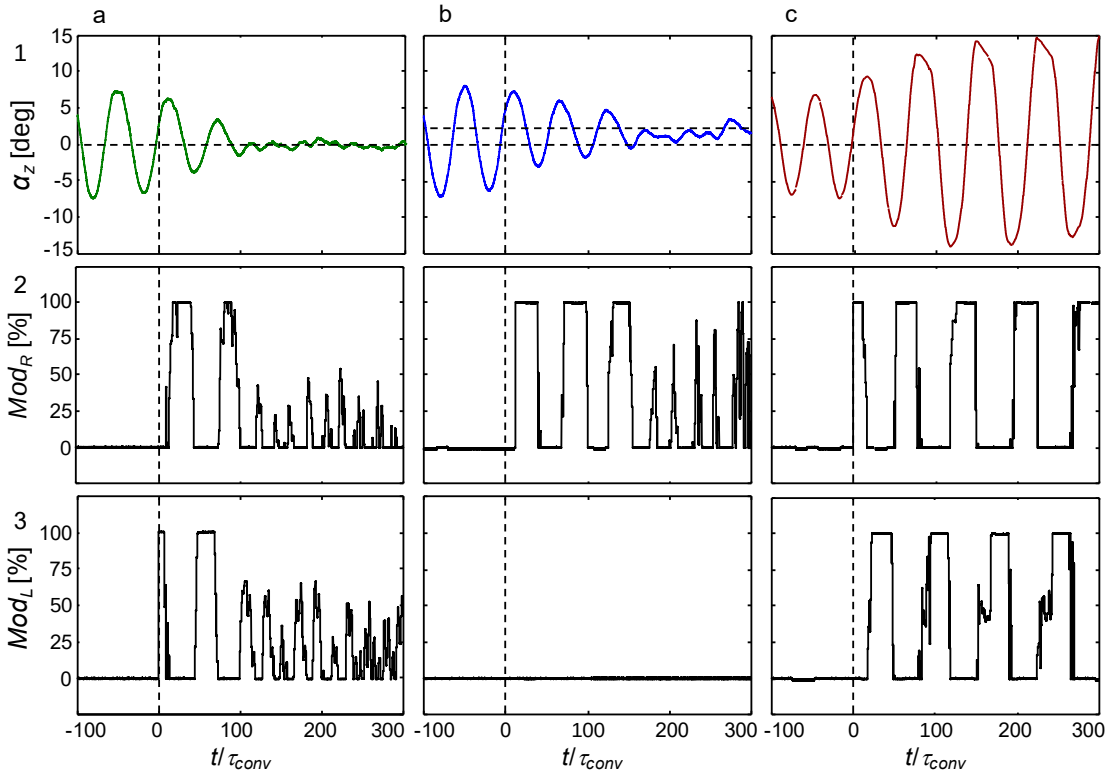

Figure 4.14. Time traces before and following the onset of closed-loop control (applied at $\alpha_z = 3^\circ$, $\dot{\alpha}_z > 0$, $-100\,\tau_{conv} < t < +300\,\tau_{conv}$) of model attitude α_z (a.1 - c.1) and of the modulation of the actuators' resonance waveforms for yaw rotation to the right $Mod_R(t)$ (a.2. - c.2) and left, $Mod_L(t)$ (a.3 – c.3) with the objective of attitude control of $\alpha_z = 0°$ (a.1 – a.3), 2° (b.1 – b.3), and amplified oscillations (c.1 – c.3) at $Re_D = 1.15 \cdot 10^5$ and $C_{\mu,max} = 0.003$.

degree of modulation and the temporal variation exhibits more rapid, and less periodic activation of the jets for disturbance rejection. The controller modulation of the actuation for a commanded attitude $\alpha_z = 2^\circ$ (Figure 4.14b.2 and 3) show that only one of the two control jets is activated demonstrating that only the $+y$ jet (or the 'right' jet) needs to be activated to overcome the restoring yawing moment of the base flow and stabilize the model and $Mod_L(t) = 0$. The modulation $Mod_R(t)$ is similar to the modulation at $\alpha_z = 0^\circ$ although longer time is needed initially to overcome the natural oscillation (approximately $150\tau_{conv}$), and the secondary rapid disturbance rejection also requires a larger degree of modulation (up to 75% compared to about 50% in Figures 4.14a.2 and 3). For the amplification of the model yaw oscillation (Figures 4.14c.1), the modulation commands $Mod_R(t)$ and $Mod_L(t)$ (Figures 4.14c.2 and 3) are nearly out of phase and the degree of modulation reaches 100% for each jet. It appears the control authority of the right jet is somewhat lower than the left jet and the controller compensates for this by using longer modulation periods as depicted by $Mod_L(t)$.

The instantaneous implementation of the three control goals selected (which can be thought of as stabilization, steady state steering, and transient steering) are shown in Figure 4.15 with $Re_D = 1.15 \cdot 10^5$ during an instantaneous trace of $2{,}400\,\tau_{conv,}$ or $34\,\tau_z$ (of the base flow), where actuation is activated for $1{,}200\,\tau_{conv}$ in the same fashion as the open-loop control shown in Figure 4.11. This control is triggered once the baseline model path crosses $\alpha_z = 3^\circ$, $\dot{\alpha}_z > 0$, which is chosen to be consistent with §**4.2** and §**4.3**, where the controller onset and termination is marked with vertical dotted lines, and in addition the zero level is marked for reference. Upon the controller onset, the model response reaches its steady state position on the order of $2\,\tau_z$, and is reduced to a new state of lower amplitude (α_{RMS} decreased from 4.9° to 0.5°, i.e., or 90% reduction) and higher frequency fluctuations. When control is terminated, it takes significantly longer ($\sim 8\,\tau_z$) to return to its baseline limit cycle, and this agrees with the time constant observed with termination of

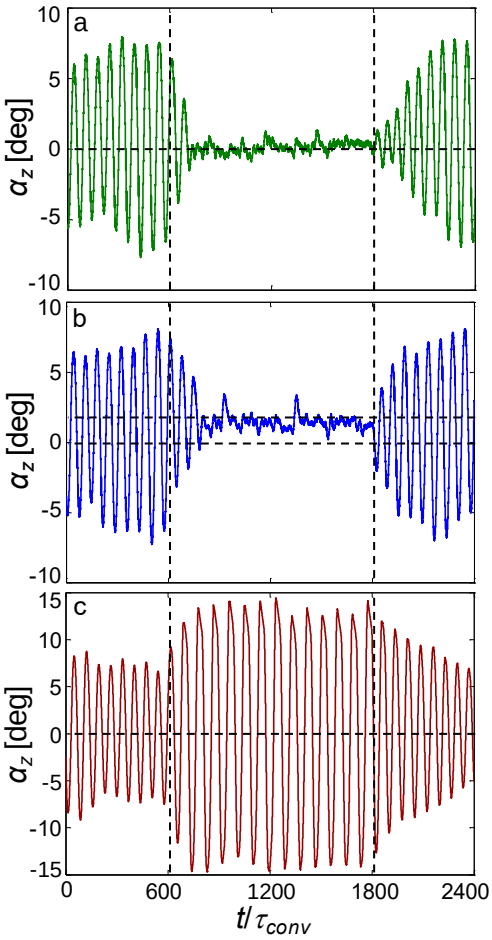

Figure 4.15. Instantaneous variation of the model attitude with PID closed-loop control with the objective of attitude control of $\alpha_z = 0°$ (a), 2° (b), and amplified oscillations (c).

open-loop control in Figure 4.11. The implementation of the controller with a goal angle of $\alpha_z = 2^\circ$ is shown in Figure 4.15b, with an additional dotted line for reference at 2°. This control scheme takes a longer time to reach a new steady state (~$3\tau_z$), about 150% longer than with the $\alpha_z = 0^\circ$ goal using both jets (Figure 4.15a), and in addition, the amplitude of oscillation is slightly larger than when it was held at 0° (α_{RMS} decreased from 4.9° to 0.7°, or 85% reduction). The results of applying a control goal of increasing the model oscillation yields a significant amplification (α_{RMS} increased from 4.9° to 8.6°, or 175% amplification), and is shown in Figure 4.15c. Similar to the suppression control ($\alpha_z = 0^\circ$

goal), the new steady state develops in ~$2\tau_z$, and requires ~$8\tau_{osc}$ after control termination to return to its baseline limit cycle.

A phase average (using 25 data sets) of the oscillation suppression control, both in activation and termination, is plotted in Figure 4.16b,c,e, and f in a similar fashion as the open-loop actuation in Figure 4.12a.1-4. The model response is plotted for ($-100\tau_{conv} < t < +300\tau_{conv}$) after the onset of controlled actuation, and the part of the path with commanded control actuation is shown in green. The phase averaged controller modulations during this period are shown in Figures 4.16a and d, for the right and left jets, respectively, where the direction of increasing time is marked by arrows, showing a CCW rotation of the right jet modulation and a CW rotation of the left jet modulation. In addition, the response segment after termination of the actuation shown in Figure 4.16c corresponds to the same dataset that was used to predict the transient model behavior in §**4.1** (cf., Figures 4.3a and 4.4a-d). Figure 4.16b shows $\dot{\alpha}_z$ vs. α_z, initially forming an ellipsoidal path, where a circular path would represent perfect harmonic motion, and then upon the onset of the jet control, the model is forced to $\alpha_z = 0^\circ$ within $2\tau_z$ (of the base flow). The phase averaged noise on this final model state is smaller than in the instantaneous suppression (compare Figure 4.15a with 4.16b), which is evidence that the induced disturbances in the model are not locked relative to the original state of the model, and are instead pseudo random determined by disturbance rejection from the controller, hence averaging to zero over these 25 realizations. The control is activated when the model crosses $\alpha_z = 3^\circ$, $\dot{\alpha}_z > 0$, which is shown in Figure 4.16d. As the model moves to either $-\alpha_z$ or $+\alpha_z$, the right jet (Figure 4.16a) and left jet (Figure 4.16d) are activated, respectively. The active jet induces a force that would oppose $\dot{\alpha}_z$, and therefore this control acts as an additional aerodynamic damper until the model reaches its goal position, where the controller transitions into a primary disturbance rejection mode. When the control is terminated (Figure 4.16c), the model returns to the baseline path at a much slower rate

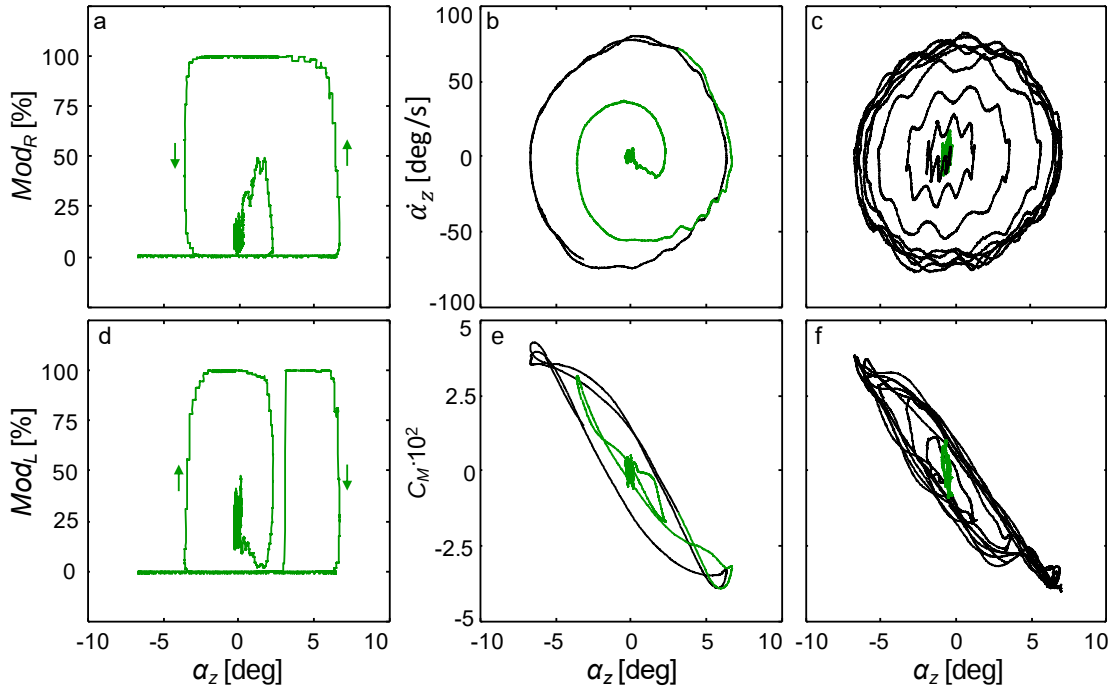

Figure 4.16. Feedback controlled model stabilization about $\alpha_z = 0^\circ$: phase-averaged traces (25 realizations) of the jet modulation commands, Mod_R (a) and Mod_L (d), angular velocity, $\dot{\alpha}_z(t)$ (b,c), and moment coefficient, C_M (e,f) for ($-100\,\tau_{conv} < t < +600\,\tau_{conv}$) after the onset at ($\alpha_z = 3^\circ$, $\dot{\alpha}_z > 0$) (b,e) and termination at $1200\,\tau_{conv}$ after onset (c,f) of feedback controlled actuation. The phase traces in the presence of control are marked in **green**.

compared to control onset, but at approximately the same rate as open-loop actuation (compare Figure 4.16c and Figure 4.12b.2). There is a higher frequency present in the path from center in Figure 4.16c not present in the open-loop deactivation ($St_z = 0.081$), which was discussed in §**4.1**, and is attributed to the initial vortex shedding and general instability of the model when it is centered and exposed to flow. Figures 4.16e shows the C_M vs. α_z phase response to the onset of jets commands for suppressing the oscillation, where the moment peaks present in the baseline diminish during the application of control. Two large peaks are still present in the first τ_z after actuation starts, but the peaks as the range of motion becomes smaller, and are not observable past $2\,\tau_z$ which is in good agreement with the open-loop suppression (in Figure 4.12b.3 the moment peaks also decreased with oscillation amplitude). The termination of the control (Figure 4.16f) takes is not fully

restored even after 600 τ_{conv}, in the same fashion as the termination of different open-loop actuations in Figures 4.12a.4 and 4.12b.4.

The controller steady offset command (α_z = 2°) is presented in Figure 4.17 in analogous fashion to Figure 4.16, with the control actuation shown in blue. The control onset is shown in Figure 4.17b and e, where the model is forced to α_z = 2°, but a longer time is needed to achieve this goal than in Figure 4.16b and e (~3 τ_{osc} compared to 2 τ_{osc}) due to the controller utilizing one jet as discussed with Figure 4.14 (the left jet is deactivated throughout this control, shown in Figure 4.17d). The control of the right jet is shown in Figure 4.17a, with the direction of increasing time marked with arrows. The modulation rotates counterclockwise (the same sense as the right jet for centered suppression in 4.16a) activating when the model is moving in -α_z. This also means the right jet does not initially activate until α_z reaches its maximum at ~6.9°, leading to an initial quarter cycle delay with no control effect, even though the controller is activated at α_z = 3°, and $\dot{\alpha}_z$ > 0. The controller also requires a larger amount of command fluctuation to hold the model still

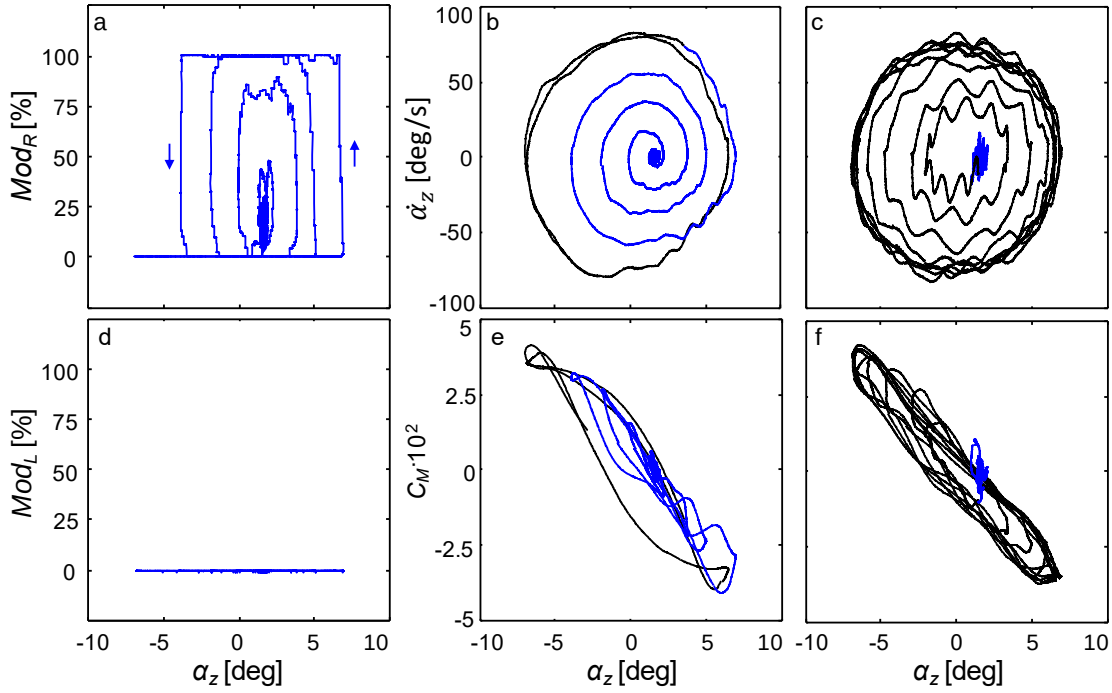

Figure 4.17. Feedback controlled model stabilization (**blue**) about α_z = 2° for the same conditions as Figure 4.16.

(compare the command fluctuations in Figure 4.16a and 4.17a at their respective goal orientations). Upon activating the control, C_M (Figure 4.17e) evolves into a path that is skewed in the direction of positive C_M and positive α_z, in contrast with the approximate symmetric path in Figure 4.16e. Along this path, there is a larger region in the moment peak at -α_z, which is similar to the steady state open-loop right jet shown in Figure 12a.3, and both peaks eventually collapse around the averaged steady state goal location. The resulting C_M fluctuations of the model around its goal $\alpha_z = 2^\circ$ has approximately 150% larger fluctuation to the control with a goal of $\alpha_z = 0^\circ$, attributed to the absence of a second control jet. Upon termination of control, shown in Figures 4.17c and f, the average path has a similar excited frequency and development as the control termination around $\alpha_z = 0^\circ$, suggesting this secondary harmonic is excited due to a model at rest being perturbed, and is roughly independent on its initial attitude.

The oscillation amplification case is investigated in detail in Figure 4.18, in an analogous fashion to the fixed angle control goals in Figures 4.16 and 4.17. The actuation of the right jet and left jet in Figure 4.18a and d, respectively show the jet modulation is activated in the opposite direction as stabilization around $\alpha_z = 0^\circ$ (the right jet is activated CW, and the left jet is activated CCW) and the actuation continuously saturates. Upon the control activation ($\alpha_z = 3^\circ$, $\dot{\alpha}_z > 0$) in Figures 4.18b and e, the ellipsoidal path is amplified to a new path with the introduction of angular velocity peaks at the extremes of motion, not observed before, and the moment peaks become much more pronounced. The increase of prominence of the moment peaks with the larger oscillation amplitude shows that the model path is more unstable than it was initially, deviating further from simple harmonic motion, with sudden large aerodynamic moments introduced at the extremes of motion. This effect shows the same trend as observed in open-loop control with two jets in Figure 4.12b.3, where the actuation decreased the oscillation amplitude and diminished these moment peak instabilities. The variation of the path is significant once the control is

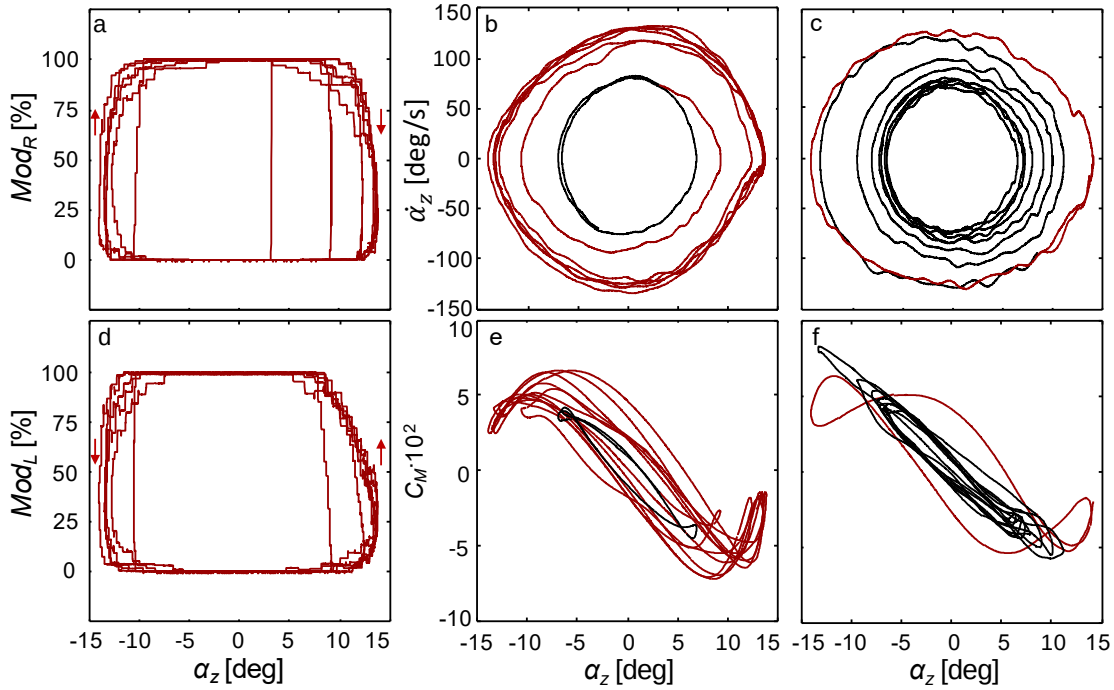

Figure 4.18. Feedback controlled oscillation amplification (**red**) about $\alpha_z = 0^\circ$ for the same conditions as Figure 4.16.

established, even with 25 phase averages, showing that the amplification amplitude does not settle within $600\tau_{conv}$ after the controller is activated, further suggesting that the amplified path is prominently unstable. Upon termination of the amplification control in Figures 4.18c and f, the model returns to the baseline path at a similar rate to the two held-stationary control schemes.

Visualizations of the wake response of the three closed-loop control methods are depicted using a series of PIV measurements taken in the central vertical plane in the same fashion as Figure 4.5c, with velocity vectors overlaid upon contours of the measured vorticity, $\hat{\zeta}_z$. These measurements are phase averaged relative to a dominant oscillation cycle of the model, considered as the period of fluctuation of model once the controller is in a 'steady' (or periodic) state, and are shown in Figure 4.19. These cycle periods at $Re_D = 1.15 \cdot 10^5$ are measured for each of the closed-loop control applications as $\tau_{z\text{-}0^o} = 0.18$s (~$20\tau_{conv}$ or $0.3\tau_z$), $\tau_{z\text{-}2^o} = 0.23$s (~$30\tau_{conv}$ or $0.4\tau_z$), and $\tau_{z\text{-amplify}} = 0.73$s (~$90\tau_{conv}$ or

$1.25\tau_z$). The data are presented in Figure 4.19a.1-8, 4.19b.1-8, and 4.19c.1-8 depicting $\alpha_z = 0^\circ$, $\alpha_z = 2^\circ$, and amplification control, respectively, with the attitude of the model marked above each figure (and the aft end superimposed in each field of view). The response of $\alpha_z = 0^\circ$ and $\alpha_z = 2^\circ$ control is not sinusoidal, and the position of the model instead is closer to a noise function around the command goal (as shown before in Figure 4.15a and 4.15b). However, for simplicity these two control cases are phase averaged at fixed yawing angle increments and presented as if the motion were sinusoidal with their measured dominant periods in Figure 4.19a.1-8 and 4.19b.1-8. Thereby, the phases can be compared to the sinusoidal response of the amplification control (and the baseline wake in Figure 4.5). For $\alpha_z = 0^\circ$ control, the jets oppose the model velocity from center, where the left jet is activated

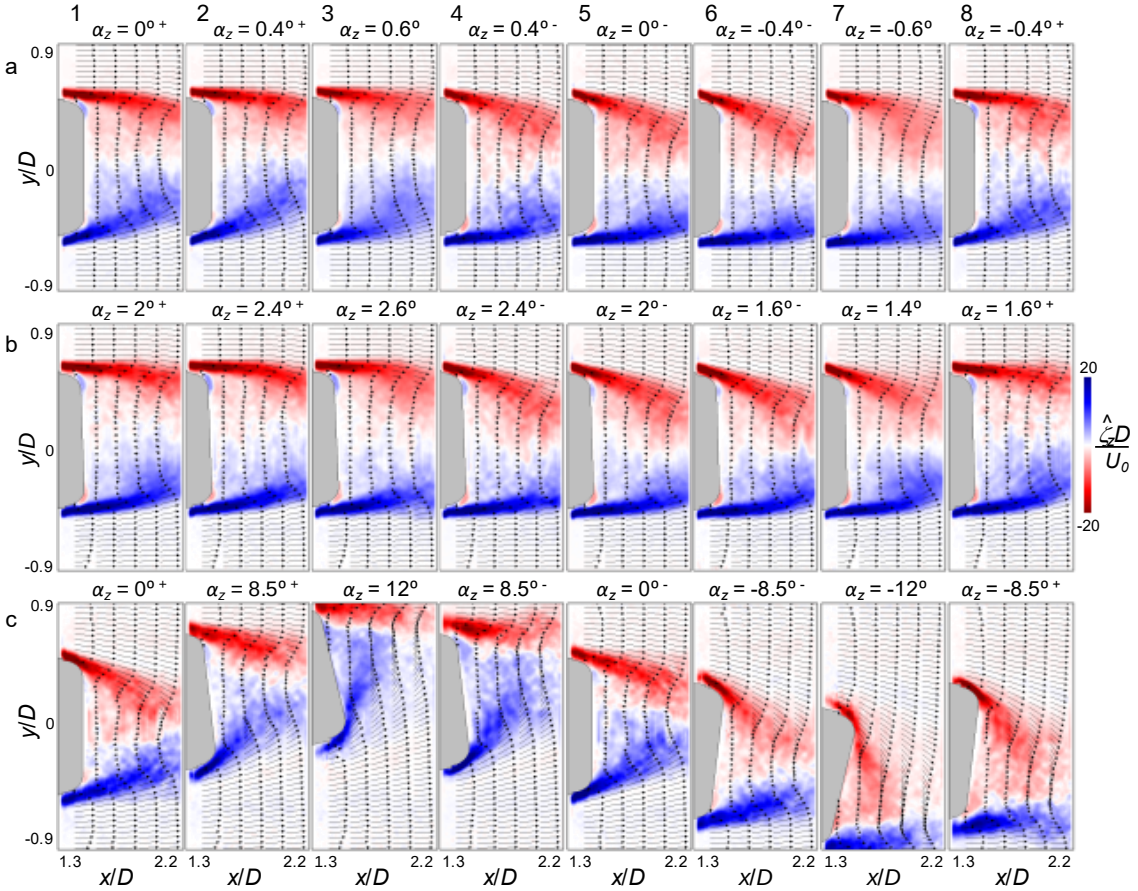

Figure 4.19. Color raster plots of the phase averaged azimuthal vorticity concentrations, $\hat{\zeta}_z(t)$, with overlaid velocity vectors in the near wake (at eight equal time increments throughout a model cycle) for the closed loop control corresponding to Figure 4.16 (in a.1-8), Figure 4.17 (in b.1-8), and Figure 4.18 (in c.1-8).

as the model moves towards +α_z (Figure 4.19a.1,2 and 8), and the right jet activates as the model moves to -α_z (Figure 4.19a.4-6), inducing a restoring force to hold the model at center. This same trend occurs in α_z = 2° control, except in this control only the right jet is utilized, and it is activated as the model moves towards -α_z (Figure 4.19b.4-6). As seen before in Figure 4.14c and 4.18, the amplification control instead activates the synthetic jets to enhance the model yaw rate, resulting in the right jet activation as the model moves towards +α_z (Figure 4.19c.1,2, and 8), and the left jet as it moves towards -α_z (Figure 4.19c.4-6). This results in a large region of CCW vorticity in the near wake when the model is at its peak in +α_z, and a symmetric large region of CW vorticity when the model is at its peak in -α_z.

As mentioned in §**4.1**, the flow control alteration of the model-wake coupling is analyzed through measuring the contribution of the newly developed, 'steady' actuation-controlled wakes in Figure 4.19 to the yawing moment of the model. This is done in an analogous fashion as implemented in the baseline flow (discussed with Equations 4.6-4.9 and Figure 4.6). Figures 4.20a-c show the time variation of $d\widehat{M}_{xyz}$ throughout the spanwise coordinate at respective fixed streamwise locations of *x/D* = 1.8 for each of the three closed-loop control actuation schemes (to be compared with Figure 4.6a in the baseline). The respective $d\widehat{M}_{xyz}$ is integrated in the spanwise direction, yielding $d\widehat{M}_{xz}$, and is shown in Figure 4.20d-f (to be compared with Figure 4.6c in the baseline). Figures 4.20a and d show the α_z = 0° control, 4.20b and e show α_z = 2° control, and 4.20c and f show the amplification control. Clearly, the α_z = 0° control shows the shear layer deflection amplitude is greatly reduced from the baseline flow, with the jet activations in the cycle vectoring the shear layer towards center (the right jet is active from ~0.25-0.75$\tau_{z\text{-}0^o}$, with the left jet active for the other half cycle). This same trend is seen in Figure 4.20b, with the roughly invariant shear layer behind the left jet and the variations in the shear layer behind the right jet caused by its activation, and both shear layers are shifted in the +*y*

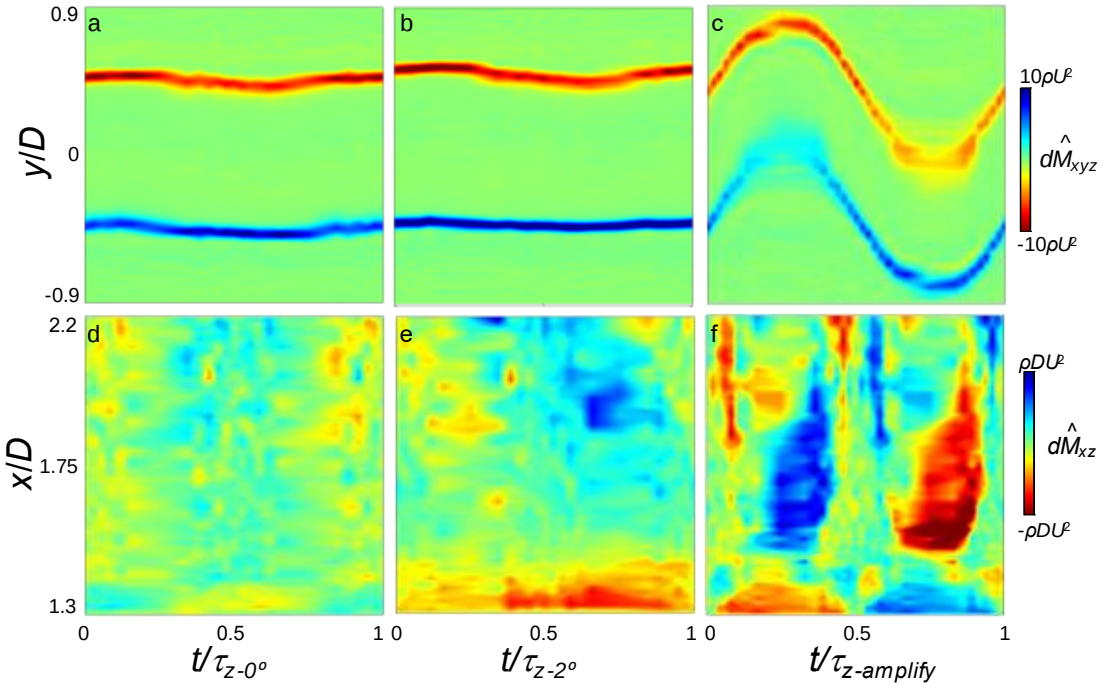

Figure 4.20. Color raster plots of the $d\widehat{M}_{xyz}$ (y, t, x = 1.8D) in the meridional x-y measurement domain (cf., Figure 4.19) (in a-c), and of $d\widehat{M}_{xz}$ (x, t) (c) in the presence of closed-loop control corresponding to Figures 4.16 (in a and d), 4.17 (in b and e), and 4.18 (in c and f).

direction (around its new α_z = 2° state). The amplification control shows a significant increase in the shear layer deflection from y/D ~±0.65 in the baseline (Figure 6a) to y/D ~ ±0.8 (Figure 4.20c) at x/D = 1.8. Once integrated in the spanwise direction, $d\widehat{M}_{xz}$ in the baseline flow (Figure 4.6c) showed there were two distinct regions in the wake (a boundary layer at x/D < 1.35, and a far wake effect at x/D > 1.85), which are also apparent in Figure 4.20d-f. For suppression around 0° (Figure 4.20d), both the contribution of the near wake and far wake to the yawing moment are effectively suppressed by the jet activation, and the wake does not appear to contribute any moment on the model. This is significant because it is commensurate with the model remaining at center, as the wake does not force it to move on the phase average. When the model is held offset (Figure 4.20e), the far wake has a notable moment fluctuation that induces a dominant positive moment contribution from $t/\tau_{2°}$ = 0.4-0.9, which is slightly delayed from the jet actuation of

$t/\tau_{2^\circ} \sim 0.25\text{-}0.75$, which is also opposed by an increase in the negative moment contribution from the boundary layer at the same time. The change in the moment contributions in the wake between $\alpha_z = 0^\circ$ control (Figure 4.20d) and $\alpha_z = 2^\circ$ control (Figure 4.20e) also suggests that the the increase of α_{RMS} from 0.4° to 0.6° in the respective control cases might be due to two contributions of the wake that roughly cancel in the offset case, as opposed to a complete reduction of all moment contributions in the centered case. A dramatic change in moment contribution is observed in the amplification control in Figure 4.20f, which induces a large vorticity in the wake at a location closer to the model (further upstream) than in the baseline, starting at $x/D = 1.45$ rather than 1.85. In addition, this large region of vorticity appears to primarily oppose the model velocity with a large positive sense from $t/\tau_{z\text{-amplify}} = 0.25\text{-}0.5$, and in contrast, the boundary layer contribution opposes of the model attitude instead with a large positive contribution from $t/\tau_{z\text{-amplify}} = 0.5\text{-}1$. The conflicting times at which these contributions occur is commensurate with the large moment peaks that occurred in C_M vs. α_z in Figure 18f, as well as the increase in hysteresis, or phase lag, in the cyclic moment.

The outcomes of these three schemes of this closed-loop controller are assessed at various flow speeds ($0.57 < Re_D < 2.0 \cdot 10^5$), and the results are shown in Figure 4.21. The representative extracted parameters are the average induced steady state deflection angle of the model with one jet activated in closed-loop, ($\bar{\alpha}_z$), and the average steady state model oscillation amplitude with two jets activated in closed-loop ($\alpha_{RMS\text{-}act}$), for either amplification (red) or suppression (green). This is presented in the same fashion as the open loop actuation variation with flow speed in Figure 4.13, and each parameter is also normalized by $\alpha_{RMS\text{-}base}$. These results show that the model controlled maximum steady deflection angle (Figure 4.21a) increases linearly with flow speed (the same as the baseline oscillation) throughout all flow speeds investigated. The green trace in Figure 4.21b displays the $\alpha_{RMS\text{-}act}$ of the steady state $\alpha_z = 0^\circ$ control compared to the baseline. The

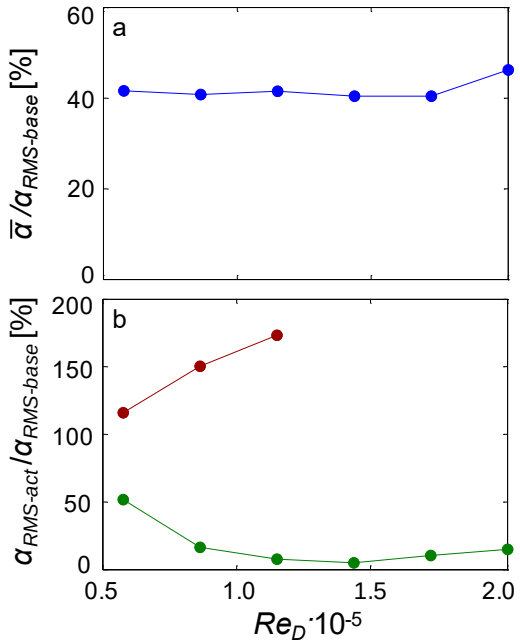

Figure 4.21. Variation with Re_D of the maximum attained stable offset angle (**blue**, a), and the RMS variations during closed-loop control about $\alpha_z = 0^\circ$ (**green**, b), and amplification around $\alpha_z = 0^\circ$ (**red**, c).

results show that the model is stabilized significantly at all flow speeds, increasing from a 50% suppression to a 95% suppression from $0.57 < Re_D \cdot 10^{-5} < 1.41$, as the jet-induced alterations of the shear layer appear to have a more pronounced effect at larger Re_D. However, when Re_D grows through $1.41 < Re_D \cdot 10^{-5} < 2.00$ the stabilization slightly weakens to 85%, and this is attributed to a lowered C_μ (from the same jet velocity and an increased free stream) that is insufficient for full stabilization (in the same fashion as $Re_D = 2.0 \cdot 10^5$ in Figure 4.13b), and this could be addressed by increasing the jet velocity. Consequently, there is a maximum reduction of the model oscillations of 95% at $Re_D = 1.43 \cdot 10^5$ under the present actuator constraints. The red line in Figure 4.21b shows the α_{RMS} of the amplification control, which has a monotonously growing amplification percentage throughout $0.57 < Re_D \cdot 10^{-5} < 1.14$ where higher Re_D excited α_z outside of the vibrometer range (~ ±15°), and therefore could not be recorded, although the trend suggests that the amplification could extend well past 200% at higher Re_D.

CHAPTER V

UNSTEADY MODEL-WAKE COUPLING IN BASIC MOTIONS

This chapter describes an investigation of the effects of varying the model's frequency of oscillations in 1-DOF through a range of 'quasi-steady' and 'highly unsteady' aerodynamic motions using the 6-DOF wire traverse (cf., Chapter **2.5**). The nomenclature for unsteady motion of an airfoil defined by Leishman (2006) is adopted for simplicity and is divided into three regimes based on the reduced frequency ($k = \pi cf/U_o$) namely 'quasi-steady', ($0 < k \leq 0.05$), 'unsteady' ($0.05 < k \leq 0.2$), and 'highly unsteady' ($k > 0.2$). The model's motions include pitch (or yaw, $\pm 3^{\circ}$, §**5.1**), vertical (or cross stream) plunge (±5 mm, §**5.2**), and streamwise displacement (§**5.3**).

5.1 Harmonic Pitching: Reduced Frequency Variations

This chapter characterizes the model aerodynamic response in terms of its aerodynamic loads (forces and moments), resolved through load cells on the 6-DOF traverse, as well as its wake structure (which is measured through both PIV and hotwire anemometry. This section investigates the model when it is harmonically pitching from $0 \leq k \leq 0.259$ in the near wake (and commensurate aerodynamic loads) in §***5.1.1***, and the far wake (and commensurate spatially-varying frequency response) in §***5.1.2***. The near wake spatial structure is characterized through PIV acquired directly downstream of the model aft end ($0 < x/D < 1.3$). Single-sensor hot wire anemometry is used for measurements of the temporal and spatial characteristics of the far-wake of the model. The hot wire sensor is placed five diameters downstream of the model (which is the same as in Chapter **III**, cf.,

Figure 2.1), and traversed using a two-stage low-profile computer controlled two-axis traverse.

5.1.1 Near-Wake Effects and Control

The harmonic pitching motion with an amplitude of $\alpha_y = \pm 3^\circ$ is presented in Figure 5.1, with the drag and lift force coefficients [Figure 5.1a-e and Figure 5-1f-j, $C = 8F/(\pi\rho D^2 U_o^2)$] as well as the pitching moment coefficient [Figure 5.1k-o, $C = 8M/(\pi\rho c D^2 U_o^2)$]. For reference, the coordinate system is chosen to be the same as in Chapter **III** (cf., Figure 3.1a). Figures 5.1a,f, and k show the a quasi-steady response at $f = 1$ Hz, (or a reduced frequency of $k = \pi fc/U_o = 0.013$), and the increased frequency to 5 Hz ($k = 0.065$, Figures 5.1b,g, and l), 10 Hz ($k = 0.130$, Figures 5.1c,h, and m), 15 Hz ($k = 0.194$, Figures 5.1d,i, and n), and 20 Hz ($k = 0.259$, Figures 5.1e,j, and o). For reference, the values of the C_D, C_L, and C_M for a static model at varying fixed angles of attack with the same geometry in Chapter **III** (cf., Figure 3.6) are superimposed in Figures 5.1a,f, and k. The baseline C_D vs α_y presented in Figure 5.1a has a quadratic shape with a minimum of $C_D = 0.24$ at $\alpha_y = 0$ and a change in magnitude of around 25% (0.24 to 0.3). As frequency is increased, the quadratic functionality in the drag with angle becomes broken and the cycle average drag increases to 0.29 at 15 Hz (Figures 5.1b-d), and then reduces to 0.28 at 20 Hz (Figure 5.1e). The shedding frequency of this model is expected to be around 100 Hz ($St_D = fD/U_o$ was measured to be ~ 0.2, for a similar axisymmetric body by Rigas et al., 2014), and the high frequency variations in C_D (as well as C_L and C_M) that are not present in the quasi-steady results are at frequencies of harmonics of the model motion near this shedding frequency. The baseline steady C_L vs. α_y presented in Figure 5.1f is quasi-linear with a slight hysteresis and a lift slope of $C_L/\alpha_y \sim 0.05$/deg. Upon increasing the pitching frequency to 10 Hz (Figures 5.1g and h), the hysteresis in the lift coefficient increases while the average lift slope remains similar, and at higher frequencies this slope diminishes to 0.03/deg and 0.025/deg at 15 Hz and 20 Hz, respectively (see Figures 5.1i and j). The tendency of the

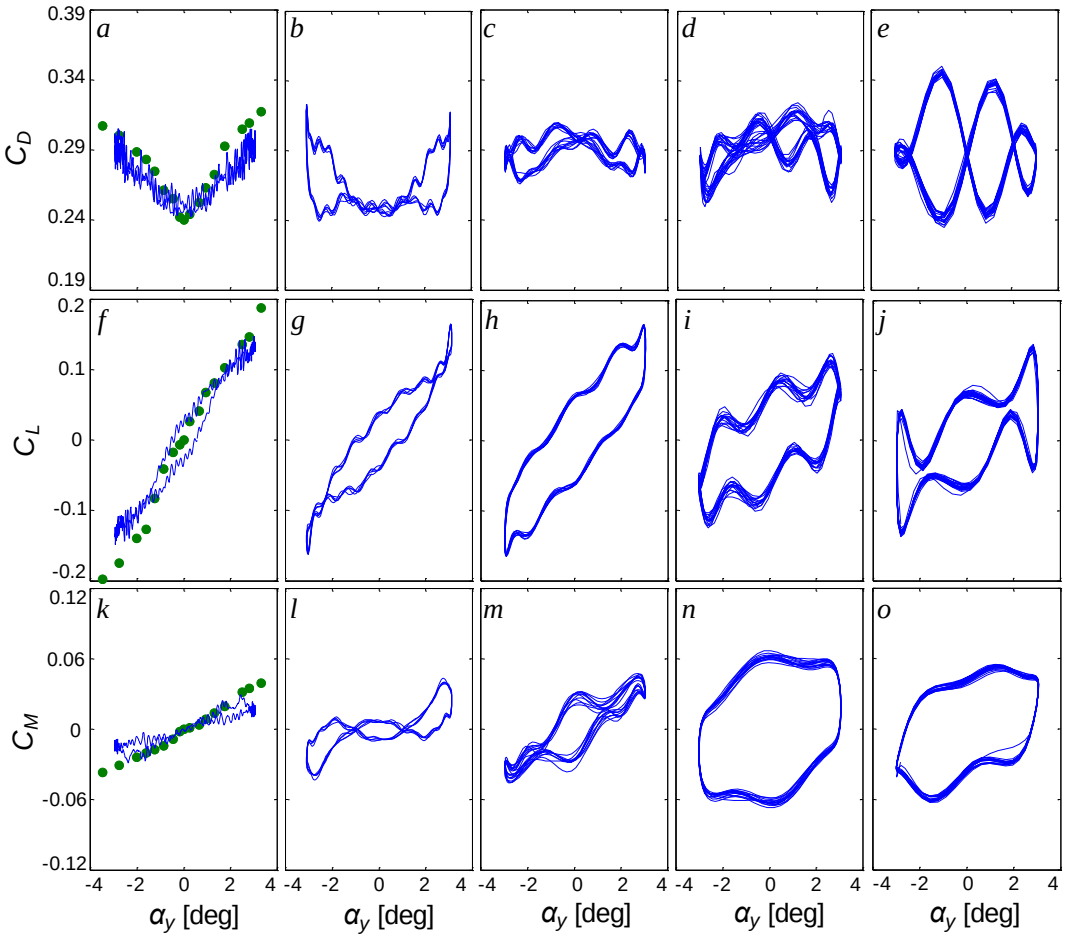

Figure 5.1. Drag (a-e), lift (f-j), and pitch (k-o) coefficients with pitching angle for the axisymmetric model with simple harmonic pitching at an amplitude of $\alpha_y = \pm 3^\circ$ at reduced frequencies of k = 0.013 (1 Hz) (a,f,k), 0.065 (5 Hz) (b,g,l), 0.130 (10 Hz) (c,h,m), 0.194 (15 Hz) (d,i,n), and 0.259 (20 Hz) (e,j,o) over a time interval of $450\tau_{conv}$ (1 second) using 100 phase averages. The drag, lift, and pitch coefficients measured on the same model geometry at static angles (●) in Chapter **III** (cf., Figure 3.6) are shown for reference.

C_L (and C_M) hysteresis to increase with frequency is attributed to unsteady effects of the flow (the magnitude of the wake response time remains roughly similar as the model cycle time decreases). The quasi-steady C_M is shown in Figure 5.1k, with an increasing slope C_M/α_y with frequency from 0.005/deg at 1 Hz to 0.01/deg at 20 Hz, with a large increase in the hysteresis of the response at higher frequencies (Figures 5.1l-o). This 'average slope' is defined as the slope of a linear fit through the dataset and does not take in account variations due to the hysteresis. In addition, having a positive average slope of C_M with

α_y implies that the model is unstable in pitch (the moment increases with an increase in the pitching angle), as expected.

The effects of open-loop continuous actuation during the pitching cycle by either one jet or both jets on the model as it pitches are investigated in Figure 5.2 (with the 'top' or the 'top' and 'bottom' jets as labeled Figure 2.1, respectively). The baseline measurements are shown in black, for reference, with single jet actuation shown in blue, both jet actuation shown in cyan, and the representative frequencies are chosen to be $k = 0.013$ ('quasi-steady', Figures 5.2a and d), 0.13 ('unsteady', Figures 5.2b and e) and 0.259 ('highly unsteady', Figures 5.2d and f), with C_L (Figures 5.2a-c) and C_M (Figures 5.2d-f). C_D does not change significantly with actuation throughout a pitch cycle from the baseline

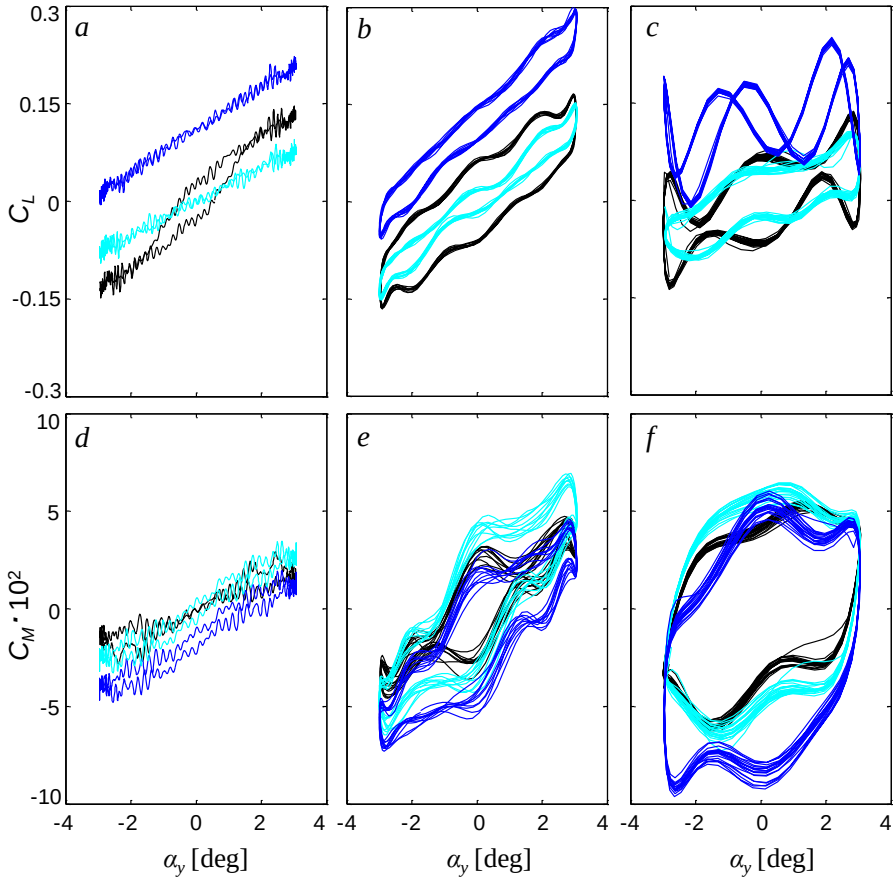

Figure 5.2. Lift (a-c) and pitching (d-f) coefficients for open-loop continuous activation of one (**blue**) and both (**cyan**) jets at $C_\mu = 4 \cdot 10^{-3}$ and $k = 0.013$ (a,d), 0.130 (b,e), and 0.259 (c,f) over a time interval of $450\tau_{conv}$ using 100 phase averages. The non-actuated cases are shown in black lines.

($\Delta C_D < 0.01$), presented in Figures 5.1a-e, and is omitted. For the representative steady top jet actuation, the C_L/α_y slope decreases to 0.03/deg, and becomes deflected by about $\Delta C_L = 0.1$ at $\alpha_y = 0$, while upon both jet actuation, the C_L/α_y slope diminishes to 0.025/deg (Figure 5.2a). The cyclic hysteresis is suppressed with both actuations, with no noticeable difference in forces in the upstroke and the downstroke. The steady C_M is shown in Figure 5.2d, has an increasing slope C_M/α_y from baseline to both jets actuated to single jet actuated of 0.005 to 0.008 to 0.010, respectively, with the top jet being centered around $C_M = -0.015$. Figures 5.2b and c show a growth of hysteresis in C_L which are unsteady effects caused due to the decrease of the model time scale when the wake reactive time scale remains the same, and in addition, the shedding frequency is excited at higher frequencies. The lift slope does not change significantly with applied actuation, but the coupling to the shedding frequency harmonics decreases with both jet actuation and increases with top jet actuation (with a magnitude change of around 50% at $k = 0.259$ in Figure 5.2c). A similar increase in hysteresis and excitation of the wake shedding frequency is found in the unsteady C_M (Figures 5.2e and f), with an additional growth in the moment slope with angle of attack (as mentioned in the discussion of Figure 5.1k-o). Unlike the steady moment in Figure 5.2d, this slope appears to be approximately unaltered with application of continuous actuation.

Next, timed open loop actuation is applied to the model in order to suppress or augment the lift force. This control was designed from the results found in Chapter **III** for quasi-steady pitching (cf., Figure 3.13), but also includes a phase offset to compensate for any unsteady aerodynamic effects (this is discussed in further detail in Appendix **B.2**). The results of the lift force augmentation and suppression control schemes are shown in Figure 5.3 in red and green, respectively, with the baseline response overlaid in black, as a reference. These will be referred to as ‘suppression’ and ‘augmentation’ actuations, which are intended to minimize and maximize the variation in the cyclic lift coefficient, respectively. Figure 5.3 shows the application of these actuation modulations at a

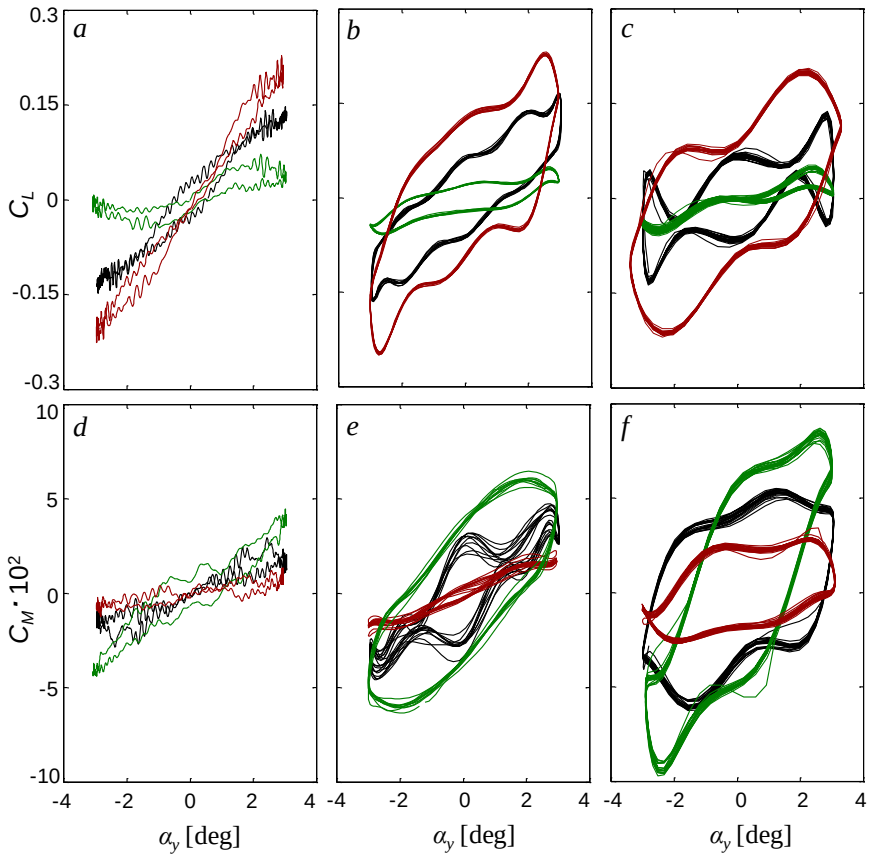

Figure 5.3. Lift (a-c) and pitching (d-f) coefficients for lift force suppression actuation (**green**) and lift force augmentation actuation (**red**) with maximum $C_\mu = 4 \cdot 10^{-3}$ for the same conditions as in Figure 5.2.

representative quasi-steady $k = 0.013$ (Figure 5.3a and d), and unsteady $k = 0.259$ (Figure 5.3d and h), and an intermediate unsteady frequency of $k = 0.130$ (Figure 5.3b and e) with the responses in C_L vs. α_y (Figure 5.3a-c), and C_M vs. α_y (Figure 5.3d-f). The baseline cases are shown in black and are the same baselines as shown in Figures 5.1 and 5.2, and the application of the suppression and augmentation actuations are shown in green and red, respectively. The maximum C_L in Figure 5.3a is suppressed to 0.05 or augmented to 0.20 from its baseline value of 0.13, leading to a 60% decrease or a 45% increase in the lift peaks. The respective case of C_M vs. α_y in Figure 5.3e shows a 30% increase or 65% decrease in C_M with C_L suppression or augmentation actuation, respectively, which can be utilized for model steering and stabilization. The resulting suppression and augmentation

effects remain significant at the unsteady $k = 0.259$ (Figures 5.3d and h), with induced changes on C_L of a 100% increase and a 45% decrease, with the respective changes on C_M of a 30% decrease and a 20% increase. The intermediate lift and moment coefficients for $k = 0.130$ (Figures 5.3c and g, respectively) show C_L suppression of 60%, and augmentations of 30%, with respective C_M augmentation of 25% and suppression of 40%, showing the jets have control authority for C_L suppression and augmentation throughout the full range of reduced frequencies tested.

To further understand the time varying 'low' frequency wake dynamics of both the controlled and uncontrolled flows, the time development of streamwise velocity, U_x, cross-stream velocity, U_z, and the planar vorticity, ζ_y in the wake behind the model is assessed. These quantities are characterized in the same interrogation window as in Chapter **III** of ($0 < x/D < 1.3$) but are extracted at a representative fixed downstream distance of $x/D = 0.5$ behind the model aft end to analyze their temporal variation for $0 < t/\tau_z < 1$ where τ_z is the time of one pitching cycle ($\tau_z = 1$s when $k = 0.013$ and $\tau_z = 0.05$s when $k = 0.259$). This data is taken with 12 phases per cycle and is presented as the phase averaged wake vectors, $\widehat{U}_x$, $\widehat{U}_z$, and $\widehat{\zeta}_y$. Figure 5.4a shows the development of the $\widehat{U}_x$ when there is no actuation present, and shows an in-phase sinusoidal wake deficit response to the sinusoidal pitch cycle. The $\widehat{U}_z$ component of the wake velocity is shown in Figure 5.4d, where $\widehat{U}_z$ is mostly downward for $t/\tau_z < 0.5$, corresponding to the wake following the model and being vectored downward when $\alpha_y > 0$, and mostly positive for $t/\tau_z > 0.5$, which corresponds to the wake being vectored by the model upward when $\alpha_y < 0$. Figure 5.4g shows the development of $\widehat{\zeta}_y$ for the baseline flow, which shows the two predominant shedding regions (or shear layers), as expected, and also follows an in-phase sinusoidal path similar to the wake deficit. Upon lift suppression actuation, the wake variation in $\widehat{U}_x$ decreases significantly throughout the cycle from the baseline, as shown in Figure 5.4b, and conversely, the wake variation in $\widehat{U}_x$ increases significantly with the augmentation

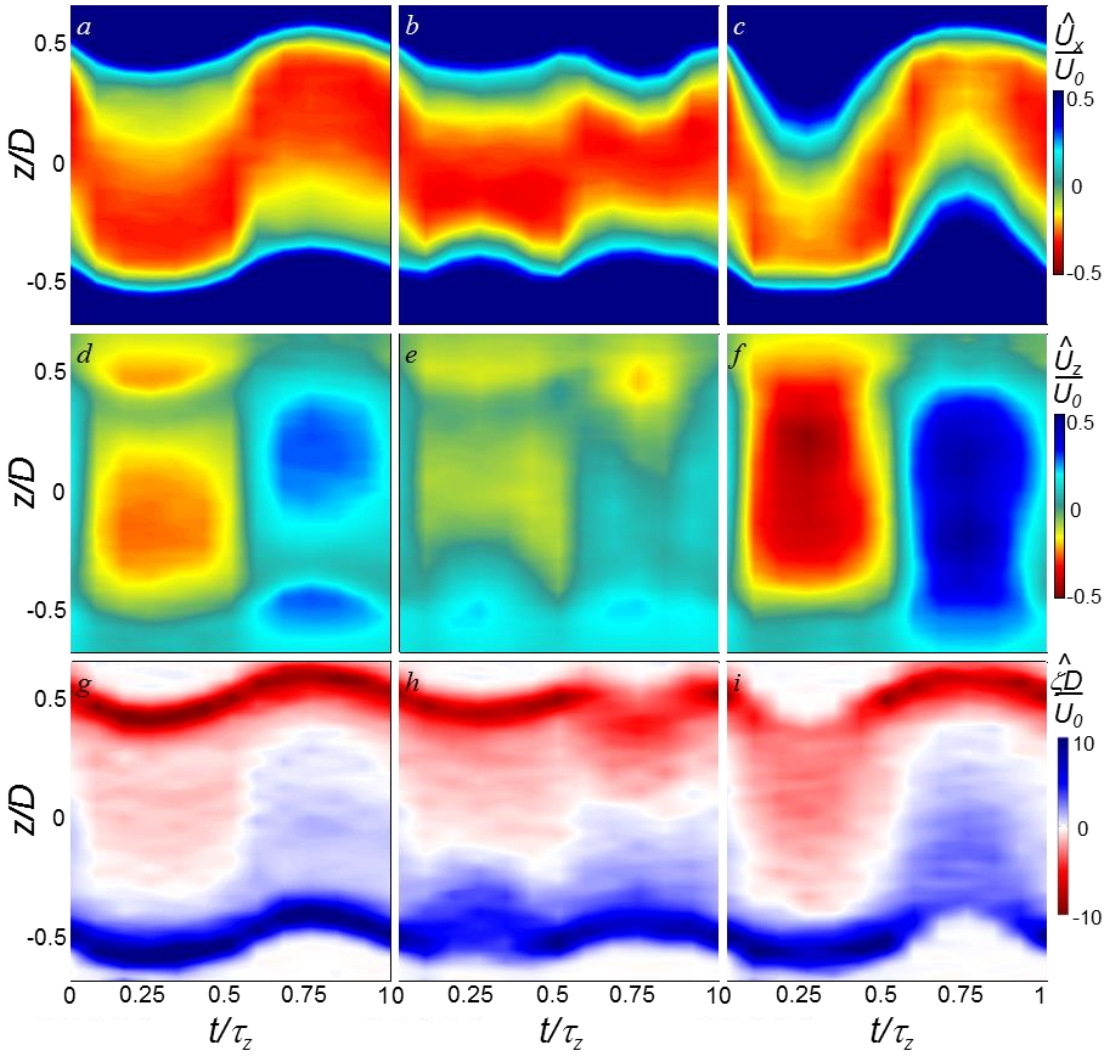

Figure 5.4. Time development of streamwise, $\hat{U}_x$ (a-c), and cross-stream, $\hat{U}_z$ (d-f), velocities and azimuthal vorticity, $\hat{\zeta}_y$ (g-i) at a streamwise location of $x/D = 0.5$ from the model aft end for $\alpha_y = \pm 3^\circ$ sinusoidal pitch at reduced frequency of $k = 0.013$, without actuation (a,d,g), and for the force cancellation (b,e,h) and augmentation (c,f,i).

actuation, as shown in Figure 5.4c. There is a different effect in the vertical direction, where lift force suppression (Figure 5.4e) causes the magnitude of the $\hat{U}_z$ to decrease significantly across the wake throughout all times, and the augmentation (Figure 5.4f) enhances the $\hat{U}_z$ development seen in Figure 5.4d. The response of $\hat{\zeta}_y$ to suppression is shown in Figure 5.4h, with a growth in the area of the shear layer upon actuation, with the bottom actuator present for $t/\tau_z < 0.5$ and the top actuator present for the other half of the cycle. There is also a notable decrease in the deviation of the zero level of $\hat{\zeta}_y$ with time in

Figure 5.4h, which may be commensurate with the decreased force measured in Figures 5.1-5.3 (i.e., the wake becomes more symmetric and the deviations in forces cancel). The $\hat{\zeta}_y$ response to lift augmentation instead involves a strong vectoring and spreading of the shear layer and an increase in the $\hat{\zeta}_y$ found in the wake, as shown in Figure 5.4i.

A detailed investigation analogous to Figure 5.4 is done for the representative 'highly unsteady' frequency, or k = 0.259 to gain a better understanding of the unsteady actuation effects and analyze their similarities and differences to the 'quasi-steady' frequency case. Figure 5.5 shows the time development of $\widehat{U}_x$ (Figure 5.5a-c), $\widehat{U}_z$ (Figure 5.5d-f), and $\hat{\zeta}_y$ (Figure 5.5g-i) for k = 0.259 (τ_z = 0.05 s). Figure 5.5a shows a temporal development of $\widehat{U}_x$ when there is no actuation present, where the wake deficit responds as a similar harmonic response to the steady frequency, with a smaller magnitude and a ~45° phase lag behind the pitching angle (compare Figure 5.5a and Figure 5.4a). The commensurate cross-stream baseline (Figure 5.4d) shows a different structure than what was observed in the lower frequency case in Figure 5.4d, where the magnitude of the cross-stream velocity diminishes by about 40%. However, there is still a similarity in both the steady and unsteady flows that $\widehat{U}_z$ is mostly negative when $\widehat{U}_x$ is deflected downward, and vice versa, showing the cross-stream velocity has the same ~45° phase lag from the steady case. The baseline $\hat{\zeta}_y$ development over the pitching cycle is shown in Figure 5.5c, which has a similar fluctuation to low frequency pitching, with a similar amplitude attenuation and phase delay observed in the streamwise wake deficit. Upon lift suppression actuation, the wake variation in $\widehat{U}_x$ decreases significantly throughout the cycle from the baseline, as shown in Figure 5.5b, and conversely, the wake variation in $\widehat{U}_x$ increases significantly with the augmentation actuation, as shown in Figure 5.5c, in the same fashion as k = 0.013 (compare Figures 5.5a-c with Figures 5.4a-c). At this 'high' frequency oscillation, there is a smaller effect in the vertical direction, compared to the low frequency, where force suppression (Figure 5.5e) does not change the magnitude of $\widehat{U}_z$ but instead slightly delays

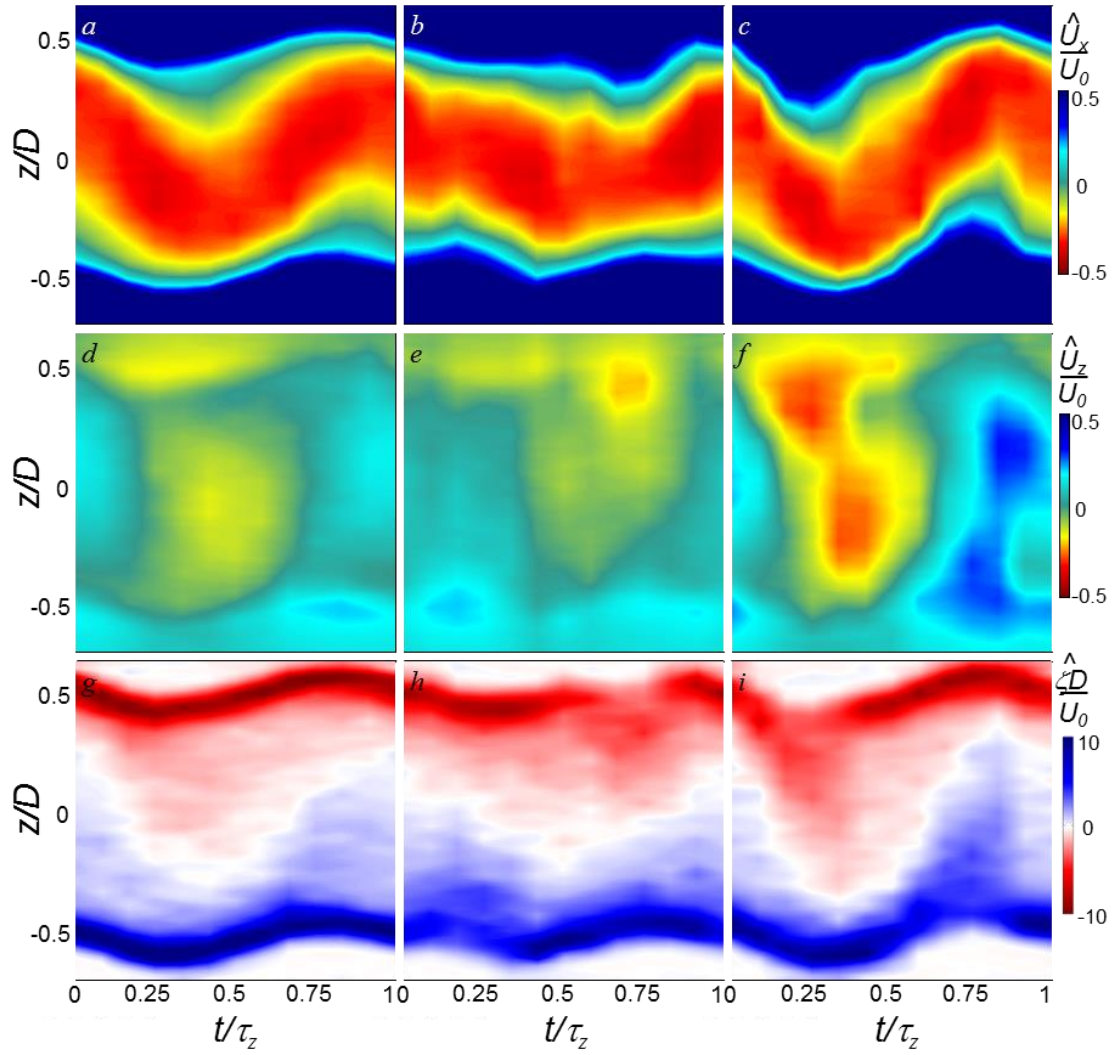

Figure 5.5. Wake data presented in the same fashion as Figure 5.4 with an unsteady reduced pitching frequency, $k = 0.259$.

its development in time. However, the augmentation (Figure 20f) dominates the baseline cross-stream development seen in Figure 5.5d, and causes a cross-stream fluctuation about four times in magnitude compared to the baseline fluctuation. The response of the planar vorticity to C_L vs. α_y suppression is shown in Figure 5.5h, which manipulates the sense of $\hat{\zeta}_y$ such that the region of zero $\hat{\zeta}_y$ remains close to the centerline. Comparing Figure 5.5h to Figure 5.4h, the change in the line of zero $\hat{\zeta}_y$ is fundamentally similar, as is the response to augmentation actuation (compare Figure 5.5h to 5.4h). It is interesting that the zero

level of vorticity trace in the near wake compares favorably to the lift force suppression and augmentation traces measured with the load cells in both the quasi-steady and heavily unsteady aerodynamic frequencies (compare Figure 5.5g-i with Figure 5.3c and Figure 5.4g-i with Figure 5.3a) This suggests that a force contribution analysis from the wake (similar to what was attempted in Chapter **IV**) may show this wake measurement contains relevant information to determine how (spatially and temporally) actuation effects the model aerodynamic loads in a fixed trajectory.

5.1.2 Far-Wake Effects and Control

This section investigates the far wake behind the model to quantify the actuation effect on the wake structure after it is no longer in the vicinity of the actuators. The data in this section are documented at $x/D = 5$ using single-sensor hot wire measurements (sampled at 10 kHz) over a grid of 19 x 19 equally-spaced measurement points within the domain $-1 < z/D,\ y/D < 1$. It is pointed out that these hotwire measurements resolve the planar velocity magnitude, q, in the x and z directions (as the hot-wire is aligned in the y direction and cannot distinguish between x and z velocity components), which is expected to have a structure mostly dominated by the wake deficit streamwise component. Figure 5.6 shows color raster plots of the magnitude of the normalized velocity, q/U_o at $U_o = 40$m/s for a stationary model aligned with the flow. The time-averaged velocity distribution in Figure

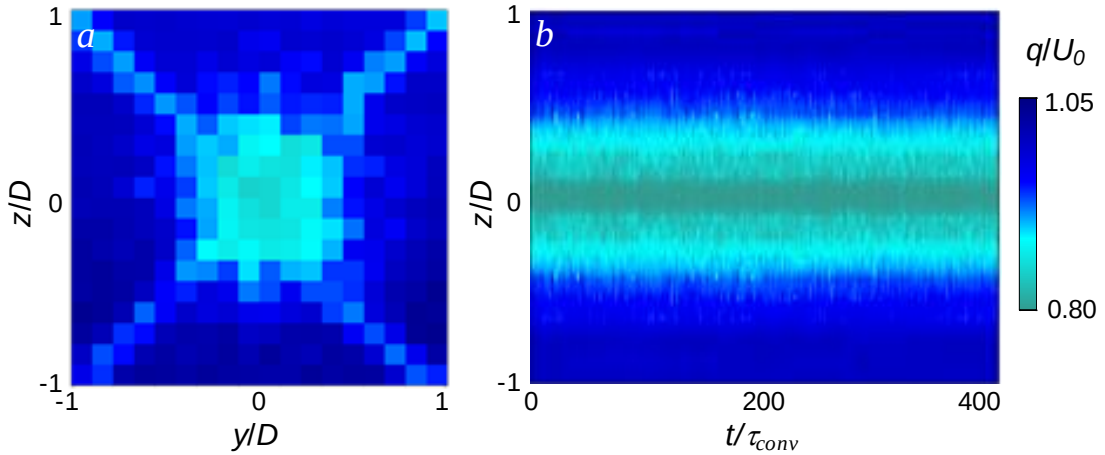

Figure 5.6. Raster plots of the ($x/D = 5$) time averaged (a) and the ($x/D = 5$, $y/D = 0$) time-resolved (b) planar velocity magnitude q in the wake of the model at $Re_D = 2.3 \cdot 10^5$.

5.6a illustrates the radial extent of the far wake (the wake of the support wires is also sensed at this streamwise location which is approximately 900 wire diameters downstream). The measurement of the drag force on the traverse showed that the measured aerodynamic drag is within 5% of the expected drag when the estimated drag of the support wires is accounted for, indicating a negligible coupling. A continuous record of the time-resolved velocity magnitude $q(z; x = 5D, y = 0)$ across the wake center plane ($y/D = 0$) is shown for reference in Figure 5.6b for $0 < t/\tau_{conv} < 400$ ($\tau_{conv} = c/U_o$), and demonstrates that the wake width based on (say) $0.92U_o$ is approximately $0.9D$.

The corresponding power spectra of the velocity magnitude (Figure 5.6b) is shown in Figure 5.7 over a range of $2.25 \cdot 10^{-3} < St_D = fU_o/D < 2.25$. These spectra exhibit two notable spectral features. First, a spectral peak $St_D = 0.237$ is present at the edge of the wake ($z/D = 0.5$) and is attributed to shedding at the dominant wake mode $m = \pm 1$ (the measurements of Rigas et al. (2014) showed that this peak is just above $St_D = 0.2$). A second, low-frequency ($St_D = 2.25 \cdot 10^{-3}$) broad spectral peak is also detected near the edge of the wake ($z/D = 0.5$). As shown by Rigas et al. (2014) this spectral peak is associated with slow ($St_D \approx 0.002$) axis switching of the dominant shedding mode $m = \pm 1$. This spectral map shows not only the dominant frequencies of the base flow, but also indicate spatial bounds (within the measurement plane) of their amplification, which are inherently

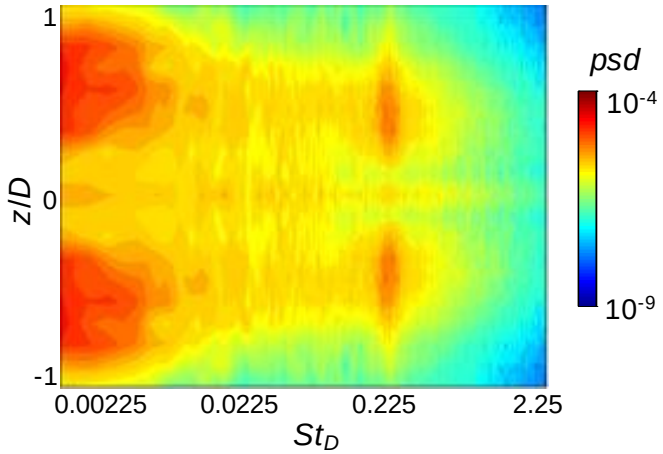

Figure 5.7. Raster plots of the power spectra of the planar vertical centerline velocity measured in Figure 5.6b.

linked to the flow stability features. The radial extent of the wake is also evident in these spectra as the power over the entire frequency range drops sharply beyond $z/D > 0.75$. In addition, the power at all frequencies also diminishes around the centerline of the wake ($z/D < 0.15$) indicating the absence (or diminution) of the mode $m = 0$.

The variation of the frequency and magnitude of the peak spectral component $m = \pm 1$ over a range of Re_D ($1.44 \cdot 10^5 < Re_D < 2.31 \cdot 10^5$) are shown in in Figures 5.8a and b. These figures show the frequency and magnitude of these spectral peaks along two orthogonal

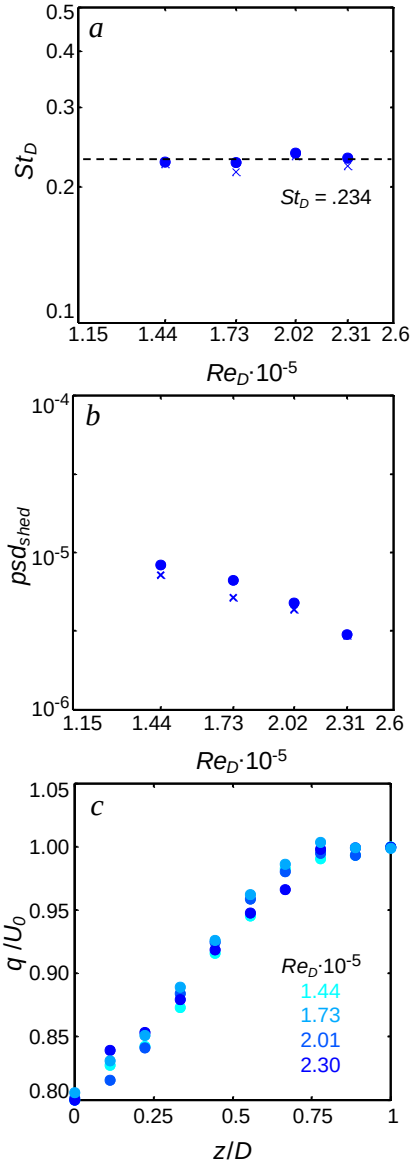

Figure 5.8. Shedding peak Strouhal number (a) and power magnitude (b) with Re_D, and time averaged planar velocity magnitude profiles (c) along the vertical (●) and horizontal (x) centerline at $x/D = 5$ with $Re_D = 1.44 – 2.31 \cdot 10^5$.

axes ($z = 0$ and $y = 0$) through the centerline of the model. The spectral maps for $1.44 \cdot 10^5 < Re_D < 2.31 \cdot 10^5$ (not shown) also show that these peaks are nominally centered near the edge of the wake at ($y/D \approx 0.5$, $z = 0$) and ($y = 0$, $z/D \approx 0.6$) indicates that the time-averaged signature of $m = \pm 1$ is indeed axisymmetric. Furthermore, Figures 5.8a and b show that the dimensionless frequency of the dominant mode ($St_D \approx 0.23$) is nearly invariant with Re_D over this range, and although the magnitude of this spectral component diminishes with increasing Re_D, (ostensibly owing to the increase in the overall spectral content with Re_D and broadening of the dominant peaks), the symmetry of this spectral component is quite good. Figure 5.8c shows that within the resolution of the present measurements, the (normalized) cross-stream velocity distribution, and, in particular, of the velocity deficit in the wake are quite similar over the range of Re_D. The maximum velocity deficit on the centerline is about 20% of the free stream velocity, while the edge of the wake (based on $q/U_o = 0.99$) is at $z/D = 0.75$.

Prior to assessing the dynamic flow control effects, the continuous flow control is characterized for the static centered axisymmetric model. The resulting near wake flow field is measured with planar PIV (U_x and U_z components), and the respective far wake is resolved with hotwire anemometry. Figure 5.9 shows time-averaged (over 400 model convective time scales, $\tau_{conv} = c/U_o$) color raster plots of the normalized planar velocity magnitude, q/U_o, where $q = (U_x{}^2 + U_z{}^2)^{0.5}$, and is presented in the cross-stream (x-z) plane of the near-wake ($x/D = 0.5$, using PIV, in Figures 5.9a,c,e) and in the spanwise (y-z) plane of the far-wake ($x/D = 5$, using hot wire anemometry, in Fig 5.9b,d,f). The flow fields are presented in the absence of actuation (Figures 5.9a and b), and with continuous actuation using a single jet (the 'top' jet at +z, in Figures 5.9c and d) and a pair of opposing jets (the 'top' and 'bottom' jets, in Figures 5.9e and f). In the absence of actuation, (Figures 5.9a and d), the flow is reasonably symmetric about the body axis, where the near wake exhibits reversed flow within the domain $x/D < 1$. The corresponding distribution of the time-averaged velocity magnitude q/U_o (Figure 5.9b) shows that the overall cross-stream width

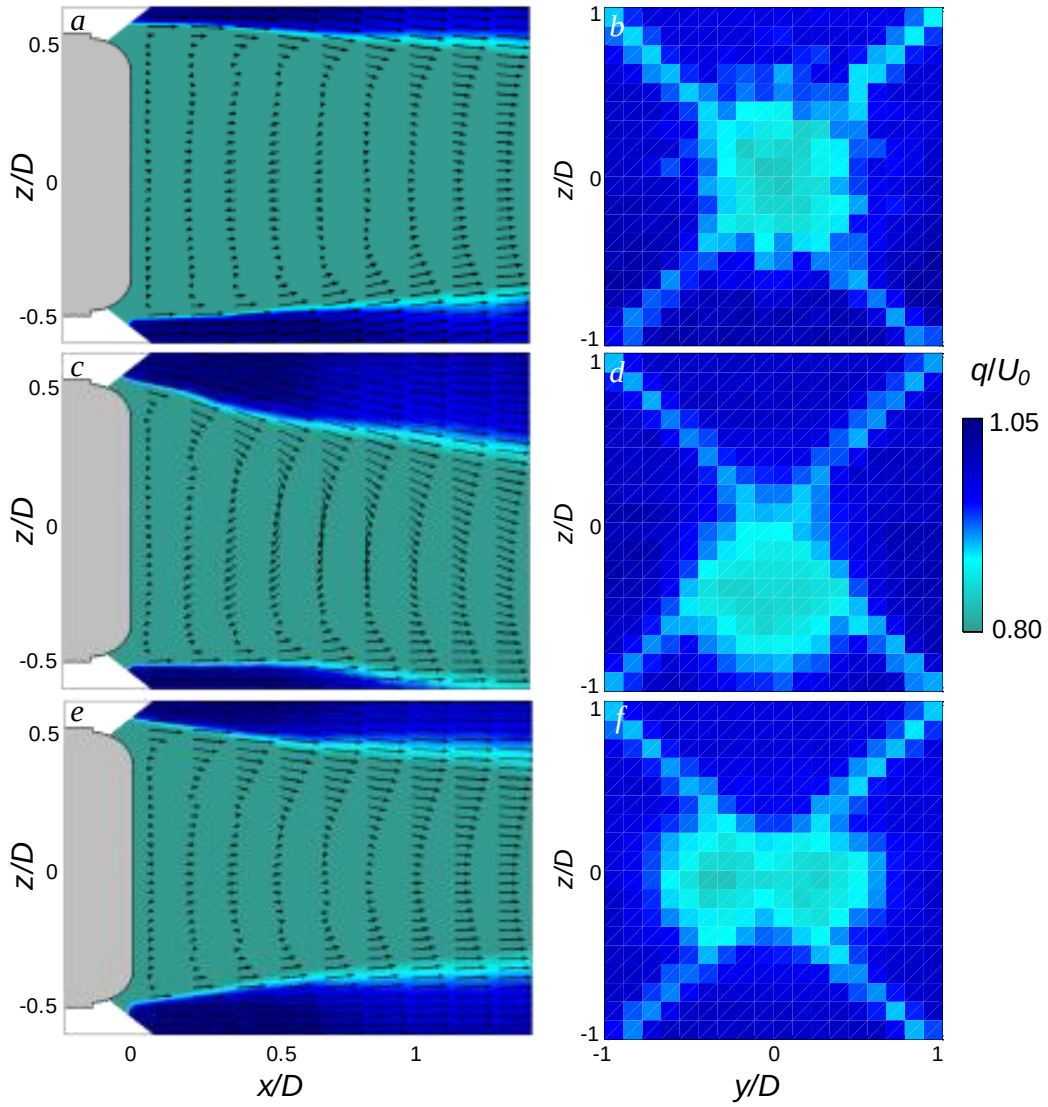

Figure 5.9. Raster plots of the planar velocity magnitude, q, for the wake behind a stationary model at $\alpha_y = 0$, for unactuated (a,b), and actuated flows by the top (c,d) and both (e,f) jets at $C_\mu = 4 \cdot 10^{-3}$, shown in the near wake centerline at $y/D = 0$ (a,c,e), and in the far wake cross-stream plane at $x/D = 5$ (b,d,f).

of the wake (based on $0.92U_o$) in the far field is narrower by about approximately 10%. When the top jet is activated ($C_\mu = 4 \cdot 10^{-3}$, Figures 5.9c) the upstream shear layer becomes partially attached to the Coanda surface and consequently, the flow along the top edge of the wake is deflected downwards at a nominal angle of 7.5°. The bottom edge of the near wake experiences less deflection and that the wake is primarily displaced downward without a significant change in its cross-stream width as is evident at the downstream edge

of the field of view (it also appears that the recirculating flow domain is shortened to $x/D < 0.9$). Figure 5.9d shows the respective deflection of the far wake. As expected, these data indicate that the deflection of the near field relaxes, and that the center of the wake is displaced vertically at a distance ($\Delta z/R \sim 0.7$) relative to the centerline of the model, but that the cross section of the wake becomes distorted. When the top and bottom jets are activated simultaneously (Figure 5.9e and f, $C_\mu = 4 \cdot 10^{-3}$) the near wake is nominally symmetric relative to the centerline, the reversed flow domain is reduced to $x/D < 0.75$, and the cross-stream width of the wake becomes narrower (by about 10% relative to the base flow at $x/D = 1.3$). The flow field in the y-z plane of the far field (Figure 5.9f) shows that the actuation leads to significant narrowing of the wake in the vertical (z) (by 30% relative to the far wake in the absence of actuation) and widening it in the horizontal (y) direction (by 40%) or increases its aspect ratio ($\Delta y/\Delta z$) to 1.33. As noted in Chapter **III**, actuation by the top jet leads to a lift increment of 0.6N ($\Delta C_L \sim 0.11$) with virtually no change in drag ($\Delta C_D \sim 0.01$), while the symmetric actuation by both the top and bottom jets results in a net increase of 0.1N in drag ($\Delta C_D = 0.02$).

The continuous actuation waveforms in Figures 5.9d and f are time-modulated to induce time dependent changes that couple to the evolution of the wake (and, consequently, in the induced aerodynamic loads on the model). This is implemented by activating the top and bottom jet pair so that they are operated out of phase during each half cycle of a time-harmonic modulating waveform (having modulation period τ_{mod}). The response of the wake clearly depends on the modulation frequency in a similar way to the dependence of the wake on pitch oscillations found in §***5.1.1***. Therefore, τ_{mod} for the *static* model is selected to be representative of quasi-steady, unsteady, and the (natural) vortex shedding pitch frequencies, where an effective k is defined off of the modulation frequency [$\pi c/(U_o \tau_{mod}) = k = 0.013$, 0.259, and 1.425, respectively]. The velocity magnitude in the far wake is measured phase-locked to the modulation waveform, and the maximum

deflection of the far wake owing to the top jet is shown in Figure 5.10 for each modulation frequency (the base flow in the absence of actuation is shown in Figure 5.10a for reference). When the modulation frequency is quasi-steady (k = 0.013, Figure 5.10b), the wake is deflected downwards, and has a similar structure to the wake that is actuated by the top jet only (cf., Figure 5.9d). When the modulation rate is increased to k = 0.259 (Figure 5.10c), it appears that the unsteady actuation begins to couple to the "natural" shedding frequencies of the model and the wake shows some evidence of such coupling that results in spanwise asymmetry of the far wake. In Figure 5.10d the modulation frequency is approximately the vortex shedding frequency (cf., predicted from Figure 5.7), which distorts the wake (the mode $m = \pm 1$ appears to be locked to the preferred direction of oscillations) and significantly increases the vertical deflection and the domain and magnitude of the velocity deficit.

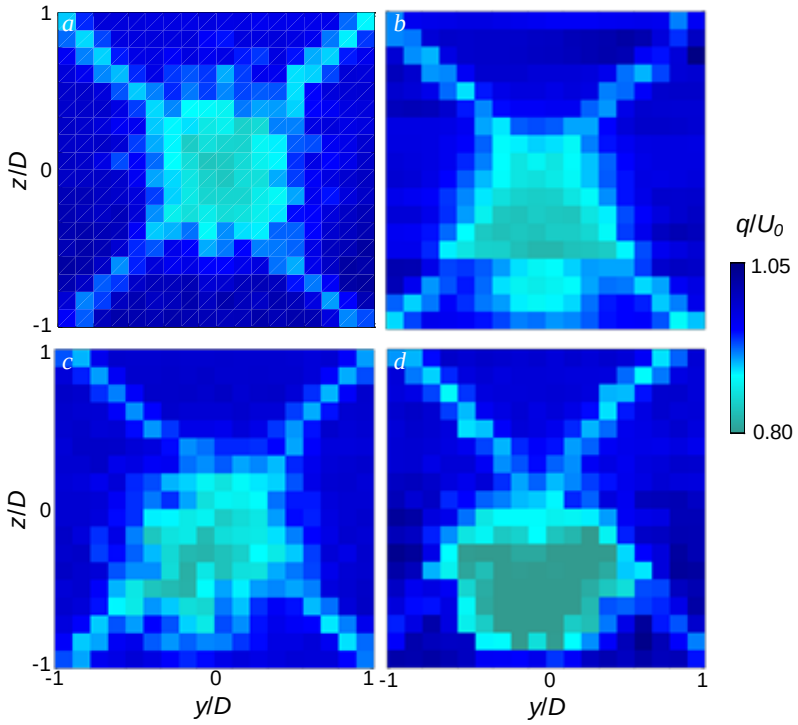

Figure 5.10. Raster plots of the peak deflection of the time averaged planar velocity magnitude, q, in the wake of the static model for unactuated (a), and sinusoidal modulation of the jets with a max $C_\mu = 4 \cdot 10^{-3}$ at an effective k = 0.013 (b), 0.259 (c), 1.425 (d).

To assess a 'far range' effect of the flow control schemes discussed in §***5.1.1***, a detailed time-resolved characterization of the wake cross-section is done by the hot-wire anemometry. Figure 5.11 shows raster plots of the normalized planar velocity magnitude, q/U_o in the far wake at $x/D = 5$ at the free stream $U_o = 40$m/s, analogous to the data presented in Figure 5b. Figures 5.11a-e show the vertical centerline of the far wake at $y/D = 0$, over a range of $z/D = 0$-1, and Figures 5.11f-j show the horizontal centerline at $z/R = 0$ over a range of $y/R = 0$-2. The results for the model pitching with quasi-steady reduced frequency $k = 0.013$ are shown in Figures 5.11c-e and 5.11h-j. For reference, the results for static and centered model are shown for an unactuated model in Figures 5.11a and f and the modulation actuated model in 5.11b and g. The force suppression and augmentation actuation schemes (Appendix **B.2**) are implemented in Figures 5.11d and i, and Figures 5.11e, and j, respectively. The unactuated pitching model is shown in Figures 5.11c and h. In comparison with the near wake, the evolved velocity profile in the far wake has only about 20% velocity deficit, as opposed to the recirculating bubble in the near wake (compare the magnitudes of the color bars Figure 5.11 and 5.4). The unactuated far-wake response in the vertical direction to the quasi-steady model motion in Figure 5.11c shows an analogous response to the respective near wake case (compare Figures 5.11c and 5.4a). The wake motion is in phase with the motion of the model aft end, with the major differences being the spread of the wake into the free stream ($\pm 0.57D$ in the near wake to $\pm 0.9D$ in the far wake), and the evolved velocity profile in the far wake with only about 20% velocity deficit, as opposed to the recirculation and stagnation region of the near wake. The unactuated/natural wake response shows that the horizontal centerline extent of the wake is maximized when the wake passes through the center (compare Figures 5.11c and h), which leads to the predominant effect of the velocity magnitude in the horizontal direction to have double the frequency of the pitching motion. Figures 5.9b and g show the actuators being activated on the *static* model to induce the aerodynamic equivalent to the dynamic motion-induced force. These results show effectiveness of the timed actuation

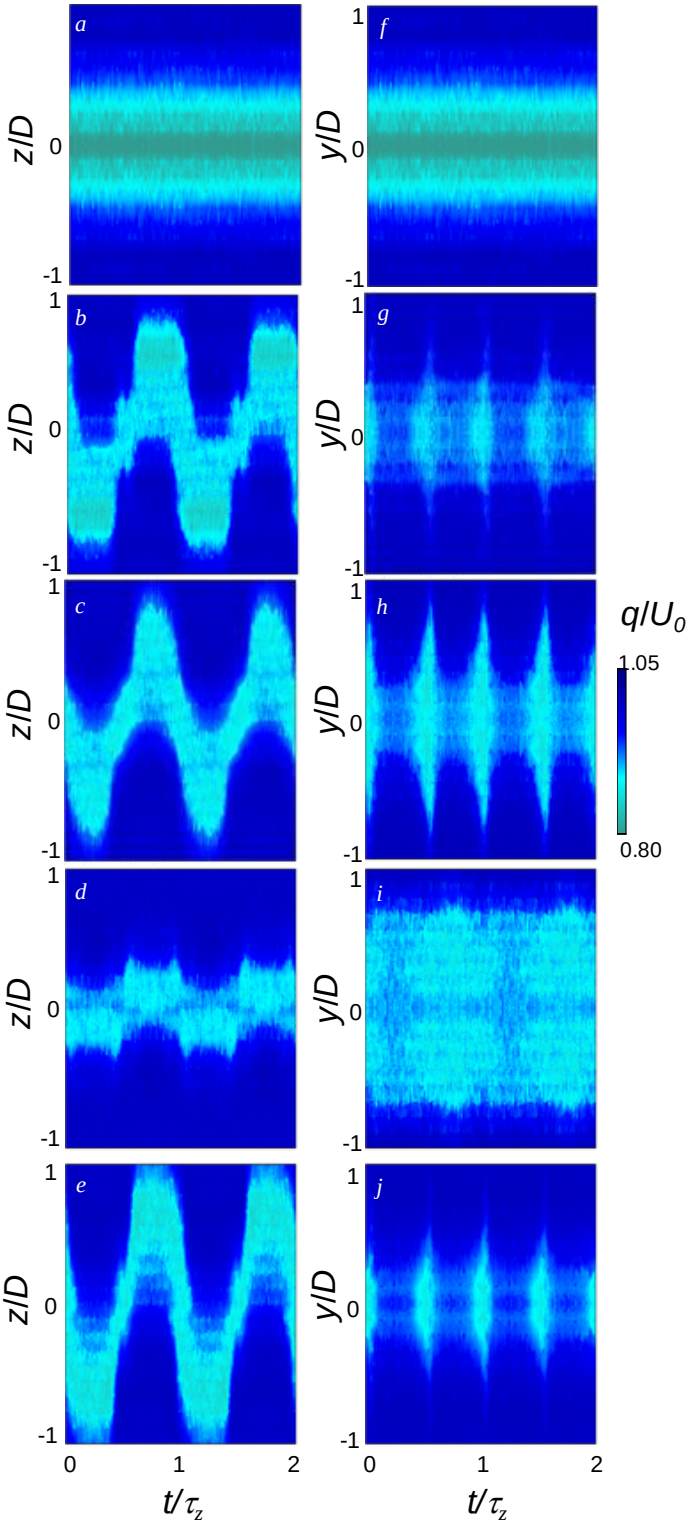

Figure 5.11. Raster plots of the phase-averaged planar velocity magnitudes, q, for the vertical centerline (a-e) and horizontal centerline (f-j) of the far wake behind a model at $x/D = 5$ when the model is stationary at $\alpha_y = 0$ and unactuated (a,f) or actuated to mimic the baseline pitch (b,g), as well as simple harmonic pitching at $\alpha_y = 3^\circ$ and $k = 0.013$ with unactuated (c,h), C_L suppression (d,i), and augmentation flow control (e,j).

in mimicking the wake response to the body motion. However, it is also seen that the sinusoidal modulation of the actuation induces a faster far wake response than sinusoidal modulation of the motion, leading the wake response to appear more like a square wave (seen in Figure 5.11b), and consequently the wake residence time in the central position becomes diminished (see Figure 5.11g). The realization of the force suppression actuation is seen in Figures 5.11d and i which shows the effective far wake decoupling from the model motion, exhibiting small velocity variations in the vertical (Figure 5.11d), and virtually no variations in the horizontal (Figure 5.11i) direction. Another feature is that this resultant wake becomes compressed in the vertical and stretched in the horizontal direction, which results in an elliptical cross section. Contrary to the suppression scenario, the force augmentation actuation scheme induces increased amplitude of the wake oscillation in the vertical direction, by about 20% of the unactuated motion, which leads to the wake area extension in the vertical direction (Figures 5.11c and e), accompanied by a decrease in the wake extent in the horizontal direction (compare Figures 15h and j).

The frequency response of the planar velocity magnitude responses shown in Figure 5.11 are presented in Figure 5.12 in analogous fashion to the power spectra shown previously in Figure 5.6 for the static model (which is placed in Figures 5.12a and f for completion). Each power spectrum in Figures 5.12a-j corresponds respectively to the flow conditions in Figure 5.11a-j. The unactuated response to the $k = 0.013$ sinusoidal pitching is shown in Figures 5.12c and h which still exhibit the two dominant frequency bands seen previously in the baseline spectra: the lower band which can be attributed to the axis switching of the dominant shedding mode, and the higher band associated with the vortex shedding. In addition, the superposed motion ($k = 0.013$) appears as bands at multiples of $St_D = 0.00225$ in the vertical direction (Figure 5.12c), and multiples of $St_D = 0.0045$ in the horizontal direction, and couples with the axis-switching mode. Figures 5.12b and g show a similar response when the model is held stationary and the force augmentation actuation

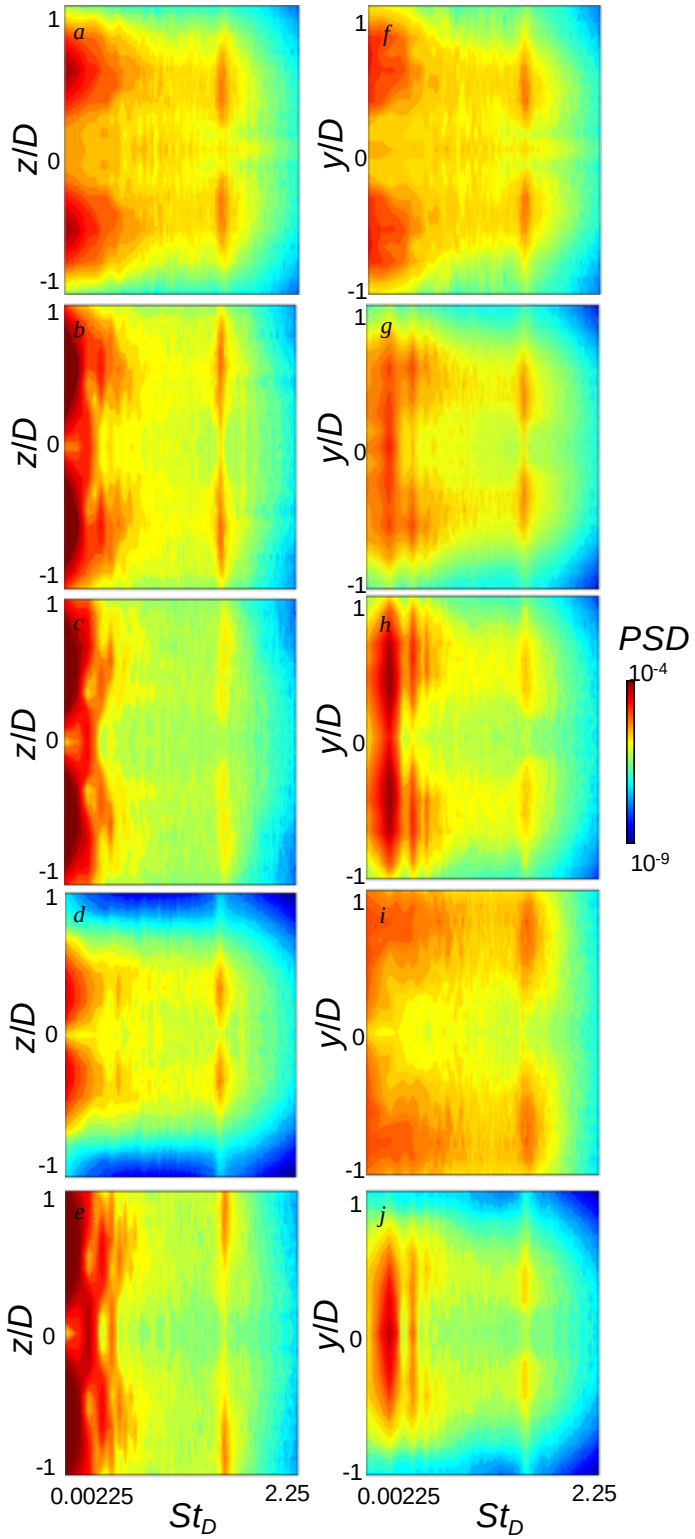

Figure 5.12. Raster plots of the respective power spectra of the $k = 0.013$ planar velocity magnitude, q, presented in Figure 5.10 for the (a-d) vertical centerline and the horizontal centerline (e-h) with the stationary model flow control (a,d), as well as the pitching model with unactuated (b,f), C_L suppression (c,g), and augmentation flow control (d,h).

is activated, with the exception that the actuation that mimics the model motion excites either the vortex shedding in the vertical direction more prominently than the actual model motion (Figures 5.12c and h). Upon the activation of suppression actuation, the power spectra become noticeably compressed in *z* (Figure 5.12d), and stretched in the *y* (Figure 5.12i) direction. This response has the frequencies attributed to the model motion and its harmonics effectively diminished, and the spectra becomes comparable to the baseline spectra compressed by ~75% in *z* and stretched by ~125% in *y* (compare Figures 5.12d and i with Figure 5.12a and f). The compression and expansion of the shedding frequency band is paired with the same alteration of the axis-switching frequencies. A different trend is seen upon force augmentation scenario, where the model motion and its harmonics are more prominent in their energy signatures, compared to the unactuated motion, but otherwise the augmented spectrum appears to be comparable to the unactuated frequency response stretched by ~125% in *z* and 75% in *y*.

Figure 5.13 presents the analogous unsteady wake investigations to the steady wakes shown in Figure 5.11. The unactuated far-wake response in the vertical direction to the quasi-steady model motion in Figure 5.13c shows an analogous response to the respective near wake case (compare Figure. 5.5a and 5.13c). The wake motion is recorded relative to the sinusoidal pitch of the model, and the measurement clearly shows a phase lag attributed to the unsteady aerodynamics. The respective cross-stream development is shown in Figure 5.13h, which shows the cross-stream extent stays at a similar level throughout the unsteady pitching cycle. Figures 5.13b and g show the actuators being activated on the *static* model to induce the aerodynamic equivalent to the dynamic motion-induced force in Figures 5.13c and h. These results show that the unsteady timed actuation mimics 60% of the wake response due to pitch, with a larger extent in the cross-stream direction. The realization of the lift suppression actuation is seen in Figures 5.13d and i and shows the effective far wake decoupling from the model motion, exhibiting a 55% vertical suppression (Figure 5.13c). Another feature is that this resultant wake becomes compressed in the vertical and

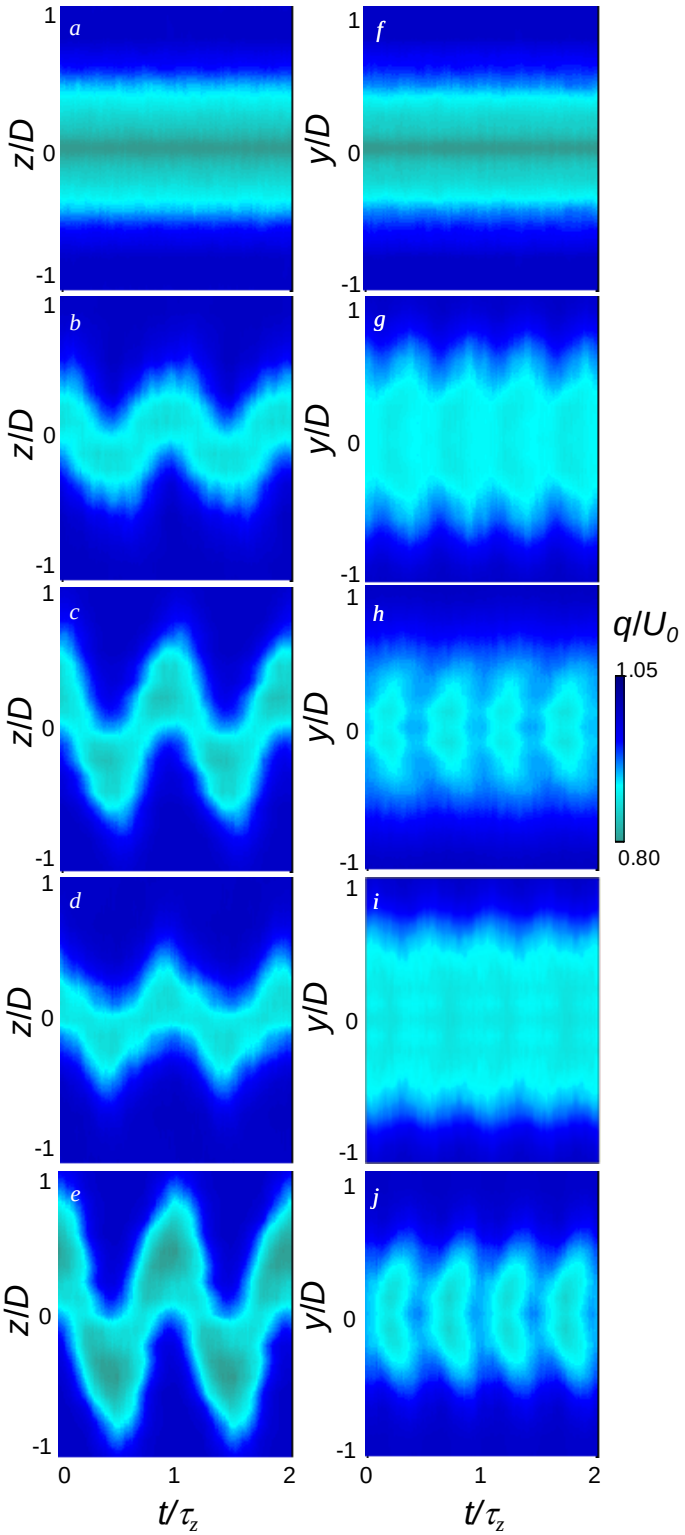

Figure 5.13. Synonymous unsteady measurement of the planar velocity measurements presented the same as Figure 5.11 for $k = 0.259$.

stretched in the horizontal direction, which results in an elliptical cross section. Contrary to the suppression scenario, the force augmentation actuation scheme induces increased amplitude of the wake oscillation in the vertical direction, by about 40% of the unactuated motion, which leads to the wake area extension in the vertical direction (Fig. 5.13e), accompanied by a decrease in the wake extent in the horizontal direction (compare Fig. 5.13h and j).

The corresponding power spectral density (*psd*) of each time-resolved flow field presented in Figures 5.13a-j is presented in Figures 5.14a-j and plotted in the same fashion as the steady far wake power spectra in Figures 5.12a-j. The unactuated response to the $k = 0.259$ sinusoidal pitching is shown in Fig. 5.14c and h which still include the two frequency bands seen previously in the baseline spectra, but with reduced power, particularly of the motions attributed to the axis switching. In addition, the superposed motion ($k = 0.259$) appears as the dominant power peaks in the flow at $St_D = 0.045$ in the vertical direction (Fig. 5.14c), and $St_D = 0.090$ in the horizontal direction (Fig 5.14h), and their harmonics. Figures 5.14b and g show a similar response when the model is held stationary and the force augmentation actuation is activated, with the exception that the actuation that mimics the model motion excites the harmonics near the vortex shedding frequency in the vertical direction and a more pronounced axis switching mode in the horizontal direction. Upon the activation of suppression actuation, the power spectra become noticeably compressed in *z* similar to the 'quasi-steady' case (compare Figures 5.14c and d), and stretched in the *y* (compare Figures 5.14h and i) direction. This response also includes an excitation of the pitch harmonics closest to the vortex shedding frequency in the vertical direction as well as a more pronounced axis switching mode, similar to the effects of actuation on the stationary model (compare Figures 5.14b and g with Figures 5.14d and i). A different trend is seen upon force augmentation scenario in Fig. 5.14e and j, where the augmented spectrum becomes stretched in *z* and compressed in *y*, without exciting the axis switching mode in the cross-stream direction.

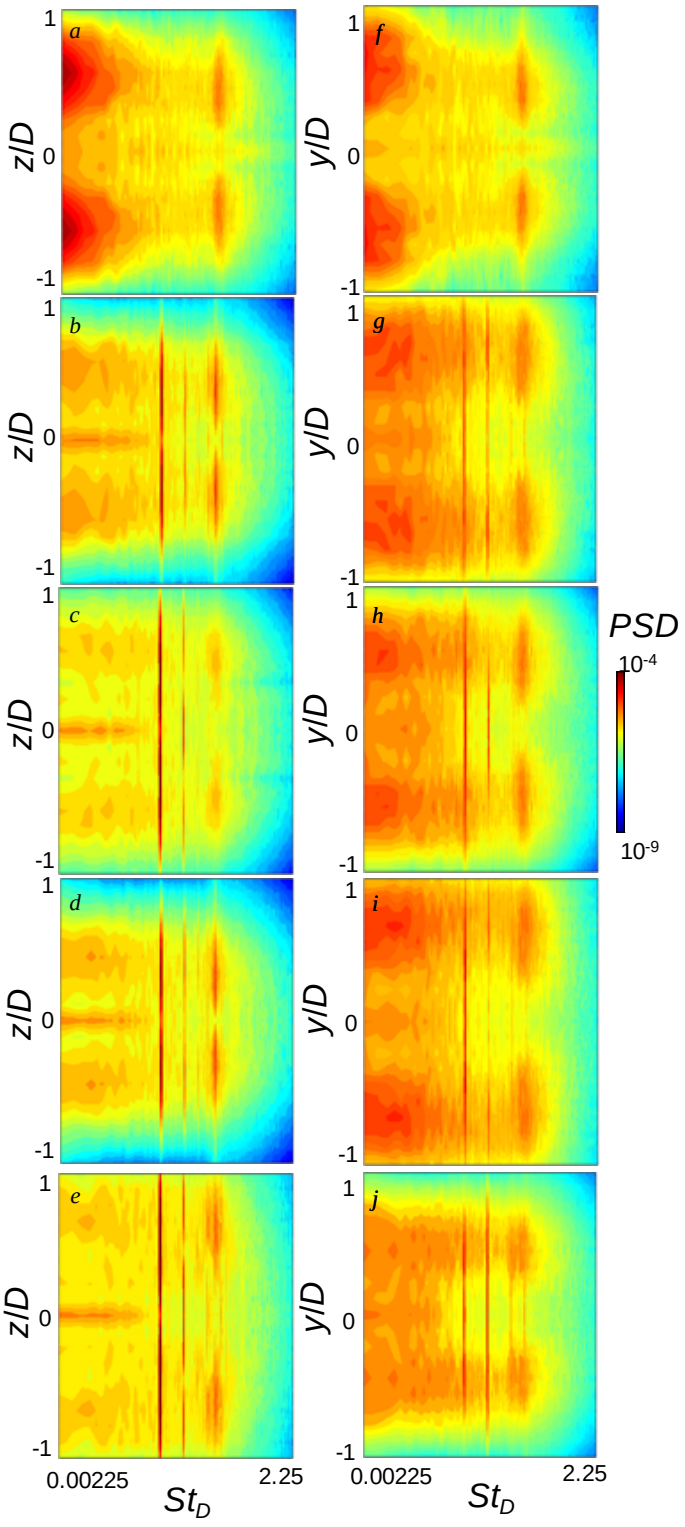

Figure 5.14. Synonymous unsteady power spectra of the planar velocity measurements measured in Figure 5.13, presented in the same fashion as Figure 5.12 for $k = 0.259$.

The resulting wakes presented in Figures 5.11 and 5.13 are quantified in Figure 5.15, using 50 points per cycle with 30 phase averages. The time traces of the vertical centroid (z_w, Figure 5.15a,c) and area (A_w, Figure 5.15b,d) of the wake bounded by $0.95U_o$ are presented. The quasi-steady wake at k = 0.013 is shown in Figures 5.15a and b and the unsteady wake at k = 0.259 is shown in Figures 5.15c and d. The unactuated response is shown in black, with the augmentation actuation in red and the suppression actuation in green. In addition, the static model case with the actuation by the top and bottom jets timed to mimic the pitching model is shown in blue, and the static unactuated model case is shown in dotted black. Figure 5.15a indicates a clear trend with the quasi-steady wake where the

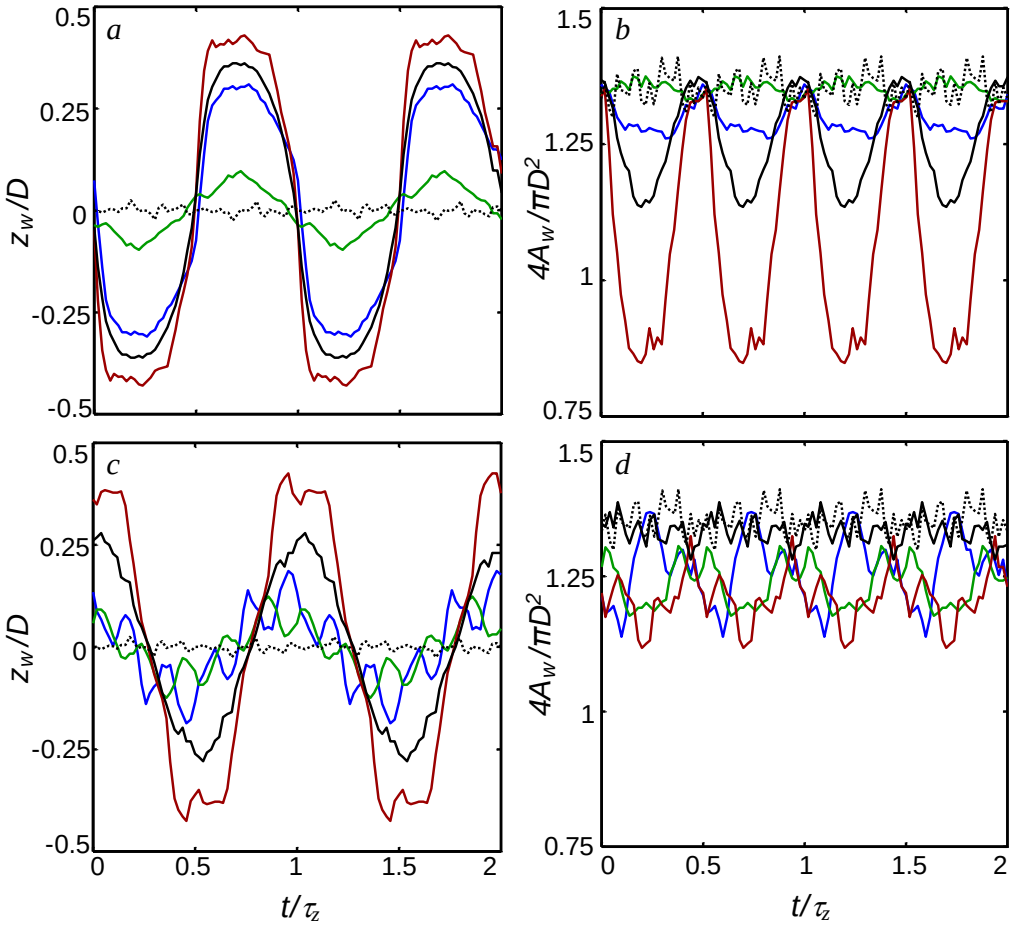

Figure 5.15. Time-resolved variation of the vertical deflection of the far wake centroid, z_w (a,c), and area, A_w (b,d) of the wake bounded by $0.95U_o$ at x/D = 5 for k=0.013 (a,b) and 0.259 (c,d) with unactuated (black), force suppression (**green**), and augmentation (**red**) on a pitching body. The case of the actuation alone on a static model (**blue**) as well as a baseline static model (dotted black) are shown for reference.

unactuated flow has a central deflection of $z_w/D = \pm 0.3$, and upon lift augmentation increases to deflections of $z_w/D = \pm 0.4$, or upon lift suppression decreases to deflection of $z_w/D = \pm 0.2$. In addition, the timed actuation on the static body nearly matches the unactuated pitching case with a deflection of $z_w/D = \pm 0.5$, which makes the amplitude difference more noticeable. Figure 5.15b shows that the unactuated wake area has a variation of $1.15\text{-}1.35 \cdot (\pi D^2/4)$ with maximum area at the centerline, and minimum area at the extremes. Upon force suppression, the wake area becomes nearly invariant along the static baseline level, and upon amplification the wake area varies ~250% the unactuated level, while the flow control alone on a static model has 50% of the area variation of the baseline level. The unsteady wakes show some departure from the quasi-steady wake responses: a phase lag ~90° in the unactuated and the amplified cases, and ~80° in the unactuated and actuation on a static model cases observed in the wake centroid presented in Figure 5.15c. The unactuated response of the wake at this frequency has a central deflection of $z_w/D = \pm 0.25$, and upon augmentation increases to deflections of $z_w/D = \pm 0.4$, and upon suppression decreases to deflection of $z_w/D = \pm 0.15$, showing an increase in the efficacy of augmentation with a slight decrease in the efficacy of suppression. The stationary actuation case has a deflection of $z_w/D = \pm 0.18$, or 70% of the unactuated level. The actuation alone and the lift suppression cases include a clear excitation of the fourth harmonic, which is attributed to coupling with the vortex shedding frequency as described in the discussion of Figure 5.14, but the excitations of this frequency in the unactuated and lift augmentation wakes are less evident. This suggests that to achieve further decoupling of the wake from the model motion, the actuation may need to include a second modulation frequency that also suppresses the excitation of the harmonic closest to the vortex shedding frequency. The area variation of the $0.95U_o$ bounded wake vs. time is a lot less structured at the unsteady frequency compared to the steady frequency (compare Figures 5.15b and d), with little variation of the area in the unactuated pitching case, and with a variation of $1.15\text{-}1.35 \cdot (\pi D^2/4)$ in the presence of all three actuation cases at $k = 0.259$.

5.2 Harmonic Plunge

This section investigates the model when it is harmonically plunging from $0 \leq k \leq 0.259$, through an analysis of the loads encountered on the model, with and without continuous actuation. This motion investigated in this chapter with a fixed $z = \pm 5$ mm ($z/D = \pm 0.056$) amplitude, shown in Figure 5.16. Figure 5.16a–e show C_D, Figure 5.16f–j show C_L, and Figure 5.16k–o show C_M with the plunging coordinate, z, analogous to Figure 5.1 for pitch, with the same flow conditions, frequencies, and timing. As the motion increases in frequency, the time averaged C_D stays around the same at 0.24, with the introduction of a higher frequency fluctuation (increasing with k in magnitude from 0.01 to 0.08 in Figure

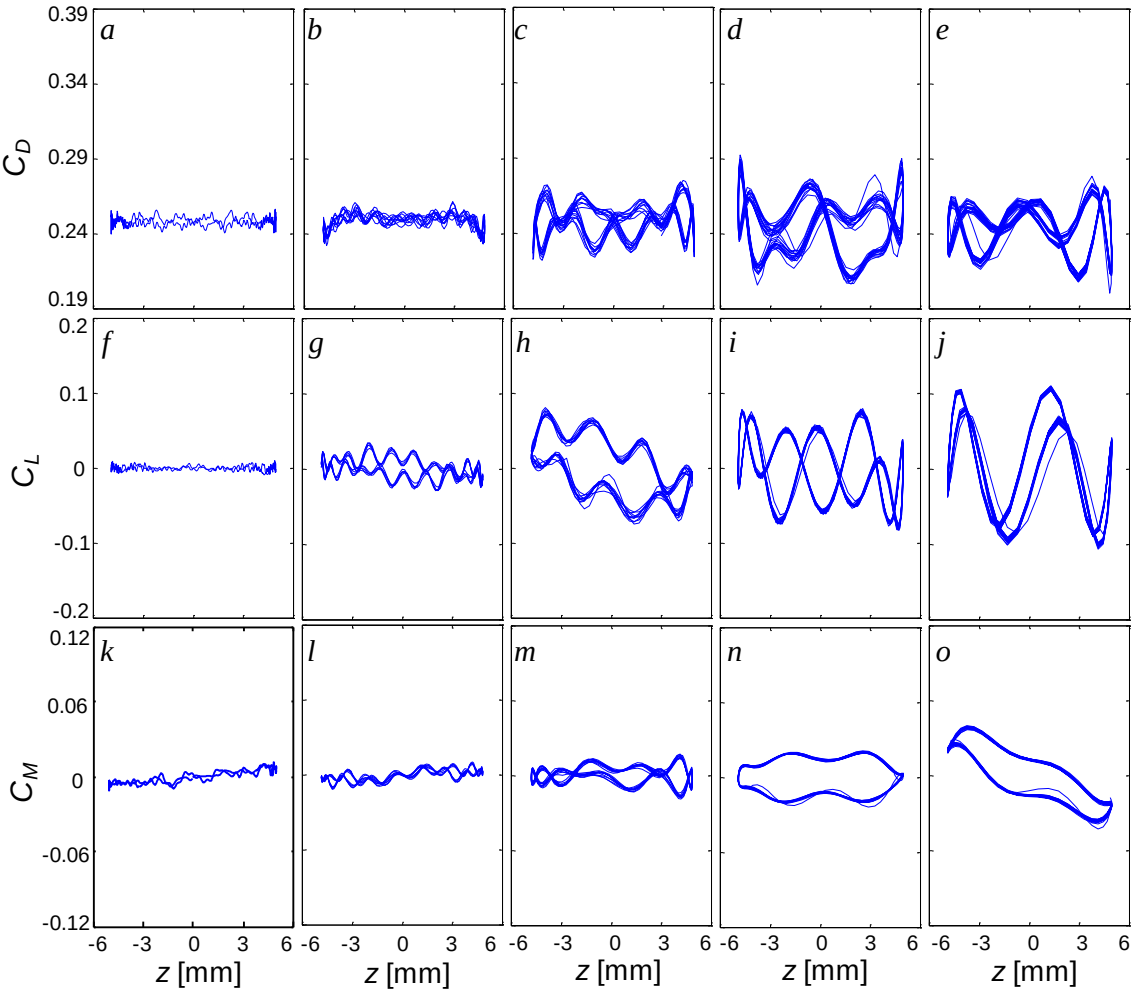

Figure 5.16. Drag (a-e), lift (f-j), and pitch (k-o) coefficients with simple harmonic plunge at frequencies of k = 0.013 (1 Hz) (a,f,k), 0.065 (5 Hz) (b,g,l), 0.130 (10 Hz) (c,h,m), 0.194 (15 Hz (d,i,n), and 0.259 (20 Hz) (e,j,o) and an amplitude of $z = \pm 5$mm, for the same conditions as in Figure 5.1.

5.16a–e) attributed to the wake instability. The quasi-steady C_L appears to be coupled to the same instability as in the drag, with a growth in fluctuation magnitude from 0 to 0.1 at k = 0 to 0.259 (Figure 5.16f and 11j). The lift also has the introduction of a small negative slope at higher frequencies (C_L/z = -0.01/mm at 10 Hz, -0.005/mm at 15 Hz, and -0.01/mm at 20 Hz in Figures 5.16h-j). This negative average slope of C_L with z implies that the model is stable in plunge, as the aerodynamic force that develops is in the opposite sense of the plunging direction. The quasi-steady C_M has slight variations, shown in Figure 5.16k, with a small or negligible slope throughout its frequency, until k = 0.259, with the introduction of a C_M/z slope of -0.005/mm (Figure 5.16o) similar to the lift at this frequency. This may be due to small deviations between the commanded zero pitching angle of the model and the resulting pitching angle, as the pitching moment is very sensitive to pitching angle at this large unsteady frequency (compare Figures 5.16o and 5.1o).

The next investigation investigates the effect of open loop actuation on a model undergoing varying frequency plunge. This is shown in Figure 5.17 with the case of no actuation (black), continuous top jet actuation (dark blue), and continuous both top and bottom jet actuation (light blue). Figures 5.17a-c show the representative quasi-steady response at k = 0.013, and Fig. 5.17d-f showing the representative unsteady response at k = 0.259, to determine the flow control effect in representative 'quasi-steady' plunge, or 'highly unsteady' plunge conditions. Figure 5.17a shows a steady C_D of 0.24 with virtually no change with top jet actuation, and a ΔC_D = 0.02 maximum increment in drag force with both actuators activated, where the maximum increment occurs at the maximum excursions (i.e., z = ±5mm). The steady C_L presented in Fig. 5.17c shows variation of the lift force coefficient with the plunging coordinate, a significant induced lift force by the top jet actuator alone of ΔC_L = 0.10, and negligible induced C_L with both jets activated. Figure 5.17e shows a slightly larger variation of the pitching moment with the plunging coordinate, with a positive slope (C_M/z = 0.001/mm), where activating the top jet nearly doubles this slope ($C_M \cdot D/z \sim 0.002$/mm), and adds an induced pitching moment of

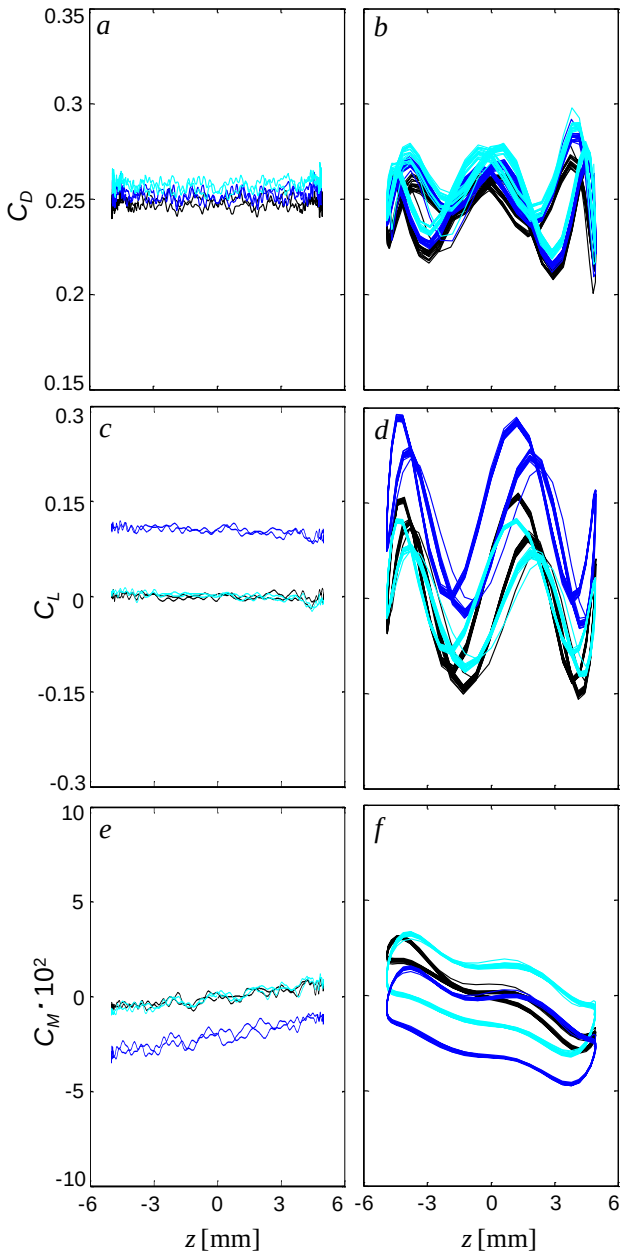

Figure 5.17. Drag (a,b), lift (c,d) and pitch (e,f) coefficients for the body with simple harmonic plunging at an amplitude of z = 5mm and a reduced frequency of k = 0.013 (a-c), and k = 0.259 (d-f) over a time interval of $450\tau_{conv}$ using 100 phase averages for unactuated (black) top jet (**blue**) and both jets (**cyan**) actuation with a continuous $C_\mu = 4 \cdot 10^{-3}$.

$\Delta C_M \sim -0.02$. Activation of both actuators reverts the moment response to the baseline response, similar to Fig. 5.17c. The unsteady C_D in Fig. 5.17b is similar (on the average) to the steady C_D of Fig. 5.17a, where it is centered about 0.24, only now with a fluctuation of approximately 0.08 peak to peak. The actuation changes are also similar; there are small

changes in drag by activating the top actuator and a slight increase in drag due to activating both actuators. A large change is observed in the unsteady C_L in Fig. 5.17d, where the unactuated response gains a negative slope (C_L/z = -0.001), with a strong coupling to the shedding frequency. Activation of either one or both actuators continuously does not appear to change the fluctuations, but activating one jet does induce a similar average lift deflection to the steady case (~0.08 to 0.1, compare Figures 5.17c and d). A similar effect happens to the unsteady C_M in Fig. 5.17f, where the baseline shape is changed from a slightly positive sloped response to a negative slope (C_M/z from 0.001/mm to -0.005/mm) with some added hysteresis, and activation of either one or both actuators induces a large change in hysteresis with a peak-peak difference in C_M of 0.06. Despite these large differences in the unsteady regime, activation of the top jet remains similar with an additional positive C_L and negative pitch C_M, similar to the actuation responses in the steady regime, and these offsets are typically larger than half of the unsteady fluctuations, indicating that timed control of actuators could be used to reduce these vibrations coupled to the shedding frequency. In the present work, further studies in this plunging motion are omitted because this body is stable at higher frequencies, and therefore this motion does not necessarily need active feedback control with the synthetic jets for stabilization.

5.3 Harmonic Streamwise Translation

This section investigates the model when it is harmonically moving in the streamwise direction from $0 \le k \le 0.259$, in a synonymous investigation to the plunge study in §**5.2**. This last basic motion chosen is a fixed amplitude x = ±5 mm (x/c = ±0.030) amplitude simple harmonic streamwise displacement, shown in Figure 5.18. C_D (Figure 5.18a–e), C_L (Figure 5.18f–j), and C_M (Figure 5.18k–o) are presented with the same frequencies, timing, and conditions as Figures 5.16 and 5.1. For this maneuver, both the motion and the freestream velocity are in the same direction, so the predominant changes occur in C_D, while the changes to C_L and C_M are attributed only to phase locking to the instability in the wake, and are approximately symmetric with zero time averaged values (Figure 5.18f–o).

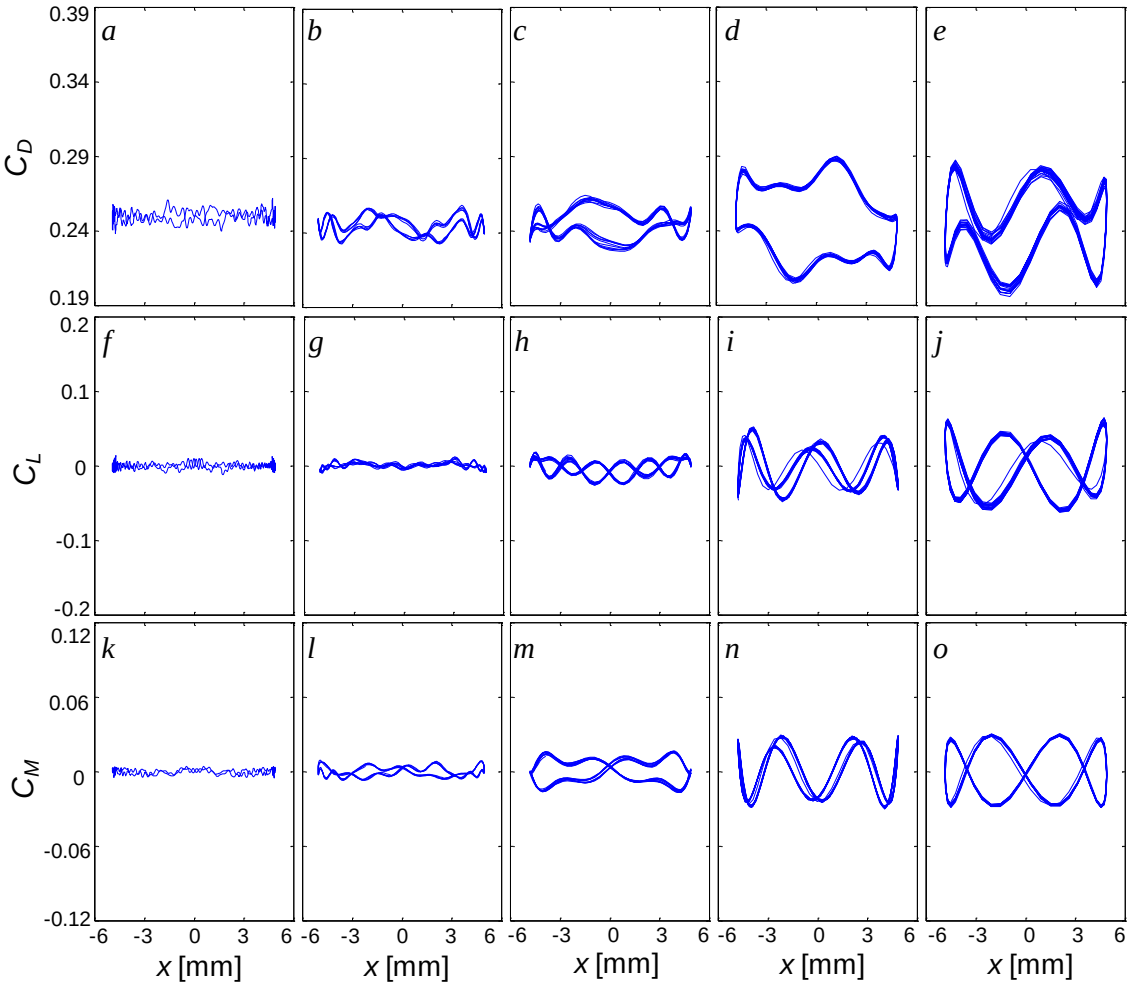

Figure 5.18. Drag (a-e), lift (f-j), and pitch (k-o) coefficients with simple harmonic streamwise displacement at frequencies of k = 0.013 (1 Hz) (a,f,k), 0.065 (5 Hz) (b,g,l), 0.130 (10 Hz) (c,h,m), 0.194 (15 Hz (d,i,n), and 0.259 (20 Hz) (e,j,o) and an amplitude of x = ±5mm, for the same conditions as in Figure 5.1.

The time averaged value of the drag retains a value of approximately 0.24, with a growth in hysteresis at 10 Hz (Figure 5.18c), which maximizes at 15 Hz (Figure 5.18d), and then decreases at 20 Hz (Figure 5.18e). For most of these drag measurements the average slope of the drag is zero, except for 15 Hz where there is a slight slope of C_D/x of −0.005/mm which suggests this motion is neutrally stable (the aerodynamic drag is roughly invariant to changes in streamwise coordinate throughout most frequencies). This can be expected as this motion can be analyzed as a fluctuation of the freestream with a value of $2\pi fx$ = ±0.0314 to 0.628 m/s, which should not induce large fluctuations in the steady drag

coefficient, and the only induced effects are expected to be induced in the unsteady aerodynamics regime.

Similar to plunge, the baseline C_D and C_L and C_M with k = 0.013 and 0.259, in the same fashion as in Figure 5.17, to quantify the effects of open loop continuous actuation in this motion. The steady C_D and C_L presented in Fig. 5.19a and b are almost the same as their respective cases in plunging in Fig. 5.17a and b in both the actuated and unactuated cases,

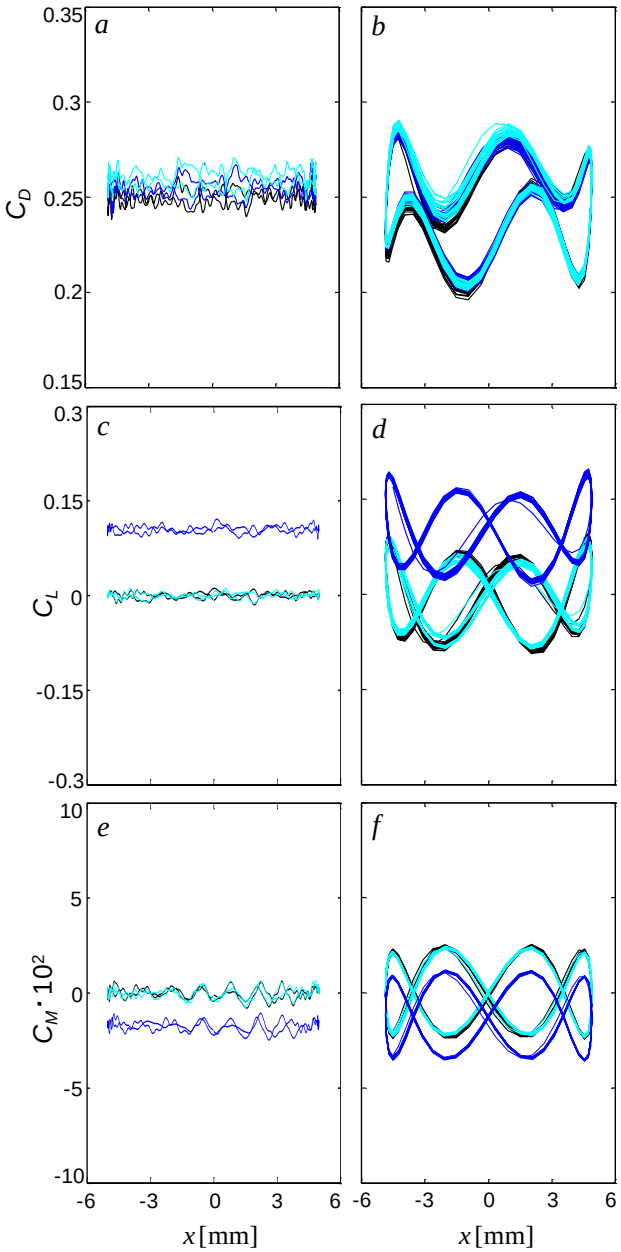

Figure 5.19. Drag (a,b), lift (c,d) and pitch (e,f) coefficients for the body with simple harmonic streamwise displacement at an amplitude of x = 5 mm and a reduced frequency of k = 0.013 (a-c), and k = 0.259 (d-f) presented in the same fashion as Figure 5.17.

with the most significant effect from the vectoring of the flow and inducing a side force. The steady C_M curve in Fig. 5.19c is slightly different than in Fig. 5.17c, where there is virtually no slope with x displacement in the unactuated and actuated responses, but the offset ΔC_M of -0.02 with the top jet actuated remains the same. When the model oscillation frequency is increased, the unsteady C_D shown in Fig. 5d gains an unactuated hysteresis with a peak to peak range of 0.09, and actuation does not have a significant effect on this fluctuation. There is an increase in hysteresis in C_L and C_M shown in Fig. 5.19e and f of 0.08 and 0.04 from the motion induced forces but actuation does not appear to change the characteristic response. The response instead behaves very similar to the steady C_L and C_M, where a single jet deflects the force coefficient by 0.1, and the moment coefficient by -0.02, returning to the baseline response upon activation of both actuators. In this Thesis, further studies in this streamwise motion are not investigated because the current actuator design is chosen for having an optimal effect in the induced lift and moment, and this motion would require a different orientation of the actuation to control its primary drag fluctuations.

CHAPTER VI

WAKE DYNAMICS WITH LISSAJOUS ROTATION AND ACTUATION

This chapter describes investigations of the effects of Lissajous rotations (e.g., coupled pitch and yaw) of the axisymmetric model through a range of 'quasi-steady' to 'highly unsteady' aerodynamic motion that is inspired by the 'natural', coupled pitch-yaw precessions free flight models. The wake dynamics are investigated using stereo PIV (cf., Chapter ***2.7.1***) that yields simultaneous measurements of the streamwise and cross-stream velocity components in the wake and are characterized using POD modes. The near wake of the static model is described in §**6.1**, and is followed by investigations of the wake in when the model is moving in prescribed Lissajous rotations that are compared to the effects of actuation on the stationary model (§**6.2**). The changes in the wake structure induced by actuation are discussed in §**6.3**, and in §**6.4** open loop actuation on the rotating model is used for enhancement or suppression of the wake response.

6.1 Static Model: Near-Wake Structure

The near wake behind the stationary model at $Re_D = 1.8 \cdot 10^5$ is measured in the interrogation region previously discussed in Chapter **II** in Figure 2.21a. The result is a 3-D velocity flow field with the streamwise velocity, U_x, in the x direction, and the cross-stream velocities, U_y and U_z, in the y and z directions, respectively. The interrogation region is chosen to be at a fixed streamwise location of $1D$ downstream of the aft end of the model, spanning $1.3D$ in y and $1.3D$ in z, ($y = \pm 0.65D$, and $z = \pm 0.65D$, centered about the model).

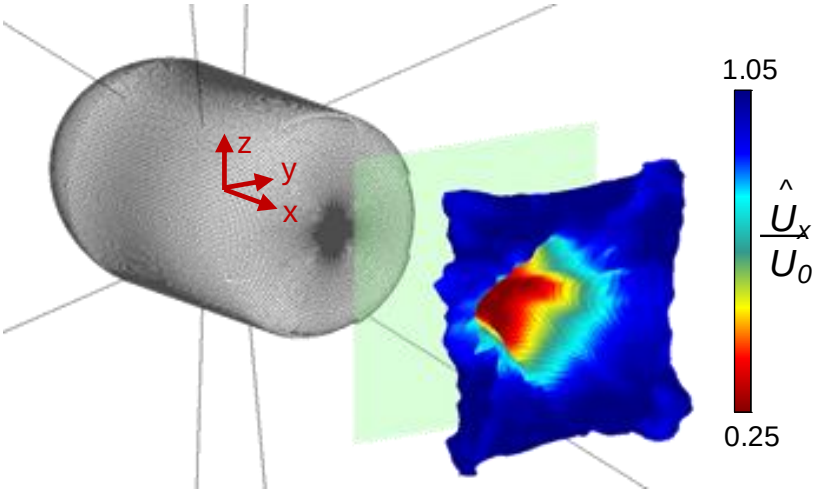

Figure 6.1. SPIV on a stationary model with $Re_D = 1.8 \cdot 10^5$ shown to scale with the global coordinate system in **red**, the interrogation region in **green**, and a stream-surface created by the average velocity field, $\hat{\vec{U}} \cdot t_{ref}$, and contoured by the average streamwise velocity, $\hat{U}_x$, where t_{ref} = 2 ms.

The resulting stream surface of the flow is shown in Figure 6.1, with a 64x64 grid of time averaged velocity vectors, $\hat{\vec{U}}$, over 600 instantaneous measurements. This surface is calculated by taking the location at which each $\vec{U}$ was measured and adding on a distance of $\hat{\vec{U}} \cdot t_{ref}$, where t_{ref} = 2 ms. This surface is also colored by the streamwise velocity component, U_x, which is the dominant component of the velocity field, and ranges from $0.3U_o$ in the center of the wake deficit behind the model to nominally U_o in the free stream, with slight reduction in the wake of the wires. For reference, the global coordinate system (x,y,z) used in this chapter is shown in red.

An in-depth analysis of the wake velocity flow field for the stationary model is shown in Figure 6.2. The equivalent averaged streamwise velocity component, $\hat{U}_x$, to Figure 6.1 is shown in Figure 6.2a, in a planar interrogation region, and in addition the projections of the wires are depicted. This baseline flow is not completely axisymmetric due to the geometry of aft end of the model, where the backward-facing steps that house the inactive actuators (see Figure 2.1b) locally displace flow from the Coanda surface, which leads to

an extension of the wake deficit region in the vertical and horizontal directions. The commensurate cross-stream velocity components ($\hat{U}_y$ and $\hat{U}_z$) are shown in Figure 6.2b as a quiver plot alongside with a contour of the averaged streamwise vorticity, $\hat{\zeta}$, calculated from these velocity components. The cross-stream velocity magnitude is significantly smaller than the streamwise velocity, with maximum values of ~$0.2U_o$ at the location of the shear layer, and approaching zero in both the wake center and in the free stream. Although this flow is nominally converging to center, there is a faint vortex structure present, which is again contributed to the geometry of the aft end of the model: the vortex structure is essentially a weak eight-lobe structure due to slowing of the radial velocity

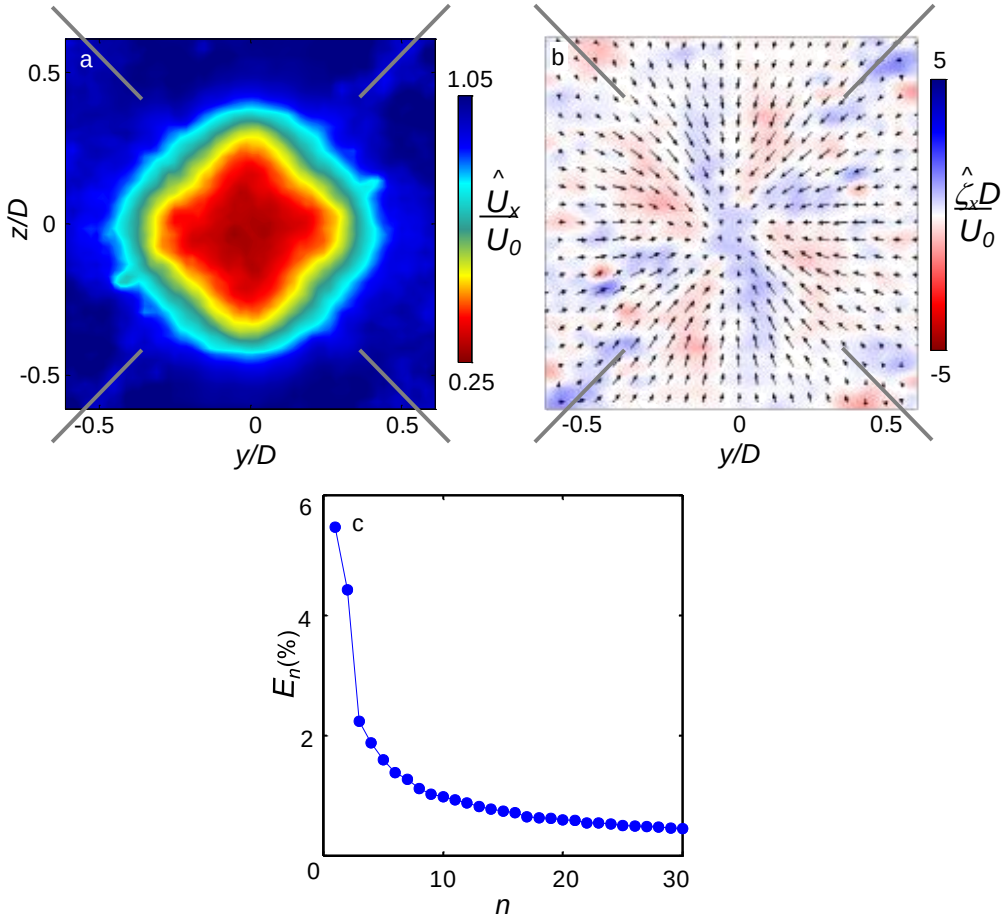

Figure 6.2. Contour plots of the averaged base flow streamwise velocity, $\hat{U}_x$ (a) and streamwise vorticity, ζ_x (b), along with the energy contributions for the first 30 modes of a POD analysis on 600 instantaneous velocity vectors (c) for $Re_D = 1.8 \cdot 10^5$ with the cross-stream location of the mounting wires shown in gray.

downstream of the inactive actuators. There are also slight contributions to the streamwise vorticity due to the wires in the corners of the interrogation region. To further investigate the structure of the wake, instantaneous velocity vectors that are used to calculate the average fields in Figures 6.2a and b are also used to extract the Proper Orthogonal Decomposition (POD) modes of the wake (where the POD method is discussed in Appendix **A.1**). The POD mode analysis is applied on the stationary model by extracting the first 30 modes from 600 snapshots of the velocity field, and the energy contribution of the first 30 modes is shown in Figure 6.2c. Based on the energy distribution, it appears the first two modes are more prominent than the rest, having a higher than 4% energy contribution, while energy fractions become reduced to less than 1% by the ninth mode.

The POD modes of the subset of $\vec{\varphi}_{\mathrm{n}}$ that correspond to the streamwise velocity, $\vec{\varphi}_{\mathrm{n,u}}$ are shown in Figure 6.3 with n = 1-8 shown in Figures 6.3a-h, respectively. The first two modes shown in Figures 6.3a and b are a rotated pair that represent a two-fold symmetry of vortex shedding from the model top left to or from the bottom right (Figure 6.3a), and the bottom left to or from the top right (Figure 6.3b). This wake structure does not seem to line up with the mounting wires, which make a 53º angle from the top in this frame of view, and instead seem to line up with 45º, which is the azimuthal center between two of the jet actuators. This suggests that the primary shedding of the model (and therefore the primary change in the wake deficit) is biased away from the backward facing steps when the jets are inactive and the model is stationary (see Figure 2.1b and compare to the shape of Figures 6.3a and b). Another interesting feature about this dataset is that the effects of the wires are not as prominent as they were in Figure 6.2, which suggests that the effect of the wire is mostly invariant with time (relative to the wake time scales). The second and third modes (Figures 6.3c and d) again form a rotated pair which now has a four-fold symmetry and this pattern continues into Figure 6.3e which has an apparent eight-fold symmetry. The pairing of POD modes stops at the fifth mode, where the sixth mode in

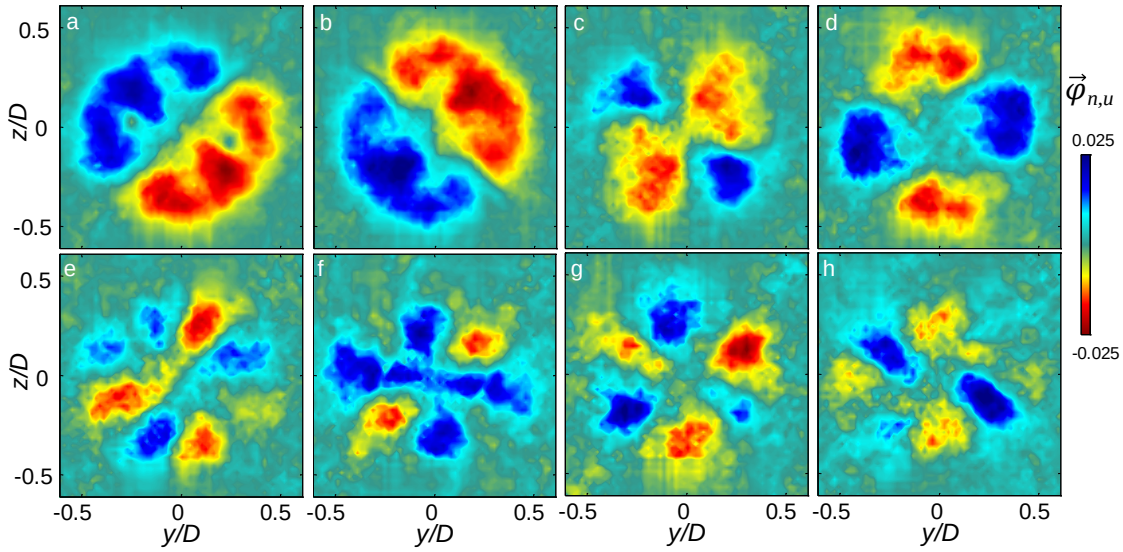

Figure 6.3. Contour plots of the streamwise velocity POD modes, $\vec{\varphi}_{n,u}$, with mode number n = 1 (a), 2 (b), 3 (c), 4 (d), 5 (e), 6 (f), 7 (g), and 8 (h) for the base flow at $Re_D = 1.8 \cdot 10^5$.

Figure 6.3f significantly differs from the fifth mode in Figure 6.3e, where it is no longer a rotated pattern of the previous mode, and it is also the first mode to have a predominant sign (i.e., the velocity change in the center is much greater than the two regions of opposite sense around it). The seventh mode in Figure 6.3g is the first mode that shows a six-fold symmetry in the velocity fluctuations. The final eighth mode in Figure 6.3h also shows six regions of alternating sign, but is dominated mostly by two neighboring regions of the same sense in the bottom right and top left.

The respective subset of $\vec{\varphi}_n$ that correspond to the cross-stream velocities, $\vec{\varphi}_{n,v}$ and $\vec{\varphi}_{n,w}$, are plotted as a quiver plot, and colored by their respective normalized vorticity, $\vec{\varphi}_{n,\zeta}$, in Figure 6.4 with the first eight modes, similar to Figure 6.3. The same pairing of the first and second mode seen in the streamwise velocity in Figures 6.3a and b is observed in the cross-stream velocities in Figures 6.4a and b, each with a predominant counter-rotating vortex pair in the top left to/from bottom right and top right to/from bottom left, respectively. The order of these pair modes could change depending on the instantaneous images (i.e., due to the left-right symmetry of this model there is no reason to believe one

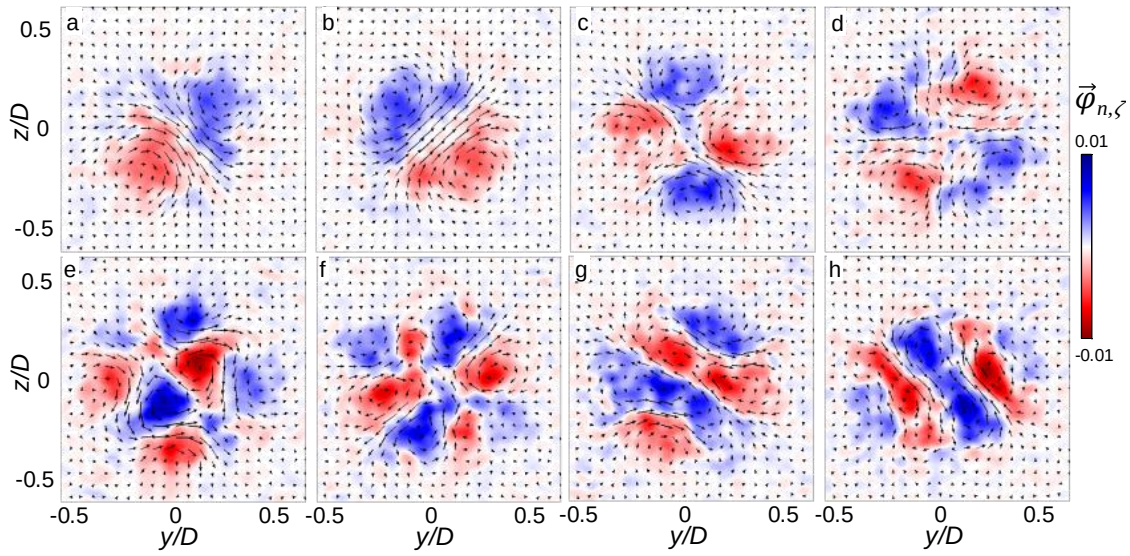

Figure 6.4. Quiver plots of the cross-stream velocities' POD modes, $\vec{\varphi}_{n,v}$ and $\vec{\varphi}_{n,w}$, with mode number n = 1 (a), 2 (b), 3 (c), 4 (d), 5 (e), 6 (f), 7 (g), and 8 (h) colored by their streamwise vorticity, $\vec{\varphi}_{n,\zeta}$, for the base flow at $Re_D=1.8\cdot10^5$.

side should always have dominant energy). The next mode pair in the third and fourth mode in Figures 6.4c and d shows two counter-rotating streamwise vortex pairs in agreement with Figure 6.3c and d. Another interesting feature that appears in the streamwise vorticity of these modes is that the maximum value occurs at locations where the sign of the streamwise velocity mode changes (compare Figures 6.4a-d to Figures 6.3a-d). The fifth and sixth modes in Figures 6.4e and f, respectively, introduce more vortex structures with some regions not clearly defined, and the seventh and eighth modes in Figures 6.4g and h, respectively, introduce a new feature of a streamwise vortex that crosses the centerline of the model which was not seen in lower modes. The last four modes also appear to have a paired structure in the cross-stream velocity modes, while Figures 6.4e and f appear similar in structure to each other, as do Figures 6.4g and h. However, these same cases show deviations in their respective streamwise velocity modes in Figures 6.3e and f and Figures 6.3g and h, showing that different modes could have a similar structure in one velocity component and not in other components. It is shown in Figure 6.3 and 6.4 that as the mode number n increases, the structure of the POD mode

starts to lose organization, and therefore for all the following POD datasets shown in the rest of this chapter, only the first four modes are analyzed for brevity.

6.2 Lissajous Rotation- and Actuation- Induced Aerodynamic Loads

The remainder of this investigation focuses on three scenarios: a dynamic bluff body, a stationary bluff body with fluidic actuation, and a dynamic bluff body with fluidic actuation. The induced dynamics are chosen to be 1:1 Lissajous rotation (combined pitch, α_y, and yaw, α_z), where pitch lags the yaw by 90º phase, and both have an amplitude of 3°. This type of motion is representative of the expected natural unstable motion of an equivalent airborne body, in the absence of roll. The frequency of this motion is varied during this study, and a representative 'quasi-steady' frequency of $k = 0.017$ ($\tau_{yz} = 1$s or $180\,\tau_{conv}$) is investigated first and shown in Figure 6.5. This executed motion is shown in Figure 6.5a, with pitch in cyan and yaw in blue. The corresponding induced lift and side force coefficients (C_L and C_S, respectively) on the model are shown in Figure 6.5b, as an average of 50 instantaneous measurements, and the force coefficients are derived from the measured forces by $C = 8F/(\rho\pi U^2 D^2)$. There is a presence of two higher frequencies in both C_L and C_S, one that corresponds to the wake shedding frequency of 83Hz (or $k = 1.434$, which corresponds to $St_D = fD/U_o = 0.234$, previously measured in Chapter **V**), and another that corresponds to a lower frequency at ~12 Hz ($k = 0.207$), which is attributed to an instability frequency of the 1:1 Lissajous motion on this model without spin. These two force coefficients are plotted against each other in Figure 6.5c, where they trace out a circle with radius of 0.11, in addition to the presence of the two instability frequencies. Next, the representative fluidic actuation is chosen to induce forces on a *stationary* model to mimic the flow-induced forces on a *moving* model. To achieve this, the synthetic jet actuation waveform amplitude is chosen to provide a jet momentum coefficient, $C_\mu = 0.004$. Independent amplitude modulations of this signal are created and sent to all four jets as described in Appendix **B.2**, which allows control of C_μ in the range of 0

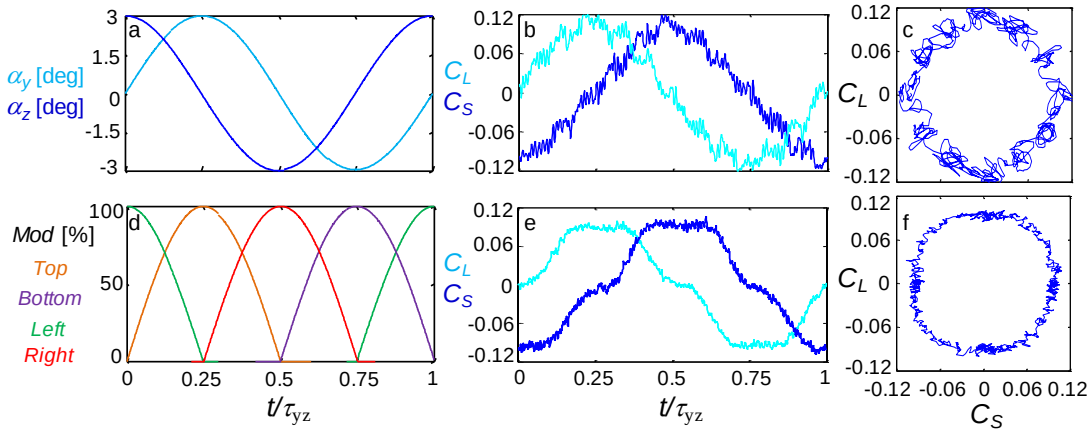

Figure 6.5. Side and lift force coefficients (b,c) induced on a model undergoing 1:1 Lissajous rotation with a phase difference of 90º (a), and the corresponding forces (e,f) on a stationary model by the actuation algorithm (d).

to 0.004. This same methodology was used before for two jets in Chapters **III** and **V** for the same model, and now is effectively extended to all four jets. Based on this prior data, the desired modulation waveform is chosen to be an overlapping sinusoidal modulation to all four jets, and is shown in Figure 6.5d. The corresponding C_L and C_S that are induced by this actuation are shown in Figure 6.5e, which indicates good agreement in magnitude with the motion-induced C_L and C_S in Figure 6.5b, with the exception that the lower frequency instability (k = 0.207) attributed to the spinning motion is no longer detected, even though the shedding instability frequency (k = 1.434) is still present. These two induced force coefficients are plotted against each other in Figure 6.5f, which shows a less circular trace than in Figure 6.5c, which is due to a faster rise time of the actuation effect in Figure 6.5e compared to the motion effect in Figure 6.5b (this effect was observed previously in Chapter **3.2**). Nevertheless, the fact that the actuation-induced forces are of the same order as the motion-induced forces in Figure 6.5 suggests that active fluidic control has sufficient authority to significantly control the motion-induced forces for the preselected 1:1 Lissajous rotation.

The frequency of the two patterns shown in Figure 6.5 is varied, while keeping the motion amplitude and fluidic modulation amplitude fixed. The resulting variations in the

C_L and C_S traces shown in Figures 6.5c and f for these increased frequencies are shown in Figure 6.6 (the resulting fluidic induced forces are depicted in green, and the motion-induced forces in blue). Figure 6.6a shows k = 0.017, which corresponds to the cases in Figure 6.5c and f plotted with each other. As k is increased to 0.086 (Figure 6.6b), the motion-induced forces start to increase while the actuation-induced forces remain roughly invariant. All the plots in Figure 6.6 are plotted in a 1 second time trace (180 τ_{conv} where τ_{conv} = c/U_o) that is the result of 50 averages to visualize the variation of the force coefficients on the same time scale. Near the motion-resonance detected before in Figure 6.5b ($k \sim 0.207$), there is a growth in the motion-induced C_L and C_S shown in blue to ~200% and ~250% of the k = 0.017 values at k = 0.172 (Figure 6.6c) and 0.207 (Figure 6.6d). However, the corresponding actuation-induced force coefficient magnitude shown in green in Figure 6.6c and d remains roughly invariant, with slight changes in its shape to have prominent maxima at the location in the paths where either C_S = 0 or C_L = 0. When the

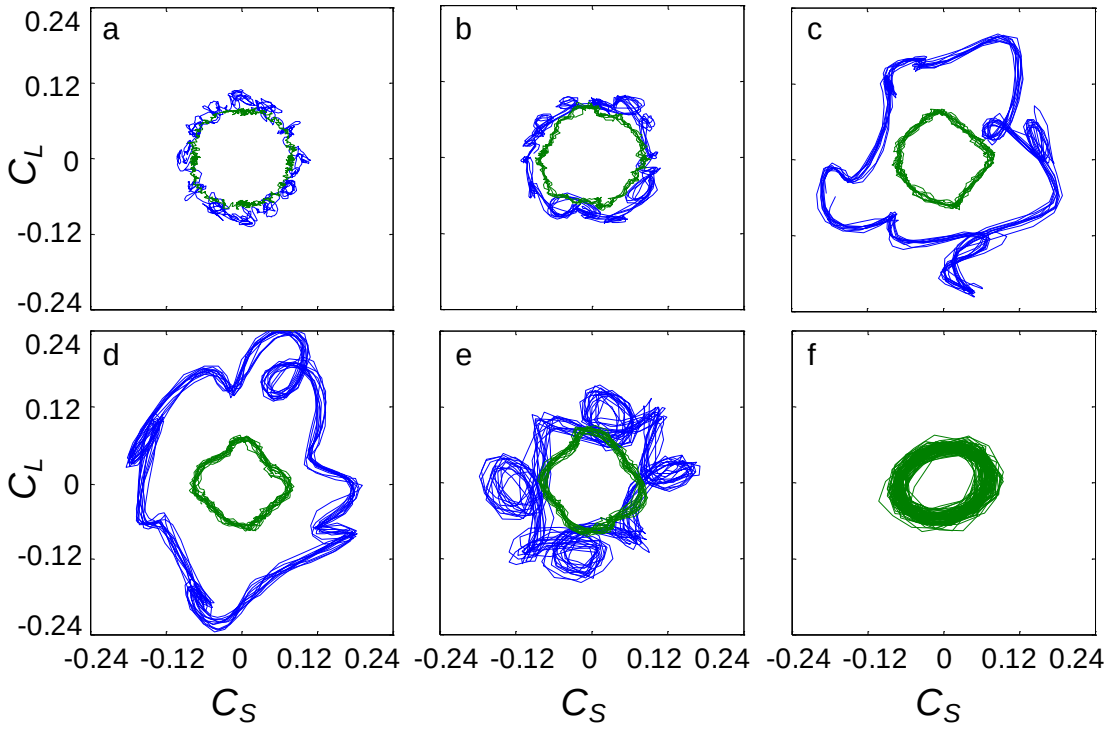

Figure 6.6. Frequency variation of C_L and C_S for 1:1 Lissajous rotation (**blue**) and actuation on a stationary model (**green**) with effective reduced frequencies at k = 0.017 (a), 0.086 (b), 0.172 (c), 0.207 (d), and 0.259 (e), and 1.434 (f), acquired over 180 τ_{conv}. Rotation-induced C_L and C_S are not acquired for k = 1.434.

frequency is increased past the motion-resonance frequency to $k = 0.259$ (Figure 6.6e), the motion-induced lift force begins to decrease in magnitude to values similar to its lower frequencies (compare the blue line in Figure 6.6e with Figures 6.6a and b). The lack of frequency variation in the actuation-induced forces continues at $k = 0.259$, shown in Figure 6.6e in green (compare Figure 6.6e and Figure 6.6d). The absence of the frequency variation of the actuation-induced force coefficients in the range of $k = 0.017$ to 0.259 is commensurate with the lack of the $k \sim 0.207$ resonance in Figure 6.5e, as opposed to the motion-induced response, which has a natural frequency present within the range of the frequency variation in Figures 6.6a-e (see Figure 6.5b). To test this hypothesis, the actuation-induced forces are modulated at the shedding frequency of $k = 1.434$ (83 Hz), shown in Figure 6.6f in green. This frequency is out of the range of the current wire-traverse control authority and therefore the motion-induced forces for this frequency are omitted from Figure 6.6f. Two features become prominent at this frequency: the response becomes biased in the side force coefficient, and the variation of the recorded actuation-induced force coefficients is much larger than they were at any lower frequency (compare Figure 6.6f with Figures 6.6a-e). This effect is also similar to the result found in the far wake pitch modulations on a stationary model in Chapter **V**, where setting the modulation frequency to the shedding frequency extended the vertical extent of the wake deficit. This approach of implementing spin modulated fluidic actuation on a stationary model at its shedding frequency is investigated further through its wake response in §**6.3**.

Next, the study of the control authority of the fluid actuation on a moving body is tested. Based on the results shown in Figure 6.6, there should be a significant impact on C_L and C_S if the fluidic actuation scheme (shown in green) is run in phase or out of phase with the Lissajous 1:1 rotation that induced the aerodynamic loads (shown in blue). In addition, it is also important to check the possible deflection of trajectory (x, y, z, α_x, α_y, and α_z), as well as the changes in the four other coefficients (drag force, C_D, and roll, C_R, pitch, C_M, and yaw, C_Y, moments), where the moment coefficients are based on the measured

moments as $C = 8M/(\rho\pi U^2 D^2 L)$. Initially, the combination of the fluidic actuation shown in Figure 6.5d and Lissajous rotation in Figure 6.5a is shown at the representative steady frequency of $k = 0.017$ in Figure 6.7 ($\tau_{yz} = 1$s or $180\,\tau_{conv}$). When the actuation and motion are in phase (referred to as the force augmentation case), the corresponding data are shown in red, and when the actuation is run 180º out of phase (force suppression), the data are shown in green, while the unactuated motion response is shown in blue for reference. The nominally zero translational components of the center of the wire mounts on the model are shown on a scale of ±2mm with streamwise displacement (x), and cross-stream

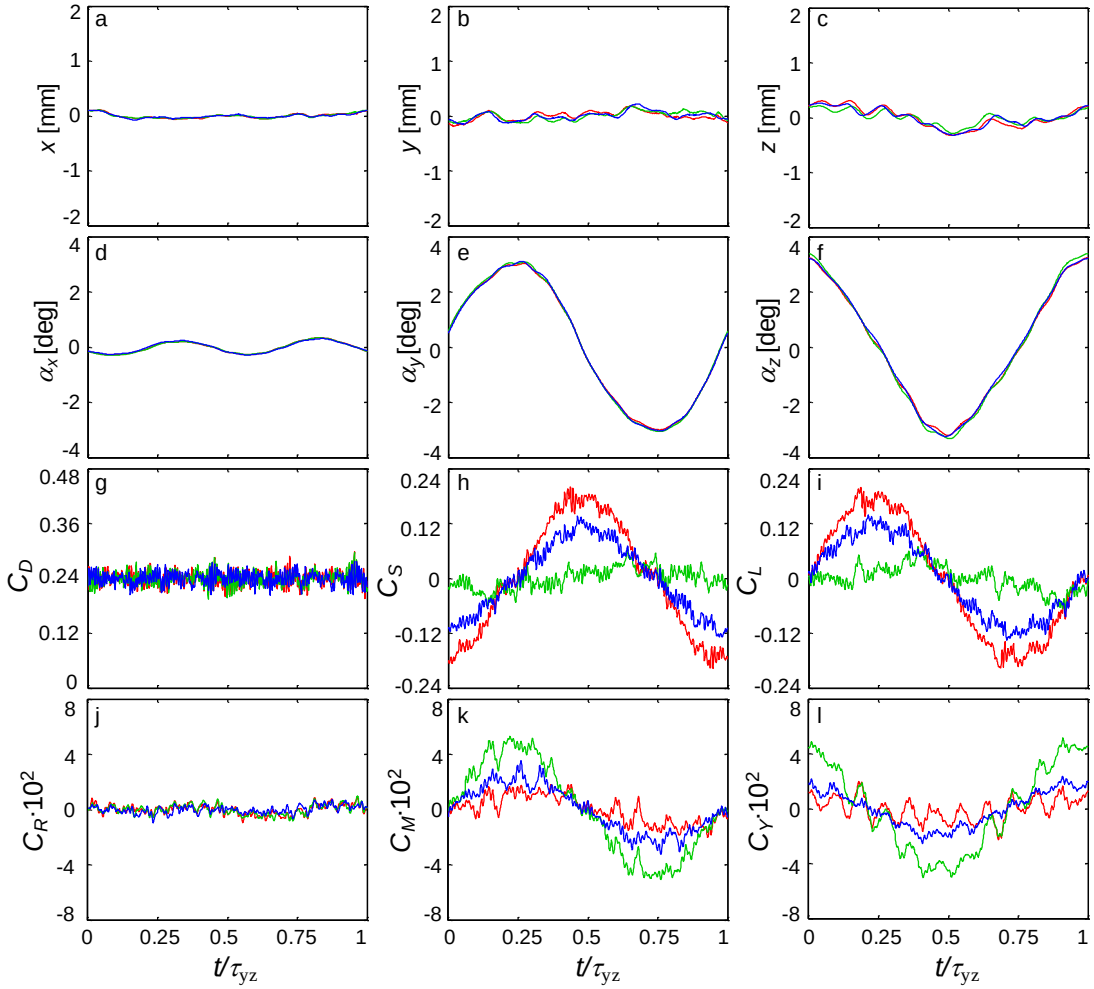

Figure 6.7. Time traces of translational (a–c) and rotational (d–f) components of the model motion, as well as the aerodynamic force (g–i), and moment (j–l) coefficients at $k = 0.017$, without (**blue**) and with actuation for the flow control schemes for the force suppression (**green**) and augmentation (**red**) at $Re_D = 1.8 \cdot 10^5$.

displacements (*y* and *z*). There are slight variations in y on the order of 0.2 mm and *z* on the order of 0.4mm, but for all translations there is almost no variation in the motion when actuation is applied, implying that the forces induced in Figures 6.7g-i are all aerodynamic and not related to inertia effects. The commanded angles of 3º α_y and α_z, 90º out of phase are shown in Figures 6.7e and f, which again have little variation due to actuation, also implying that the moment responses in Figures 6.7j-l are entirely aerodynamic. There is a slight variation of the roll angle from the commanded value of 0 in Figure 6.7d, but it is around 0.3º and is invariant with actuation and therefore is considered negligible. The commanded force suppression (green) and force augmentation (red) are shown with their C_S and C_L in Figures 6.7h and i, respectively, indicate significant control authority over these two coefficients with a suppression of 60% or an augmentation of 35%, respectively. This control negligibly varies the drag seen in Figure 6.7g, where it is initially a value of 0.24 (close to the expected value of 0.25, cf., Hoerner, 1965), and the actuation does not significantly increase or decrease C_D (within the resolution of this time trace of about 0.02). Likewise, the roll moment, shown in Figure 6.7j appears to be roughly invariant (with small periodic fluctuations attributed to fluctuations in the roll angle, compare Figure 6.7j and Figure 6.7d), and almost no change is induced due to the actuation. Similar to this model undergoing a pure pitching motion with no yaw (cf., Chapters **III** and **V**), the force suppression actuation appears to augment the aerodynamic moments C_Y and C_M by about 50%, and the force augmentation actuation appears to suppress the aerodynamic moments by about 30%, as seen in Figures 6.7k and l. This suggests that this actuation could also be applied for control of the aerodynamic moments instead of the aerodynamic forces, if desired. In addition, the motion-resonance frequency is more clearly depicted in the moment traces in Figures 6.7k and l than in the force traces (compare with Figures 6.7h and i).

A frequency variation of the force suppression (green) and augmentation (red) control schemes, shown in Figure 6.8, is implemented (similar to that of Figure 6.6), where the

side with lift force variation is shown in Figures 6.8a,c,e,g, and i and the yaw with pitch moment variation is shown in Figures 6.8b,d,f,h, and j. Again, the Lissajous rotation without actuation is shown in blue, where the force coefficient traces in Figures 6.8a,c,e,g and i in blue are the same as the blue traces in Figures 6.6a-e. For $k > 0.017$, the command given to the synthetic jet modulation waveform is modified to include a phase lag relative to the motion, such that the suppression effect is maximized. The respective amplification at that frequency is then chosen as the same command as suppression, 180° out of phase (the details about this flow control approach are discussed in Appendix **B.2**). The amplification effect is then The lowest frequency shown in Figures 6.8a and b shows the same result as in Figure 6.7, with approximately a 60% suppression and 35% augmentation in the forces, respectively, as well as a 30% augmentation and 50% suppression in the moments, respectively. This trend continues with little change in the actuation effect, and small changes in the baseline structure as the reduced frequency is increased to $k = 0.086$ (Figures 6.8c and d). When the motion is increased to near its spin instability (k increases to 0.207, see Figures 6.8e-h), the effect of the actuation *increases* from its initially invariant level that was seen in Figure 6.6. This shows the effect of the actuation changing with the orientation of the model (and possibly also with the model dynamics) similarly to what was seen previously when this model was varied under pitch and the jet momentum was held constant (cf., Chapter **III**). This new increase in control authority at $k = 0.207$ yields a force suppression of ~80% and an augmentation of ~100% (Figure 6.8g), as well as a moment augmentation of ~40% and suppression of ~80% (Figure 6.8h). Also, the shedding frequency of the model becomes noticeably coupled to the motion in Figures 6.8e-h, with a response which is approximately nine times faster than the motion in Figures 6.8e and f, and approximately eight times faster than the motion in Figures 6.8g and h. As the reduced frequency is increased above the spin resonance, the force induced by both the flow and the actuation decrease, while the moments induced by the flow and actuation appear to decrease at a slower rate, with the induced moments (Figure 6.8j) remaining a larger

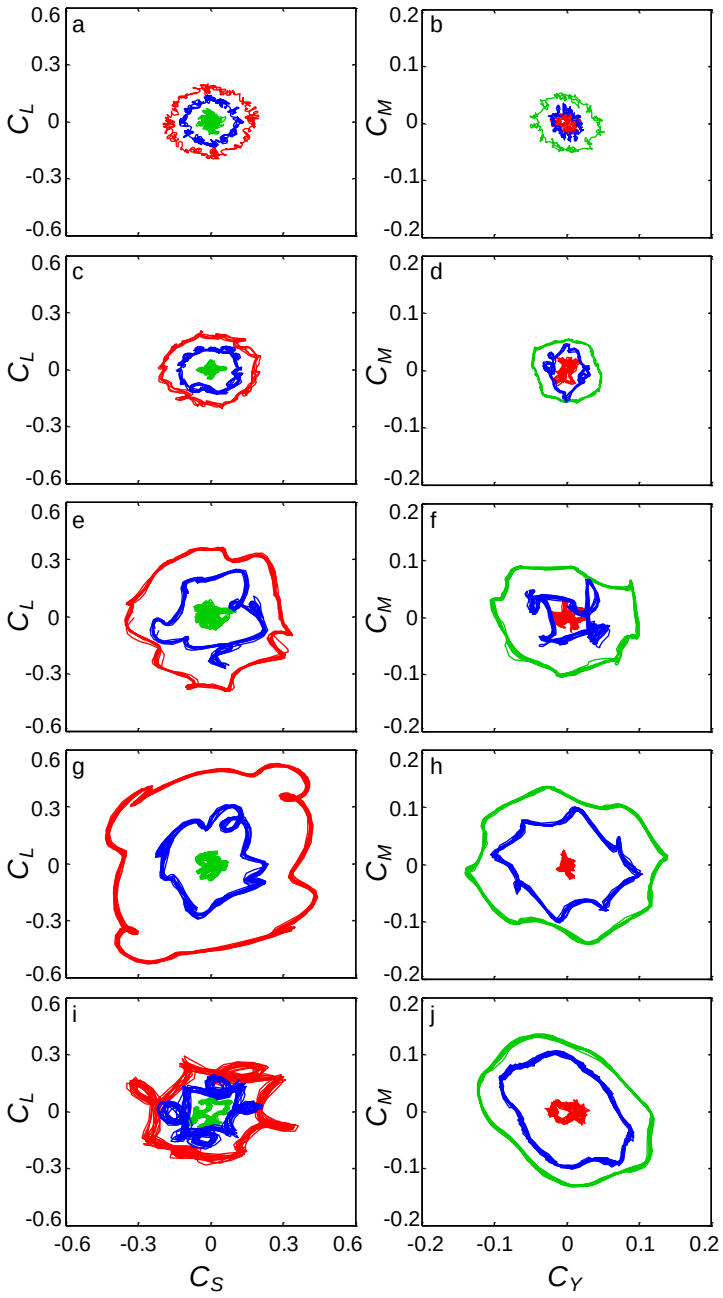

Figure 6.8. Phase plots of lift and side force coefficients (left column) and pitch and yaw moment coefficients (right column) on the model at k = 0.017 (a), 0.086 (b), 0.172 (c), 0.207 (d), and 0.259 (e) without (**blue**) and with the flow control schemes for the force suppression (**green**) and augmentation (**red**) at $Re_D = 1.8 \cdot 10^5$.

fraction of their steady moments (Figure 6.8b), when compared to the ratio of the induced forces (Figure 6.8i) to their representative steady values (Figure 6.8a).

Upon analyzing the frequency effect on the forces and actuation outcomes, the resonance case of $k = 0.207$ ($\tau_{yz} = 0.083$s or $15\,\tau_{conv}$) is selected as the representative 'highly unsteady' frequency for the remainder of this chapter. Although Figure 6.8 gives a detailed description of the forces and moments, and their changes with actuation, it does not include any information about the model attitude. To depict this further the force coefficients and moment coefficients are plotted with their respective angle of attack in Figure 6.9. Similar to Figures 6.6 and 6.8, the dataset is plotted over a 1 second measurement ($12\,\tau_{yz}$ or $180\,\tau_{conv}$), and this motion is plotted in Figures 6.9a and b with time. Again, like the steady frequency in Figures 6.7e and f, there is almost no variation in the motion with actuation, and inertia effects of the force and moment coefficients can be ignored. Each of the aerodynamic load coefficients is plotted with the angle that induces the most variation (i.e. C_L and C_M are plotted with α_y, and C_S and C_Y are plotted with α_z). Figure 6.9c shows C_S with α_z, which is comparable to the variation of C_L with α_y in Figure 6.9d, with the exception that C_S increases with negative α_z, while C_L increases with positive α_y. This sign reversal is an artifact of the coordinate system chosen (see Figure 6.1); as the model moves in positive pitch ($+\alpha_y$), the lift force increases in the $+z$ direction, but the side force increases in the $-y$ direction for the model moving in positive yaw ($+\alpha_z$). Figure 6.9e shows C_Y with α_z, which is also paired with the variation of C_M with α_y in Figure 6.9f. In this case both of the slopes are of the same sense, as the model is unstable (i.e., as the model pitches in α_y or α_z, its moment tends to be in the same sense to continue motion in the same direction). Another interesting feature is that the augmentation of force coefficients (Figures 6.9c and d in red) increases the hysteresis in the C_S vs. α_z and C_L vs. α_y paths, while suppression of the force coefficients (Figures 6.9c and d in green) decreases the hysteresis in the force vs. angle path. There is a different trend in the moment where although hysteresis in C_Y vs. α_z and C_M vs. α_y is dramatically reduced with force augmentation (Figures 6.9e and f in red), the hysteresis in C_Y vs. α_z and C_M vs. α_y is also

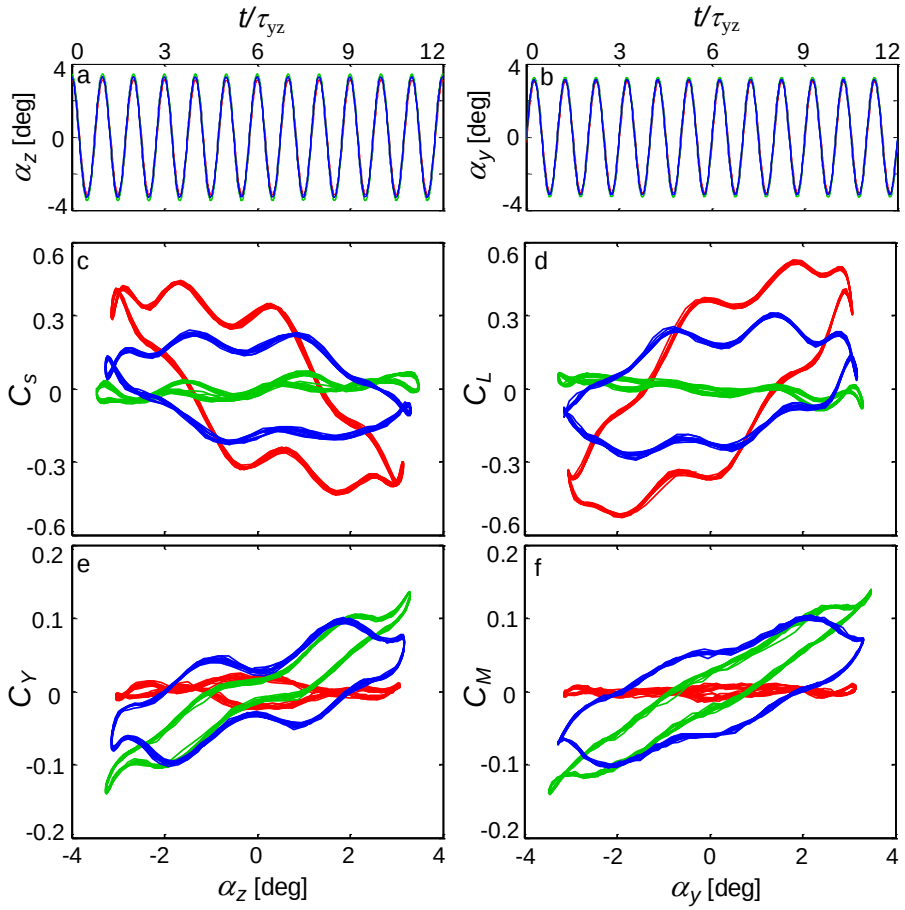

Figure 6.9. Angular motion (a,b), as well as angular variation in induced force (c-d), and moment (e-f) coefficients for k = 0.207 without (**blue**) and with the flow control schemes for the force suppression (**green**) and augmentation (**red**) at $Re_D = 1.8 \cdot 10^5$.

slightly decreased in the force suppression actuation (Figures 6.9e and f in green). The hysteresis in force and moment coefficients with angle of attack is expected in unsteady flow, as the wake response lags the model motion. In addition, the shedding frequency further affects all the dynamics seen in Figures 6.9c-f, where each trace shows a prominent higher frequency attributed to the vortex shedding.

6.3 Stationary Actuation vs. Unactuated Rotation Wake Structure

This section further investigates the wake response of the representative unsteady 1:1 Lissajous rotation (k = 0.207) depicted in Figure 6.6d. For the present investigation the wake is characterized with phase-locked PIV measurements over 600 averages and 12 phases throughout the motion cycle. The wake response lags the model motion by ~30º at

this reduced frequency which is in agreement with both the measured hysteresis in the baseline aerodynamic load measurements in Figure 6.9 as well as the prior study of phase-lag response at varying *k* in pure pitching motion conducted in Chapter **V**. For simplicity, the velocity fields chosen to represent this phase averaged wake response are the four phases where the wake deficit is most horizontally and vertically deflected at t/τ_{yz} = 0.083, 0.333, 0.583, and 0.833 (representative phases of 30º, 120º, 210º and 300º with respect to the motion, where τ_{yz} = 0.083s is the time of one motion cycle). The resulting streamwise velocity measured in these four phases is shown in Figures 6.10a-d for the furthest wake deflections in +*y*, -*z*, -*y*, and +*z*, respectively. In comparison to the baseline flow in Figure 6.2a, the effect of the wires is similar, and the wake deficit is smaller than it was when the model was stationary. In addition, the phases show symmetry as expected, where Figure 6.10a and Figure 6.10c are similar to mirror images of each other across *y* = 0, and Figures 6.10b and d are also symmetric across *z* = 0. For comparison, the streamwise wake behind the model when the sinusoidal modulation fluidic control scheme from Figure 6.5d is applied on a *stationary* model in the equivalent phases to Figures 6.10a-d are shown in

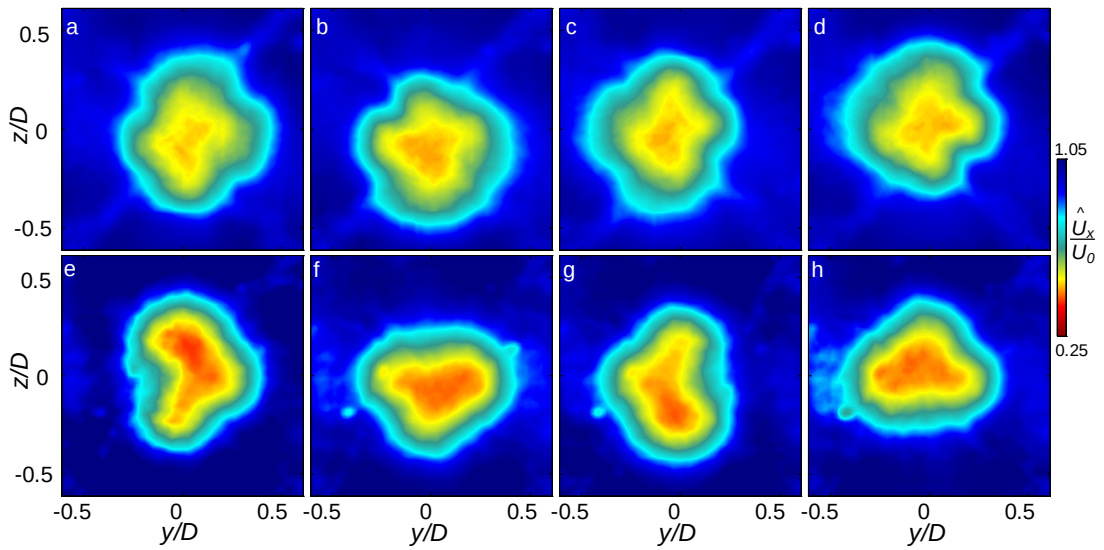

Figure 6.10. Phase-locked color raster plots of streamwise velocity component, $\hat{U}_x$, at t/τ_{yz} = 0.083(a,e), 0.333 (b,f), 0.583 (c,g), and 0.833 (d,h) for the force coefficients shown in Figure 6.8d on a stationary model with flow control actuation (a-d) and for a 1:1 Lissajous motion without flow control (e-h).

6.10e-h, respectively. There are some key differences: as the wake deficit for actuation alone is larger than the wake deficit for motion alone, and the actuation leaves a prominent concave disruption in the wake deficit on the side where the fluidic actuator is activated (see the left side of Figure 6.10e). However, these flow fields show that a similar wake to a precessing model can be induced on a stationary model with the synthetic jets, demonstrating the control authority that was observed in the forces measured in §**6.2** (compare Figures 6.10a-d with 6.10e-h, respectively). The cross-stream velocity for the motion-induced and actuation-induced flow fields are omitted as they show similar effects seen in the streamwise velocity analysis.

The wake structure of the Lissajous motion-induced and stationary actuation-induced wakes are analyzed using the same POD analysis as in Figures 6.4 and 6.5 on a 7,200 image dataset formed by appending 600 instantaneous measurements for 12 phases. The result is shown in Figure 6.11 with the streamwise velocity modes, $\vec{\varphi}_{n,u}$, for n = 1 (Figures 6.11a and e), 2 (Figures 6.11b and f), 3 (Figures 6.11c and g), and 4 (Figures 6.11d and h) of the motion-induced wakes (cf., Figures 6.10a-d) shown in Figure 6.11a-d and of the actuation-induced wakes (cf., Figures 6.10e-h) shown in Figures 6.11e-h. The first two modes of the motion-induced wakes resemble the first two modes of the baseline wake structure with a 45º rotation (compare Figures 6.11a and b with Figures 6.3a and b). This rotation of the primary sign change in the first two streamwise velocity modes shows that the preferential shedding (with highest energy) is now in the direction of yaw alone and the direction of pitch alone. It is argued that this results from the model longest residence times at its outmost positions where it moves slowest due to the nature of sinusoidal motion. This phenomenon is not observed for the actuation-induced wakes where the first two modes (Figures 6.11e and f) remain unchanged in orientation and instead only slightly change in structure from the first two modes of the baseline case (Figures 6.3a and b). A new mode that was not present in the POD modes of the baseline appears as the third strongest mode in the motion-induced in wake in Figure 6.11c which represents the increase or decrease

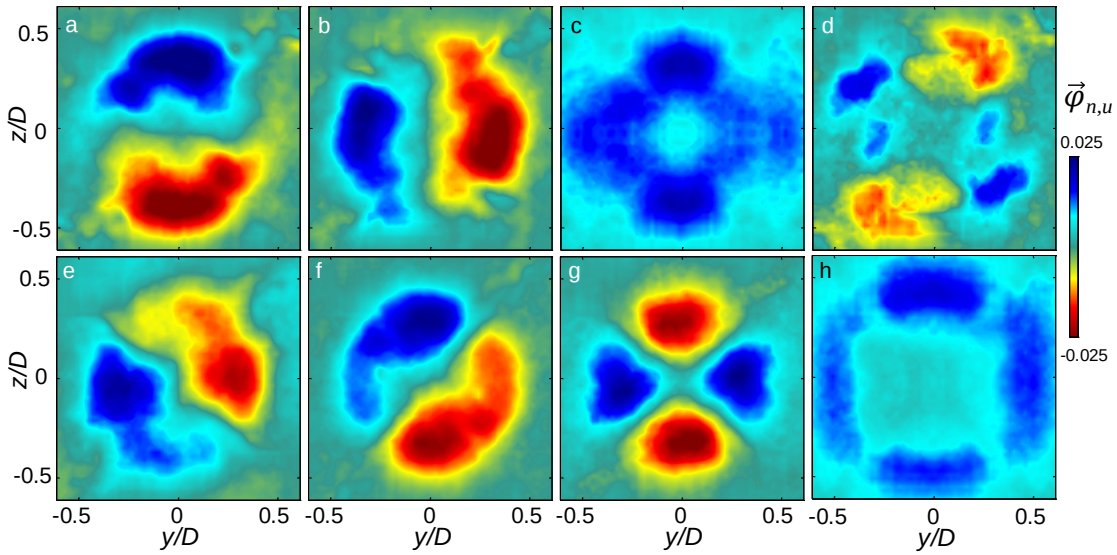

Figure 6.11. Contour plots of the POD modes n = 1 (a,e), 2 (b,f), 3 (c,g), and 4 (d,h) of streamwise velocity, $\vec{\varphi}_{n,u}$, for the equivalent Lissajous rotation without flow control (a-d, cf., Fig 6.10a-d) and for the overlapping sinusoidal modulation actuation on a stationary model (e-h, cf., Fig. 6.10e-h).

of velocity in the shear layer with respect to the free-stream and central region. This mode appears to have a similar shape to the baseline wake deficit on a stationary model (compare Figure 6.11c with Figure 6.2a), which suggests that the lack of axisymmetry in this mode may also be attributed to the model geometry. Figure 6.11d shows the fourth mode in the motion-induced wake which is similar in shape to the third mode of the baseline flow (compare Figure 6.11d and Figure 6.3c), with slight variations in structure. The third mode in the actuation-induced wake is shown in Figure 6.11c, which can be related to the fourth mode of the baseline flow (compare Figure 6.11g with Figure 6.3d). The new motion that is induced by the spinning actuation is shown in Figure 6.11h in the fourth mode, which is similar to the third mode of the motion-induced flow. This suggests that the difference that is observed between the streamwise velocity in the motion-induced wakes of Figures 6.10a-d and actuation-induced wakes of Figures 6.10e-h are synonymous with the change in shape of the dynamic modes (Figures 6.11c and g) as well as the increased energy in this mode when the wake deflection is motion-induced.

The coupling of the motion-induced and actuation-induced wakes together is investigated further in §**6.4**, and the remainder of this section considers the effect of the spinning actuation on the wake of a stationary model when the modulation frequency is increased to the model shedding frequency of k = 1.434 (commensurate with the forces measured in Figure 6.6f). However, because the overlapping sinusoidal actuation is applied at a much higher frequency, the phase lag between the wake and the actuation is increased to around ~210º, where this number was derived through the measured actuation force output and its corresponding modulation command (Figure 6.6f). Similar to the dataset in Figure 6.10, the flow fields are measured through phase-averaged PIV with 600 instantaneous realizations of 12 different phases, of which four representative phases are shown in Figure 6.12. The velocity fields chosen to represent this phase-averaged wake response are the four phases where the wake deficit is most horizontally and vertically deflected at t/τ_{yz} = 0.583 (Figures 6.12a and e), 0.833 (Figures 6.12b and f), 0.083 (Figures 6.12c and g), and 0.333 (Figures 6.12d and h), which are equivalent to phases of 210º, 300º, 30º and 120º with respect to the actuation modulation, where τ_{yz} = 0.012s is the period of one modulation cycle. The representative phases are shown in Figure 6.12 with a contour plot of the phase averaged streamwise velocity, $\widehat{U}_x$, in Figures 6.12a-d and a quiver plot of the cross-stream velocities, $\widehat{U}_y$ and $\widehat{U}_z$, in Figures 6.12e-h, with an overlaid raster plot of the streamwise vorticity, $\hat{\zeta}_x$. Clearly, there are large differences in this flow field from the equivalent actuation-induced flow field at k = 0.207 (Figures 6.10e-h), as the magnitude of the velocity deficit decreases, and the span of the velocity deficit increases. In addition, the vertical deflection of the velocity deficit region is similar to the lower frequency (compare Figures 6.12b and d with Figures 6.10b and d), but the horizontal deflection is much larger (compare Figures 6.12a and c with Figures 6.10b and d). This increased deflection in the horizontal direction is investigated further in the cross-stream velocities in Figures 6.12e-h, where in Figures 6.12e and g, a third significant counter-clockwise

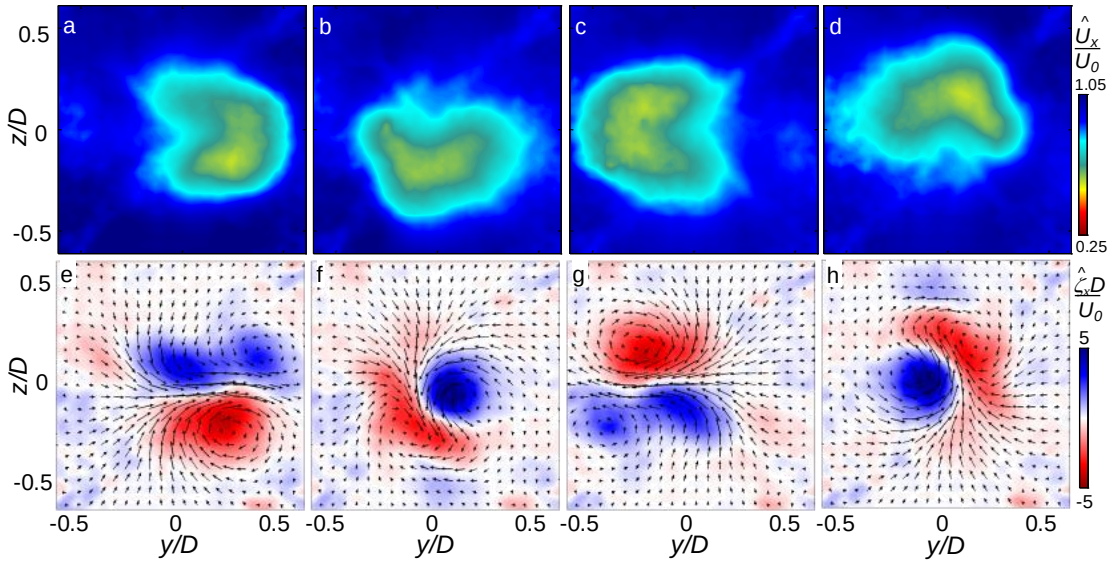

Figure 6.12. Phase-locked contour plots of streamwise velocity, $\hat{U}_x$ (a–d), and the cross-stream velocities $\hat{U}_y$ and $\hat{U}_z$ colored by the streamwise vorticity $\hat{\zeta}_x$ (e–h) at t/τ_{yz} = 0.583(a,e), 0.833 (b,f), 0.083 (c,g), and 0.333 (d,h) for the flow control actuation scheme on a stationary model, modulated at the model shedding frequency k = 1.434 (83 Hz).

vortex appears in the flow, when the streamwise velocity wake deficit is deflected horizontally. If this vortex were removed, the magnitude of the streamwise vorticity in all of the phases would look similar to each other (compare the two vortices in Figures 6.12f and h with the primary two vortices in Figures 6.12e and g). This suggests that this extra shedding vortex which could, in principle, have been formed at any angle in this field of view, due to its axisymmetry, is maintained in the yawing direction, perhaps due to slight imbalances in the strength of the actuation. This result implies that timing the fluidic actuation to the shedding frequency of the wake even when the actuation is axisymmetric (has equal commands in the pitching and yawing directions) can maintain the shedding instability in a preferential pitch-yaw direction over a much larger time scale, suggesting that with the implementation of the right sensors for detecting the flow instability these fluidic actuators may be implemented for *control* of the vortex shedding.

The structure of the wake when actuation is modulated at the shedding frequency (Figure 6.12) is also investigated analogous to the streamwise POD modes shown in Figure

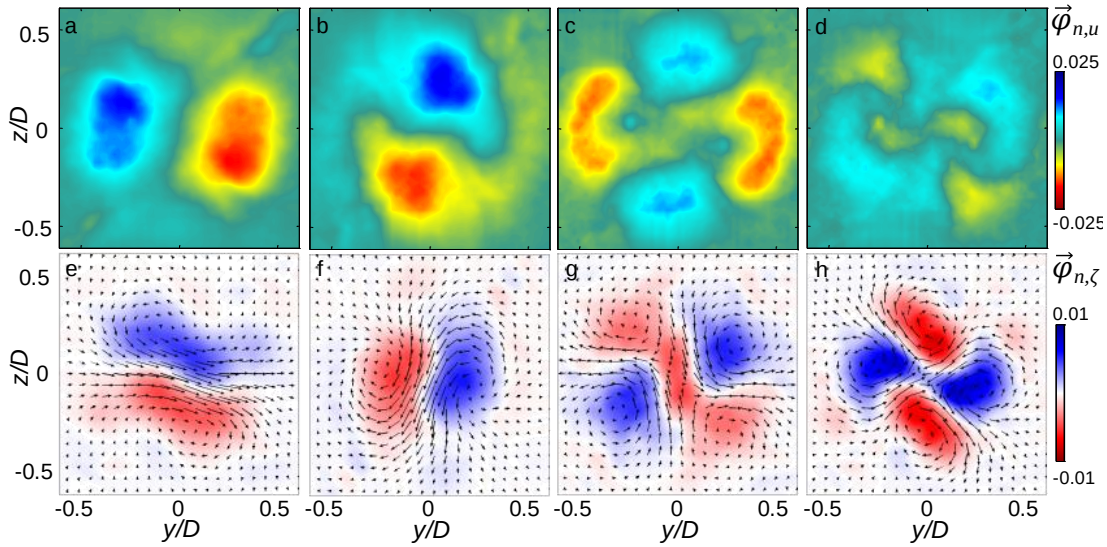

Figure 6.13. Contour plots of the POD modes n = 1 (a,e), 2 (b,f), 3 (c,g), and 4 (d,h) of streamwise velocity, $\vec{\varphi}_{n,u}$ (a–d), and the cross-stream velocity, $\vec{\varphi}_{n,v}$ and $\vec{\varphi}_{n,w}$ (e–h) colored by their streamwise vorticity, $\vec{\varphi}_{n,\zeta}$, for the flow control actuation shown in Fig. 6.12.

6.11a-d, and presented in Figures 6.13a-d. The first two modes (Figures 6.13a-b) represent a paired two-fold symmetry, similar to actuation at the lower frequency (Figures 6.11e-f), without a bias along 45º from the top, instead being biased in the pitch and yaw directions. These structures, although induced on a stationary model, clearly resemble those of the motion-induced wake of Figures 6.11a-b. Figure 6.13c and d are similar to the modes of the fourth mode of the lower frequency modulation (with weak four-fold symmetry, compare Figures 6.13c-d with Figures 6.11d), but have a more diffuse structure. The mode depicted in Figure 6.11h corresponding to the shear layer dynamics induced by the actuation at k = 0.207 is not present in the first four modes at k = 1.434. The commensurate first four modes of the cross-stream velocity are shown in Figures 6.13e-h (in the same fashion as Figure 6.4a-d on the stationary unactuated model). The addition of the new vortex in the yaw direction in Figures 6.12e and f is reflected in the fact that the first two modes in Figures 6.13e and f are now no longer rotated pairs. The mode that corresponds to shedding in the yawing direction has a secondary vortex encompassed in its mode (which is also the mode that has the most energy contribution). The second, third, and fourth

modes are more diffuse versions of similar structures observed in the unactuated flow modes with slight changes in structure (compare Figures 6.13f-h with Figures 6.4b-d). These results show that the fluidic actuation, in this scenario, does not only excite the highest energy mode, but changes its coupled spatial distribution as well.

6.4 Dynamic Model: Controlled Near-Wake Structure

This section further investigates the near wake effects of the fluidic control schemes for force suppression and augmentation on a body undergoing 1:1 Lissajous rotation at k = 0.207, synonymous with the forces depicted in Figure 6.8g and h. The application of both of these actuations are shown in Figure 6.14, with the force suppression in Figures 6.14a-d and the force augmentation in Figures 6.14e-h. This wake is characterized with phase-locked PIV measurements in the same fashion as in Figure 6.10a-d with the streamwise velocity fields, $\widehat{U_x}$, at t/τ_{yz} = 0.083 (Figures 6.14a and e), 0.333 (Figures 6.14b and f), 0.583 (Figures 6.14c and g), and 0.833 (Figures 6.14d and h), which are representative phases of 30º, 120º, 210º, and 300º with respect to the motion, where τ_{yz} = 0.083s. The force suppression actuation shown in Figures 6.14a-d is the combined effect of the Lissajous 1:1 rotation induced wake (Figures 6.10a-d) and the actuation-induced wake control scheme shown in Figures 6.10e-h run out of phase in order to have opposing effects. When the force suppression scheme is applied, wake responds to the effect of activation of the right jet (Figure 6.14a), the streamwise velocity wake deficit region develops a similar structure to when this actuation was applied on a stationary body (compare Figures 6.14a and Figure 6.10g, noting the actuation in Figures 6.10e-h is 180º out of phase with the actuation in Figures 6.14a-d). The main difference between Figures 6.14a-d and Figures 6.10e-h is that the vertical and horizontal extent of the wake deflection is altered and reduced (compare Figures 6.14a and c showing less horizontal deflection and slightly more vertical deflection to Figures 6.10g and e, and likewise compare Figures 6.14b and d to Figures 6.10f and h). With this fluidic actuation, the wake deficit region now is concave in the direction the wake would have deflected without actuation, minimizing the motion induced deflection, and

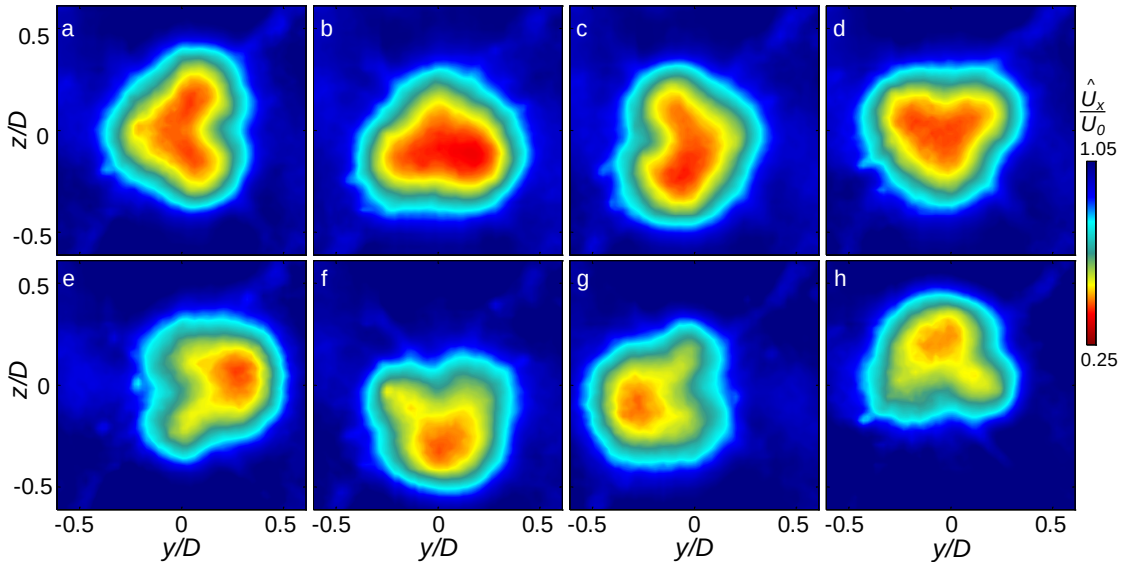

Figure 6.14. Phase-locked contour plots of streamwise velocity component, $\widehat{U}_x$, at t/τ_{yz} = 0.083(a,e), 0.333 (b,f), 0.583 (c,g), and 0.833 (d,h) for the force suppression (a-d) and the force augmentation (e-h) flow control schemes at $Re_D = 1.8 \cdot 10^5$ and $k = 0.207$.

increasing the magnitude of the wake deficit to a level similar to the baseline flow (compare Figures 6.14a-d with Figure 6.2a). Figures 6.14e-h shows the force augmentation with fluidic actuation, where the same flow control pattern of Figures 6.10e-h is applied on the model, similar to Figures 6.14a-d, except that the actuation is in phase with the motion-induced response. Figure 6.14e shows an increased deflection of the deficit in $\widehat{U_x}$ to the centerlines of $y = 0$ and $z = 0$. Because the wake response to this actuation in Figures 6.14e-h is tilted in a counter-clockwise direction compared to the nominally vertical and horizontal phases seen before in Figures 6.10a-h, the wake lags the model development by slightly more than 30º in phase measured in the baseline (i.e., the phase-averaged $\widehat{U_x}$, response lags the model to a larger extent under the force augmentation control). This increase in phase lag is commensurate with the increase in force hysteresis measured in the force augmentation case shown in red in Figures 6.9c-d relative to the unactuated case shown in blue. It is emphasized that these flow control schemes not only decoupled / enhanced the coupling of the *wake* response (shown in Figure 6.14), but they also consequently decoupled / enhanced the coupling of the aerodynamic forces from the model

motion (as shown earlier in Figures 6.9c-d), which shows substantial control authority for disturbance rejection of wake-induced forces that may potentially be implemented on this model in flight for stabilization or steering.

The unsteady wake structures of the force suppression and augmentation flow control schemes applied in Figure 6.14 for the model undergoing Lissajous rotation are analyzed with the same POD mode analysis used in Figure 6.11 and shown in Figure 6.15. The streamwise velocity modes, $\vec{\varphi}_{n,u}$, for n = 1 (Figures 6.15a and e), 2 (Figures 6.15b and f), 3 (Figures 6.15c and g), and 4 (Figures 6.15d and h) are shown for the force-suppressed wakes of Figures 6.14a-d in Figures 6.15a-d and of the actuation-induced wakes in Figures 6.14e-h shown in Figures 6.15e-h. For both the force suppression and augmentation cases, the first two modes (Figures 6.15a-b and Figures 6.15e-f) have the signature two-fold symmetry seen before in the baseline flow, actuation alone, and motion alone cases (Figures 6.3a-b, Figures 6.10a-b, and Figures 6.10e-f, respectively). However, the tilting angle of the actuated cases is modified, where the first two suppression modes are tilted counterclockwise from the baseline modes (compare Figures 6.15a-b with Figures 6.10a-b) and the first two augmentation modes are tilted in the opposite, clockwise, direction

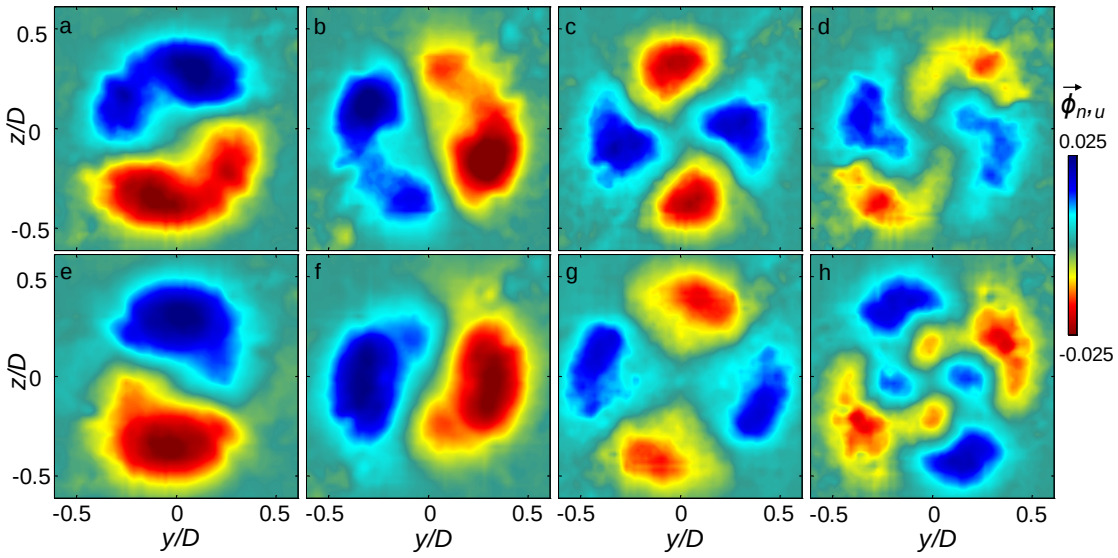

Figure 6.15. Contour plots of the POD modes n = 1 (a,e), 2 (b,f), 3 (c,g), and 4 (d,h) of streamwise velocity $\vec{\varphi}_{n,u}$ for the force suppression (a-d) and force augmentation (e-h) flow control of Figure 6.14.

(compare Figures 6.15e-f with Figures 6.10a-b). These modes in essence show that the suppression and augmentation actuations have the opposite effect on the baseline flow induced by Lissajous rotation, and the force suppression modes are altered to closer resemble the baseline modes shown in Figures 6.3a-b. Effectively, it suggests that this actuation transforms the structure of the flow around this dynamic body to a structure that is reminiscent of the flow on a static body, and is decoupling the wake from the model motion. Following the same analysis, the coupling of the flow response to the motion is enhanced with model actuation. The third and fourth mode of the suppression actuation are similar to the baseline flow as well (compare Figures 6.15c and d with Figures 6.3d and c). The respective third and fourth mode of the augmented flow show an increased tilting angle and are further spread out in the radial direction than the suppressed mode (compare Figures 6.15c-d with Figures 6.15g-h). These modes also show a progression of the wake coupling from Figure 6.15d (decoupled) to Figure 6.11d (no actuation) to figure 6.15h (increased coupling), as seen in the suppressed mode in Figure 6.15d, where the structure spreads out and new wake features develop closer to the center.

The combined result of the time development of all of the wake studies performed in this chapter are compared in Figure 6.16 through a trace of the horizontal centerline (i.e. $z = 0$ with varying y) of all twelve phase averaged PIV flow fields which are equally spaced phases in time. All of these y-t data sets are taken with a frequency of actuation or motion set to $k = 0.207$ ($\tau_{yz} = 0.083$) at a $Re_D = 1.8 \cdot 10^5$ and $x/D = 1.9$ (i.e., one diameter downstream of the aft end of the model). The measured phase averaged velocities $\widehat{U_x}$, $\widehat{U_y}$, and $\widehat{U_z}$, are shown in Figures 6.16a-e, 6.16f-j, and 6.16k-o, respectively, and the measured streamwise vorticity, $\widehat{\zeta_x}$, is shown in Figures 6.16p-t. The wake responses of a stationary model without actuation (seen previously in Figure 6.2) and with actuation (seen previously in Figures 6.10e-h) are shown in Figures 6.16a,f,k, and p, and Figures 6.16b,g,l, and q, respectively. The wake responses of a dynamic 1:1 Lissajous rotating model are shown

without actuation (Figures 6.16c,h,m and r), with force suppression actuation (Figures 6.16d,i,n, and s), and with force augmentation actuation (Figures 6.16e,j,o, and t). The analysis is focused on two aspects of the applied flow control: ***i)*** the appropriate actuation on a stationary model (Figures 6.16b,g,l, and q) can successfully mimic the effect dynamic motion has in the wake downstream of an axisymmetric bluff body (Figure 6.16c,h,m, and r), and ***ii)*** timed fluidic actuation on a dynamic body can significantly decouple the wake response from the motion response, or alternatively enhance this coupling. These effects are clearly demonstrated in $\widehat{U_x}$, where the extent of the time development of the wake deficit on a stationary model resembles the wake deflection from the dynamic model (compare Figures 6.16b and c). If the fluidic actuation in Figure 6.16b is applied out of

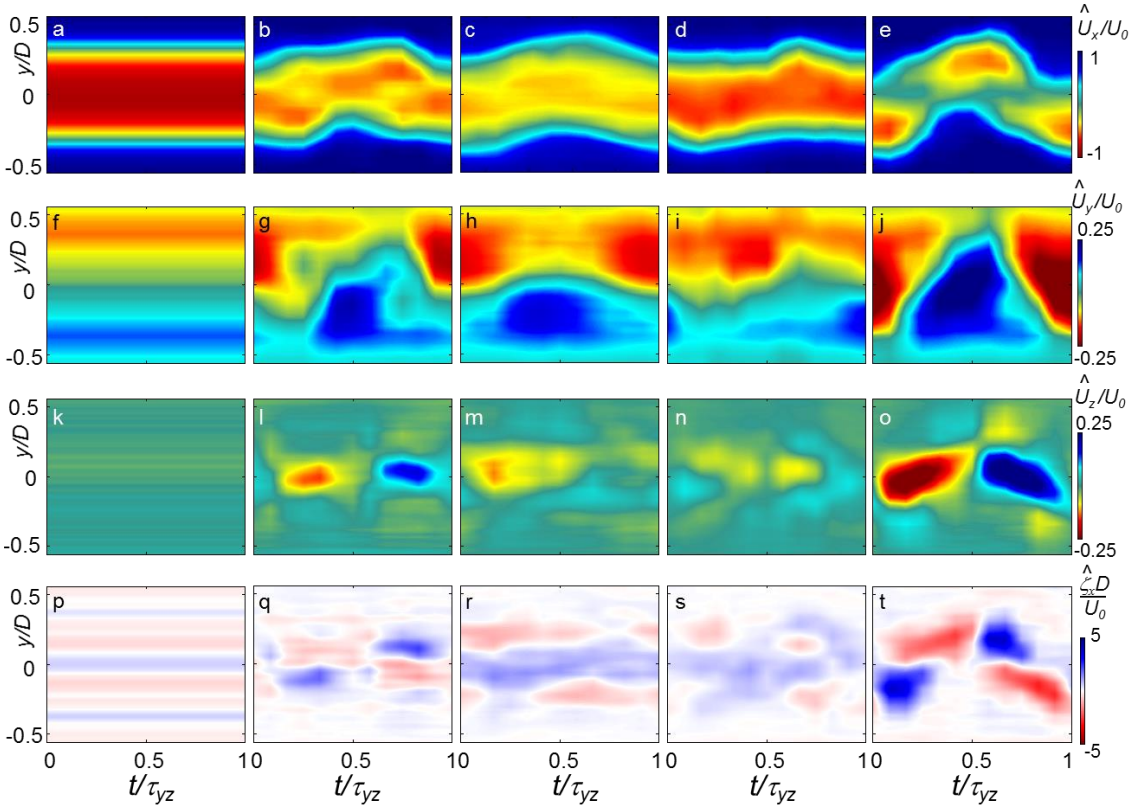

Figure 6.16. Time resolved streamwise velocity $\widehat{U}_x$ (a-e), cross-stream velocities $\widehat{U}_y$ (f-j) and $\widehat{U}_z$ (k-o), and the $\hat{\zeta}_x$ (p-t) along the horizontal symmetry line (z = 0) at x/D = 1 downstream of the aft end of the model, for the stationary model without (a,f,k,p), and with (b,g,l,q) spinning sinusoidal modulated actuation, and the model moving with 1:1 Lissajous rotation at 3º for unactuated (c,h,m,r), suppression (d,i,n,s), and augmentation (e,j,o,t) flow control, with all datasets at k = 0.207 and $Re_D = 1.8 \cdot 10^5$.

phase with the model rotation in Figure 6.16d, the wake becomes decoupled and resembles the wake of a static body without actuation (compare Figures 6.16a and d), and if the fluidic actuation is in phase (Figure 6.16e), the deflection of the velocity deficit is larger with the model motion (i.e., the coupling is enhanced). The cross-stream velocity, $\widehat{U_y}$, shown in Figures 6.16f-j which is in-line with the actuators that effect the horizontal centerline of the wake shows the largest changes when actuation is present (in Figures 6.16g, i, and j) which dominate the motion-induced wake (Figure 6.16h), even for the force suppression case which causes a slight reduction in the deflection of $\widehat{U_y}$, but is still smaller than the reduction of the deflection in $\widehat{U_x}$. The force augmentation introduces the largest values of $\widehat{U_y}$ (see Figure 6.16j), which is larger than the effect of $\widehat{U_y}$ in the actuation alone (Figure 6.16g) and motion alone (Figure 6.16h) combined. The cross-stream velocity, $\widehat{U_z}$, shown in Figures 6.16k-o has the smallest variation of all the velocity components, and shows slight deviations with actuation (compare Figures 6.16k and l) or with motion (compare Figures 6.16k and m), that seem to slightly decrease with force suppression (Figure 6.16n) or to significantly enhance with force augmentation (Figure 6.16o). The streamwise vorticity, $\widehat{\zeta_x}$, is shown in Figures 6.16p-t which initially has a band structure commensurate with the weak eight lobe structure seen before in Figure 6.3b shown in Figure 6.16p. Upon actuation (Figure 6.16q), $\widehat{\zeta_x}$ changes into a two-band structure which switches sign when actuation is effecting the wake (at t/τ = 0.083 and 0.583, respectively). This structure is far less organized when the model is rotating without actuation (Figure 6.16r) where there appears to be a three-band structure with the outer bands severed at the extremes of motion. For the force suppression actuation scheme shown in Figure 6.16s, $\widehat{\zeta_x}$ changes into a predominant weak counterclockwise field with little structure. Alternatively, with force augmentation actuation the two band structure shown with actuation is reintroduced except the clockwise $\widehat{\zeta_x}$ lobes are the dominant features (compare Figures 6.16t and q).

The final figure in this chapter summarizes the effects of all the actuation and rotational motion studied in a spinning motion through tracking the centroid of the respective wake deficit regions (which are defined by having a velocity magnitude of $|\overrightarrow{U}| < 0.8U_o$). This centroid location is extracted as y_c and z_c, in the PIV interrogation plane, $1D$ behind the model aft end, and is converted into a wake angle with respect to the center of model motion as $\theta_y = \text{atan}\left(\frac{y_c}{1.9D}\right)$, and $\theta_z = \text{atan}\left(\frac{z_c}{1.9D}\right)$ where $1.9D$ is the streamwise position of the wake measurements relative to where the model pivots as it rotates. Figure 6.17 shows these two representative angles of the velocity deficit region plotted against each other with the model undergoing Lissajous rotation (Figure 6.17a, in closed symbols), and on a stationary model with applied actuation (Figure 6.17b in open symbols). The moving model without actuation at $k = 0.207$ is shown in blue in Figure 6.17a, and the application of force suppression and augmentation actuations are shown in green and red, respectively. In addition, there are representative markers in each data trace: the triangle represents when the Lissajous motion and sinusoidal modulation actuation strategies (shown in Figures 6.5a

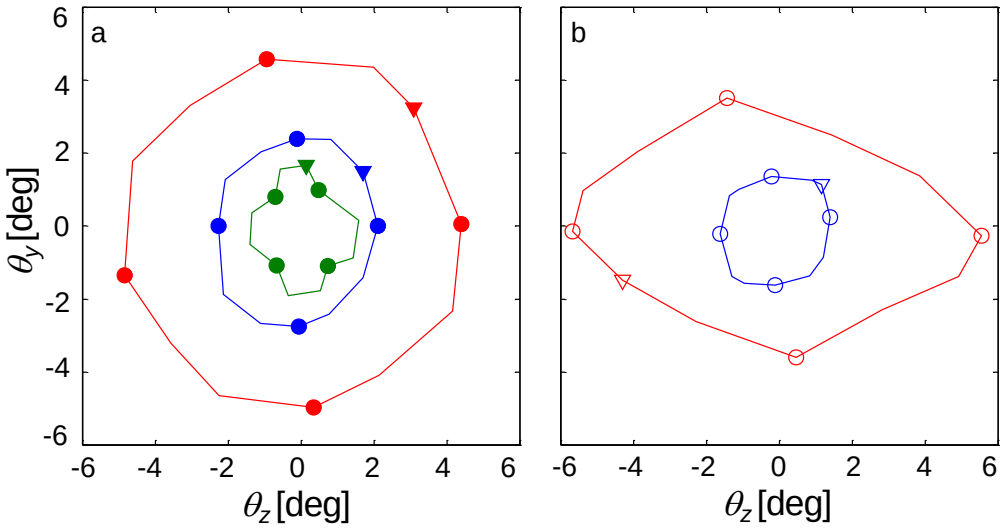

Figure 6.17. Angular deflection of the centroid (θ_y, θ_z) of the wake region defined by $|\vec{U}| < 0.8U_o$ for the $k = 0.207$ moving model without (**blue**), and with force suppress (**green**), and augment (**red**) actuations (a), and the stationary model with actuation modulation at $k = 0.207$ (**blue**) and 1.434 (**red**) (b).

and d, respectively) are first applied in time, and the circles mark phases that were used to illustrate the corresponding PIV flow fields of the actuation (i.e., the wake deflections shown in blue circles in Figure 6.17a correspond to the phase averaged flow fields in Figures 6.10a-d). Figure 6.17a clearly shows that upon augmentation actuation (red), the wake deflection is increased by ~80% (from a ~2.5º to ~4.5º radius of deflection) of the unactuated value, and likewise the suppression actuation reduces the wake deflection by ~40% (from an ~2.5º to ~1.5º radius of deflection) of the baseline value. The change in phase response of the augmented wake observed in Figure 6.14 is clearly present in Figure 6.17a, as the red curve is tilted counterclockwise. In addition, the wake angles, θ_y with θ_z, of the suppressed wake centroid do not trace a circular path in time, where the actuation appears to have more of an effect near the points shown in circles (which is also when a maximum single jet actuation effect occurs in the wake, as opposed to a combination of two jet effects). However, these results still demonstrate substantial control authority, similar to what was seen in the lift and side forces in Figure 6.9. Figure 6.17b shows the deflection of the wake of the stationary model with the spinning actuation at $k = 0.207$ (blue) and $k = 1.434$ (red). These data show that the wake of a stationary model can be effectively controlled to a similar level as a dynamic model that is pitching and yawing out of phase (in this case, the actuation induced a ~1.5º radius of deflection in the wake, which was 60% of the dynamic model ~2.5º). The red trace in Figure 6.17b shows the coupling of the fluidic actuation to the natural shedding frequency (commensurate with Figure 6.12), where the phase lag of the actuation onset is approximately 210º from the first PIV phase presented. This result shows that in addition to controlling forces induced by the body dynamics, these actuators have the potential to control forces induced by the natural shedding frequency as well, which can possibly be implemented to increase stabilization (or steering) control authority of airborne bodies in future work.

CHAPTER VII

FREE 3-DOF MODEL: RESPONSE AND CONTROL

Building on the control authority of the present actuation approach on the aerodynamic loads and the near wake dynamics as discussed in Chapter **VI**, this chapter demonstrates the utility of this flow control approach for controlling the model's dynamics in 'free' 3-DOF motion (pitch, yaw, and roll, cf., Chapter **2.6**). The model's flow-induced base instability is characterized in §**7.1**. The effects of open-loop actuation on the dynamics of the model are investigated in §**7.2** and compared with the 1-DOF motion response (cf., Chapter **4.3**). A closed-loop flow controller (described in Appendix **B.3**) is used for prescribing desired trajectories in pitch and yaw (regardless of roll orientation) in §**7.3** and the results are compared with attitude control of the 1-DOF model (cf., Chapter **4.4**) and with the controlled wake dynamics of a rotating model (cf., Chapter **6.4**). Finally, §**7.4** describes a DMD analysis of the wake structure and dynamics when the model is controlled in pitch and yaw to a desired attitude.

7.1 Dynamic Response of the Freely Precessing Model

A primary objective of the present research is to investigate the receptivity of the coupled body/wake motion to flow manipulation in examples of free flight and effect the desired attitude characteristics that overcome the natural response to the flow. To begin with, the baseline response of the 3-DOF freely precessing (roll, pitch, and yaw) model to its interaction with the embedding flow is characterized in detail, with coordinate systems for the model, and its sting support, defined in Chapter **II** (cf., Figure 2.18). In the present investigations, the Reynolds number of the model is high enough so that initial flow perturbations (e.g., by coupling to its near wake) rapidly amplify, and the model oscillates within a finite envelope of vertex angles between its centerline and the flow direction. In

free motion, small asymmetries in the model enclosure and non-uniform friction effects in the gimbal bearing can bias the temporal variations in the vertex angle. In the present experimental setup, the mounting wires to the sting that supports the model are not spaced equally in the azimuthal direction in order to control the sting roll angle, and, as a result, the sting is slightly less stable in yaw than in pitch. In the absence of flow control, this slight asymmetry causes the model time periodic oscillations to be directionally biased in yaw. An illustration for an oscillation is shown in Figure 7.1 at $U_o = 28$ m/s ($\tau_{conv} = c/U_o = 5.9$ ms, $Re_D = 1.62 \cdot 10^5$). Figures 7.1a, c, and e show an eight-second time trace of the model angular positions in α_x (roll), α_y (pitch), and α_z (yaw), respectively, and the corresponding spectra (frequency resolution of 0.05 Hz) are shown in Figures 7.1b, d, and f. Each of these traces exhibits distinct frequency and amplitude responses in roll

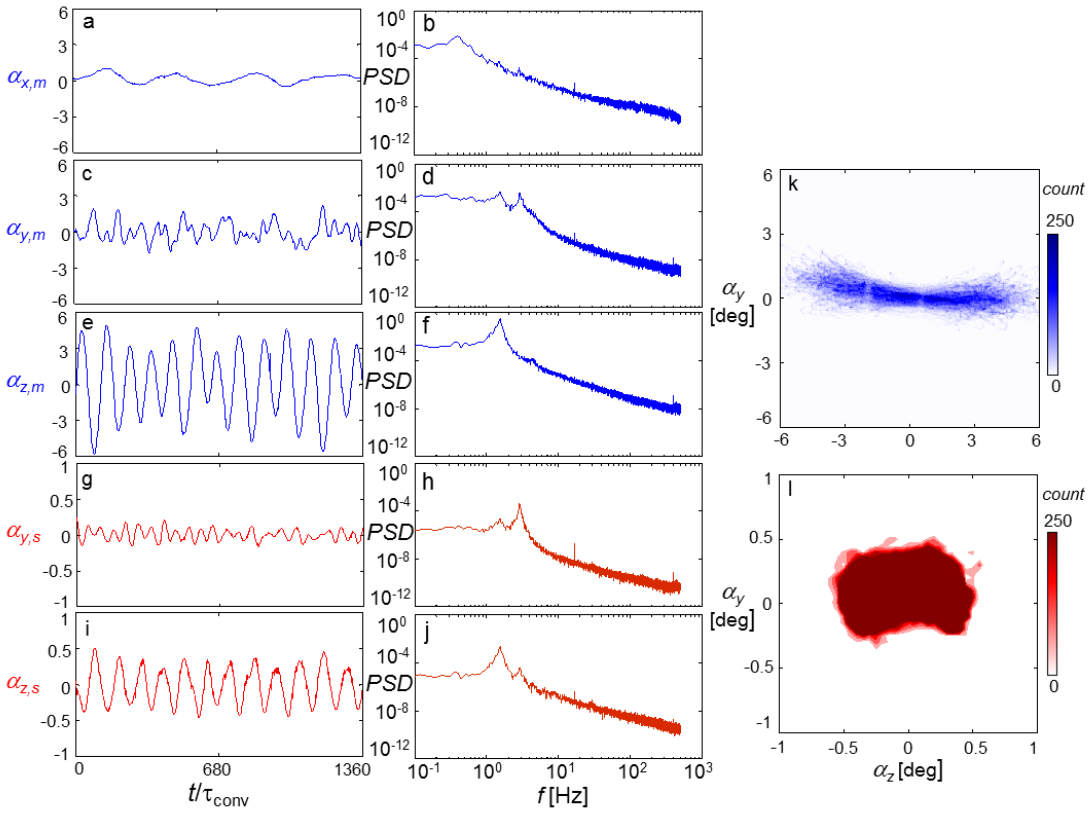

Figure 7.1. Flow induced dynamics of the model (in **blue**) and sting (in **red**) at $Re_D = 1.62 \cdot 10^5$ for instantaneous time traces of roll (a), pitch (c,g) and yaw (e,i), and their respective power spectra (b,d,f,h,j), along with histograms of the respective pitch and yaw over 25 measurements (k,l).

(f_x = 0.4 Hz, 0.7°), yaw (f_z = 1.55 Hz, 5.2°), and pitch (f_y = 2.90 Hz, 1.5°), with a characteristic baseline period that is defined off of the average time of a yaw cycle: τ_z = 0.65 s (approximately $110\,\tau_{conv}$). These data show that the characteristic pitch frequency is two times the higher than the corresponding yaw frequency and the pitch spectrum also contains a second peak at the yawing frequency. Although the support sting is commanded to be held stationary, Figures 7.1g and i show that the sting pitch and yaw angles vary with amplitudes of 0.25° and 0.5° respectively, and the spectra of the sting motion (Figures 7.1h and j) contain the model yaw and pitch frequencies indicating the model and sting are indeed coupled (§**7.3** shows that this coupling can be effectively enhanced or suppressed with actuation). The data for the base motion of the model are binned into a 2-D histogram of the yaw and pitch angles over 200 seconds ($34{,}000\,\tau_{conv}$ or $310\,\tau_z$ with a bin width of $\Delta\alpha_y = \Delta\alpha_z = 0.05°$) and plotted for the model (Figure 7.1k) and sting (Figure 7.1l). These histograms show that the model undergoes its maximum pitch excursion at the extremes of the yawing angle, and its path is more exaggerated in yaw than the sting (compare the scatter in Figures 7.1k and l).

The root-mean-square (RMS) amplitudes of oscillation in roll ($\alpha_{x,RMS}$, Figure 7.2a), pitch ($\alpha_{y,RMS}$, Figure 7.2b), and yaw ($\alpha_{z,RMS}$, Figure 7.2c), vary with Re_D, and are shown for the sting (red) and model (blue) throughout $1.32\cdot10^5 < Re_D < 1.92\cdot10^5$ using $310\,\tau_z$ records. Figure 7.2a shows the roll amplitude which has the smallest excursion, approximately twice as small as the pitch response and significantly smaller than the yaw response, although it grows throughout the measured range of Re_D. Figures 7.2b and c show that the RMS of the sting pitch and yaw, as well as the model pitch, increase with Re_D throughout the range $1.32\cdot10^5 < Re_D < 1.92\cdot10^5$. The model yaw however (the primary excursion) only increases to $Re_D = 1.62\cdot10^5$, with a maximum RMS level of 4° (about 5.6° amplitude), and then decreases to 3.1° (about 4.4° amplitude) at $Re_D = 1.92\cdot10^5$. Throughout the entire range of Re_D, the pitch to yaw ratio of the model increases (from

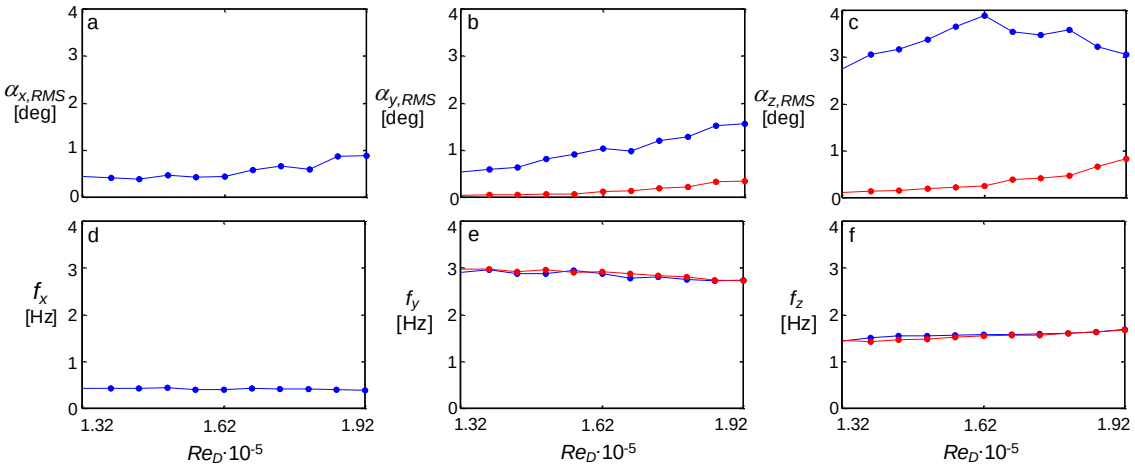

Figure 7.2. Variations of the model (**blue**) and sting (**red**) average RMS amplitude (a-c) and characteristic frequency (d-f) in roll (a,d), pitch (b,e), and yaw (c,f) with Reynolds number.

17% at $1.32 \cdot 10^5$ to 55% at $1.92 \cdot 10^5$), while the pitch to yaw ratio of the sting remains nearly invariant (about 42%) indicating that the asymmetries in the experimental setup become less relevant at higher wind speeds. The corresponding variation of the characteristic frequencies (f_x, f_y, f_z) with Re_D for both the sting and model responses are shown in Figures 7.2d-f in roll, pitch, and yaw, respectively. Figure 7.2d shows the roll excursion is approximately six times slower than the pitch disturbance and three times slower than the yaw disturbance. Figure 7.2e shows that the disturbance frequency of the model and the sting in pitch is the same, suggesting that the flow initially disturbs the coupled model-sting system together and the difference in amplitude develops afterwards. Figure 7.2f also shows the matching disturbance frequency between the model and sting in yaw, but in addition shows the yawing frequency grows with Re_D (as opposed to Figure 7.2e where the pitching frequency decays with Re_D), indicating that the disturbance frequencies in pitch and yaw are not harmonics of each other even though they differ by nearly a factor of two. The majority of the remaining investigations are conducted at $Re_D = 1.62 \cdot 10^5$ for which the sting dynamics are considered stable and negligible (having an amplitude of less than 0.25°).

The near wake behind the unactuated model at $Re_D = 1.62 \cdot 10^5$ is measured using SPIV (cf., Figure 2.21b) yielding a time resolved (500 Hz) 3-D velocity field including the streamwise (U_x) and cross-stream velocities (U_y and U_z) velocity components, in the *x*, *y*, and *z* directions, respectively. The interrogation region is placed in the *y*-*z* plane at $x/c = 0.9$ (or $0.25D$ downstream of the aft end of the model), spanning $1.8D$ in *y* and in *z* ($y = \pm 0.9D$, and $z = \pm 0.9D$, centered about the streamwise axis of the model gimbal). The instantaneous measurements are not always resolved over the full interrogation window, (depending on the seeding particle density), and therefore the recorded set of 2,500 images is reconstructed out of the first 20 modes of a proper orthogonal decomposition (POD) algorithm of the wake, which is discussed in detail in Appendix **A.1**.

Following the POD reconstruction of the flow field, the streamwise vorticity, ζ_x, is calculated for each instantaneous velocity field. Figures 7.3a-d show an instantaneous reconstructed flow field with velocity components U_x (Figure 7.3a), U_y (Figure 7.3b), U_z (Figure 7.3c) and ζ_x (Figure 7.3d) using color raster maps on a 55×55 grid. The key features in this flow field are the velocity deficit at the center of the streamwise direction (Figure 7.3a), and inner and outer layers of cross-stream velocities of opposing senses (Figure 7.3b and Figure 7.3c). Because the primary oscillation is in the yaw direction, the horizontal velocity (U_y) is typically larger in magnitude than the vertical velocity (U_z). The corresponding vorticity field (Figure 7.3d) also has two dominant concentrations of opposing sign, although the dominant magnitudes typically coincide with the largest cross-stream velocity (compare Figures 7.3b and d). In order to characterize the time-dependence of the flow behind the model (and later characterize the differences effected by the actuation), four-second time traces of *u*, *v*, *w*, and ζ_x along the *y* axis ($-0.75 < y/D < 0.75$ and $z/D = 0$ in Figures 7.3a-d), and the z axis ($-0.75 < z/D < 0.75$ and $y/D = 0$ in Figures 7.3a-d) are shown in Figures 7.3e-h and Figures 7.3i-l, respectively. The time evolution of the streamwise velocity shown in Figures 7.3e and i shows a primary deviation in the horizontal centerline, comparable to the yaw dynamics, and a secondary deviation in the

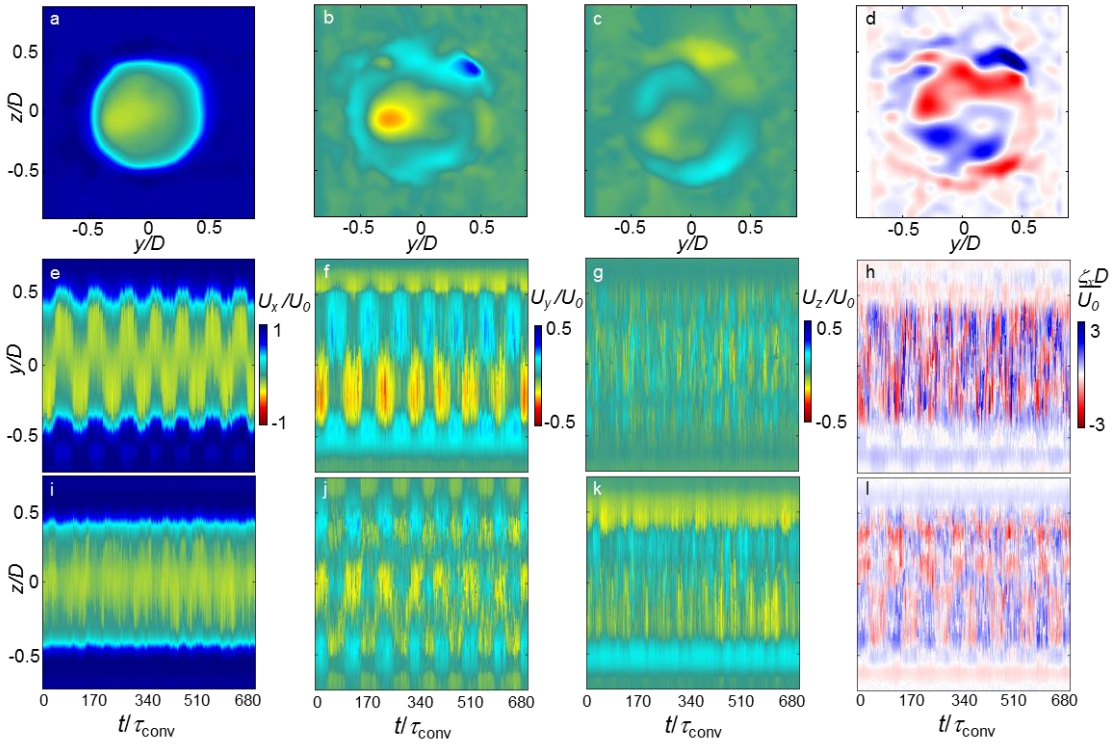

Figure 7.3. An instantaneous snapshot of the wake behind the unactuated model (a-d), and time-traces of the horizontal centerline (e-h) and vertical centerline (i-l) streamwise U_x (a,e,i), and cross-stream U_y (b,f,j) and U_z (c,g,k) velocity components, and streamwise vorticity (d,h,l) at $Re_D = 1.62 \cdot 10^5$.

vertical centerline comparable to the pitch dynamics (compare Figure 7.3e with Figure 7.1e, and Figure 7.3i with Figure 7.1c). Other features are in the horizontal centerline U_y (Figure 7.3f), and the vertical centerline U_z (Figure 7.3k) components, both of which have an outer layer where flow is advected towards the center, and an inner layer whose sign of oscillation depends on the pitch and yaw location of the model, where the magnitude of these regions approach 30% of the freestream speed. By comparison, these effects are smaller and more diffused in the horizontal centerline U_z (Figure 7.3g) and vertical centerline U_y (Figure 7.3j) although still with a periodic pattern that is aligned with model motion. An interesting feature of this wake is that the horizontal centerline vorticity has the same structure as the vertical centerline velocity even though it is measured in different locations (compare Figure 7.3k and Figure 7.3h), and the same holds for the horizontal velocity and vertical vorticity (compare Figure 7.3f and Figure 7.3l). This suggests that

part of the driving aerodynamic force that maintains the instability in the model yaw (as well as horizontal wake development) is induced by the structure of the streamwise vorticity concentrations in the vertical direction.

The POD modes of the subset of $\vec{\varphi}_n$ that correspond to the streamwise velocity, $\vec{\varphi}_{n,u}$ are shown in Figure 7.4a-g with n = 1-7, respectively, along with the energy contribution of these modes (Figure 7.4h). The first mode shown in Figure 7.4a which represents the yaw instability in the wake is 9% of the total energy, and has approximately three times the next modal energy. The second mode (Figure 7.4b) represents the pitch instability and is similar to a rotated version of the first mode, with 3% of the total energy. The next four modes (Figures 7.4c-f) have a similar structure with a central velocity contribution and two dominant external contributions which are attributed to fluctuations in the shear layer. The seventh mode is a two-lobe structure which has a preferential shedding in the diagonal direction which is similar to a mode observed in the fixed spin trajectory model (cf., Figure 6.3a in Chapter **VI**) when the model was in a fixed stationary centered position, which has a diagonal directional preference in the modes that is attributed to the preferential shedding off of the aft end model due to the actuators and Coanda surface.

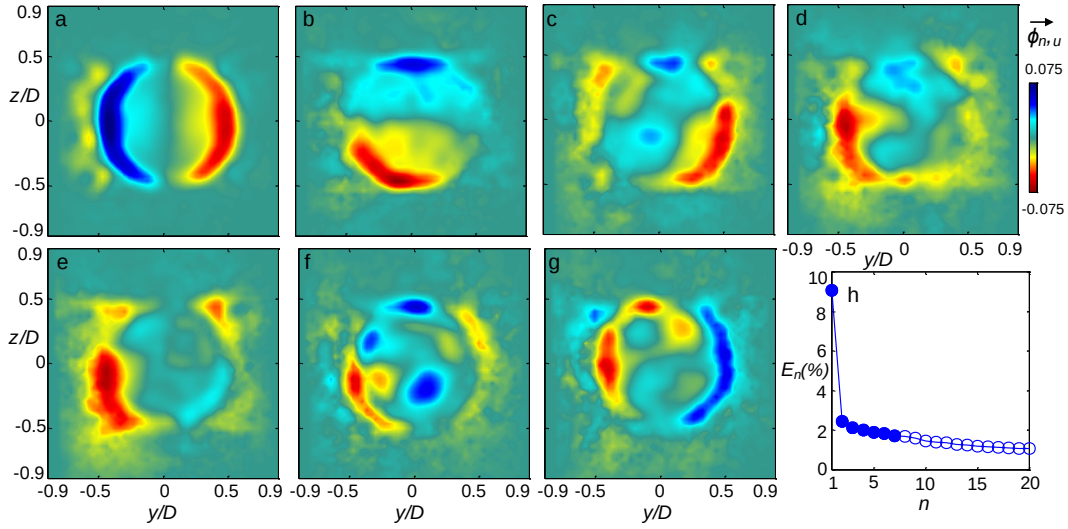

Figure 7.4. Contour plots of the streamwise velocity POD modes, $\vec{\varphi}_{n,u}$, with mode number n = 1 (a), 2 (b), 3 (c), 4 (d), 5 (e), 6 (f), and 7 (g), and the energy distribution (h) of the modes for the base flow at $Re_D = 1.62 \cdot 10^5$.

The cross-stream velocity modes, $\vec{\varphi}_{n,v}$ and $\vec{\varphi}_{n,w}$, and their respective normalized vorticity, $\vec{\varphi}_{n,\zeta}$, are plotted in Figure 7.5 with the first seven modes, similar to Figures 7.4a-g. The pairing of the first and second mode seen in the streamwise velocity in Figures 7.4a and b is observed in the cross-stream velocities in Figures 7.5a and b, each with predominant counter-rotating vorticity concentrations, where the counter-rotating concentration pair in the vertical direction in Figure 7.5a effect a larger area of the wake. In the cross-stream velocity modes, it becomes apparent that modes 3 (Figure 7.5c) and 6 (Figure 7.5f) are rotated pairs with an internal vertical structure that is centered between two external opposing vortices. Likewise, modes 4 (Figure 7.5d) and 5 (Figure 7.5e) are rotated pairs with an internal vorticity concentration that is off center from two external vorticity pairs. The modes 3-6 are associated with the shear layer dynamics as mentioned in the discussion of Figures 7.4d-f, but the cross-stream modes primarily indicate whether the flow fluctuations cross through the center of the wake (modes 3 and 6 in Figure 7.5c and f), or are asymmetric about the center of the wake (modes 4 and 5 in Figure 7.5d and e). Although the streamwise velocity component of the seventh mode was similar to a

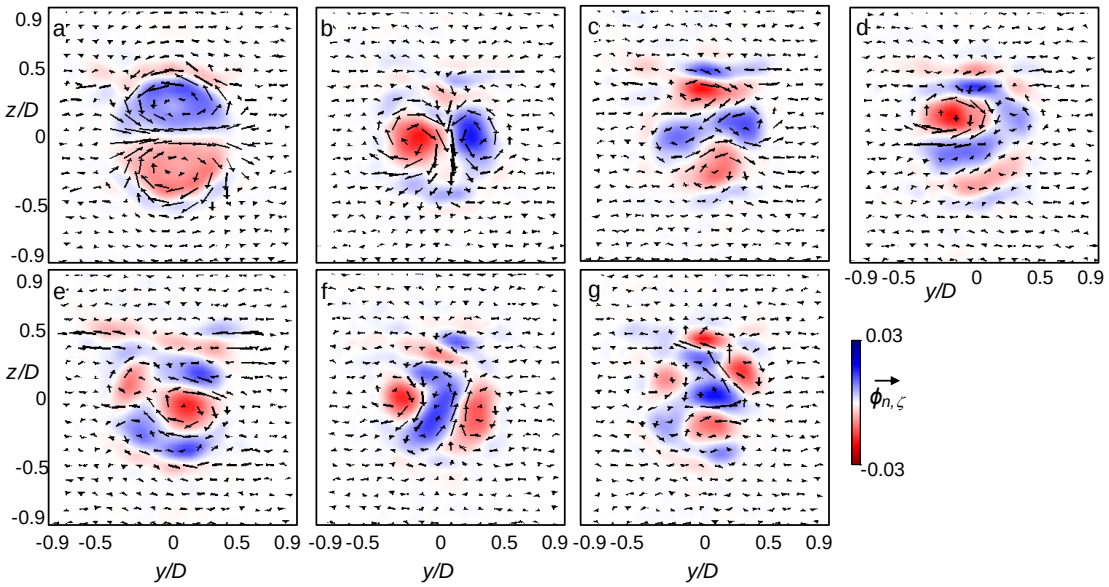

Figure 7.5. Quiver plots of the cross-stream velocities' POD modes, $\vec{\varphi}_{n,v}$ and $\vec{\varphi}_{n,w}$, with mode number n = 1 (a), 2 (b), 3 (c), 4 (d), 5 (e), 6 (f), and 7 (g), colored by their streamwise vorticity, $\vec{\varphi}_{n,\zeta}$, for the base flow at $Re_D = 1.62 \cdot 10^5$.

mode observed on the stationary model, the commensurate cross-stream velocity component of this mode is significantly different (Figure 7.5g), having four counter-rotating vorticity pairs instead of a single one that spreads across the entire wake. This difference is attributed to the vorticity structure breaking up and becoming less organized when the wake drives model oscillation as opposed to when the model is constrained to a fixed, centered orientation.

7.2 Open-Loop Actuation

The effect of open-loop actuation is investigated at U_o = 28 m/s ($Re_D = 1.62 \cdot 10^5$) using single-jet or four-jets control. Instantaneous pitch (α_y) and yaw (α_z) angles of the model are measured over sampling intervals of three seconds where actuation is activated $t = 0$. The angular velocities, $\dot{\alpha_y}$ and $\dot{\alpha_z}$, as well as the corresponding accelerations are computed from time series of the angles and used to compute the aerodynamic moments on the model using Equation (2.2) in Chapter **II**. The pitch and yaw moment coefficients (C_M and C_Y) are then calculated from these moments as $C_{M,Y} = \frac{M_{y,z}}{\frac{\pi}{8}\rho U^2 D^2 c}$. Phase plots of the angular velocities and aerodynamic moments plotted against the instantaneous angle (in both pitch and yaw) are shown in Figure 7.6 in three separate regimes: unactuated in black ($-170 < t/\tau_{conv} < 0$), 'transient' in cyan ($0 < t/\tau_{conv} < 170$), and the controlled dynamics in blue ($170 < t/\tau_{conv} < 340$). Figures 7.6a, b, e, and f show single-jet actuation while Figures 7.6c,d,g, and h show four-jets actuation, with phase plots of the pitch rate (Figures 7.6a and c), yaw rate (Figures 7.6b and d), pitch moment (Figures 7.6e and g), and yaw moment (Figures 7.6f and h). Although the motion excursion is significantly larger in yaw than in pitch, the magnitudes of the unactuated moments are similar; the maximum in the pitch moment is approximately 80% of the yaw moment without actuation. In addition, the baseline yaw moment response (Figures 7.6f and h, black trace) agrees with the yaw response of the model constrained to a free 1-DOF yaw motion (cf., Chapter **IV**). Upon activating single-jet control (jet 3, where the jets are numbered in Figure 2.17), α_y gains a

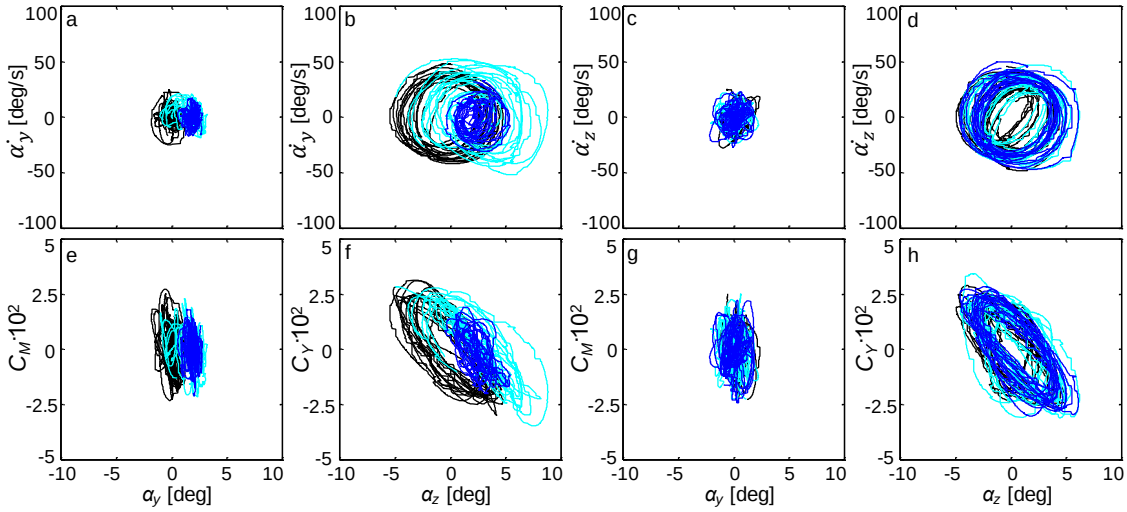

Figure 7.6. Phase plots of 10 instantaneous traces of the model pitch rate, $\dot{\alpha}_y$ (a,c), yaw rate, $\dot{\alpha}_z$ (b,d), and moment coefficients, C_M (e,g) and C_Y (f,h), for open loop actuation by a single jet (a,b,e,f) and all four jets (c,d,g,h) for t/τ_{conv} = -170 to 0 (black), 0 to 170 (**cyan**), and 170 to 510 (**blue**) after the onset of actuation at a fixed C_μ = 0.003 and $Re_D = 1.62 \cdot 10^5$.

bias of 2° and decreases in the fluctuations in position and velocity of about 40% (Figure 7.6a), and in its moment by about 30% (Figure 7.6e). A similar trend occurs in α_z, with a bias of 2° and decreases in fluctuations of its position and velocity of about 60% (Figure 7.6b), and of its moment by about 50% (Figure 7.6f). Although the transient behavior in α_y shown in cyan is a somewhat direct transition between the unactuated and actuated states, α_z instead has a significant amount of overshoot, with a growth of amplitude from 5.5° to 7° about a bias of 2° and then a collapse into its developed amplitude of 2.5°. This transition from the unactuated flow to the new developed amplitude occurs in about 1 second (approximately 1.5 baseline oscillation periods, τ_z, and 170 convective time scales, τ_{conv}). In contrast, four-jets actuation (Figures 7.6c, d, g and h) does not have a well-defined state transition, where the actuated dynamics appear to be similar to the unactuated model with a slight increase of the fluctuations in α_z and $\dot{\alpha}_z$ during the transition (see Figure 7.6d and h) and almost no changes in pitch (see Figures 7.6c and h). The significance of the lack of change in the system response with four-jets actuation, along with the overshoot

and temporary increased vibrations with activation of an open-loop single-jet, shows the need for timed actuation in controlling this free responding model, which is discussed further in the closed-loop control section, §**7.3**. This result is unlike the two-jet control in Chapter **4.3**, where suppression of the oscillation occurred, and this is presently attributed to the effects of the extra two jets (e.g, in the two-jets case for a yawing motion the reduction of oscillations might be decreased if the two out-of-plane jets were activated).

The wake behind the model upon the onset of the open-loop actuations shown in Figure 7.6 is analyzed using the time-dependent PIV measurements along the wake *y* and *z* axes that are shown in Figures 7.7a-h and Figures 7.7i-l for single-jet and four-jets actuation, respectively. These data are presented in a similar fashion to Figures 7.3e-l over a four-second time trace ($680\,\tau_{conv}$), with actuation applied at $t = 0$. First, the single-jet actuation is analyzed in detail in Figures 7.7a-h (control is applied using jet 1, rather than jet 3 in Figure 7.6), which leads to an attitude bias in $-\alpha_y$ and $+\alpha_z$, and can be clearly observed in Figures 7.7a and e, with the model wake having a bias in $+y$ and $+z$ by about 10 mm each. The time evolution of the U_x velocity for the single-jet actuation shows a reduction of the wake oscillation by about 40% at $t = 340\,\tau_{conv}$ and about 70% at $t = 510\,\tau_{conv}$ in the horizontal direction (Figure 7.7a), while the oscillation amplitude does not noticeably change in the vertical direction (Figure 7.7e). This development of the wake deficits in the horizontal and vertical directions is comparable with the development of the yaw and pitch angular velocities (compare Figure 7.7a with Figure 7.6b and Figure 7.7e with 7.6a). The U_y component of the wake velocity in the horizontal centerline is altered by the jets from its initially symmetric distribution by losing its negative *v* band at $y/D = 0.5$ and gaining a large region of positive *v* (see Figure 7.7b). The actuation also develops a 'rolling' feature in the wake with a $-U_y$ component at $z/D = 0.5$, and a $+U_y$ component at $z/D = -0.5$. This rolling feature is not observed in the horizontal wake centerline, and similar to the baseline flow, the U_z component of the wake is not significant on the horizontal centerline (cf., Figure 7.7c and Figure 7.1g). The U_z component in the vertical direction is similar to the

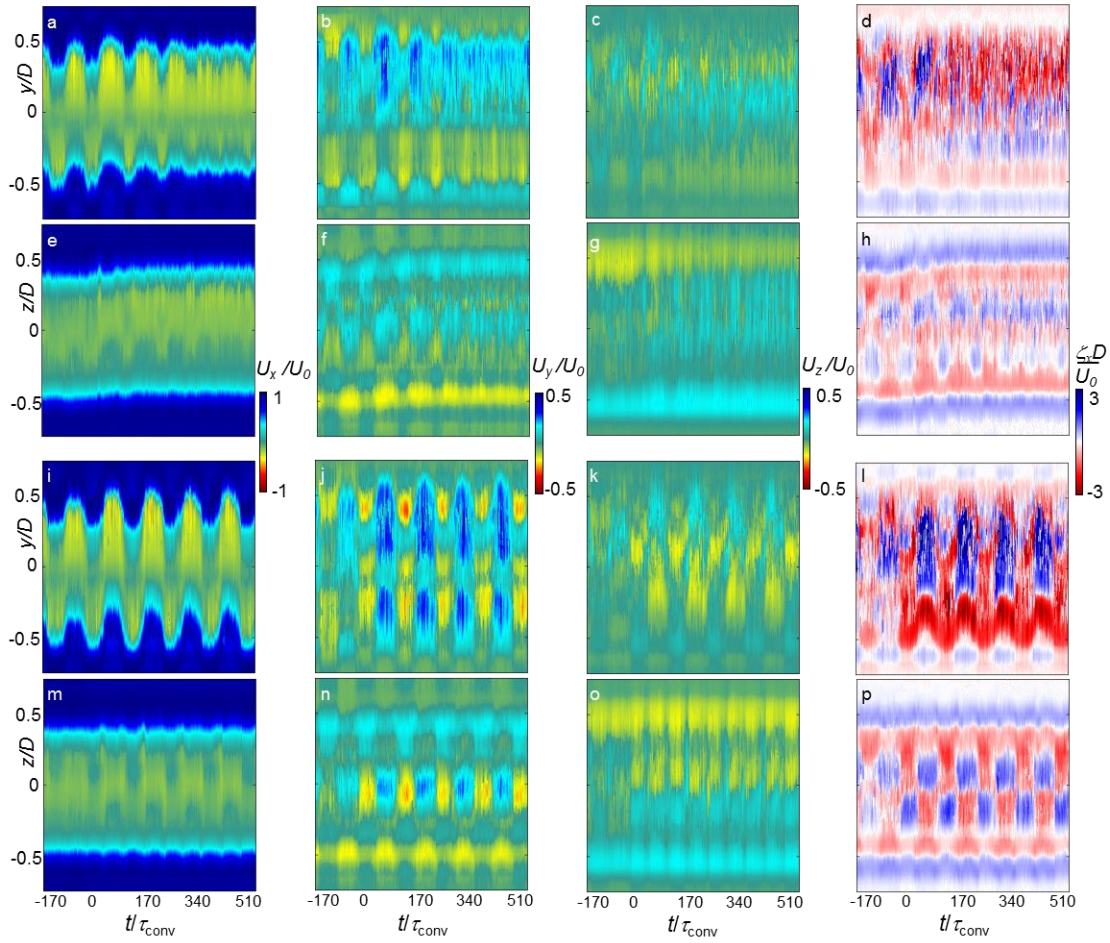

Figure 7.7. The time-traces of the horizontal centerline (a-d, i-l) and vertical centerline (e-h, m-p) streamwise, U_x (a,e,i,m), and cross-stream U_y (b,f,j,n) and U_z (c,g,k,o) velocity components, and streamwise vorticity z_x (d,h,l,p) for the open-loop single-jet (a-h) and four-jets (i-p) actuation applied at $t = 0$, at a fixed $C_\mu = 0.003$ and $Re_D = 1.62 \cdot 10^5$.

U_y component in the horizontal direction where it is also dominated by a $+U_z$ component throughout the wake, but this added positive velocity region is added in the inner wake, and the -*w* band at $z/D = 0.5$ remains intact. The streamwise vorticity, ζ_x, becomes more organized in the horizontal centerline of the wake (Figure 7.7d), where the time-dependent oscillations of vorticity develop into a predominantly negative ζ_x at $y/D > 0$, and bands of alternating signs of ζ_x for $y/D < 0$, which are roughly time-invariant. Figure 7.7h shows that the structure of ζ_x does not have a significant change in the vertical centerline, and primarily is only translated in the +*z* direction. Next, the open-loop four-jets actuation is shown in Figures 7.7i-p. For this actuation, the oscillation of the location of the wake

deficit increases in both y and z, as shown in Figures 7.7i and m, respectively. The horizontal centerline U_y component shown in Figure 7.7j shows the introduction of oscillating negative and positive regions with magnitudes larger than the baseline, with a slightly larger positive component attributed to slight mismatches in the strength of the synthetic jet actuators. Similar to the single-jet, the four-jets actuation develops a 'rolling' feature in the wake seen by the $-U_y$ component at $z/D = 0.5$, and a $+U_y$ component at $z/D = -0.5$ in Figure 7.7n. The corresponding baseline U_y component has bands of the same sense, and did not have the 'rolling' feature in the vertical centerline (see Figure 7.3j). The cross-stream U_z components of the wake in both the vertical and horizontal centerlines are similar to the baseline flow, with a notable increase in magnitude in the inner wake region ($|y/D| < 0.4$ in Figure 7.7k, and $|z/D| < 0.4$ in Figure 7.7o). This trend is also true with the vorticity, seen in Figures 7.7l and p, where the structure remains similar to the baseline with an increased magnitude in the inner wake, except this increase is significantly more substantial in the horizontal centerline as opposed to the vertical centerline (compare Figures 7.7l and p).

The POD modes of the wake behind the model with open-loop actuation are calculated using the wake data that was used in Figure 7.7 (using 2,500 images over a five-second trace, or $850\,\tau_{conv}$, or $7.7\,\tau_z$). The streamwise component of these modes, $\vec{\varphi}_{n,u}$ is shown in Figure 7.8 for the open-loop single-jet (Figures 7.8a-e) and the four-jets (Figures 7.8f-j) actuation with $n = 1$ (Figures 7.8a and f), 2 (Figures 7.8b and g), 3 (Figures 7.8c and h), 4 (Figures 7.8d and i), along with the energy contribution of these modes (Figures 7.8e and j). Single-jet open-loop actuation leads to three new streamwise velocity modes that were not observed in the absence of actuation, where the only repeating mode is attributed to the yaw instability (compare Figure 7.8b and Figure 7.4a), but this mode now has the second highest energy contribution, as opposed to the dominant contribution (dropping from 9% in the baseline to 5.5%). The new highest energy mode in Figure 7.8a is most comparable to the unactuated pitch instability mode (Figure 7.4b), except that the entire mode is rotated

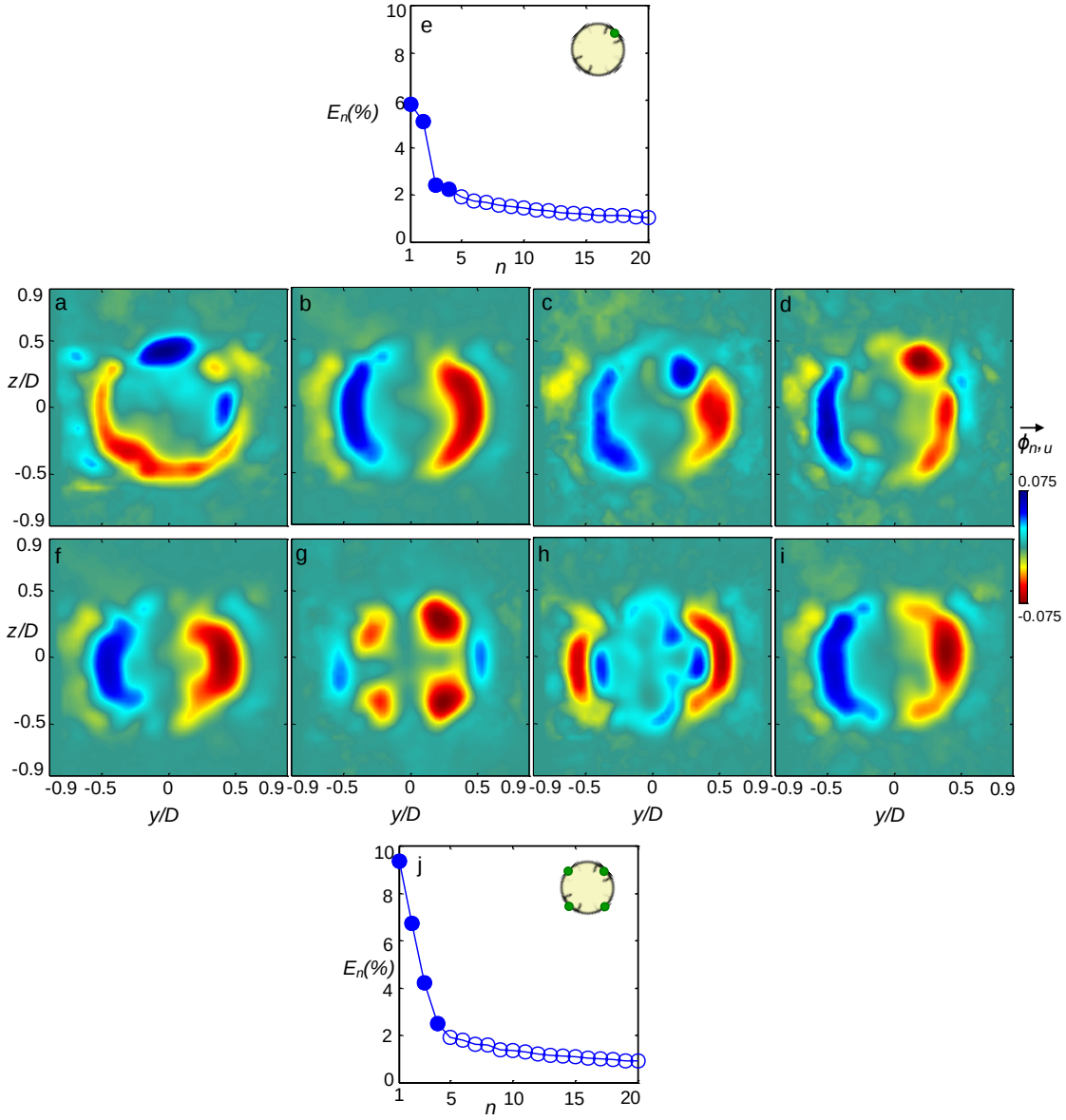

Figure 7.8. Contour plots of the streamwise velocity POD modes, $\vec{\varphi}_{n,u}$, with mode number n = 1 (a,f), 2 (b,g), 3 (c,h), and 4 (d,i) for open-loop single-jet (a-e), and four-jets (f-j) actuations, and the energy distribution of the modes (e,j) for $Re_D = 1.62 \cdot 10^5$.

by about 45°, while the top right velocity lobe is severed in a location which coincides with the active jet. The third and fourth modes in Figures 7.8c and d are both variations of the unactuated yaw instability mode, with a severed velocity distribution is downstream of the active jet, where the difference between these modes is determined by the severed velocity concentration sense, which is either the opposite (Figure 7.8c) or the same (Figure 7.8d) as

the unactuated mode. Compared to the unactuated flow, the 9% energy in the baseline yaw instability is redistributed to three different mode shapes with varying influence by the active jet (mode 2-4), while the pitch mode is energized from 3% to 6%, with a change in shape due to the active jet, becoming a new dominant mode. Four-jets actuation compresses the highest energy unactuated mode in the *z* direction, but remains intact with a similar energy percentage of the flow (see Figures 7.8f and j). In addition, a secondary mode that resembles the highest energy baseline mode appears as mode 4 (compare Figures 7.8i and 7a). Modes 2 (Figure 7.8g) and 3 (Figure 7.8h) are two new modes that are not present in the unactuated flow and are attributed to continuous jet actuation, where mode 2 shows a four-lobe distribution downstream of the active jets (with an additional velocity concentration in the $\pm y$ extremes, attributed to the oscillation of the model). The shape of mode 3 is a central lobe that is concave at the location of the jets, surrounded by an external velocity distribution of opposing sense in the $\pm y$ direction but absent in the $\pm z$ direction. The energy distribution after applying the four-jets control has some differences from the baseline energy distribution (compare Figures 7.8j and 7h), where it introduces two new high energy modes (mode 2 and 3) and has more energy in its yaw fluctuations (between mode 1 and 4) which is commensurate with the slight model yaw oscillation growth upon actuation observed in Figures 7.6d and h, and Figure 7.7i.

In order to characterize the new dynamic states of the model achieved with open-loop actuation (beyond the transitory state), multiple different open-loop actuation programs are applied. These programs are recorded over 25 instantaneous traces, each at $t = 340\,\tau_{conv}$ to $1700\ \tau_{conv}$ following the onset of actuation ($34000\,\tau_{conv}$ total data), and the data are binned into a histogram of the resulting model yaw and pitch coordinates (with a bin width of $\Delta\alpha_y = \Delta\alpha_z = 0.05°$), which is the same as in Figures 7.1k and l. Five open-loop actuation programs are investigated in Figure 7.9: single-jet (Figure 7.9b), two adjacent jets in the pitch direction (Figure 7.9c), two opposite jets (Figure 7.9d), two adjacent jets in the yaw direction (Figure 7.9e), and four-jets (Figure 7.9f). Figure 7.9a shows the flow in the

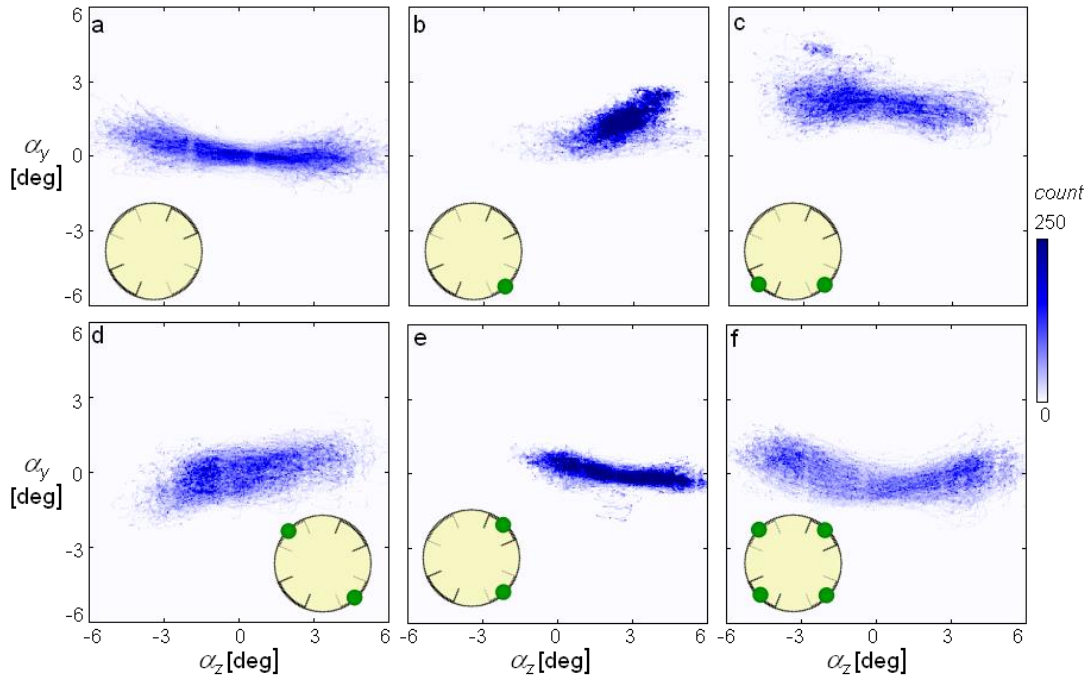

Figure 7.9. Spatial histograms of flow-induced dynamics of the model over 25 instantaneous measurements of 680 τ_{conv} for the unactuated flow (a), along with actuation by open-loop single-jet (b), two adjacent jets in the pitch direction (c), two opposite jets (d), two adjacent jets in the yaw direction (e), four-jets (f), at $Re_D = 1.62 \cdot 10^5$.

absence of actuation using the data in Figure 7.1k, and is included for reference. The application of single-jet control shown in Figure 7.9b biases the motion by about 2° yaw and 1.5° in pitch, and reduces the oscillation by about 60% (in agreement with Figures 7.6b and 7.7a), and this offset direction depends on which jet is activated (jet 3 is active in Figure 7.9b), where different offsets can be implemented by utilization of different jets. Upon activation of the lower two jets (jets 2 and 3, Figure 7.9c), the model becomes biased at about 2.5° in pitch and centered in yaw, while its yaw oscillations are reduced by 20% while its pitch oscillations are increased by 5%. When the right side jets are active (jets 1 and 3, Figure 7.9e), the model becomes biased at about 2.5° in yaw, while remaining approximately centered in pitch, and its oscillation amplitude is reduced by 40% in both yaw and pitch. Figure 7.9d shows the effect of two opposing actuators (jets 3 and 4), where the actuation effectively rotates the α_y with α_z response (the slope changes from -0.23 to

+0.31, compare Figures 7.9a and d), but the yaw amplitude is only reduced 25%, while the pitch amplitude is not significantly altered. Finally, four-jets actuation has a slightly detrimental response, increasing the oscillation amplitudes in yaw and pitch by about 5% and 10%, respectively (in agreement with the data shown in Figures 7.6c, d, g, and h, and Figures 7.7i-p). The induced dynamics in Figures 7.9d and f show that the effects of open-loop actuation on the model dynamics are less pronounced when the active jets are opposite to each other.

7.3 Closed-Loop Precession Control

For this 3-DOF model, a closed-loop coupled PID feedback controller was designed to provide command signals to the synthetic jets which is discussed in detail in Appendix **B.3**. The effect of this closed-loop feedback driven controller is initially examined at U_o = 28 m/s ($Re_D = 1.62 \cdot 10^5$) with two different control algorithms aimed at holding the model at center and to amplify its pitch, and they are evaluated using the same procedure depicted in Figure 7.6. Figures 7.10a, b, e, and f show the flow controller activated with a goal of holding the model at $\alpha_y = \alpha_z = 0°$, and Figures 7.10c, d, g, and h show the control goal of amplifying the pitch motion, with phase plots of the pitch (Figures 7.10a and c), yaw (Figures 7.10b and d) rates, and pitch (Figures 7.10e and g), and yaw (Figures 7.10f and h) moments. Upon activation of the 'hold-center' control, the model achieves a new state of ±1° in both pitch and yaw within about 0.1 seconds (approximately $0.15\,\tau_z$ or $17\,\tau_{conv}$) regardless of where the control started in the model motion cycle. This is equivalent to a reduction of the model oscillation by 35% in pitch (Figure 7.10a) and 83% in yaw (Figure 7.10b). The commensurate moments, C_M and C_Y, are each reduced to ±0.015, or an equivalent reduction of 33% (Figure 7.10e) and 50% (Figure 7.10f), respectively. For the pitch amplification goal (Figures 7.10c, d, g, and h), the resulting controlled motion has the interesting feature that $\dot{\alpha_y}$ and C_M begin to resemble a larger amplitude version of the unactuated $\dot{\alpha_z}$ and C_Y (compare the actuated traces in Figures

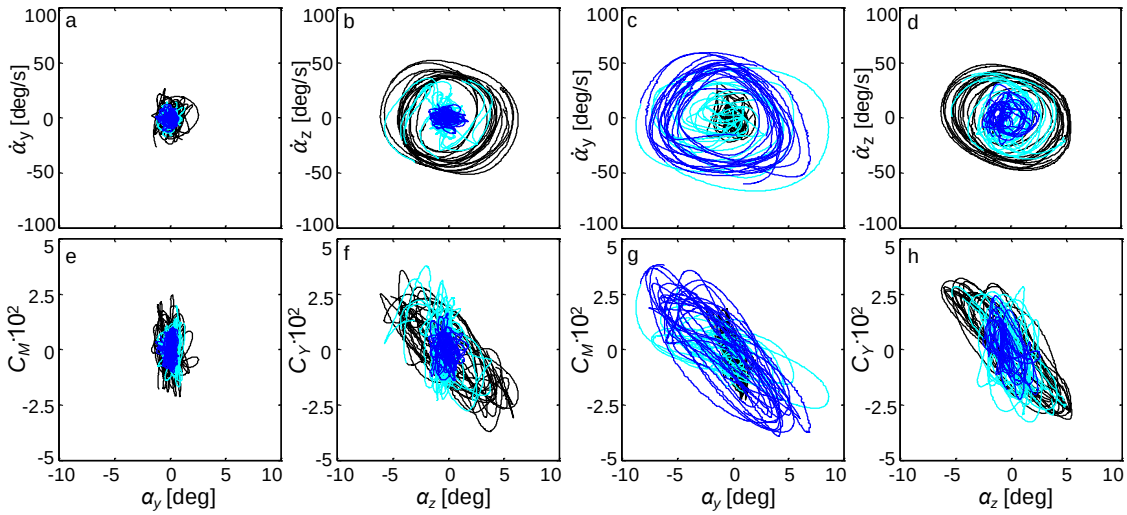

Figure 7.10. Phase plots of closed-loop actuations: hold-center (a,b,e,f) and amplify-pitch (c,d,g,h) presented in the same fashion as the data in Figure 7.6 using a maximum $C_\mu = 0.003$.

7.10c and g to the unactuated in Figures 7.10d and h). Furthermore, the controlled yaw response during pitch amplification resembles the uncontrolled pitch response (compare the actuated traces in Figures 7.10d and h to the unactuated in Figures 7.10c and g). The combination of these two control algorithms shows that with appropriate feedback control the direction of the baseline instability in this model can be effectively rotated or even minimized.

The evolution of the near wake upon the onset of the closed-loop actuation shown in Figure 7.10 is analyzed in detail in Figure 7.11, with the PIV-measured time development of the wake centerlines presented in Figures 7.11a-h and Figures 7.11i-l for hold-center and pitch amplification control cases, respectively. These data are presented in a similar fashion to the data for open-loop actuation in Figures 7.7a-l. For the hold-center actuation, the horizontal and vertical wake deficits shown in Figures 7.11a and e are immediately transitioned into a higher frequency response of about 4 Hz, where the extent of the horizontal oscillation is significantly reduced, with a slight increase in the vertical extent. This higher frequency response continues in the cross-stream velocities U_y and U_z, which have a similar actuation structure to the baseline flow, with a much higher periodic

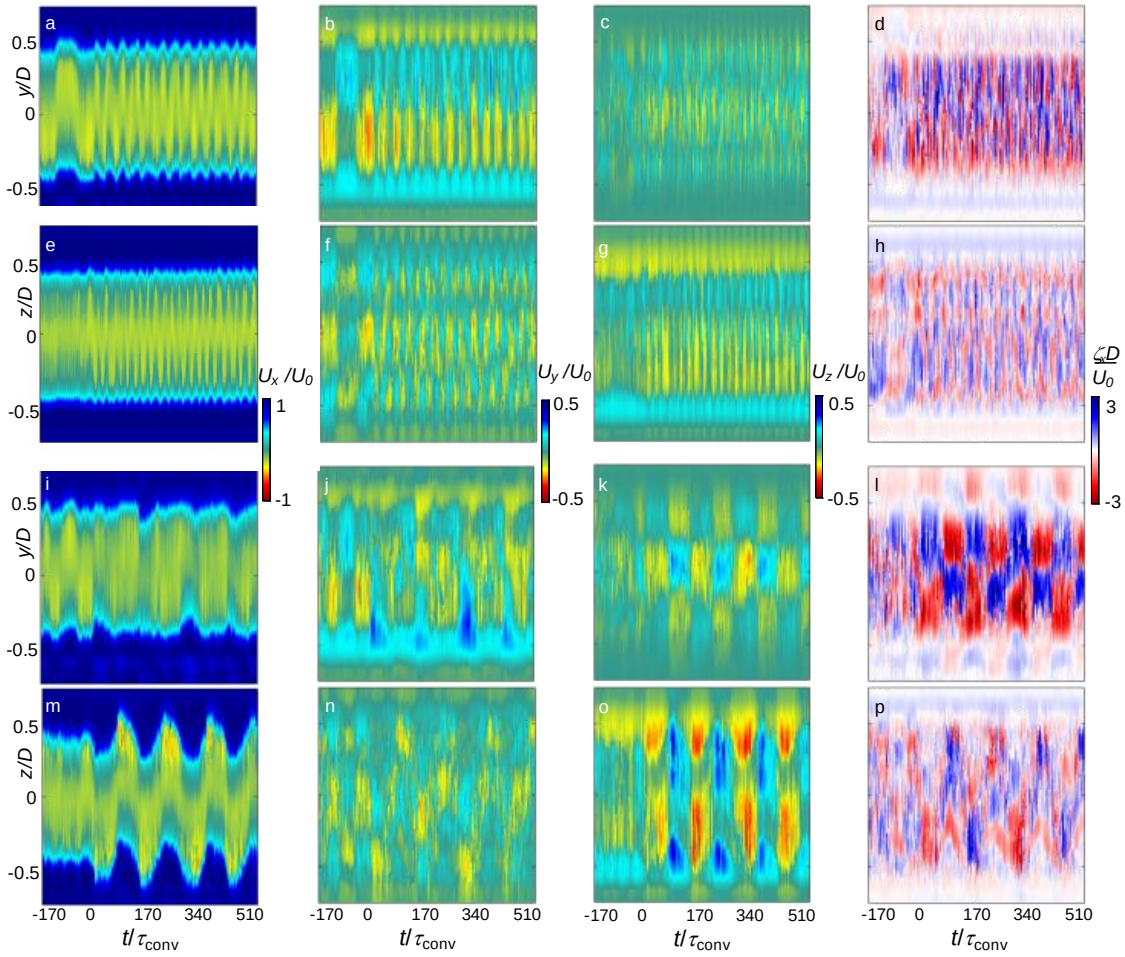

Figure 7.11. The time development of the wake for the closed-loop control algorithms hold-center (a-h), and amplify-pitch (i-p), presented in the same fashion as the data in Figure 7.7, using a maximum $C_\mu = 0.003$.

frequency (compare Figures 7.11b, c, f, and g with Figures 7.3f, g, j, and k). This control restores symmetry to the flow, where the actuation-induced horizontal centerline U_y resembles the vertical centerline U_z (compare Figures 7.11b and g), and the horizontal centerline U_z resembles the vertical centerline U_y (compare Figures 7.11c and f), which is expected when the model is centered and not moving, due to its azimuthal symmetry. This trend is consistent for the streamwise vorticity, ζ_x, where both the horizontal and vertical centerlines show similar traces, each with an inner-wake region full of rapidly oscillating, low-amplitude concentrations of vorticity, and the outer-wake having a weak band structure (compare Figures 7.11d and h). The structure of the wake with closed-loop hold-

center actuation is also in excellent agreement with low-speed stereo PIV velocity and vorticity time traces measured on a static centered model at a downstream location of $x/D = 1$ in Chapter **VI**. In the presence of pitch amplification control (Figures 7.11i-p), the original oscillations over the wake deficit are horizontally reduced (Figure 7.11i) while new vertical oscillations are introduced with a larger magnitude than the unactuated yaw oscillations (compare Figure 7.11m with Figure 7.3e). In addition, the U_z velocity throughout the centerlines has a larger amplitude than the U_y velocity (compare Figures 7.11k and o with Figures 7.11n and j), with the highest amplitude oscillation introduced in the actuated vertical centerline U_z component, which resembles the same structure as the baseline U_y component (compare Figure 7.11o to Figure 7.3f). The horizontal and vertical ζ_x fluctuations associated with pitch amplification now resemble the unactuated vertical and horizontal fluctuations, respectively, with the exception that the magnitude of the actuated ζ_x in the wake throughout the horizontal centerline has a more significant magnitude (compare Figure 7.11l with Figure 7.3l and Figure 7.11p with Figure 7.3h). The significance in these wake measurements is that the actuation for pitch amplification effectively switches the yaw dynamics and the pitch dynamics in the wake (equivalent to switching the horizontal and vertical centerline measurements), which is commensurate with the switched yaw and pitch motions and moments measured in Figures 7.10c, d, g, and h.

The respective POD modes of the wake behind the model with closed-loop actuation are calculated using the wake data in Figure 7.11 (a set of 2,500 images for a five-second trace or $850\,\tau_{conv}$ or $7.7\,\tau_z$), equivalent to the open-loop actuation POD modes in Figure 7.8. The streamwise component of these modes, $\vec{\varphi}_{n,u}$ is shown in Figure 7.12 for the hold-center (Figures 7.12a-e), and pitch amplification (Figures 7.12f-j) closed-loop actuations already discussed in Figures 7.10 and 7.11, as well as an additional closed-loop actuation goal for yaw amplification (Figures 7.12k-o). The first four modes are shown in Figure 7.12 with $n = 1$ (Figures 7.12a,f, and k), 2 (Figures 7.12b,g and l), 3 (Figures 7.12c, h,

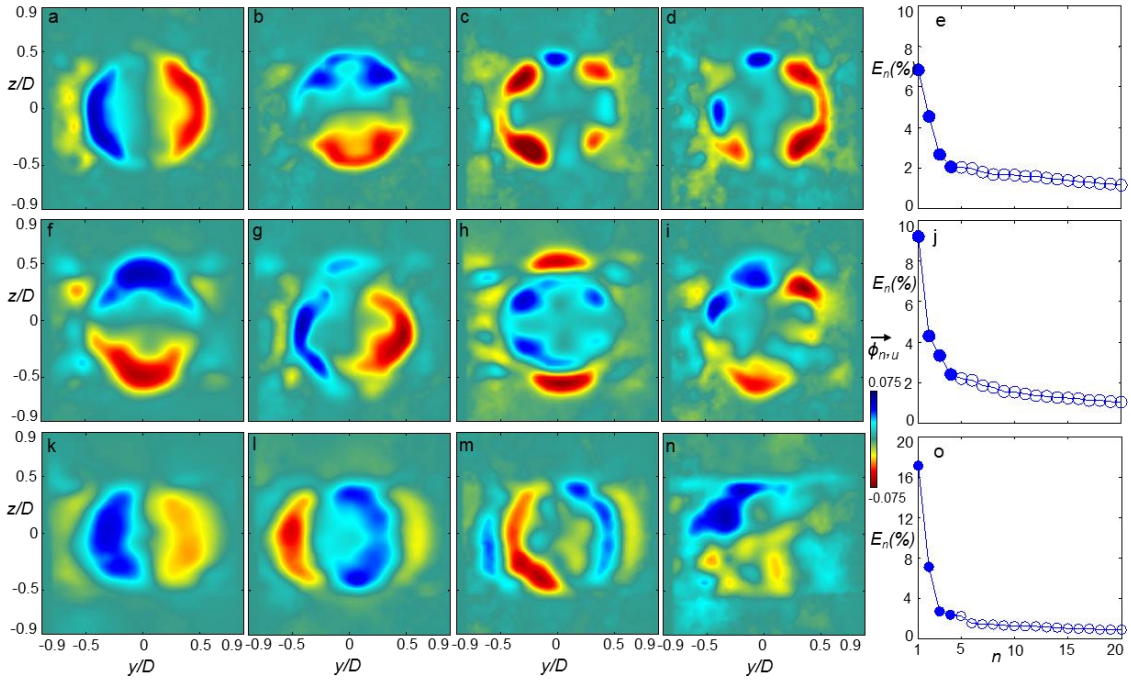

Figure 7.12. Contour plots of the streamwise velocity POD modes, $\vec{\varphi}_{n,u}$, with mode number n = 1 (a,f,k), 2 (b,g,l), 3 (c,h,m), and 4 (d,i,n), and the energy distribution of the modes (e,j,o) for Re_D =1.62·10^5, for closed-loop oscillation suppression (a-d), pitch amplification (f-i), and yaw amplification (k-n).

and m), 4 (Figures 7.12d, i, and n), along with the energy distribution of these actuated flows (Figures 7.12e, j, and o). The hold-center actuation changes the baseline modes significantly, restoring symmetry between the first and second mode in pitch and yaw (compare Figures 7.12a and b with Figures 7.4a and b). In addition, the energy between these modes are more evenly distributed, changing from 9% and 3% without actuation to 7% and 5% with the hold-center actuation, as shown in Figure 7.12e. Modes 3 and 4 were not present in the baseline flow and resemble mode 2 from the open-loop all-four actuation (compare Figures 7.12c and d with Figure 7.8g). The key difference between the closed-loop hold-center and the open-loop all-four modes is that the effects of the jets result in an asymmetric pair with a larger effect on the left (Figure 7.12c) and right (Figure 7.12d) side, respectively. This paired asymmetry in these two modes represent a left and right fluctuation introduced by the controlled closed-loop actuation to oppose the natural yaw instability of the model, and it is hypothesized the open-loop four-jets actuation was not

able to reduce the unactuated yaw oscillation because it did not have significant asymmetric wake dynamics in the cross-stream direction to induce an opposing yawing moment. Application of the pitch amplification switches the energy contribution of the first and second modes of the baseline flow (Figures 7.12f and g), from 9% and 3% to 5% and 9%, respectively (Figure 7.12j). This switch of the pitch and yaw instabilities is commensurate with the switch in forces and wakes discussed in both Figures 7.10c, d, g and h and Figures 7.11i-p. In addition, the new third and fourth modes introduced by actuation have not been observed in previous actuation programs and primarily extend in the pitch direction with either a symmetry in the yaw direction (mode 3, Figure 7.12h) or a weak anti-symmetry in the yaw direction (mode 4, Figure 7.12i). The third closed-loop controller goal is a yaw amplification actuation which is similar to the pitch amplification. Upon yaw amplification control, the structure of the unactuated pitching mode is rotated and diffused, and its energy is dropped from the second to the fourth mode (Figure 7.12n). The three highest modes that are present are all preferentially in the yaw direction, with the first mode being the equivalent of the unactuated first mode (Figure 7.12k). Mode 2 in yaw amplification is a rotated version of mode 3 in pitch amplification (compare Figures 7.12l and h), while a new mode 3 is introduced that appears to be excitation of the model roll (Figure 7.12m). This new closed-loop control significantly increases the energy in the yaw modes from 9% to a total of 27% split across three modes, while reducing the energy of all the other measured modes, as shown in Figure 7.12o.

Two new actuation programs that use only two adjacent synthetic jet actuators for trajectory control are introduced for which the controller uses only derivative feedback to oppose the natural oscillations of the model. In these programs, the model reaches equilibrium when the nominal aerodynamic force induced by an active jet balances the flow-induced aerodynamic force. The control programs utilize either jets 1 and 3 (denoted as 'hold-left'), to hold the model in positive yaw (nose to the left), or jets 2 and 3 (denoted as 'hold-up'), to hold the model in positive pitch (nose up). Figure 7.13 shows histograms

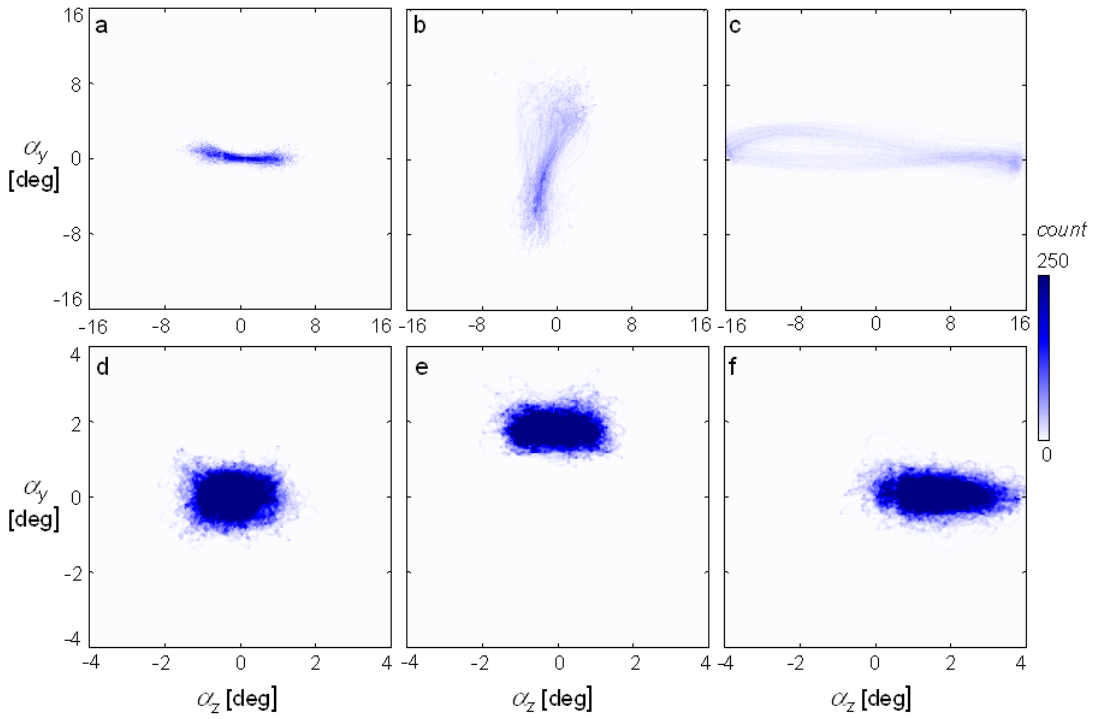

Figure 7.13. Spatial histograms of flow-induced dynamics of the model for closed-loop actuations: hold-center (a), hold pitch up (b), hold yaw left (c), unactuated (d), amplify-pitch(e), and amplify-yaw (f), presented in the same fashion as the data in Figure 7.9.

of the closed-loop actuated model dynamics (the data recording is the same as in the open-loop actuations in Figure 7.9). Amplification of the pitch or yaw (Figures 7.13b and c, respectively) yield (±8.5°, ±2.5°), or (±1.9°, ±16.2°) in (pitch, yaw), respectively. The motion data for the base flow (±1.5° pitch and ±5.5° yaw, and the same data as in Figure 7.1k) are plotted in Figure 7.13a, for reference. Figure 17d shows the closed-loop hold-center actuation with a fluctuation of ±1° in both pitch and yaw around its goal of 0°. Both the hold-left and hold-up actuation cause a similar fluctuation with different offsets: ±1.5° yaw and ±0.6° pitch around an offset 2° pitch (Figure 7.13e), and ±1.6° yaw and ±0.8° pitch around an offset 2° yaw (Figure 7.13f), respectively. For these new stabilized body states, the closed-loop control reaches its new established state in less than 0.2 seconds (approximately $0.3\,\tau_z$ or $34\,\tau_{conv}$) after activation, with the hold-center actuation having the fastest transient of about 0.15 seconds (approximately $0.23\,\tau_z$ or $25\,\tau_{conv}$). Figures 7.13e-f

demonstrate that the model can be controlled to a preferential angle (with about ±1° of high frequency fluctuation) at 2° pitch or yaw (hold-up and hold-left) with two adjacent jets, indicating that alternative control can easily be attained using the other two combinations of adjacent jets for hold-right, and hold-down. Intermediate attitudes can then, in principle, be achieved by using a weighted superposition of these four control programs. For example, equal weights would yield the hold-center command shown in Figure 7.13d (although there would be slightly larger error due to the lack of proportional control). Even if the model was excited in roll, it could still be controlled in the same manner, although the model would stabilize in the direction that corresponds to the midpoint of the two active jets (not necessarily in pure pitch or in yaw, depending on the roll angle). The combination of these control algorithms shows an ability to induce transient steering in a controlled direction (Figures 7.13b and c), or effectively stabilize the model (Figures 7.13d-f).

Closed-loop stabilization control of the model (cf., Figures 7.13a-c) is next applied for varying wind speeds, $1.32 \cdot 10^5 < Re_D < 1.92 \cdot 10^5$ (Figure 7.14). These closed-loop control programs are characterized by the maximum average offset value following either hold-up or hold-left actuation ($\bar{\alpha}_x$, $\bar{\alpha}_y$, and $\bar{\alpha}_z$ in Figures 7.14a-c), the RMS oscillations when applying the hold-center actuation ($a_{x,RMS}$, $a_{y,RMS}$, and $a_{z,RMS}$, in Figures 7.14d-f), and their hold-center oscillation frequencies (f_x, f_y, and f_z, in Figures 7.14g-i). These data are calculated from 25 instantaneous $1360\,\tau_{conv}$ time traces (the same number of samples as Figures 7.13a-c) with the model roll, pitch, and yaw in blue, and sting pitch and yaw in red. When the model is held at a fixed offset angle, the roll offset (0.5°) is approximately invariant with Re_D (Figure 7.14a), the pitch offset (2.0°) decreases with Re_D (Figure 7.14b), and the yaw offset (1.8°) increases with Re_D (Figure 7.14c). The offset angle actuations are not applied for $Re_D > 1.62 \cdot 10^5$. The RMS oscillations of model pitch, for hold-center, show a reduction of the oscillation to 0.25° at $Re_D = 1.32 \cdot 10^5$, and to 0.55° at $Re_D = 1.92 \cdot 10^5$, with corresponding reductions of 50% to 65% from the model motion in

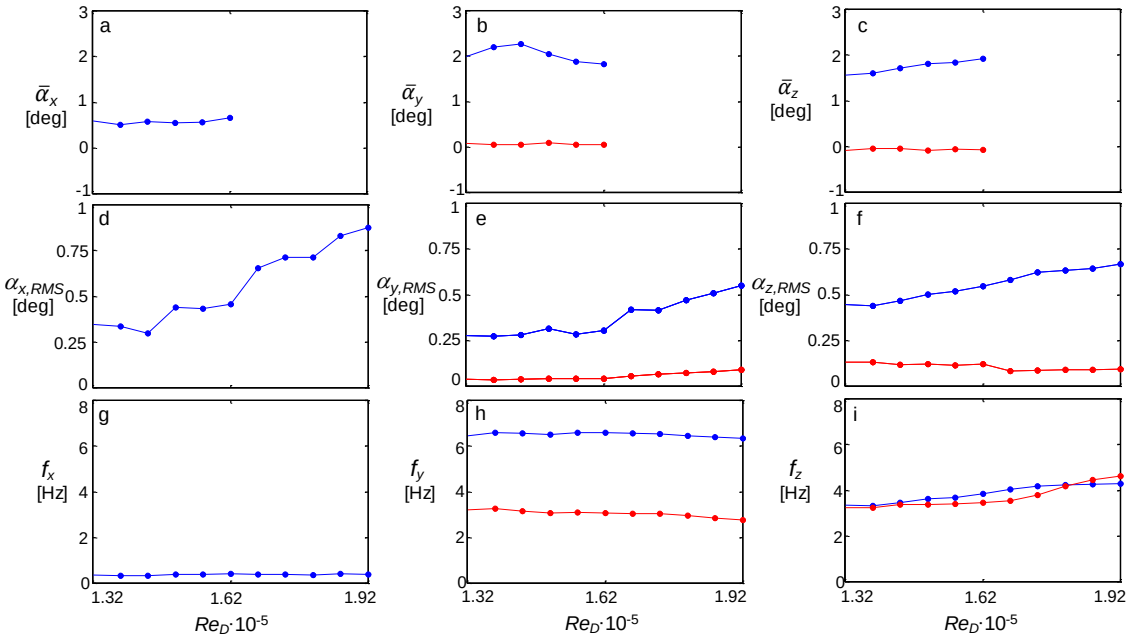

Figure 7.14. Model (**blue**) and sting (**red**) closed-loop control induced maximum deflections with hold-right or hold-up actuations (a-c), hold-center RMS amplitude (d-f) and hold-center characteristic frequency (g-i) in the roll (a,d), pitch (b,e), and yaw (c,f) directions, with Reynolds number.

the absence of actuation (cf., Figure 7.14e and Figure 7.2b). Similarly, the RMS oscillations of model yaw for hold-center show a reduction of the oscillation to 0.45° at $Re_D = 1.32 \cdot 10^5$, and to 0.70° at $Re_D = 1.92 \cdot 10^5$, with corresponding reductions of 85% to 75% from the model motion in the absence of actuation (cf., Figure 7.14f and Figure 7.2c). The application of closed-loop hold-center actuation also reduces the sting oscillation by 30% at $Re_D = 1.32 \cdot 10^5$ and 85% at $Re_D = 1.92 \cdot 10^5$. This control does not have a significant effect on either the roll oscillation (cf., Figure 7.14d and Figure 7.2a) or its commensurate characteristic frequency (cf., Figure 7.14g and Figure 7.2d). Figure 7.14h shows that application of the hold-center control does not alter the pitch frequency of the sting, but more than doubles the model pitching frequency from 3 to 6.6 Hz, effectively forcing the model frequency to be a harmonic of the sting frequency. In contrast, both the yaw oscillation frequency of the sting and the model increase two-fold at $Re_D = 1.32 \cdot 10^5$ to a factor of 2.5 at $Re_D = 1.92 \cdot 10^5$, (cf., 7.14i and 7.2f) remaining close to the same characteristic frequency at all wind speeds tested.

The results in Figures 7.13 and 7.14 indicate that the model can be directionally controlled with disturbance rejection within 2° in pitch and yaw. To test the control robustness, the sting is now subjected to a commanded disturbance time-harmonic (2 Hz) trajectory of 2° in pitch and yaw that are 90° out of phase, provided by the wire-mounted traverse. Two different closed-loop actuation programs are applied with the objective of external disturbance rejection. The first program commands the model orientation to follow the sting orientation (effectively keeping the model attitude locked to a 'target'), and the second program commands the model to preserve its orientation (selected to be 0°) regardless of the (changing) sting orientation at $Re_D = 1.62 \cdot 10^5$ (Figure 7.15). The trajectories of the model and sting in the absence of actuation are shown in Figures 7.15a and d, respectively, and application of the 'sting-follow' control is shown in Figures 7.15b and e, and the 'sting-rejection' control is shown in Figures 7.15c and f. The commanded sting motions through the wire traverse are selected to be very stiff (the changes in the sting

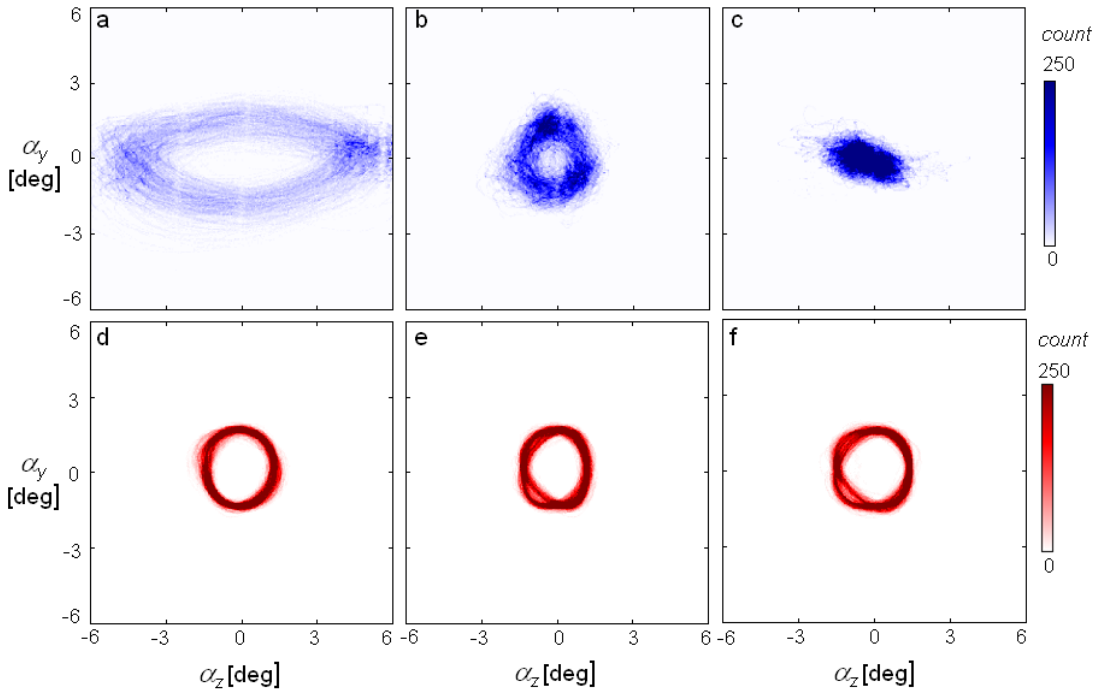

Figure 7.15. Spatial histograms of the model (**blue**, a-c) and sting (**red**, d-f) dynamics over 25 instantaneous measurements of 680 τ_{conv} for the unactuated flow (a,d), and closed-loop flow control for the model to follow the sting motion (b,e), and to remain centered independent of the sting (c,f) at $Re_D = 1.62 \cdot 10^5$.

trajectory with application of the flow control programs are small) to emphasize the induced changes in the model dynamics (Figures 7.15d-f). The unactuated model dynamic response to the sting disturbance shown in Figure 7.15a is approximately a superposition of the controlled sting dynamics with the model dynamics when the sting is held center (compare Figure 7.15a to Figures 7.15d and 7.1k). The application of 'sting-follow' control effectively forces the trajectories of the model and sting to be within ±0.5° in pitch and yaw (compare Figures 7.15b and e). The alternative 'sting-rejection' control (Figure 7.15c) fixes the model attitude to 0° regardless of the sting orientation with a fluctuation of ±1.5° in yaw and ±1° in pitch. Figures 7.15b and c indicate that this actuation can induce a controlled directional bias of the model attitude of ±2° in pitch or yaw even when it is subject to external disturbances.

7.4 Wake Structure and Stability Estimates

The effects of the closed-loop actuation on the structure and dynamics of the wake are characterized using snapshot dynamic mode decomposition (described in Appendix **A.2**). The result yields normalized spatial modes, $\psi_{n,}$ with corresponding frequencies, f_n, and growth rates, a_n. Figure 7.16 shows a data set when 999 modes are calculated from 1000 snapshots over $340\,\tau_{conv}$ for the unactuated flow (Figures 7.16a, e, i), and for steady state closed-loop actuations ($170\,\tau_{conv}$ after activation): hold-center (Figures 7.16b, f, j), pitch-amplify (Figures 7.16c, g, k) and yaw-amplify (Figures 7.16d, h, l). Figure 7.16 shows the variation of mode weight d_n with mode frequency ($0.48 < f < 240$ with steps of $f = 0.24$) (Figures 7.16a-d), along with color raster plots of the streamwise velocity component of representative DMD modes, $\psi_{n,u}$. Because DMD modes are in general not orthogonal the representative modes are selected such that they are unique, i.e, ψ_1 (Figures 7.16e-h) is selected for all of them, and a higher representative mode is also selected (Figures 7.16i-l) that does not encompass the same dynamics (e.g., for the baseline, ψ_2 at $f = 2.16$ Hz is a similar yaw mode to ψ_1 at $f = 1.68$ Hz and is omitted in favor of the pitch mode ψ_3 at

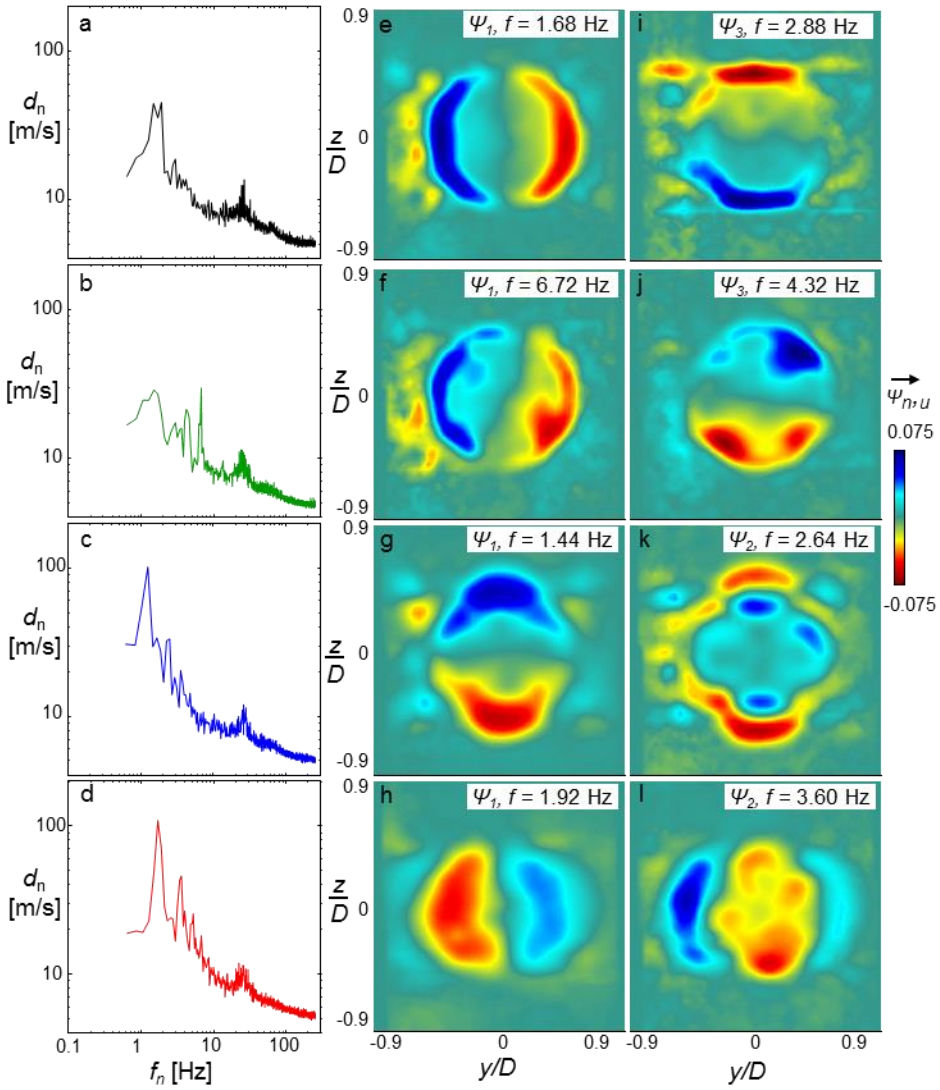

Figure 7.16. DMD spectral distributions (a-d) and color raster plots of the streamwise velocity distributions of dynamic modes, $\Psi_{n,u}$ (e-l), for the unactuated flow (a, e, i) and closed-loop actuation goals: hold-center (b, f, j), pitch amplify (c, g, k), and yaw-amplify (d, h, l). The mode order (i.e., the nth peak frequency) and respective frequency are noted.

2.88 Hz). The modes are determined by the largest spectral peaks of d_n. In the base flow, ψ_1 (1.6 Hz) and ψ_3 (2.88 Hz), respectively capture the highest modes of the yaw and pitch instabilities (Figures 7.16e and i), and demonstrate that the primary oscillations in the wake are confined to narrow bands within arcs at the oyer edges of the wake that scale with the diameter of the bluff body, and are similar to the first two POD modes presented in Figure 7.4a and b. When hold-center actuation is applied (Figure 7.16b, f, and j) the spectral

components of the yaw and pitch instabilities are attenuated and two higher spectral components emerge at 4.32 and 6.72 Hz coupled with the new dominant modes that are nearly symmetric with respect to the *y* or *z* axes and spread more towards the center of the wake as a result of the attenuation in of the fluctuation in the model attitude. The actuation that leads to amplification of the pitch and yaw excursions of the model are associated with large spectral peaks at (nearly) the frequencies of the instabilities of the base flow with several harmonics appearing (Figures 7.16c and d). While ψ_1 for the pitch and yaw amplification (Figures 7.16g and h) is similar to the corresponding primary yaw and pitch modes in the base flow, the actuated modes spread farther in the direction of excursions and into the center of the wake. Furthermore, the higher modes ψ_2 (Figures 7.16k and l) have distinct three lobes where the central lobe has the opposite sense of the outer lobes, similar to the POD modes in Figure 7.12h and l. Although the DMD modes in Figure 7.16 are in principle similar to the POD modes in §**7.3**, these results are significant because they depict the actual fluctuation in space corresponding to the two primary characteristic wake frequencies in pitch and yaw, and yield a more intuitive representation.

A unique feature of the DMD analysis is that it enables estimates of the amplification or attenuation of the individual modes. For this analysis, the wake data is pre-filtered by the 40 highest energy POD modes (approximately 50% of the energy) and the growth rates and frequencies of the 40 largest dynamic modes are computed. Initially, the limit cycle growth rates are plotted (each calculated over the same duration as Figure 7.16 a-d) and are marked along with their respective frequencies in Figures 7.17a, c, e, and g corresponding to the actuation programs of Figures 7.16a-d. Next, the transient phenomenon is investigated. For this purpose, this same DMD calculation is carried out within different time windows of the same duration, with the central snapshot of the window varying in time from one second before actuation (-170 τ_{conv}) to one second afterwards (170 τ_{conv}), where the actuation onset is take to be at $t = 0$. In other words, if the central snapshot was at 340 τ_{conv}, the data would be the same as in Figures 7.17a,c,e, and g. The time-evolution

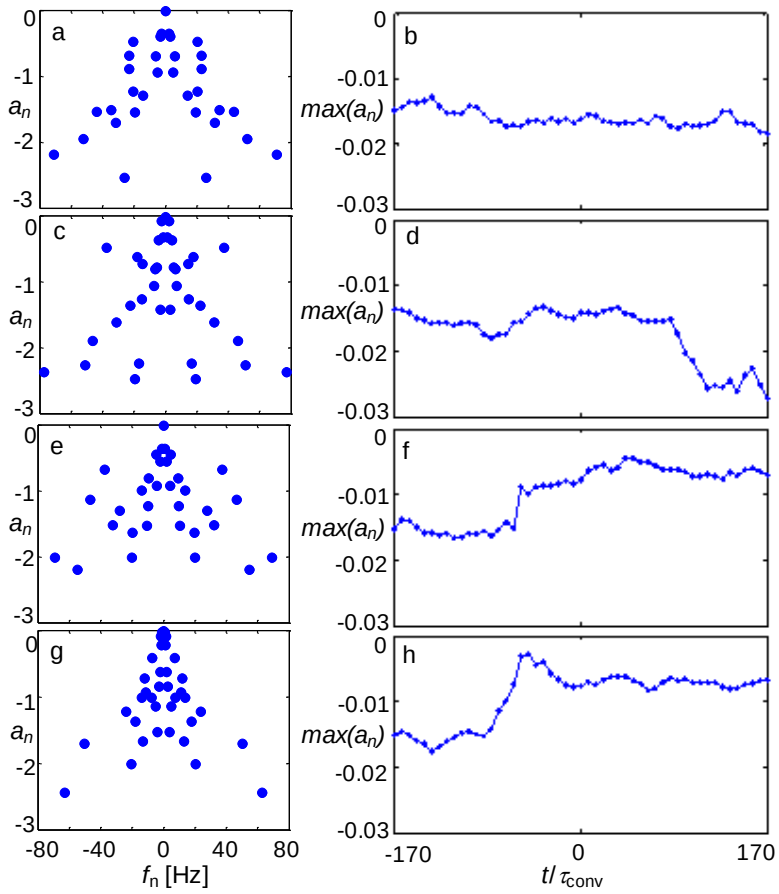

Figure 7.17. DMD growth rates (40 modes) (a,c,e,g) and the time development of the growth of the least stable mode within a 2 sec (340 τ_{conv}) interval with actuation starting at t = 0 (b,d,f,h). This data is depicted for the unactuated flow (a,b), and the actuated closed-loop control for hold-center (c,d), pitch-amplify (e,f), and yaw-amplify (g.h).

(plotted using the time of the center of each window) of the least stable mode of each actuation program is plotted in Figures 7.17b, d, f, and h. Clearly, the computation window straddles the unactuated and actuated flows, and extends from the pseudo-stable limit cycle of the base flow to sufficiently long after the actuation reaches a new limit cycle. Therefore, all of the modes in this reduced order analysis are stable (have a negative growth rate). In addition, a narrower window would better capture the transition associated with the onset of the actuation, but would be limited by noise in the snapshots. Nevertheless, these findings indicate that the timing of the change in magnitude (attenuation) of the least stable wake mode is in concert with the controlled model dynamics discussed in §**7.3**. Namely, the wake instabilities decrease for hold-center actuation (Figure 7.17d), and increase with

the amplification in either pitch or yaw directions (Figurse 7.17f and h). This change in the wake stability occurs over 0.15s, in agreement with the transient closed-loop moments in Figure 7.10, although the transition does not occur at the actuation onset ($t = 0$), which is attributed to the effect of the rolling window size.

CHAPTER VIII

CONCLUSIONS

The research presented in this dissertation focused on the unsteady flow mechanisms associated with aerodynamic flow control of the coupling between an axisymmetric bluff body and its wake using fluidic actuation at the flow boundary. It was hypothesized that active alteration of the wake of the moving body can enable prescribed modification of the time-dependent aerodynamic loads, and thereby can lead to active control of its motion and stability. The present investigations utilized several configurations of wire-mounted axisymmetric models integrated with individually-controlled miniature synthetic jet actuators that induced partial flow attachment over the model aft end, and thereby directly altered the wake dynamics. The flow dynamics were investigated when the model motion was either uncoupled from or coupled to the flow control-induced aerodynamic loads. The interactions between the actuation and the flow over the model were investigated using load cells, particle image velocimetry (PIV), hot-wire anemometry, and a real-time motion analysis camera system. This section discusses the major findings of the present investigations

8.1 Aerodynamic Control of Prescribed Static and Moving Platforms

The near-wake dynamics and induced aerodynamic loads the wire-mounted axisymmetric model where investigated over a range of prescribed motion configurations where the motion of the model was nearly decoupled from the variation in aerodynamic loads that are effected either by the interaction with the cross flow or by fluidic actuation (using an array of aft-mounted synthetic jet actuators cf., Chapter **2.1**).

The investigations commenced using a static model and in the presence of low-frequency pitch oscillations (reduced frequency $k = \pi cf/U_o < 0.013$, $Re_D = 2.3 \cdot 10^5$) where

the model was mounted in an axisymmetric hoop frame (Chapter **2.3**) using eight wires that enabled programmed motions using shape memory alloy (SMA) segments (the aerodynamic loads of the wires were assessed and subtracted). Synchronized activation of the support enabled arbitrary commanded model attitudes in combinations of pitch (or, by symmetry, yaw) with a range of $\alpha_y = \pm 3^\circ$ at 0.5 Hz to $\pm 1^\circ$ at 5 Hz.

These investigations demonstrated that the aerodynamic loads on the model can be actively tailored by time-dependent actuation to suppress or augment the loads that are effected by the base (unactuated) flow. The effects of the actuation on a static model (of $\alpha_y < \pm 4.5^\circ$) showed that the while the normal aerodynamic force (C_L) of the base flow and the actuation-induced force increments were comparable over this range, the actuation induced moment increments, were similar to the base flow pitching moment (C_M) at $\alpha_y < \pm 0.5^\circ$ and smaller (10% at $\alpha_y = \pm 4.5^\circ$) through the rest of the range. The actuation-induced aerodynamic moment by an actuator on the side of the pitch attitude has the same sense as the pitch angle, and therefore initially acts to further destabilize the motion. The optimal pitch angle for the maximum magnitudes of actuation-induced increments ΔC_L and ΔC_M occurs when the actuator on the same side of the pitch attitude, $\alpha_y \sim \pm 1°$, at which the coupling of the actuation to the aft separating shear layer segment is optimal. Temporal variation of the actuation induced aerodynamic loads were assessed during motion in the range $0 < \alpha_y < 1.5^\circ$ (at a rate of 0.24 rad/s) and demonstrated that the actuation can lead to either suppression or augmentation of C_L when the actuation is present on the same or opposite side of the model attitude, respectively. Actuation that increases C_L decreases C_M, and vice versa. During time-periodic pitch ($k = 0.013$, α_y amplitude 1.5°), the actuation induces significant changes in the wake topology that are similar to the corresponding static changes in α_y. Over this range of pitch angles the actuation can restore nearly streamwise-aligned wake that is accompanied by nearly complete suppression of C_L. In contrast, actuation that intensifies the wake asymmetry enhances C_L.

These findings led to the design, manufacturing, and implementation of a novel eight-wire (each integrated with a load cell) 6-DOF traversing mechanism that enabled realization of 'highly unsteady' ($k < 0.259$) dynamic states of the axisymmetric tunnel model (cf., Chapters **V** and **VI**). The traverse utilized a real-time (1,000 Hz) controller for executing the model motion by timed activation of eight servo motors (±8° roll, ±15° pitch, and ±9° yaw and up to 50 mm streamwise, cross-stream, and vertical translation). At 20 Hz the motions are limited to combinations of 3° rotations or 5 mm translations. The motion of the traverse was recorded in six degrees of freedom by an external *VICON* camera system (600 fps) that was used as a sensor for a trajectory controller.

Fluidic control of motion-induced aerodynamic forces and moments using amplitude modulation of the synthetic jet actuation waveforms was investigated during prescribed sinusoidal oscillations in rotation (pitch or yaw, but not roll) and translation (streamwise and cross-stream) over a wide range of reduced frequencies ($0.013 < k < 0.259$, $Re_D = 2.3 \cdot 10^5$, Chapter **V**). Similar to the actuation of the model mounted in the hoop frame, the actuation was utilized to either suppress the aerodynamic moment and augment the force or vice versa. These investigations demonstrated that as the oscillation frequency of the model increased, the aerodynamic loads of the base flow that are coupled to the shedding frequency changed in magnitude with a negligible amplitude at lower reduced frequencies ($k = 0.013$) growing up to amplitudes of about 50% of the cyclic fluctuations at $k = 0.0259$. In addition, because the model time scale is decreased to the order of the convective time scale, there is a phase delay (or phase shift) in the response, typically with attenuation of the cyclic averaged forces and moments. Open-loop fluidic actuation with adjustable phase offset of relative to the model oscillation was implemented for suppression and enhancement of the aerodynamic loads (pitch moment and lift force) and indicated a robust flow control effect over the full range of the pitch frequencies, with typical variations of 25% to 150% in force and 50% to 175% in moment relative to the base flow (uncontrolled) levels.

Along with the aerodynamic loads, the actuation also has a profound effect on the structure of both the near wake (characterized using PIV within the domain $0 < x/D < 1.6$, $y/D = 0$, $-0.6 < z/D < 0.6$), and the far-wake (characterized using hot-wire measurements at $x/D = 5$, $-1 < y/D < 1$, $-1 < z/D < 1$). *These investigations demonstrated that open-loop actuation on a stationary model can alter the evolution of the wake in a manner that is similar to the effects of the model pitch motion in the absence of actuation.* While at a lower reduced frequency, the effects of the actuation on the global wake characteristics were nearly identical to the corresponding flow features of the uncontrolled flow over the pitching body. The control authority of the far-wake at a fixed actuation level diminished somewhat as k was increased to 0.259. The effects of the actuation were demonstrated at 'quasi-steady' (e.g., $k = 0.013$) when the wake response during a given phase of the oscillation is similar to corresponding static pitch angle, and 'highly unsteady' (e.g., $k = 0.259$) when there is a significant phase lag between the wake response and the body motion. Spatial and spectral characterization of the far wake indicated distinct spectral bands: the pitching frequency (and its higher harmonics), narrow-band high frequency corresponding to vortex shedding ($St_D \approx 0.234$), and broad low frequency band ($St_D \approx 2 \cdot 10^{-3}$) that is attributed to axis switching of the vortex shedding. The results showed that both the dynamics of the near- and far-wake are significantly decoupled from the model pitching when the cyclic aerodynamic lift force is deliberately diminished by the actuation, causing suppression of 80% and 50% in the wake excursion at $k = 0.013$ and 0.259, respectively. Alternatively, the active enhancement of the lift force increases the wake excursion by 20% and 40% at $k = 0.013$ and 0.259, respectively.

The traverse-driven prescribed motions of the model were extended to include combined pitch/yaw over a range of reduced frequencies that were designed to mimic possible natural unstable motions of a similar airborne platform in the absence of roll (cf., Chapter **V**). The evolution of the wake flow was characterized using stereo PIV measurements within the y-z plane ($1.3 < y/R,\ z/R < 1.3$) at $x/D = 1$. Time-dependent

actuation was effected using independent harmonic modulation of the resonance waveform of each of the four independent synthetic jet modules (two opposing jets for pitch or yaw) over the same range of reduced frequencies ($0.017 < k < 0.259$, $Re_D = 1.73 \cdot 10^5$). The actuation led to active enhancement or suppression of the cyclic aerodynamic forces (lift and side forces) and moments (pitch and yaw moments), with negligible effect on the drag or roll moment. It was demonstrated that the structure of the near wake of the *stationary model* in the presence of spin-modulated actuation (by phasing the actuation waveforms) was similar to the wake of the *moving model* in a "natural" unstable pitch/yaw motion at amplitudes of up to 3º. While similar to the earlier findings in pure pitch, these finding proved that cross-talk between the jets was minimal (i.e., the jets affecting pitch did not affect yaw cancellation/augmentation and vice-versa). While at a lower reduced frequency, the aerodynamic loads induced by the actuation were nearly identical to the corresponding aerodynamic loads of the base flow over the dynamic pitch/yaw body, as k increases at a given actuation level, the control authority diminishes somewhat at 0.207 (the resonance frequency of the pitch/yaw motion), and then increased with k up to 0.259. When the actuation on the stationary model was applied at its vortex shedding frequency ($k = 1.43$, $St_D = 0.234$) it resulted in a strong coupling as demonstrated by the change in structure energy distribution of the wake POD modes.

Two flow control strategies inspired by the earlier studies were demonstrated when the model was undergoing combined pitch/yaw motions. The first strategy focused on decoupling the wake response from the model motion, and was designed to render the wake response invariant and equivalent to the wake of a nominally static model. The second strategy intensified the response of the wake to the prescribed motion of the body to mimic larger angular pitch/yaw deflection. These strategies were applied at reduced frequencies within the range $0.017 < k < 0.259$ and demonstrated up to 75% reduction or 100% augmentation of the motion-induced side and lift forces. Alternatively, the actuation led to variation of the motion-induced pitch and yaw moments resulting in up to 80% reduction

or 40% augmentation, without affecting the roll moment. Measurement of the velocity distribution in the near wake showed that when the actuation to decouple the wake from the model motion was applied, the first four POD modes became similar to the modes of the stationary model in the absence of actuation, even though the body was still moving, and there was a 40% suppression in the motion of the wake centroid (defined about $0.8U_o$). Alternatively, when the actuation enhanced the coupling to the wake, the POD modes were extended radially, commensurate with the increase in wake deflection, and there was an 80% augmentation in the motion of the wake centroid.

8.2 Aerodynamic Flow Control in 'Free Flight'

Trajectory control of a free flight axisymmetric body using time-dependent fluidic actuation was investigated in 1- and 3-DOF using two separate experimental setups. The first, 1-DOF setup utilized a single wire mounting of a free yawing model and the second setup used the 8-wire traverse to support a sting with a free-pivoting model in pitch, yaw, and roll.

A 1-DOF support system based on a vertical steel wire of a wind tunnel model (through its center of pressure at $x = 0.18c$) was designed and built to enable 'free' model dynamic motion in yaw, in the absence and presence of aerodynamic flow control (using a pair of opposing jet actuators, Chapter **IV**), and its motion was characterized using a laser vibrometer. In the absence of actuation, the interaction of the cross flow with the model leads to natural time-periodic yaw oscillations which are attributed to a phase lag between the wake responses (and in turn force/moment response) and the model attitude. The lateral oscillation frequency (1.7 Hz at 20 m/s) was predicted based on the static lift coefficient on the wire-mounted model ($C_L/\alpha_y = 0.05$/deg). This approach can also be used to predict the oscillation frequency for different mounting wire locations and free stream speeds. The dominant oscillation amplitude is proportional to the free stream speed in the range $0 < Re_D \cdot 10^{-5} < 2.3$, while the oscillation frequency increases monotonically with Reynolds number (the Strouhal number decreases down to 0.007). Yaw moment contributions from

the wake were estimated from measurements of the near wake and have a net effect that weakly opposed the yawing angle, in agreement with the resulting semi-stable oscillations.

Transient coupling between the onset of jet actuation and the flow/wake response reveal that a critical element in the evolution of the flow is the cumulative effect of a train of small-scale vortical structures that form at the jet orifice during consecutive actuation cycles that leads to alterations of the wake dynamics. The onset of the actuation is accompanied by the shedding of a large-scale starting vortex that is advected into the near wake and is associated with the initial change in the aerodynamic loads. The coupling between the actuation jets and the near wake was used to characterize the time scale at which the full effect actuation is established. The transient effects of the actuation onset die out within less than two convective time scales (i.e., fifteen jet cycles in the present study). 'Open-loop' actuation was used in an effort to understand the long term coupling of the actuation with the model motion and demonstrated that activating one control jet shifted the center of the body oscillation, with a deflection that is proportional to the initial oscillation amplitude. Activation of the opposing control jets acted like a damper owing to deviations between the opposing moments during the oscillation cycle resulting in suppression of the model deflections by up to 60% (depending on Re_D).

To fully exploit the capabilities of active flow control to steer the attitude of the dynamically yawing 1-DOF model, a PID closed-loop control was developed and utilized to command a desired trajectory. The model measured displacement was used as the control input (as in open loop control, the PID controller employs amplitude modulation of the carrier waveform to both control jets). The resulting wake dynamics under closed-loop fluidic control were also analyzed through their moment contribution in the near wake or far wake, showing the fluidic control can intensify or suppress domain within the flow field that contribute to a yaw moment that deflects the model away from center and thereby lead to amplification or suppression of yaw oscillations. The present experiments demonstrated that this closed-loop control was capable of dramatically suppressing the

model unstable yaw oscillations (in excess of 90%). In reversed operation, the same control approach can dramatically amplify natural oscillation by more than 175% of the natural amplitudes. For a wide range of speeds, closed-loop control could also deflect the body at a maintained steady nonzero yaw angle within 15% of the range of the natural oscillation.

A 3-DOF system (Chapter **VII**) was designed to investigate the reciprocal coupling dynamics between an axisymmetric platform that is free to precess in pitch, yaw, and roll in response to flow-induced aerodynamic loads. The model was attached to an upstream wire-mounted sting through a low-friction gimbal bearing within its front end that enables nearly-free rotations in pitch, yaw, and roll, and the temporal attitude and displacement of the sting could be manipulated in 6-DOF using the eight wire traverse (cf., Chapters **V** and **VI**). In the absence of actuation, the interaction of the cross flow with the model led to natural, time-periodic roll, pitch, and yaw oscillations whose characteristic amplitudes and frequencies all varied with tunnel speed.

Open-loop actuation that was independent of the model attitude was applied to assess the long term coupling of the actuation with the model response for combinations of one, two, and all four actuation jets. These effects were derived from the model dynamic orientation and its near-wake response using step-like transition from an unactuated state to continuous actuation. It was found that the characteristic time scale needed for reaching a quasi-steady response to the actuation varies with tunnel speed and was within 150 convective time scales or $0.6\,\tau_z$ at $Re_D = 1.92 \cdot 10^5$ (τ_z is the nominal baseline oscillation period, extracted from the baseline yawing motion). Activation of a single control jet shifts the center of the body oscillation by about 2° in pitch and yaw, and suppresses the amplitude of natural oscillations of the model by approximately 60%. The model response to actuation by combinations of two *adjacent* jets can affect the yaw and pitch coupling by orienting the model by up to 2.5° in pitch or in yaw while suppressing the amplitude of its natural oscillation by 20% or 40%, respectively. However, the actuation by an *opposing*

jet pair is less effective and leads to damping of the pitch-yaw coupling with a 25% reduction in oscillations. Simultaneous actuation with all four jets resulted in a 5% increase in the model oscillations.

To fully exploit the capabilities of active flow control to achieve a desired attitude of the freely-precessing bluff body, a closed-loop controller based on the earlier 1-DOF PID controller was utilized to effect a required trajectory. This controller consists of two independent PD controllers that generated amplitude modulation commands of all four jets to target minimizations in pitch and yaw, respectively, dependent on the model 3-DOF orientation (their commanded amplitude modulations are superposed to generate the signal to the actuators). The alteration of the near-wake structure and dynamics under closed-loop control are analyzed using the measured three velocity components and the streamwise vorticity. It is shown that suppression or amplification of the natural oscillations of the model yields changes the model cross-stream velocity along with the magnitude and extent of the wake deficit and the structure of vorticity concentrations within the inner wake, which lead to significant changes in the wake stability characteristics. The alteration of the near-wake structure and dynamics under closed-loop control are analyzed using dynamic mode decomposition (DMD) from high speed SPIV measurements of the velocity field in the near wake which revealed changes in the symmetry of the primary dynamic modes in their frequency response.

The present experiments demonstrated that PD closed-loop control can significantly suppress model oscillation by more than 80% over the present range of Re_D, and that at $Re_D = 1.92 \cdot 10^5$ this suppression occurs within $0.1\,\tau_z$ (about 20 convective time scales). Furthermore, the same control scheme could be inverted for amplification of the natural yaw or pitch oscillation by more than 225% of the amplitude of the base flow. In addition, this controller was used to effect a steady deflection of the model attitude (within ±2°) in pitch or yaw, when the wire-supported sting was stationary. This segment of the investigations was extended by prescribing controlled external disturbances to the sting

using the 6-DOF in which the sting precessed at $\pm 2^{\circ}$ in pitch and yaw, 90° out of phase, and the controller could impose a desired directional attitude that either tracked the sting motion (within 0.5°), or decoupled the model from the moving sting using the actuation for effective disturbance rejection.

8.3 Discussion of the Outcome of the Original Research Goals

The effects of aerodynamic flow control using fluidic actuation on the coupling between stationary moving axisymmetric bluff bodies and their near-wakes, and the effects of this control approach on the aerodynamic loads were explored in wind tunnel investigations. This Thesis was guided by four specific goals whose outcome is discussed in this section.

The first research goal was to characterize the effects of fluidic actuation using azimuthal, aft-body synthetic jets on the evolution and structure of the near-wake of a stationary axisymmetric model and on the ensuing aerodynamic loads. The present investigations demonstrated that segmented attachment of the separated flow downstream of the model aft end can induce aerodynamic force increments that are similar in magnitude to the forces induced by the base flow within attitude angles of $\sim 3^{\circ}$. In fact, the actuation is capable of either imposing a symmetric near-wake on the deflected on the deflected body or significantly enhance its inherent asymmetry. Because the aerodynamic effects are derived from the interaction of the actuation jet with the cross flow over the model, the effect of actuation is not symmetric about the streamwise direction but rather develops a local maximum at an attitude angle of about 1° indicating the importance of optimization of details of the geometry of the fluidic interaction. This is significant because mismatch of forces induced by opposing actuation jets (on both sides of the model) can lead to precession in free-moving platforms. It is shown that the primary aerodynamic loads on the base model at a given attitude angle are the normal and drag forces and the rotating moment in the plane of the offset angle (the side and yaw loads are secondary). However, while actuation induces similar changes in the normal force and moment the drag penalty

is significantly smaller (typically on the order of $\Delta C_D \sim 0.01$ per actuator). These findings illustrate the potential for exploiting aerodynamic flow control to substitute either rifling (spin) or fins in which the initial drag penalty is larger than $\Delta C_D \sim 0.04$, coupled with the potential for active trajectory control and a net drag decrease.

The second goal of the present research focused on investigations of the model-wake coupling during motion in a controlled prescribed trajectory. These investigations demonstrated that open-loop actuation on a stationary model can alter the evolution of the wake in a manner that is similar to the effects of the model pitch motion in the absence of actuation. These findings were applied to a moving model and showed that within the present range of reduced frequencies ($0 < k < 0.259$), the actuation effectively decoupled the wake dynamics of a moving model from its motion (by about 75%) as assessed by a reduction of the cyclic lift force. This is a powerful result because the wake deficit far downstream of a *moving, controlled* model becomes similar to the wake of a *stationary* model, that is accompanied by reduction of the fluctuations in the aerodynamic force throughout the cycle. While the accompanying aerodynamic moments induced by the actuation have an opposite sense to the induced force and smaller magnitude compared to the base flow moment, they also have significant control authority when the model is 'free' to respond in rotation about the primary axes. In fact, the actuation can stabilize wake-induced model rotation within 2-3 baseline oscillations. The present investigations also demonstrated that amplitude modulated actuation of the resonance wave form of fluidic synthetic jet actuations is rather effective by simultaneously combining the effects of both low- and high- frequency actuation. While the former couples to the unstable frequencies of the near wake (and the shedding frequency of the model), the latter is an effective tool for enhancing the coupling to the cross flow through collective interactions of small-scale vorticity concentrations that are formed at the resonant actuation waveform.

Elucidation of the receptivity of the coupled model/wake to fluidic actuation in motion that mimics some elements of 'free' flight was the third goal of the present investigations.

Free motion was investigated using 1-DOF (yaw) and 3-DOF (roll, pitch, and yaw) models. The free yawing model demonstrated that open-loop actuation could have a profound influence on the evolution of the dynamics of wake-induced vibrations. The actuation enables prescribed model attitude and a reduction in the variance of the model attitude by 2.5° (compared to 7° in the base flow). These investigations also demonstrated that the disparate response of opposing or adjacent jets during the model motion owing to variation of their interaction with the cross flow can be exploited for refinement of the control effectiveness by incorporating knowledge of the flow receptivity. Although the range of operating Reynolds number in the present experiments was limited by the wind tunnel, the results with the variation with Reynolds number (e.g., the steady deflection angle had a roughly linear increase of 2° to 3° within the range $0.57 < Re_D \cdot 10^{-5} < 2.0$) indicate that similar aerodynamic flow control strategies can applied to projectiles with a wide range of launch speeds.

These results were extended to a 3-DOF bearing-mounted model attached to a fixed sting supported by the 6-DOF which shoes that the same strategy that was applied in 1-DOF yaw can be extended independently to both yaw and pitch, and, in principle, can be done to roll. Specifically, stabilization of the model can be effected in either pitch or yaw even when the actuators are not aligned in either the pitch or yaw directions indicating fluidic actuation can be utilized to stabilize the attitude of an airborne platform within a range of combined pitch and yaw at angles that are within some critical angle. As part of these investigations, it was hypothesized that this fluidic control approach can then be used to implement "as eye on target" control, i.e., staying on a trajectory regardless of flow induced disturbances. This was demonstrated by deliberate dynamic changes in the attitude of the sting mount. The ability to attenuate or amplify the natural oscillation of the model indicates that closed-loop control can be used to effect time-dependent steering of a model attitude or stabilize it in free flight (without spin) regardless of the azimuthal position of the actuators (although the controller did need a sensor to know what its real-time

orientation was). Because the model was well-balanced, roll was not explicitly investigated and the controller was not corrected for roll rate. However, it is anticipated that the present control approach could be used during roll with an additional controller logic that delays the actuation onset relative to the roll.

Finally, an important goal of the present investigations was the development of a dynamically-controlled wind tunnel traverse mechanism in 6-DOF. This traverse allowed controlled, coupled variation in model dynamics in multiple degrees of freedom during wind tunnel investigations and enabled investigations of the wake dynamics and of the ensuing aerodynamic loads in the absence and presence of aerodynamic flow control.

8.4 Design Methodology Using the Present Findings

This Section provides a summary overview of the key findings for design implementation.

Chapter **II** provides a description of the wind tunnel hardware and software that could be helpful for design of wind tunnel models under trajectory control or free motion in multiple degrees of freedom: This chapter includes detailed descriptions of the wind tunnel facility (§**2.1)**, the wind tunnel model and synthetic jet fabrication (§**2.2**), the quasi-steady SMA traverse assembly (§**2.3**), discussion of the design elements of the 'free' 1-DOF model (§**2.4**), description of the components and control design of the eight-wire trajectory tracking traverse including a demonstration of 6-DOF motion in pitch and yaw (§**2.5**), discussion of the design elements of the 'free' 3-DOF model (§**2.6**), and, finally, a description of the PIV system that was used in Chapters **III**-**VII** (§**2.7**).

The investigation of the coupling between aerodynamic loads and wake structure during time-stationary or slow changes in model attitude (quasi-steady aerodynamics), and of the changes in this coupling by fluidic actuation are described in Chapter **III**. These results can be used in future investigations of separation control on different model geometries and include discussions of the effects on the near wake and aerodynamic loads induced by aft-end synthetic jet actuation on a static model over a range of pitching angles (§**3.1,** and

§**3.2**), and of the wake structure when the actuation renders the lift force invariant during pitch (§**3.3**).

The dynamics of a 'free' 1-DOF yawing body that is driven by the flow in the absence and presence of control are discussed in Chapter **IV**. These results could be useful in other investigations of controlled actuation on free moving models (e.g., the effectiveness of open- and closed-loop actuation with Reynolds number is depicted Figures 4.13, and 4.21, respectively). This chapter discusses the characteristics of the model's flow-induced motion in the absence of actuation (§**4.1**), measurements of actuation-effected wake and model deflections on the moving model on the time scales of the actuation and of model oscillations (§**4.2** and §**4.3**), and implementation of specific control objectives of a closed-loop PID controller (§**4.4**). Details of the design of the PID controller are included in Appendix **B.1**.

The effects of prescribed time-harmonic motion (pitch, plunge, and streamwise displacement) using the wire mounted 6-DOF traverse [from $k = 0.013$ ('quasi-steady') to 0.259 ('highly unsteady'] are discussed in Chapter **V**. This chapter describes the effects of actuation on the base flow and the aerodynamic loads during pitch motion including 'suppression' and 'augmentation' of the lift force (§**5.1**, with flow control commands generated in Appendix **B.2**), and the effects of continuous actuation during plunge (§**5.2**), and streamwise translation (§**5.3**).

The flow over the model in a prescribed (rigid) coupled pitch-yaw rotation that mimics free-flight instabilities of the model and its near wake and the use of actuation to control these instabilities are described in Chapter **VI**. These results provide insight into the effects of flow- and actuation-induced aerodynamic loads in harmonic 2-DOF rotation ($0.013 < k < 0.259$) for the static model using near wake velocity and vorticity measurements and POD modes (§**6.1**, the POD analysis is described in Appendix **A.1**). In addition, the aerodynamic loads during coupled rotation in the absence and presence of actuation (§**6.2**, with flow control commands also described in Appendix **B.2**), a

comparison of POD modes in respective absence and presence of actuation on the rotating and stationary model (§**6.3**), and the POD modes of the wake behind actuation-suppressed and actuation-augmented aerodynamic loads (§**6.4**) are characterized.

Finally, the control authority of fluidic actuation on an axisymmetric model that is free to respond to induced aerodynamic loads in 3-DOF (pitch, yaw, and roll) is described in Chapter **VII**. These results demonstrate stabilization or steering control on the axisymmetric model when its center of gravity is co-located with the axis of rotation upstream of the center of pressure and include a description of the flow induced dynamics and the coupled dynamics of the near wake in the absence of actuation (§**7.1**), the effects of open-loop actuation on the aerodynamic loads and wake (§**7.2**), the implementation of a coupled PD feedback controller (described in Appendix **B.3**) for effecting new dynamic states of the model and the variations with flow Re_D (Figure 7.14, §**7.3**). The commensurate DMD modes of these new dynamic wake states are presented in §**7.4** (the DMD approach is described in Appendix **A.2**).

8.5 Recommendations for Future Work

It is hoped that the present research will spur future investigations of the effects of active flow control on the trajectory and guidance of bluff bodies:

1) Controlled vortex shedding

A key finding of the present investigations was that amplitude-modulated actuation can regulate vortex shedding from the bluff model and impose clear spatial and temporal distributions of vorticity concentrations within the wake. An enticing research direction is the suppression of shedding of coherent vorticity concentrations altogether using feedback-controlled modulation of the actuation waveform. This approach could directly contribute to mitigation of vortex induced vibrations on 2- and 3-D bluff bodies that can accommodate active flow control.

2) Application to 3-D wing models in unsteady motion

It is anticipated that the present investigations can be extended to moving 3-D wing models using the same eight-wire traverse (recent investigations have focused primarily on pitch and plunge of axisymmetric models). A potential technical challenge in this approach may be weight minimization of a scale models, but is appears that new light-weight materials in 3-D printing could be used in this application. Such investigations may lead to new insight of potential flow control strategies for overcoming instabilities that occur in highly unsteady flows including aeroelastic effects.

3) Implementation on airborne models in the absence and presence of spin.

The present work demonstrates that the synthetic jet actuation on a scale model projectile can effectively stabilize a model at an arbitrary roll angle during pitch and yaw. This control approach can be directly implemented on a launched non-spinning projectile (in the absence of rifling) for stabilization and steering along a desired trajectory. Such investigations will be clearly dependent on the implementation of suitable sensing of the trajectory. Synthetic jet actuation could be used for control since the earlier investigations of McMichael et al. (2004) demonstrated that these actuators can be designed to withstand the launch loads. Alternatively, multiple, azimuthal fluidic actuators can also be used on a spinning platform and potentially compensate for spin-yaw lock in, or gyrations that can occur if the projectile is launched too fast at a fixed spin rate. The flow controller will need to be modified for actuation during roll, by proper phasing or staging.

APPENDIX A

DECOMPOSITION APPROACHES

A.1 Proper Orthogonal Decomposition (POD)

To further investigate the structure of the wake in Chapters **VI** and **VII**, instantaneous velocity vectors are used to calculate the average fields to extract the Proper Orthogonal Decomposition (POD) modes of the wake:

$$\vec{X}(t) - <\vec{X}> = \sum_{n=1}^{NN} A_n(t) \cdot \vec{\varphi}_n \tag{A.1}$$

where $\vec{X}(t)$ is an instantaneous state vector in a dataset to be reconstructed with POD modes, $<\vec{X}>$ is the time averaged value of $\vec{X}(t)$, $\vec{\varphi}_n$ is the *n*th POD mode, $A_n(t)$ is the weighted time coefficient of the nth POD mode, and *NN* is the rank of the data set (i.e. the maximum independent vectors either spatially or in time). The analysis for the POD modes of the stationary model is performed by extracting the first N_{set} modes when the state $\vec{X}(t)$ is chosen to be a column vector of $U_x(t)$, $U_y(t)$, and $U_z(t)$ concatenated vertically, and the dataset includes *NN*+1 time realizations. In addition, as $\vec{\varphi}_n$ is effectively an eigenvalue of $\overrightarrow{X^*} \cdot \overrightarrow{X^*}^T$, and the energy percentage of each mode can be defined through the commensurate eigenvalues λ_n:

$$E_n(\%) = \frac{100|\lambda_n|^2}{\sum_{i=1}^{NN}|\lambda_i|^2} \tag{A.2}$$

where λ_n is the eigenvalue of the corresponding eigenvector $\vec{\varphi}_n$.

$\vec{\varphi}_n$ consists of components in the three velocity components in the analyses in this paper. Typically, the modes are presented in term of the streamwise velocity (which is spatially symmetric around the center of the model at a fixed streamwise plane), and a representative cross-stream velocity picture. To simplify these coupled cross-stream modes, a quiver plot

is used to combine the cross-stream velocities, and the modes are also used to calculate their respective normalized streamwise vorticity:

$$\vec{\varphi}_{n,\zeta} = \delta \cdot \left(\frac{d\vec{\varphi}_{n,w}}{dy} - \frac{d\vec{\varphi}_{n,v}}{dz} \right) \quad \text{(A.3)}$$

It is emphasized that this vorticity mode is derived from the result of the POD analysis and is not a direct result of the POD analysis (i.e., it is not a POD mode of the vorticity field). The derivatives are taken in Equation (A.3) using a 3x3 stencil and a first order centered analysis, and therefore $\vec{\varphi}_{n,\zeta}$ is normalized by the grid spacing between velocity vectors, δ, which is uniform in the *y* and *z* directions of all the data sets measured. For Chapter **VI**, 30 modes of 600 instantaneous vector fields are used, and for Chapter **VII**, 20 modes of 2500 instantaneous vector fields are used.

A.2 Dynamic Mode Decomposition (DMD)

The effects of the closed-loop actuation on the structure and dynamics of the wake are characterized using snapshot dynamic mode decomposition (DMD, e.g., Tu and Rowley, 2012). In this approach, the velocity field at a given time is concatinated as a vector, $\vec{X}$, at time *t*, and compared to field at a subsequent time step $\vec{X}$', at time $t+\delta t$. A time shift operator *A* is estimated such that $A\vec{X} \sim \vec{X}$' for a sequence of snapshots such that its eigenvectors $\vec{\psi}_n$ are the dynamic modes, and the complex eigenvalues $\lambda_{n,dmd}$ yield estimates of the frequency and growth rate of each mode $f_n = \text{imag}[(\log(\lambda_{n,dmd}))/(2\pi\delta t)]$ and $a_n = \text{real}[(\log(\lambda_{n,dmd}))/(\delta t)$, respectively. Currently the time shift operator is estimated by prefiltering the DMD modes by POD modes, and through this analysis any DMD mode required will be a superposition of the POD modes measured. The velocity field snapshots are obtained from high speed stereo PIV (cf., Chapter **2.7.3**) records (5 seconds, at 500 fps) of the wake in the absence and presence of actuation. The analysis is implemented using the three velocity components [$U_x(t)$, $U_y(t)$, and $U_z(t)$]. Each dynamic modes is scaled by a weight d_n, such that the sum of all modes resconstructs the first snapshot in the dataset and thereafter they change with time depending on their eigenvalues, as performed in (Tu, 2013):

$$\sum_1^{N\text{set}} d_n \vec{\psi}_n = \vec{X}|_{t=0}, \quad \sum_1^{N\text{set}} d_n \vec{\psi}_n(\lambda_n)^m = \vec{X}|_{t=m\Delta t} \tag{A.4}$$

where N_{set} is the number of resolved dynamic modes. For Chapter **VII**, data sets with 999 modes of 1000 instantaneous vector fields are used in Figure 7.16, and data sets of 40 modes of 1000 instantaneous vector fields are used in Figure 7.17. These 1000 vectors are a subset of the entire time series which is 3000 vector fields in length with a frame rate of 500 frames per second, and for these datasets actuation is induced at frame number 500, which is set to $t = 0$.

APPENDIX B

FLOW CONTROL STRATEGIES

B.1 PID Feedback Control of a Free 1-DOF Model

This section discusses the development and implementation of a closed-loop PID flow controller in Chapter **IV** to activate the synthetic jets as a function of the 1-DOF model yawing angle. A PID controller is chosen to be implemented, which uses the difference in the goal outputs, $(\alpha_g, d\alpha_g/dt)$, from the sensor (vibrometer) inputs, $(\alpha_z, d\alpha_z/dt)$, as proportional and derivative errors and then uses a numerical integral (through Simpson's 3/8 rule) to obtain the integral error. This controller updates at f = 100Hz in the present study, and its diagram is shown in Figure B.1. A command signal is created as a weighted superposition of all three of these using respective coefficients (κ_D, κ_P, and κ_I). The present implementation of this controller modifies the algorithm of a basic PID controller by using the measured value of the velocity rather than the numerical derivative of the error. Each

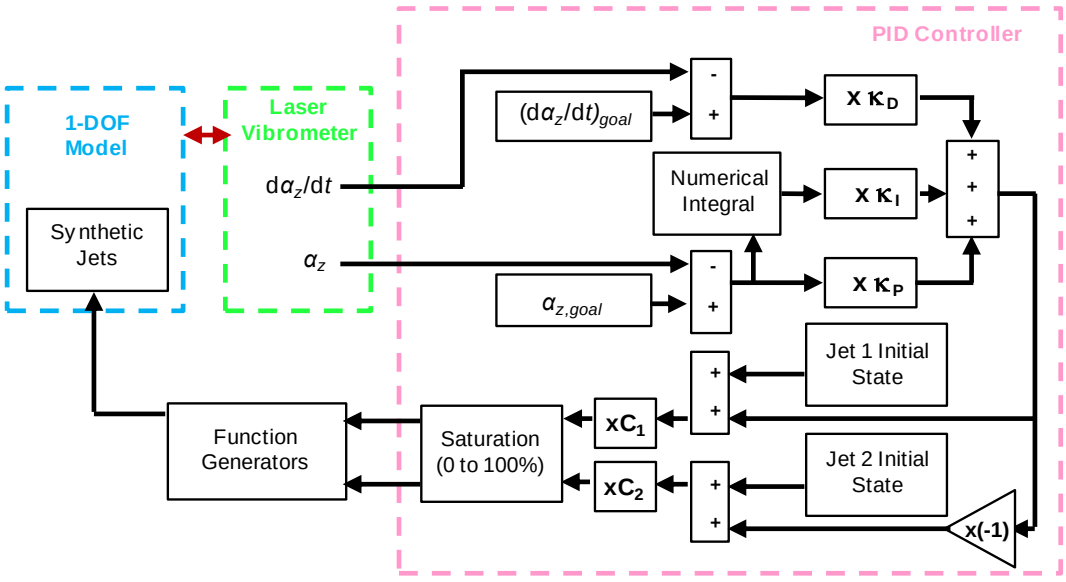

Figure B.1. Schematics of the closed-loop PID controller for the 1-DOF model.

jet is allowed to be set at an initial amplitude-modulation state in the absence of a control signal (for instance, the jets could initially be partially activated for open-loop suppression). The command signal is added onto the initial state of the right jet (jet 1, the jet that will influence the model to move in $+\alpha_z$) and subtracted off from the initial state of the left jet (jet 2). Additionally, the jets relative amplitudes are scaled by C_1 and C_2 coefficients in the controller, to correct for their relative strength. These two command signals are saturated as a modulation command and sent to external function generators and corresponding amplifiers to transform the signal into an actuation wave packet, where the maximum modulation amplitude corresponds to an output jet momentum coefficient of $C_\mu = 0.003$.

Determination of the optimal control coefficients is found through individual iteration when the model goal is set to hold the model steady at $\alpha_z = 0^\circ$, as shown in Figure B.2. To measure an individual coefficient efficacy, α_{RMS} is measured, where the ideal control coefficients produce minimal α_{RMS}. Initial alteration of these coefficients revealed the control was most sensitive to the κ_D coefficient, and this coefficient was varied first in Figure B.2a, with $\kappa_P = \kappa_I = 0$. For a negative κ_D coefficient, α_{RMS} increased significantly, causing the controller to effectively act as a negative aerodynamic damper, and for a positive κ_D coefficient, α_{RMS} quickly diminished to an asymptotic value of 0.48° at $\kappa_D > 10\frac{s}{\text{deg}}$, with the operation κ_D chosen to be safely in this region at $\kappa_D = 40\frac{s}{\text{deg}}$. Secondly, the κ_P coefficient is varied with this pre-set κ_D, and $\kappa_I = 0$, as shown in Figure B.2b. The variation of α_{RMS} was much less sensitive to this coefficient, where the minimized value was found to be $\alpha_{RMS} = 0.43^\circ$ at $\kappa_P = 1.5\frac{1}{\text{deg}}$. Finally, the κ_I coefficient is varied with the chosen κ_D and κ_P, as shown in Figure B.2c. This led to the minimal $\alpha_{RMS} = 0.40^\circ$, at $\kappa_I = 75\frac{1}{\text{deg}\cdot\text{s}}$, which is used as the operational κ_I coefficient.

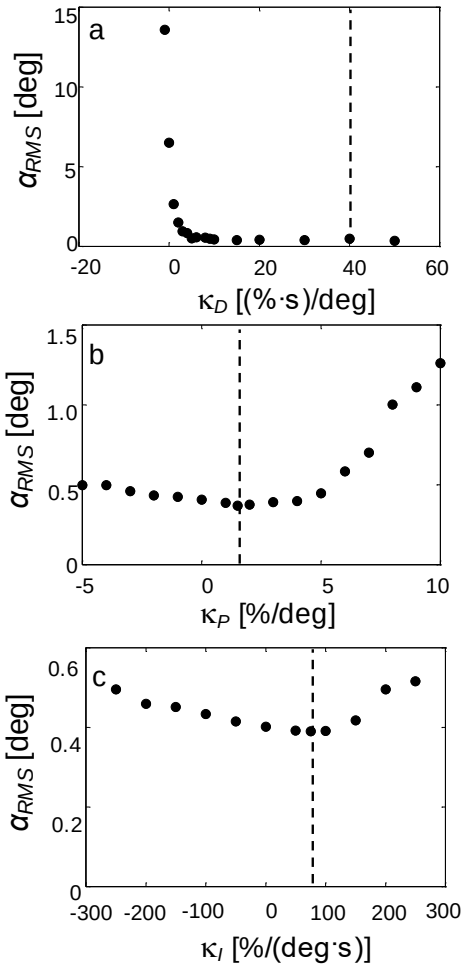

Figure B.2. Determination of κ_P, κ_I, and κ_D (U_o = 20 m/s, maximum C_μ=0.003) for suppression of model oscillations: varied κ_D , κ_I=κ_P=0 (a), varied κ_P , κ_D = 40s/deg, κ_I = 0 (b), and varied κ_I , κ_D = 40s/deg, κ_P = 1.5/deg (c). Selected operational parameters are shown by dashed lines.

For the yaw amplification control, a typical PD controller response would be dependent on the magnitude of the desired pitch, and therefore to implement the maximum amplification, the yaw goal is instead set to 0° and the controller coefficients determining the pitch motion (κ_P and κ_D) are multiplied by -1, causing the controller to drive the model to its maximum instability in yaw around 0°.

B.2 Open-Loop Flow Control in 'Rigid' Pitch or Lissajous Rotation

Results shown from continuous actuation in Chapter **V** clearly demonstrated that the hybrid actuation approach has a significant control authority (on both the lift force and the

pitch moment, but this section will focus specifically on the lift force) throughout the full range of the pitching dynamics $0 < k < 0.259$. The main objective of the present study is to apply such a control approach to control the aerodynamic forces (C_L vs. α_y path) on the body undergoing dynamic pitch. A decrease of C_M growth with α_y can be used to stabilize the model, and increasing the C_M growth with α_y can be used to accelerate steering. This is a coupled system where the baseline C_L and C_M are both increasing with α_y, yet the induced forces by the synthetic jet actuators are in opposite senses, therefore increasing growth of C_M vs. α_y (for accelerated steering) simultaneously reduces growth of C_L vs. α_y, and likewise decreasing growth of C_M vs. α_y (for stabilization) simultaneously increases growth of C_L vs. α_y. As it was assessed in Chapter **III**, the control authority ΔC_L relative to the baseline path of C_L was larger than ΔC_M relative to the baseline path of C_M, and therefore it is chosen to focus the flow control on augmentation of the C_L vs. α_y path as a case that can be used for stabilization, and cancellation of the C_L vs. α_y path as a case that can be used for accelerated steering. As it was discussed in Chapter **II**, the ΔC_L and ΔC_M

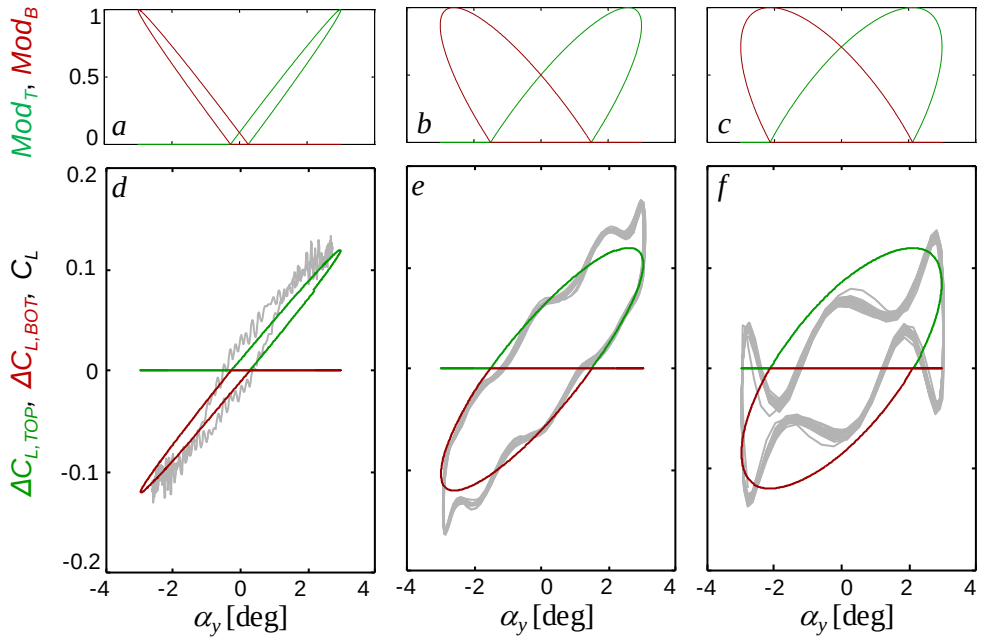

Figure B.3. Synthetic jet modulation strategy for force augmentation (a-c), and estimated actuator induced force (d-f) with top jet in **green** and bottom jet in **red** for $k = 0.013$ (a,d), 0.130 (b,e), and 0.259 (c,f). The non-actuated force response is shown in gray. The modulation schemes for force cancellation are 180° out of phase.

induced by an equivalent synthetic jet varied linearly with $C_\mu < 3 \cdot 10^{-3}$, and such a relationship is utilized in the current control scheme. Modulation commands, Mod_T and Mod_B, are tailored for each jet to each of the baseline lift force responses measured throughout a few different frequencies [k = 0.013 (Figure B.3d), 0.130 (Figure B.3e) and 0.259 (Figure B.3f)], shown in grey. With a jet momentum of $C_\mu = 3 \cdot 10^{-3}$ corresponding to 100% modulation, there is an induced $\Delta C_L \sim 0.1$ when the model is centered, based on Figure 3.1. Therefore, using this to estimate the magnitude of the actuation-induced lift force, the only variable to alter is the phase of the actuation modulation (here sinusoidal modulation is implemented due to its success in Figure 3.13). Figure B.3a-c show the resultant estimated jet modulation signals with varying k = 0.013 (Figure B.3a), 0.130 (Figure B.3b) and 0.259 (Figure B.3c), where the only free parameter of variation used was the phase of the modulation signals. Here the top jet is shown in green and the bottom jet is shown in red, and the plan is that the estimated induced lift force should be in phase with the pitch induced lift force for force augmentation. Once the force augmentation modulation command is designed, the force cancellation is generated by running the jets 180° out of phase. The corresponding predicted induced ΔC_L is plotted over the baseline traces in Figures B.3d-f for the same values of k. The phase of these modulation commands was chosen such that the predicted augmented C_L is most similar to the baseline C_L, leading to the chosen modulation command phase lags of 5° (k = 0.013, Figure B.3a and d), 25° (k = 0.130, Figure B.3b and e), and 40° (k = 0.259, Figure B.3c and f), relative to α_y.

The actuation generation used in Chapter **VI** is the exact equivalent, except there was an additional force provided by the side actuators to control the side forces. This actuation made the assumption that cross-talk between actuators in the yaw directions and the pitch directions would be minimal, and this assumption is validated through the greater than 50% suppression seen throughout all Reynolds numbers measured in the Lissajous rotation trials in Chapter 6.2.

B.3 Coupled PD Feedback Control of a Free 3-DOF Model

A proportional-derivative (PD) controller is implemented similar to the PID controller used for controlling the 1-DOF bluff body model (cf., **B.1**), which uses the difference between the prescribed and actual (measured) coordinates, ($\alpha_{y,goal}$, $\alpha_{z,goal}$), and (α_y,α_z), as a proportional error for feedback. The derivative of this error is calculated numerically through a low-pass filter. This controller (Figure B.4) updates at a rate of 1,000 Hz (the same update frequency as the wire traverse). Two command signals are created using a weighted superposition with four respective controller coefficients ($\kappa_{D,y}$ and $\kappa_{P,y}$ for pitch, and $\kappa_{D,z}$ and $\kappa_{P,z}$ for yaw), to determine the needed magnitudes of actuation in the pitch and yaw directions. These two command signals are then divided into four jet activation signals dependent on the roll angle of the model (for instance, if jets 1 and jet 3 are aligned with the vertical axis, their activation would only be determined by the pitch command, and the activation of jets 2 and 4 would only be determined by the yaw command), and in general

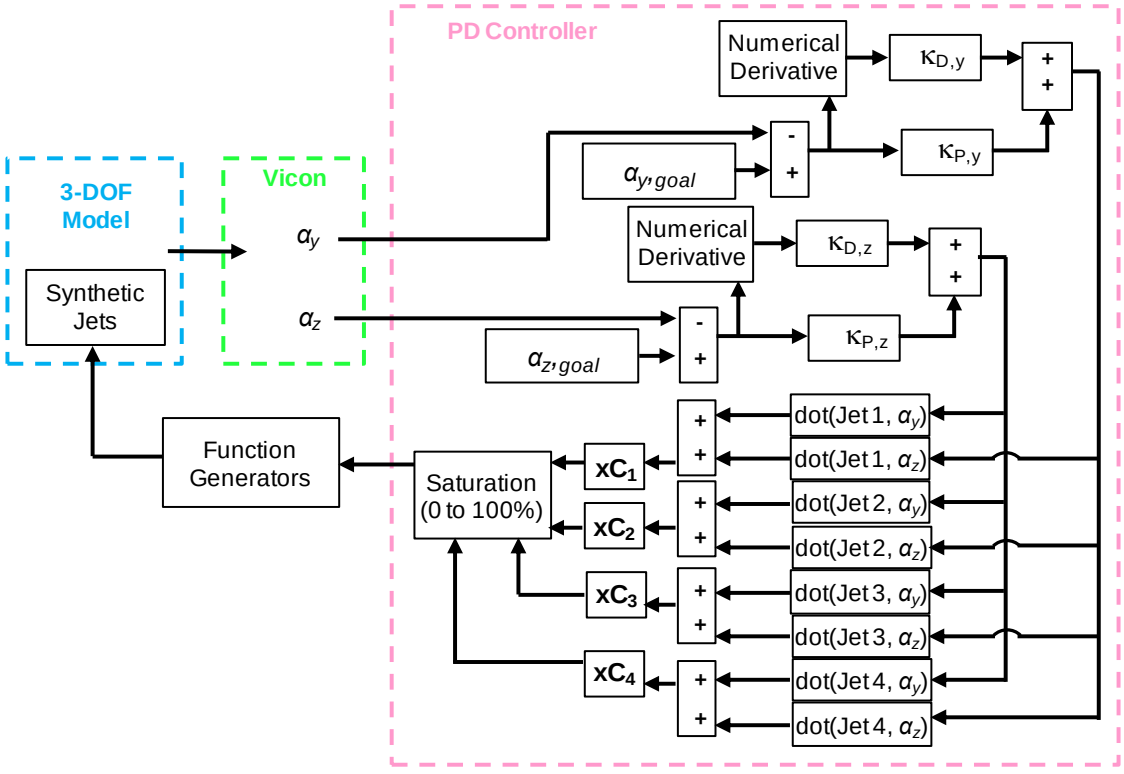

Figure B.4. Schematics of the closed-loop dual PD controller for the 3-DOF model.

all four jet activation signals are effected by each command signal. Additionally, the jets relative amplitudes are also allowed to be scaled by C_1, C_2, C_3, and C_4 coefficients in the controller, to correct for their relative strength. These jet signals are then saturated from 0 to 100% (i.e., they can only apply force in one direction and can never be negative or larger than their maximum expulsion force). The resultant signals are sent as amplitude modulation signals to external function generators and corresponding amplifiers to transform each signal into an actuation wave packet for a synthetic jet (with the same carrier frequency of f_{act} = 0.9 kHz), where the maximum modulation amplitude corresponds to an output jet momentum coefficient of C_μ = 0.003.

For the pitch or yaw amplification control, a typical PD controller response would be dependent on the magnitude of the desired pitch, and therefore, to implement the maximum amplification, the preferred goal (say, pitch) is instead set to 0° and the controller coefficients determining the pitch motion ($\kappa_{P,y}$ and $\kappa_{D,y}$) are multiplied by -1, causing the controller to drive the model to its maximum instability in pitch around 0°. For this amplification, the yaw would still be set to a goal of 0° with controller coefficients remaining the same for stabilization in that axis. If amplify yaw is implemented instead, the same inversion of the yaw controller coefficients are inverted ($\kappa_{P,z}$ and $\kappa_{D,z}$) while leaving the pitch coefficients the same for stabilization around 0°.

REFERENCES

Abramson, P., Vukasinovic, B., and Glezer, A. “Direct Measurements of Controlled Aerodynamic Forces on a Wire-Suspended Axisymmetric Body.” *Experiments in Fluids*, 50.6 (2011): 1711-1725.

Abramson, P., Vukasinovic B., and Glezer, A. "Fluidic Control of Aerodynamic Forces on a Bluff Body of Revolution." *AIAA Journal*, 50.4 (2012): 832-843.

Abruzzo, B. A., and Recchia, T. G. (2016). “Online Calibration of Inertial Sensors for Range Correction of Spinning Projectiles.” *Journal of Guidance, Control, and Dynamics*, 39.8 (2016): 1922-1924.

Achenbach, E. “Experiments on the Flow Past spheres at Very High Reynolds Numbers.” *Journal of Fluid Mechanics*, 54.3 (1972): 565-575.

Achenbach, E. “Vortex Shedding from Spheres.” *Journal of Fluid Mechanics*, 62.2 (1974): 209-221.

Amitay, M., Honohan, A., Trautman, M., and Glezer, A. “Modification of the Aerodynamic Characteristics of Bluff Bodies using Fluidic Actuators.” *28th AIAA Fluid Dynamics Conference* (1997).

Amitay, M., Smith, D. R., Kibens, V., Parekh, D. E., and Glezer, A. “Aerodynamic Flow Control Over an Unconventional Airfoil Using Synthetic Jet Actuators. *AIAA Journal*, 39.3 (2001): 361-370.

Amitay, M., and Glezer, A. “Role of Actuation Frequency in Controlled Flow Reattachment Over a Stalled Airfoil.” *AIAA Journal*, 40.2 (2002): 209-216.

Amitay, M., and Glezer, A. “Flow Transients Induced on a 2D Airfoil by Pulse-Modulated Actuation.” *Experiments in Fluids*, 40.2 (2006): 329-331.

Ausseur, J., Pinier, J., and Glauser, M. “Flow Separation Control Using a Convection Based POD Approach.” *3rd AIAA Flow Control Conference* (2006).

Bacon, D. L. “Model Supports and Their Effects on the Results of Wind Tunnel Tests.” *NACA Technical Notes*, 130 (1923).

Barrett, R. “Aeroservoelastic DAP Missile Fin Development.” *Smart Materials and Structures*, 2.2 (1993): 55-65.

Barrett, R. M., and Lee, G. M. "Design and Testing of Piezoelectric Flight Control Actuators for Hard-Launch Munitions." *Smart Structures and Materials 2004: Smart Structures and Integrated Systems* (2004).

Bearman, P. W., and Harvey, J. K. "Control of Circular Cylinder Flow by the Use of Dimples." *AIAA Journal*, 31.10 (1993): 1753-1756.

Berger, E., and Wille, R. "Periodic Flow Phenomena." *Annual Review of Fluid Mechanics*, 4.1 (1972): 313-340.

Berger, E., Scholz, D., and Schumm, M. "Coherent Vortex Structures in the Wake of a Sphere and a Circular Disk at Rest and Under Forced Vibrations." *Journal of Fluids and Structures*, 4.3 (1990): 231-257.

Berkooz, G., Holmes, P., and Lumley, J. L. "The Proper Orthogonal Decomposition in the Analysis of Turbulent Flows. *Annual Review of Fluid Mechanics*, 25.1 (1993): 539-575.

Beyers, M. E. "Unsteady Wind-Tunnel Interference in Aircraft Dynamic Experiments." *Journal of Aircraft*, 29.6 (1992): 1122-1129.

Bisplinghoff, R. L., Ashley, H., and Halfman, R. L. *Aeroelasticity*. Dover Publication Incorporated (1996).

Bohorquez, P., Sanmiguel-Rojas, E., Sevilla, A., Jimenez-Gonzalez, J. I., and Martinez-Bazan, C. "Stability and Dynamics of the Laminar Wake Past a Slender Blunt-Based Axisymmetric Body." *Journal of Fluid Mechanics*, 676 (2011): 110-144.

Brika, D., and Laneville, A. "Vortex-Induced Vibrations of a Long Flexible Circular Cylinder." *Journal of Fluid Mechanics*, 250 (1993): 481-508.

Brücker, C. "Spatio-Temporal Reconstruction of Vortex Dynamics in Axisymmetric Wakes." *Journal of Fluids and Structures*, 15.3 (2001): 543-554.

Brzozowski, D. P., Culp, J. R., Kutay, A. T., Muse, J. A., and Glezer, A. "Closed-Loop Aerodynamic Flow Control of a Free Airfoil." *4th AIAA Flow Control Conference* (2008).

Brzozowski, D. P. "Dynamic Control of Aerodynamic Forces on a Moving Platform Using Active Flow Control." *PhD Dissertation*. Georgia Institute of Technology (2011).

Carberry, J., and Sheridan, J. "Wake States of a Tethered Cylinder." *Journal of Fluid Mechanics*, 592 (2007): 1-21.

Chen, W. L., Xin, D. B., Xu, F., Li, H., Ou, J. P., and Hu, H. "Suppression of Vortex-Induced Vibration of a Circular Cylinder Using Suction-Based Flow Control." *Journal of Fluids and Structures*, 42 (2013): 25-39.

Choi, H., Jeon, W. P., and Kim, J. "Control of Flow Over a Bluff Body." *Annual Review of Fluid Mechanics*, *40* (2008): 113-139.

Chomaz, J. M., Huerre, P., and Redekopp, L. G. "Bifurcations to Local and Global Modes in Spatially Developing Flows." *Physical Review Letters*, *60*.1 (1988): 25-28.

Corke, T. C., Tillotson, D., Patel, M. P., Su, W. J., and Toledo, W. (2008). "Radius Flow Vectoring for Projectile Drag and Steering Control Using Plasma Actuators." *4th AIAA Flow Control Conference* (2008).

Englar, R. J. "Circulation Control Pneumatic Aerodynamics: Blown Force and Augmentation and Modification - Past, Present and Future." *AIAA Fluids 2000 Conference and Exhibit* (2000).

Ericsson, L. E., and Reding, J. P. "Review of Support Interference in Dynamic Tests." *AIAA Journal*, 21.12 (1983): 1652-1666.

Every, M. J., King, R., and Weaver, D. S. "Vortex-Excited Vibrations of Cylinders and Cables and Their Suppression. *Ocean Engineering*, 9.2 (1982): 135-157.

Feng, C. C. "The Measurement of Vortex Induced Effects in Flow Past Stationary and Oscillating Circular and D-Section Cylinders." *PhD dissertation*, University of British Columbia (1968).

Feng, L. H., Wang, J. J., and Pan, C. "Effect of novel synthetic jet on wake vortex shedding modes of a circular cylinder." *Journal of Fluids and Structures*, 26.6 (2010): 900-917.

Flemming, F., and Williamson, C. H. K. "Vortex-Induced Vibrations of a Pivoted Cylinder." *Journal of Fluid Mechanics*, 522 (2005): 215-252.

Fresconi, F., and Plostins, P. "Control Mechanism Strategies for Spin-Stabilized Projectiles. *Proceedings of the Institution of Mechanical Engineers, Part G: Journal of Aerospace Engineering*, 224.9 (2010): 979-991.

Freund, J. B., and Mungal, M. G. "Drag and Wake Modification of Axisymmetric Bluff Bodies Using Coanda Blowing." *Journal of Aircraft*, 31.3 (1994): 572-578.

Frost, G., and Costello, M. "Linear Theory of a Rotating Internal Part Projectile Configuration in Atmospheric Flight." *Journal of Guidance, Control, and Dynamics*, 27.5 (2004): 898-906.

Gilka, G., Luchtenburg, D. M., Thiele, F., and Morzynski, M. “Dynamic Characterization of an Actuated Bluff Body Wake.” 5th *European Conference on Computational Fluid Dynamics, ECCOMAS CFD* (2010).

Govardhan, R., and Williamson, C. H. K. “Resonance Forever: Existence of a Critical Mass and an Infinite Regime of Resonance in Vortex-Induced Vibration.” *Journal of Fluid Mechanics*, 473 (2002): 147-166.

Goyta, S., Mueller-Vahl, H., and Greenblatt, D. “Tethered Cube Stabilization by Means of Leading-Edge DBD Plasma Actuation.” *Experiments in Fluids*, 54.1 (2013): 1-16.

Griffin, S., Crooks, R., and Mole, P. “Vane Support System (VSS) - A New Generation Wind Tunnel Model Support System.” *29th AIAA Aerospace Sciences Meeting* (1991).

Guilmineau, E. “Computational Study of Flow Around a Simplified Car Body.” *Journal of Wind Engineering and Industrial Aerodynamics*, 96.6 (2008): 1207-1217.

Harkins, T. E., and Brown, T. G. “Using Active Damping as a Precision-Enhancing Technology for 2.75-Inch Rockets.” *US Army Research Laboratory, ARL-TR-1772* (1999).

Higuchi, H., Sawada, H., and Kato, H. “Sting-Free Measurements on a Magnetically Supported Right Circular Cylinder Aligned with the Free Stream.” *Journal of Fluid Mechanics*, 596 (2008): 49-72.

Hoerner, S. F. *Fluid-Dynamic Drag: Practical Information on Aerodynamic Drag and Hydrodynamic Resistance*. Hoerner Fluid Dynamics (1965).

Honohan, A. M., Amitay, M., and Glezer, A. “Aerodynamic Control Using Synthetic Jets.” *AIAA Fluids 2000 Conference and Exhibit* (2000).

Hotelling, H. “Analysis of a Complex of Statistical Variables into Principal Components.” *Journal of Educational Psychology*, 24.6 (1933): 417-520.

Hsiao, F. B., Shyu, J. Y., and Liu, C. F. “Control of Wall-Separated Flow by Internal Acoustic Excitation.” *AIAA Journal*, 28.8 (1990): 1440-1446.

Huerre, P., and Monkewitz, P. A. “Local and Global Instabilities in Spatially Developing Flows.” *Annual Review of Fluid Mechanics*, 22.1 (1990): 473-537.

Jitpraphai, T., and Costello, M. “Dispersion Reduction of a Direct Fire Rocket Using Lateral Pulse Jets.” *Journal of Spacecraft and Rockets*, 38.6, (2001): 929-936.

Kearney, J. M. “Active Control Using Distributed Active Bleed.” *PhD Dissertation*. Georgia Institute of Technology (2015).

Kim, I., and Pearlstein, A. J. “Stability of the Flow Past a Sphere.” *Journal of Fluid Mechanics*, 211 (1990): 73-93.

Kim, J., and Choi, H. (2005). “Distributed Forcing of Flow Over a Circular Cylinder.” *Physics of Fluids (1994-Present)*, 17.3 (2005).

Kosambi, D. D. “Statistics in Function Space.” *Journal of Indian Mathematics Society*, *7*.1 (1943): 76-88.

Kostas, J., Soria, J., and Chong, M. S. “A Comparison Between Snapshot POD Analysis of PIV Velocity and Vorticity Data.” *Experiments in Fluids*, 38.2 (2005): 146-160.

Krakovich, A., Eshbal, L., and van Hout, R. “Vortex Dynamics and Associated Fluid Forcing in the Near Wake of a Light and Heavy Tethered Sphere in Uniform Flow.” *Experiments in Fluids*, 54.11 (2013): 1-17.

Lambert, T. J., Vukasinovic, B., and Glezer, A. “Unsteady Aerodynamic Flow Control of a Wire-Suspended, Moving Axisymmetric Body.” *50th AIAA Aerospace Sciences Meeting* (2012).

Lambert, T. J., Vukasinovic, B., and Glezer, A. “Yaw Control of a Moving Axisymmetric Body using Synthetic Jets.” *51st AIAA Aerospace Sciences Meeting* (2013).

Lambert, T. J., Vukasinovic, B., and Glezer, A. “Aerodynamic Flow Control of a Moving Axisymmetric Bluff Body.” *52nd AIAA Aerospace Sciences Meeting* (2014).

Lambert, T. J., Vukasinovic, B., and Glezer, A. “Unsteady Aerodynamic Loads Effected by Flow Control on a Moving Axisymmetric Bluff Body.” *53rd AIAA Aerospace Sciences Meeting* (2015a).

Lambert, T. J., Vukasinovic, B., and Glezer, A. “Active Decoupling of the Axisymmetric Body Wake Response to a Pitching Motion.” *Journal of Fluids and Structures*, 59, (2015b): 129-145.

Lambert, T. J., Vukasinovic, B., and Glezer, A. “Aerodynamic Control of Coupled Body-Wake Interactions.” *54th AIAA Aerospace Sciences Meeting* (2016a).

Lambert, T. J., Vukasinovic, B., and Glezer, A. “A Six Degrees of Freedom Dynamic Wire-Driven Traverse.” *Aerospace*, 3.2 (2016b): 11.

Lambert, T. J., Vukasinovic, B., and Glezer, A. “Aerodynamic Flow Control of Wake Dynamics Coupled to a Moving Bluff Body.” *8th AIAA Flow Control Conference* (2016c).

Leishman, G. J. *Principles of Helicopter Aerodynamics with CD Extra*. Cambridge University Press (2006).

Leonard, A., and Roshko, A. “Aspects of Flow-Induced Vibration.” *Journal of Fluids and Structures*, 15.3 (2001): 415-425.

Leu, T. S., and Ho, C. M. “Control of Global Instability in a Non-Parallel Near Wake.” *Journal of Fluid Mechanics*, 404 (2000): 345-378.

Lumley, J. L. “The Structure of Inhomogeneous Turbulent Flows.” *Atmospheric Turbulence and Radio Wave Propagation* (1967): 166-178.

Ma, X., and Karniadakis, G. E. “A Low-Dimensional Model for Simulating Three-Dimensional Cylinder Flow.” *Journal of Fluid Mechanics*, 458 (2002): 181-190.

Massey, K., and Flick, A. “Mechanical and Jet Actuators for Guiding a Small Caliber Subsonic Projectile.” *25th AIAA Applied Aerodynamics Conference* (2007).

McMichael, J., Lovas, A., Plostins, P., Sahu, J., Brown, G., and Glezer, A. *Microadaptive Flow Control Applied to a Spinning Projectile*. Army Research Laboratory (2004).

Mittal, R., and Najjar, F. M. “Vortex Dynamics in the Sphere Wake.” *30th AIAA Fluid Dynamics Conference* (1999).

Monkewitz, P. A., and Nguyen, L. N. “Absolute Instability in the Near-Wake of Two-Dimensional Bluff Bodies.” *Journal of Fluids and Structures*, 1.2 (1987): 165-184.

Munshi, S. R., Modi, V. J., and Yokomizo, T. “Fluid Dynamics of Flat Plates and Rectangular Prisms in the Presence of Moving Surface Boundary-Layer Control.” *Journal of Wind Engineering and Industrial Aerodynamics*, 79.1 (1999): 37-60.

Murphy, C. H. “Symmetric Missile Dynamic Instabilities.” *Journal of Guidance, Control, and Dynamics*, 4.5 (1981): 464-471.

Murphy, C. H. “Some Special Cases of Spin-Yaw Lock-In.” *Journal of Guidance, Control, and Dynamics*, 12.6 (1989): 771-776.

Nagib, H. M., Reisenthel, P. H., and Koga, D. J. “On the Dynamical Scaling of Forced Unsteady Separated Flows.” *AIAA Shear Flow Control Conference* (1985).

Naghib-Lahouti, A., Lavoie, P., and Hangan, H. “Wake Instabilities of a Blunt Trailing Edge Profiled Body at Intermediate Reynolds Numbers.” *Experiments in Fluids*, 55.7 (2014): 1-15.

Nemat-Nasser, S., and Guo, W. G. “Superelastic and Cyclic Response of NiTi SMA at Various Strain Rates and Temperatures.” *Mechanics of Materials*, 38.5 (2006): 463-474.

Newman, B. G. “The Deflection of Plane Jets by Adjacent Boundaries—Coanda Effect.” *Boundary Layer and Flow Control*, 1 (1961): 232-264.

Nicolaides, J. “A History of Ordnance Flight Dynamics.” *AIAA Atmospheric Flight Mechanics Conference* (1970).

Obukhov, A. M. “Statistical Description of Continuous Fields.” *Trudy Geofizicheskogo Instituta, Akademiya Nauk SSSR*, 24, (1954): 3-42.

Oertel Jr., H. “Wakes Behind Blunt Bodies.” *Annual Review of Fluid Mechanics*, 22.1 (1990): 539-562.

Ollerenshaw, D., and Costello, M. “Simplified Projectile Swerve Solution for General Control Inputs.” *Journal of Guidance, Control, and Dynamics*, 31.5 (2008): 1259-1265.

Pattinson, J., Lowenberg, M. H., and Goman, M. G. “Multi-Degree-of-Freedom Wind-Tunnel Maneuver Rig for Dynamic Simulation and Aerodynamic Model Identification.” *Journal of Aircraft*, 50.2 (2012): 551-566.

Platou, A. S. “Magnus Characteristics of Finned and Nonfinned Projectiles.” *AIAA Journal*, 3.1 (1965): 83-90.

Ploumhans, P., Winckelmans, G. S., Salmon, J. K., Leonard, A., and Warren, M. S. “Vortex Methods for Direct Numerical Simulation of Three-Dimensional Bluff Body Flows: Application to the Sphere at Re= 300, 500, and 1000.” *Journal of Computational Physics*, 178.2 (2002): 427-463.

Pugachev, V. S. “The General Theory of Correlation of Random Functions.” *Izvestiya Rossiiskoi Akademii Nauk. Seriya Matematicheskaya*, 17.5 (1953): 401-420.

Price, Jr., D. A. “Sources, Mechanisms, and Control of Roll Resonance Phenomena for Sounding Rockets.” *Journal of Spacecraft and Rockets*, 4.11 (1967): 1516-1525.

Prosser, D. T., and Smith, M. J. “A Physics-Based, Reduced-Order Aerodynamics Model for Bluff Bodies in Unsteady, Arbitrary Motion.” *Journal of the American Helicopter Society*, 60.3 (2015): 1-15.

Raffel, M., Willert, C., and Kompenhans, J. *Particle Image Velocimetry: A Practical Guide*. Verlag, Berlin (1998)

Rigas, G., Oxlade, A. R., Morgans, A. S., and Morrison, J. F. (2014). Low-dimensional dynamics of a turbulent axisymmetric wake. *Journal of Fluid Mechanics*, *755*, R5.

Rinehart, C., McMichael, J. M., and Glezer, A. “Transitory Flow and Force Development on a Body of Revolution Using Synthetic Jet Actuation.” *41st AIAA Aerospace Sciences Meeting* (2003).

Rinehart, C. S. “Aerodynamic Forces Induced by Controlled Transitory Flow on a Body of Revolution.” *PhD Dissertation*. Georgia Institute of Technology (2011).

Rival, D., and Tropea, C. “Characteristics of Pitching and Plunging Airfoils Under Dynamic-Stall Conditions.” *Journal of Aircraft*, 47.1 (2010): 80-86.

Rogers, J., and Costello, M. “Flight Dynamics and Control Authority of a Projectile Equipped with a Controllable Internal Translating Mass.” *AIAA Atmospheric Flight Mechanics Conference and Exhibit* (2007).

Roshko, A. "On the Development of Turbulent Wakes from Vortex Streets." *Journal of the Aeronautical Sciences*, 22.2 (1955): 124-132.

Sahu, J. *Time-Accurate Computations of Free-Flight Aerodynamics of a Spinning Projectile with and without Flow Control*. Army Research Laboratory (2006).

Sakamoto, H., and Haniu, H. “A Study on Vortex Shedding from Spheres in a Uniform Flow.” *Journal of Fluids Engineering*, 112.4 (1990): 386-392.

Sanmiguel-Rojas, E., Sevilla, A., Martínez-Bazán, C., Chomaz, J. M., "Global Mode Analysis of Axisymmetric Bluff-Body Wakes: Stabilization by Base Bleed." *Physics of Fluids (1994-Present)*, 21.11 (2009).

Sarioglu, M., Akansu, Y. E., and Yavuz, T. “Control of the Flow Around Square Cylinders at Incidence by Using a Rod.” *AIAA Journal*, 43.7 (2005): 1419-1426.

Schmid, P. J., Meyer, K. E., and Pust, O. “Dynamic Mode Decomposition and Proper Orthogonal Decomposition of Flow in a Lid-Driven Cylindrical Cavity. *8th International Symposium on Particle Image Velocimetry* (2009).

Schmid, P. J. “Dynamic Mode Decomposition of Numerical and Experimental Data.” *Journal of Fluid Mechanics*, 656 (2010): 5-28.

Schumm, M., Berger, E., and Monkewitz, P. A. “Self-Excited Oscillations in the Wake of Two-Dimensional Bluff Bodies and their Control.” *Journal of Fluid Mechanics*, 271 (1994):17-53.

Sigurdson, L. W. “The Structure and Control of a Turbulent Reattaching Flow.” *Journal of Fluid Mechanics*, 298 (1995): 139-165.

Simpson, M. W. “Buoyancy-Induced, Columnar Vortices with Application to Power Generation. *PhD Dissertation*. Georgia Institute of Technology (2015).

Sirovich, L. “Turbulence and the Dynamics of Coherent Structures Part I: Coherent Structures.” *Quarterly of Applied Mathematics*, 45.3 (1987): 561-571.

Strykowski, P. J., and Sreenivasan, K. R. “On the Formation and Suppression of Vortex ‘Shedding’ at Low Reynolds Numbers.” *Journal of Fluid Mechanics*, 218 (1990): 71-107.

Taylor, G. S., Gursul, I., and Greenwell, D. I. “Investigation of Support Interference in High-Angle-of-Attack Testing.” *Journal of Aircraft*, 40.1 (2003): 143-152.

Tu, J. H., and Rowley, C. W. “An Improved Algorithm for Balanced POD Through an Analytic Treatment of Impulse Response Tails.” *Journal of Computational Physics*, 231.16 (2012): 5317-5333.

Tu, Jonathan H. “Dynamic Mode Decomposition: Theory and Applications.” *PhD Dissertation*, Princeton University (2013).

Tuttle, M. H., and Gloss, B. B. “Support Interference of Wind Tunnel Models: A Selective Annotated Bibliography.” *NASA Technical Memorandum*, 81909 (1981).

Weickgenannt, A., and Monkewitz, P. A. “Control of Vortex Shedding in an Axisymmetric Bluff Body Wake.” *European Journal of Mechanics-B/Fluids*, 19.5 (2000): 789-812.

Williams, D. R., Acharya, M., Bernhardt, J., and Yang, P. “The Mechanism of Flow Control on a Cylinder with the Unsteady Bleed Technique.” *29th AIAA Aerospace Sciences Meeting* (1991).

Williamson, C. H. K., and Roshko, A. “Vortex Formation in the Wake of an Oscillating Cylinder.” *Journal of Fluids and Structures*, *2*.4 (1988): 355-381.

Williamson, C. H. K. “Three-Dimensional Vortex Dynamics in Bluff Body Wakes.” *Experimental Thermal and Fluid Science*, 12.2 (1996): 150-168.

Williamson, C. H. K., and Govardhan, R. “Vortex-Induced Vibrations.” *Annual Review of Fluid Mechanics*, 36, (2004): 413-455.

Woo, G. T. K., Crittenden, T., and Glezer, A. “Transitory Control of a Pitching Airfoil Using Pulse Combustion Actuation.” *4th AIAA Flow Control Conference* (2008).

Woo, G. T. K. “Transitory Control of Separated Shear Layer Using Impulsive Jet Actuation.” *PhD Dissertation*. Georgia Institute of Technology (2014).

Zdravkovich, M. M. “Review and Classification of Various Aerodynamic and Hydrodynamic Means for Suppressing Vortex Shedding.” *Journal of Wind Engineering and Industrial Aerodynamics*, 7.2 (1981): 145-189.

VITA

Thomas John Lambert was born in Henderson, Nevada to Joan Dickie and Robert Henry Lambert. He grew up with an older brother Robert Michael, and they took frequent trips while young to visit extended family on their mother's side in Baltimore, Maryland, and extended family on their father's side in Alden, Michigan. Thomas attended Carnegie Mellon in Pittsburgh, Pennsylvania in 2006 and achieved B.S. degrees in Mechanical Engineering and Physics in 2010. In Fall of 2010, he attended Georgia Institute of Technology to pursue his doctorate in Mechanical Engineering and shortly afterward joined Professor Ari Glezer's Fluid Mechanics Research Laboratory. During his time at Georgia Tech, he earned an M.S. in Mechanical Engineering in Fall of 2013. Throughout his time in the Fluid Mechanics Research Laboratory, he published two peer-reviewed journal manuscripts and eight conference proceedings, one of which was recently named best paper for the 8th AIAA Flow Control Conference in 2016.